Quantum control of molecular spins using Electron Spin Resonance

Jakub Mrożek

Magdalen College
University of Oxford

A thesis submitted for the degree of Doctor of Philosophy

Hilary 2022

Abstract

Molecular magnets have been demonstrated to be promising candidates for quantum-coherent nanodevices, due to their long relaxation times and design flexibility. Building and scaling such devices presents several challenges. In this thesis, two problems related to scalability of molecular magnet architectures are investigated using electron spin resonance.

Using electric fields, rather than magnetic fields, to operate quantum devices, would radically improve addressability of individual spins. Electric field sensitivities of several molecular magnets, including frustrated Cu_3 triangles, Cr_7Ni and Cr_7Mn rings and crystals of HoW_{10} complexes, are investigated through pulse sequences incorporating static electric fields. We find spin-electric couplings of various magnitudes, significant enough to manipulate the parameters of respective Hamiltonians to enable selective excitation and we demonstrate such excitation in the HoW_{10} molecule. We identify a path towards improving electric field sensitivities, through coupling structural distortions exhibiting high electric polarizability with the molecular spin Hamiltonian.

To operate assemblies of multiple molecular magnets as quantum devices, robust multiqubit gates, able to modify the amount of entanglement in the system, need to be implemented. Quantum state tomography may be employed to investigate the practical fidelity of such a gate and real entanglement it generates. Focusing on a weakly coupled dimer of two spin-$\frac{1}{2}$ molecules, we propose an implementation of a two-qubit entangling gate followed by quantum state tomography using ensemble electron spin resonance. We investigate the limitations and requirements of the gate and the tomography procedure through theoretical arguments, simulations and experiments. We conclude that while challenging, reaching and demonstrating actual entanglement is within our capabilities using ensembles of molecular magnet dimers.

Quantum control of molecular spins using Electron Spin Resonance



Jakub Mrożek

Magdalen College

University of Oxford

A thesis submitted for the degree of

Doctor of Philosophy

Hilary 2022

Acknowledgements

Personal

This thesis would not be possible without the immense support I received during my time in Oxford. This is the place where I express my gratitude towards the most important contributors.

Firstly, I would like to thank my supervisor Prof Arzhang Ardavan for his positivity, optimism, his ability to always motivate me and make me excited and fall in love with physics, especially when the experiments were not going well. I am grateful to Arzhang for cultivating a friendly atmosphere in the group, being able to always explain the most complicated concepts in a simple manner, directing and daring me to take challenges and simply always being there when I needed him.

I would like to thank Dr Junjie Liu for always supporting me with his hands-on expertise, many shared experimental sessions in CAESR, his great sense of humour, and numerous acts of kindness, like bringing my badly made poster to my first big conference in London.

Dr Will Myers was always ready to provide support and guidance when it comes to technical matters, and he was very patient with me constantly breaking things, so I owe him a huge thank you. I would also like to thank Dr Alice Bowen for teaching me DEER, the discussions we had about the tomography procedure and overall help, and Edmund Little for our measurement sessions, great ideas and pushing to continue with this project.

Thank you to Leonie Woodland and Zhiwei Dai for great work and giving me one more reason to come to the lab every day. I would also like to thank people who I have worked with very little or not at all, but who nevertheless taught me something and provided companionship in the Physics Department: Fran, Matt B., Dave, Sandoko, Matthew S., Gabriel, Misha, Miska, Viviane, Brian, Henrik, Anu, Mariella, and many others.

Thank you to all my friends, especially all the Poles from the Oxford Polish Society, and all the dancers from Oxford's salsa and bachata scene, these two groups and individuals within them were a source of much needed entertainment and support, accepted me and made me feel at home in this beautiful city. There is no space to list everybody, but I am going to highlight my COVID cycling companions

Zuza and Aleks, my gym buddy Marta, my dancing teachers Sergio and Brennan, and the master organizer, salsa DJ, friend and emergency landlord Gwyneth.

I would like to thank my parents for always believing in me, even when I did not believe in myself.

Lastly, I would like to thank everybody who is reading this right now, especially if they are not obligated to do so. You were a major source of motivation to write this document.

Abstract

Molecular magnets have been demonstrated to be promising candidates for quantum-coherent nanodevices, due to their long relaxation times and design flexibility. Building and scaling such devices presents several challenges. In this thesis, two problems related to scalability of molecular magnet architectures are investigated using electron spin resonance.

Using electric fields, rather than magnetic fields, to operate quantum devices, would radically improve addressability of individual spins. Electric field sensitivities of several molecular magnets, including frustrated Cu_3 triangles, Cr_7Ni and Cr_7Mn rings and crystals of HoW_{10} complexes, are investigated through pulse sequences incorporating static electric fields. We find spin-electric couplings of various magnitudes, significant enough to manipulate the parameters of respective Hamiltonians to enable selective excitation and we demonstrate such excitation in the HoW_{10} molecule. We identify a path towards improving electric field sensitivities, through coupling structural distortions exhibiting high electric polarizability with the molecular spin Hamiltonian.

To operate assemblies of multiple molecular magnets as quantum devices, robust multiqubit gates, able to modify the amount of entanglement in the system, need to be implemented. Quantum state tomography may be employed to investigate the practical fidelity of such a gate and real entanglement it generates. Focusing on a weakly coupled dimer of two spin-$\frac{1}{2}$ molecules, we propose an implementation of a two-qubit entangling gate followed by quantum state tomography using ensemble electron spin resonance. We investigate the limitations and requirements of the gate and the tomography procedure through theoretical arguments, simulations and experiments. We conclude that while challenging, reaching and demonstrating actual entanglement is within our capabilities using ensembles of molecular magnet dimers.

Contents

List of Figures **xi**

List of Abbreviations **xv**

1 Introduction **1**
1.1 Motivation 1
1.2 Structure of this thesis 3

2 Foundations of Electron Spin Resonance **7**
2.1 General Spin Hamiltonian 8
2.1.1 Zeeman terms 9
2.1.2 Dipolar interaction 10
2.1.3 Exchange interaction 12
2.1.4 Hyperfine interaction 13
2.1.5 Higher order terms 13
2.2 Spin ensemble and thermal state 15
2.3 Pulsed ESR 16
2.3.1 Pulse ESR instrumentation 16
2.3.2 Quantum description of the spin state 20
2.3.3 Liouville space and product operators 21
2.3.4 Rotating frame and other interaction pictures 22
2.3.5 Pulses as operators 24
2.3.6 Hahn Echo 27
2.4 Relaxation 28
2.4.1 Longitudinal relaxation 29
2.4.2 Transverse relaxation 30
2.5 Selected pulsed ESR experiments 32
2.5.1 Echo-detected field sweep 32
2.5.2 Nutation and bandwidth measurement 33
2.5.3 Pulse calibration 34
2.6 Continuous Wave ESR 35
2.6.1 Modulation 35

3 Molecular magnets as qubits **37**
3.1 Molecular magnets and quantum computers 37
3.1.1 Well defined and scalable qubits 38
3.1.2 Operation and quantum gates 39
3.1.3 Initialization and readout 41
3.1.4 Relaxation and error correction 42
3.2 Properties of Cr_7Ni and Cr_7Mn molecular magnet rings 42
3.3 Properties of HoW_{10} crystals 44
3.3.1 Clock transitions and symmetry breaking in HoW_{10} crystals 47

4 Electric fields and ESR **49**
4.1 Motivation 49
4.2 Spin Electric Coupling Hamiltonians 50
4.2.1 The role of inversion symmetry 51
4.2.2 Breaking of chirality under electric fields 52
4.3 Detecting a Spin Electric Coupling using ESR 53
4.3.1 Continuous wave ESR 54
4.3.2 Pulsed ESR under static electric field 55
4.3.3 Using non-resonant E-field manipulation to enhance selectability in devices 59

5 Dynamics of dimer spin-$\frac{1}{2}$ systems **61**
5.1 Mathematics of a two spin-$\frac{1}{2}$ system 62
5.1.1 Hamiltonian of a two spin-$\frac{1}{2}$ system 62
5.1.2 Rotating frames 62
5.2 Fidelity and an amount of entanglement as metrics 64
5.2.1 State fidelities 65
5.2.2 Process fidelity 67
5.2.3 Positive partial transpose and log-negativity 67
5.3 NMR quantum computing 68
5.3.1 Pure, pseudo-pure states and entanglement 69
5.3.2 Entangling gate 70
5.3.3 NMR readout and state tomography 72
5.4 Double Electron-Electron Resonance 73
5.4.1 DEER pulse sequences 74
5.4.2 DEER background 75
5.4.3 Orientational averaging of the dipolar interaction 76
5.4.4 Low temperature DEER 78

6 Investigation of the Spin Electric Coupling in molecular magnets 81
6.1 Spin Electric Coupling in exchange coupled systems 82
6.1.1 Spin Electric Coupling in Cu_3 complexes 82
6.1.2 Spin Electric Couplings in Cr_7Ni and Cr_7Mn rings 86
6.2 Spin Electric Coupling in the HoW_{10} complex 88
6.2.1 Experimental setup 89
6.2.2 Origins of Spin Electric Coupling 91
6.2.3 Orientational dependence of Spin Electric Coupling 93
6.2.4 Implementing an A-gate using the SEC in the HoW_{10} complex 96
6.3 Future directions 98

7 Two-qubit entangling gate in a molecular dimer system using ESR 101
7.1 Definition of the problem 102
7.2 Building blocks of the entangling gate 103
7.2.1 Initial state 104
7.3 Tomography 105
7.3.1 DEER-assisted tomography 106
7.3.2 Tomography of the thermal state 112
7.3.3 Fidelity in the high-temperature regime 112
7.4 Simulations of the physical gate fidelity 114
7.4.1 Methodology 114
7.4.2 Effects of the physical interaction 115
7.4.3 Effects of the imperfect gate phases and amplitudes 119
7.4.4 Effects of finite pulse durations 123
7.4.5 Effects of decoherence 129
7.5 Full Spinach simulations of the experiment 130
7.5.1 Methodology 130
7.5.2 Simulation structure 132
7.5.3 Recovering the density matrix from the simulated and experimental time traces 133
7.5.4 Simulation parameters and results 136
7.6 Entanglement experiments 142
7.6.1 Calibration procedures 143
7.6.2 DEER standard measurements 143
7.6.3 Cr_7Ni ring dimer crystals measurements 149
7.7 Future directions 155

Appendices

A Tables **159**
A.1 Extended Stevens Operators 159
A.2 Simulation parameters for isotropic coupled entangling gate tomography 159

B Miscellaneous topics in ESR tomography **161**
B.1 Examples of the NMR and ESR tomography 161
B.1.1 General comments 161
B.1.2 Pure state $|{+}{+}\rangle$ 164
B.1.3 Pure Bell state $\frac{1}{\sqrt{2}}(|00\rangle + |11\rangle)$ 167
B.1.4 Entangling the thermal state 170
B.2 Variable phase tomography equations 173
B.2.1 Evolution equations with variable phase pulses 173
B.2.2 Systematic phase error tomography 174
B.3 Least squares fitting of the parameters in the tomography procedure 175

List of Figures

2.1 Simplified diagram of a pulsed ESR spectrometer 17
2.2 Pulse sequence corresponding to the Hahn echo experiment. 27
2.3 Pulse sequence of the inversion recovery experiment 30
2.4 Example data from an inversion recovery experiment 30
2.5 Measurement of the phase memory time in Cu_3 complex 32
2.6 Pulse sequence of the echo detected transient nutation experiment . 33
2.7 Example data from nutation experiment 34

3.1 Possible structure of a Cr_7M ring molecule (M = Ni, Mn) 43
3.2 Approximate structure of the Ho $(W_5\ O_{18})_2$ complex 46
3.3 Low field energy level diagram of the HoW_{10} molecule 47
3.4 Echo Field Sweep spectra of the HoW_{10} with overlayed calculated transition frequencies 48

4.1 Pulse sequence used in the pulsed ESR investigation of the SEC . . 57
4.2 Pulse sequence to invesigate the linearity of SEC with varying voltage 57
4.3 Pulse sequences for measurements of just the quadratic/linear part of the SEC 58

5.1 Pulse sequence of the entangling gate. 71
5.2 3-pulse DEER pulse sequence 74
5.3 4-pulse DEER pulse sequence 76
5.4 Example 3-pulse DEER data 77

6.1 Probe geometry for E-field measurements with solution samples . . 83
6.2 Molecular structure of $Cu_3(saltag)(py)_6$ 83
6.3 Data from the SEC detection measurements on Cu triangles 85
6.4 Typical data from the SEC detection experiment in Cr_7Mn/Ni rings 86
6.5 Voltage and time dependence of the echo magnitude in Cr_7Mn rings 87
6.6 Magnetic field and voltage dependence of SEC in Cr_7Mn complexes 88
6.7 Data from the SEC detection measurements in HoW_{10} complex . . 91
6.8 Field and frequency dependence of the Spin Electric Coupling in the HoW_{10} complex 93

6.9 Angles describing the frames and vectors in HoW_{10} SEC measurement 94
6.10 Orientational dependence of the Spin Electric Coupling in the HoW_{10} complex 96
6.11 Pulse sequence used for the E-field addressability experiment 97
6.12 Selecting a molecular subpopulation using the E-field 98

7.1 Entangling gate pulse sequence 104
7.2 DEER-assisted tomography sequence 107
7.3 Full entangling gate tomography pulse sequence 110
7.4 Calculations of entanglement properties in dimer spin $\frac{1}{2}$ systems. . . 118
7.5 Parameters of the gate 120
7.6 Effects of a systematic B_1 error on the entangling gate 121
7.7 Parameters of the tomography procedure 122
7.8 Effects of a systematic B_1 and phase error on the tomography procedure 123
7.9 Fidelity and log-negativity of the entangling gate as a function of pulse and overall gate duration 126
7.10 Fidelity and log-negativity of the entangling gate vs gate duration and amplitudes 127
7.11 Example calculated time traces from a tomography process with finite duration $t = 0.2\frac{\pi}{\omega_{ee}}$ pulses 127
7.12 Calculated process fidelity of the tomography with long pulses . . . 128
7.13 Calculations of the systematic effect of the characteristic relaxation times T_1 and T_2, at $0K$ 131
7.14 Fidelities of several simulated systems with isotropic exchange coupling 137
7.15 Example time traces from the simulation of one of the exchange coupled sets of parameters 137
7.16 The magic dimer model 138
7.17 Example simulated time traces of the dipolar magic dimer set of parameters 140
7.18 Fidelities of the final state in the magic dimer 141
7.19 Results of the low temperature tomography simulations 142
7.20 Calibrating the amplitude of a double π pulse 144
7.21 Bis-nitroxide structure 145
7.22 Hahn echo tomography sequence 145
7.23 Absorption spectrum of the bis-nitroxide sample 146
7.24 Selected time traces from the Hahn echo tomography experiment . . 147
7.25 Results of the Hahn echo tomography experiment 147
7.26 Comparison between time traces collected in 1II Hahn echo and 1XY entangling gate measurements 148

7.27 Time traces from the entangling gate tomography experiment with the bis-nitroxide sample 149
7.28 Results of the tomography process applied to the entangling gate at high temperature 150
7.29 The structure of the Cr_7Ni/Ti_7Ga rotaxane crystal 151
7.30 Angle-resolved echo-detected field sweep data collected from the Cr_7Ni dimer system 153
7.31 Selected results of the DEER experiment on the Cr_7Ni dimer crystal 154

List of Abbreviations

AWG . . . . . Arbitrary Waveform Generator

CÆSR . . . . . Centre for Advanced Electron Spin Resonance

CW . . . . . Continuous Wave

DEER . . . . . Double Electron Electron Resonance

3P DEER . . . 3 pulse DEER

4P DEER . . . 4 pulse DEER

EDMR . . . . Electrically Detected Magnetic Resonance

EE . . . . . Electron-Electron

ESO . . . . . Extended Stevens Operators

ESR, EPR . . Electron Spin Resonance / Electron Paramagnetic Resonance

EZ . . . . . Electron Zeeman

FT . . . . . Fourier Transform

HF . . . . . Hyperfine

IST . . . . . Irreducible Spherical Tensors

MPFU . . . . Microwave Pulse Forming Unit

NISQ . . . . . Noisy Intermediate-Scale Quantum (Devices)

NMR . . . . . Nuclear Magnetic Resonance

NQ . . . . . Nuclear Quadrupolar

NZ . . . . . Nuclear Zeeman

PELDOR . . . Paramagnetic Electron Double Resonance

PPT . . . . . Positive Partial Transpose

SEC . . . . . Spin-Electric Coupling

STM . . . . . Scanning Tunelling Microscopy

TWT . . . . . Travelling Wave Tube

ZFS . . . . . Zero-Field Splitting

1 Introduction

Contents

1.1 Motivation 1
1.2 Structure of this thesis 3

1.1 Motivation

Since Feynman's original proposal [1], and later the publication of Grover's [2] and Shor's [3] algorithms, quantum computing has grown into a major pursuit, possibly defining the present era of technology [4]. Through the search for a reliable architecture for quantum computing and development of quantum science, the field broadened to encompass other quantum-coherent phenomena [5] and grew in multiple new directions, including quantum sensing, quantum communication, quantum simulation and storage. As the development of universal quantum computers based on superconducting circuits [6–8], ionic traps [9] or spins in semiconductors [10–12] slowly moves to the industry in the Noisy Intermediate-Scale Quantum (NISQ) [13] era, aiming to obtain quantum supremacy [14, 15], it leaves behind many unique and fascinating alternatives.

A particular one looks at a single molecule, the smallest unit that can be engineered, as its primary focus. A molecular nanomagnet is an artificial molecule, a collection of metallic ions stabilized by organic ligands. It is characterized by a well-defined non-zero ground state spin, whose coherence is protected by its carefully designed geometry. Advances in supramolecular chemistry allow for a precise design of such a molecule, as well as assemblies of multiple molecules. Molecular magnets are interesting because of the flexibility of their structures, allowing for exchange of ligands and ions, and fascinating as they allow the observation of lasting coherent quantum effects on a scale of a molecular cluster.

Molecular magnets were first proposed as a quantum computing architecture over 20 years ago [16, 17] and since then, numerous molecular complexes have been synthesized and characterized. The main characterization tool was Electron Spin Resonance (ESR) [18, 19], which enables insight into low-energy spin Hamiltonians of molecular complexes with unpaired electrons. One of the requirements for quantum computation is long relaxation times [20], and there are now several families of molecular magnets that could be operated and stay coherent long enough to facilitate simple quantum algorithms.

What are the next steps for molecular magnets? Operating single qubits and qudits with long decoherence times is a solid base, from which devices will need to be scaled, either by assembling larger molecular complexes and increasing the dimension of their Hilbert spaces, or by building top-down devices and coupling them with classical electronics [21]. For the scaling to be successful, multiple challenges need to be addressed.

One of them is the issue of driving an individual molecular qubit on a surface, while it is surrounded by other qubits with similar transition frequencies. Magnetic fields naturally interact with the spins, but because they are generated by loops of current and do not have sources or sinks, as miniaturization continues, it will be challenging to constrict them over a selected molecule and not affect its neighbours. Electric fields, on the other hand, do have sources and sinks and only require two electrodes and a voltage across them to be generated. It is for this reason

certain quantum dot architectures already utilize electric fields to drive their qubits [10, 11, 22, 23], and molecular magnet devices using electric fields for driving have been built [24]. In the context of molecular magnets, it is interesting to ask what are the properties of such a molecule that enable strong coupling between its spin and an external electric field. Exploring this topic constitutes the first research project described in this thesis.

As the size of the quantum system increases to multiple qubits, a universal set of quantum gates needs to include gates that are able to generate quantum entanglement between them [25, 26], because without entanglement, quantum computing is not possible [27, 28]. After a successful demonstration of weak dipolar coupling in a dimer spin-$\frac{1}{2}$ system based on two Cr_7Ni molecular nanomagnets, which is sufficient to create entanglement [29], it is time to implement such a gate. Such an implementation needs to be characterized via quantum state tomography procedure, which may be inspired by an analoguous procedure from Nuclear Magnetic Resonance (NMR) [30, 31]. Real entanglement was previously observed between electron and nuclear spins using ESR [32, 33] and two-qubit entangling gates were commonplace in NMR quantum computing. The latter systems were however never truly entangled, as this requires higher purity[1] of the initial state that could ever be achieved in NMR in realistic conditions [34, 35], owing to insufficient polarization of the ensemble thermal state at attainable temperatures. The electron spin is more easily polarizable in external magnetic field, enabling real entanglement resulting from entangling gates operated on high purity initial states. Exploration of this possibility is the topic of the second research project described in this thesis.

1.2 Structure of this thesis

In this thesis, introductory topics have been distributed across 4 background chapters, relating to different aspects of the work presented in the following 2 research chapters.

[1] Defined as $\mathrm{Tr}\left(\rho^2\right)$, where ρ is a density matrix describing a mixed quantum state.

In Chapter 2, basic principles of ESR, the main experimental technique used in this work, are presented and discussed. Concepts crucial for understanding and analysis the experiments and simulations performed are introduced.

In Chapter 3, molecular magnets in the context of quantum-coherent nanoscience and quantum information are discussed. A short review of the state of the field is followed by the discussion of the properties of the molecular nanomagnet complexes investigated in this work, Cr_7Ni/Mn single wheels and dimer systems, as well as the HoW_{10} nanomagnet crystal. The first two Chapters introduce concepts relevant for most of the work discussed in this thesis.

In Chapter 4, the Spin-Electric Coupling (SEC) is discussed. The review of ways electron spin may couple to an external electric field in the spin Hamiltonian, including the theoretical model of a triangular frustrated complex coupling through chirality, is followed by a discussion of techniques for investigation of SEC in molecular magnets using ESR. This Chapter relates directly to the research included in Chapter 6.

Chapter 5 discusses the dynamics of 4-level quantum systems of coupled spin-$\frac{1}{2}$ complexes. Tools for quantifying entanglement and fidelity in quantum information processing of such systems are introduced, followed by a discussion of Nuclear Magnetic Resonance Quantum Computing and specifically the methods of performing two-qubit gates and performing the full density matrix tomography within it. The Chapter ends with discussion of Double Electron-Electron Resonance (DEER), an ESR technique developed to investigate the weak dipolar couplings in spin complexes. It contains background specific for the research presented in Chapter 7.

In Chapter 6, the research involving the investigation of the SEC in several molecular magnets is presented. The copper triangles $Cu_3(saltag)(py)_6$ [36, 37] and their $CuZn_2$ analogue are discussed first. Then, the investigation of the origins of SEC (or lack thereof) in Cr_7Ni and Cr_7Mn rings is presented. They are followed by the description of the nature of the SEC in HoW_{10} complexes, and certain ways it might be utilized. The Chapter concludes with the discussion of the future directions for the SEC project.

Chapter 7 is devoted to the topic of an entangling gate in a weakly coupled dimer spin $\frac{1}{2}$ system and the density matrix tomography necessary to confirm the quality of such a gate. The proposal for a full density matrix tomography procedure is described first. Then, imperfections in the system affecting the gate and the tomography procedure are analyzed through simulations of increasing degree of complication. Next, experimental data from attempts to realize the entangling gate and tomography are presented. The Chapter ends by describing the next possible steps for this project.

2

Foundations of Electron Spin Resonance

Contents

2.1 General Spin Hamiltonian 8
2.1.1 Zeeman terms 9
2.1.2 Dipolar interaction 10
2.1.3 Exchange interaction 12
2.1.4 Hyperfine interaction 13
2.1.5 Higher order terms 13
2.2 Spin ensemble and thermal state 15
2.3 Pulsed ESR 16
2.3.1 Pulse ESR instrumentation 16
2.3.2 Quantum description of the spin state 20
2.3.3 Liouville space and product operators 21
2.3.4 Rotating frame and other interaction pictures 22
2.3.5 Pulses as operators 24
2.3.6 Hahn Echo 27
2.4 Relaxation 28
2.4.1 Longitudinal relaxation 29
2.4.2 Transverse relaxation 30
2.5 Selected pulsed ESR experiments 32
2.5.1 Echo-detected field sweep 32
2.5.2 Nutation and bandwidth measurement 33
2.5.3 Pulse calibration 34
2.6 Continuous Wave ESR 35
2.6.1 Modulation 35

Electron Spin Resonance (ESR)[1] spectroscopy is an experimental method of

[1]It is commonly called Electron Paramagnetic Resonance (EPR), however this name is not

studying the properties of paramagnetic materials through the interaction between a spin of an unpaired electron and a magnetic field. This work concentrates on the technique of pulsed ESR [18], which is discussed in more detail than the older continuous wave (CW) ESR [38–40].

The analysis of ESR results is possible due to the theoretical construction known as the spin Hamiltonian, which restricts the infinite-dimensional full Hamiltonian describing the wavefunctions of bound electrons to a tractable, finite form. This chapter starts by discussing the spin Hamiltonian and specific terms relevant to this work, and continues by presenting theoretical and practical foundations of pulsed ESR, ending with some of its relevant specific applications. It is not a comprehensive review of all pulsed ESR. The interested reader is directed to the classic monograph by Schweiger and Jeschke [18].

2.1 General Spin Hamiltonian

The most important tool in theoretical analysis of ESR species is the Spin Hamiltonian [18, 41], originally derived as procedure based on perturbation theory from more general Hamiltonians governing bound electrons in crystals [41, 42]. The spin Hamiltonian only contains spin and angular momentum degrees of freedom, packaging the translational degrees of freedom into the coefficients of the magnetic terms. The spin Hamiltonians thus only reproduce the lowest energy states of the exact electronic Hamiltonians, and operate on reduced subspaces.

The conventional spin Hamiltonian describing a system containing n effective electron spin operators $\hat{S}^k$ (either spin $\frac{1}{2}$ electrons, or coupled total spin operators), and m nuclear spin operators $\hat{I}^j$ is [18]:

$$\begin{aligned}\hat{H}_{\text{spin}} = \sum_k^n \left[\hat{H}_{EZ}(\boldsymbol{B}, \hat{\boldsymbol{S}}^k) + \hat{H}_{ZFS}(\hat{\boldsymbol{S}}^k)\right] + \sum_j^m \left[\hat{H}_{NZ}(\boldsymbol{B}, \hat{\boldsymbol{I}}^j) + \hat{H}_{NQ}(\hat{\boldsymbol{I}}^j)\right] + \\ + \sum_{k\neq l}^n \hat{H}_{EE}(\hat{\boldsymbol{S}}^l, \hat{\boldsymbol{S}}^k) + \sum_{j\neq i}^m \hat{H}_{NN}(\hat{\boldsymbol{I}}^j, \hat{\boldsymbol{I}}^i) + \sum_k^n \sum_j^m \hat{H}_{HF}(\hat{\boldsymbol{S}}^k, \hat{\boldsymbol{I}}^j)\end{aligned} \tag{2.1}$$

used in this work due to the appearance of topics from quantum computing and entanglement in later chapters, where EPR stands for Einstein-Podolsky-Rosen.

These terms effectively describe the interactions between magnetic fields and spins, between different spins, and specific higher order terms that can be thought of an interaction of a spin with itself, such as the zero-field splitting (ZFS) or anisotropy terms. Each of these terms is important in specific ESR experiments. However in this work, the most important ones are the electron Zeeman terms (EZ), the hyperfine terms (HF), and the electron-electron (EE) interaction terms, which are divided into dipolar (anisotropic) and exchange (isotropic) contributions, and the following sections will only focus on these.

The above Hamiltonian only contains terms until the second order, which is sufficient for the description of the most ESR experiments. The ZFS term may be replaced by the extended Stevens operators term $\sum_k^n \hat{H}_{ESO}(\hat{\boldsymbol{S}}^k)$ [43, 44], which parametrizes the higher order spin terms for systems with $J > \frac{1}{2}$ total angular momentum.

The spin Hamiltonian description may also be extended by including the interactions with the external electric field $\boldsymbol{E}$. The most common way of describing them is through modification of the parameters discussed above, and not new perturbation terms. This is the topic of Chapters 4 and 6.

2.1.1 Zeeman terms

The most important interaction in ESR is the Zeeman interaction between a magnetic field and a magnetic moment. The basic Hamiltonian term of the electron spin Zeeman interaction is, in frequency units:

$$\hat{H}_{EZ} = \frac{\mu_B}{\hbar} \boldsymbol{B} \cdot \boldsymbol{g} \cdot \hat{\boldsymbol{S}} \tag{2.2}$$

where $\boldsymbol{B}$ is the magnetic field vector, $\hat{\boldsymbol{S}}$ is the Cartesian vector of spin operators and $\boldsymbol{g}$ is the electronic g-tensor, describing the interaction. The g-tensor is a symmetric tensor, which means it can be described by 6 numbers. A typical choice is to use three principal values g_z, g_y, g_x and three Euler angles, describing the orientation. The g-tensor is the only parameter needed to fully characterize the Zeeman interaction of a particular electron spin. It contains contributions from the molecular environment

through the admixture of excited states with a non-zero orbital angular momentum $\hat{\boldsymbol{L}}$ and thus it may become anisotropic due to the spin-orbit interaction.

Note that through the application of the static magnetic field $\boldsymbol{B}_0 = [0, 0, B_0]$, the Zeeman term is the origin of the splitting of spin energy levels. It is also the origin of the oscillatory terms in the Hamiltonian, as we will see later in 2.3. Thus the orientation of a particular molecule affects both the energy splitting and thus its resonance frequency, and the effective amplitude of the driving term.

Whenever $g_x = g_y = g_z = g$, we say the g-tensor is isotropic or spherically symmetric. In this case, the Zeeman interaction may be simplified:

$$\hat{H}_{EZ} = \frac{\mu_B}{\hbar} g \boldsymbol{B} \cdot \hat{\boldsymbol{S}} \tag{2.3}$$

This case will be used as an example justifying most experimental pulse sequences. What it means is that the orientation of the molecule does not affect its magnetic properties. Note that even if the g-tensor is theoretically isotropic, this does not mean that in the experiment, all the spin packets will have the same exact resonance frequency. Each of the g-tensor components might be characterized by a g-strain, an error or a broadening, which might originate from a variety of factors, such as each molecule being slightly different shape, unresolved hyperfine interaction [29], or it might be a mathematical way to describe the effect of a nonuniform B_0 field.

Systems where any two principal values of the g-tensor are different are called non-isotropic. If exactly two of these are equal, such a system is called axial. For axial systems, a common notation is to use $g_\parallel = g_x = g_y$ and $g_\perp = g_z$.

For a free electron, the g-factor ≈ 2.00232, which has its origins in the Dirac equation, which predicts a value of 2, and the small correction originates from quantum electrodynamics. The free-electron value is often used as a reference point in experiments, since many species will have similar g-tensor values.

2.1.2 Dipolar interaction

One form of spin-spin interaction is the dipolar interaction. Classically, it is the interaction between a magnetic dipole and a magnetic field created by another

magnetic dipole in its vicinity. Dipolar interactions occur between bound spins, modifying spin Hamiltonians of investigated systems, as well as between any two spins in a sample solution, contributing to decoherence. Assuming a magnetic dipole is due to a localized electron spin (point-dipole approximamtion), and it interacts with another electron spin, the Hamiltonian of a dipolar interaction, in frequency units, is given by [45]:

$$\hat{H}_{dd} = \frac{1}{r^3}\frac{g_1 g_2 \mu_0 \mu_B^2}{4\pi}\left[\hat{\boldsymbol{S}}^1 \cdot \hat{\boldsymbol{S}}^2 - 3\frac{1}{r^2}(\hat{\boldsymbol{S}}^1 \cdot \boldsymbol{r})(\hat{\boldsymbol{S}}^2 \cdot \boldsymbol{r})\right] \tag{2.4}$$

where $\boldsymbol{r}$ is the vector between the two spins $\hat{\boldsymbol{S}}^1$ and $\hat{\boldsymbol{S}}^2$, g_1 and g_2 are their electronic g-factors and μ_B is the Bohr magneton. The inverse cube dependence on r is what makes it possible to measure the distance between two spins by estimating the strength of the dipolar interaction through ESR experiments [46]. When dipolar interactions with other spins in the solution are a main contribution to decoherence, this unwanted interaction is thus directly proportional to the concentration of the sample in the solvent.

To turn the above Hamiltonian into a useful form, the strength of the dipolar coupling D needs to be compared to the Zeeman energies ω_1, ω_2 of the two spins:

$$D = \frac{1}{r^3}\frac{g_1 g_2 \mu_0 \mu_B^2}{4\pi} \tag{2.5}$$

with an external magnetic field B_0 in the z direction. If $D \ll \omega_1, \omega_2$ (high-field approximation), one may drop terms resulting from the expansion of the Eq. 2.4, which in the rotating frame (see 2.3.4, discussed in more detail in 5.1.2) rotate fast compared to the experimental time scale [2], resulting in [45]:

$$\hat{H}_{dd} = D(1 - 3\cos^2\theta)\left[\hat{S}_z^1\hat{S}_z^2 - \frac{1}{2}\left(\hat{S}_x^1\hat{S}_x^2 + \hat{S}_y^1\hat{S}_y^2\right)\right] \tag{2.6}$$

where θ is the angle between the vector $\boldsymbol{r}$ and the quantization axis of the spin, represented here by the direction of the magnetic field B_0, z. The dipolar coupling is purely anisotropic, as if expressed in the tensor form $\hat{H}_{dd} = \hat{\boldsymbol{S}}^1 \cdot \boldsymbol{D} \cdot \hat{\boldsymbol{S}}^2$, the

[2] Several other approximations are used in different experimental regimes, characterized by relative values of D, ω_1 and ω_2 [45], but here we restrict ourselves to the regime most common for the interaction of two electrons in ESR.

$\boldsymbol{D}$ is traceless, and the dipolar coupling will be referred in parts of this work as the anisotropic coupling.

2.1.3 Exchange interaction

The exchange interaction between two electrons is purely quantum in its nature and comes from the overlap of electron orbitals, and the possibility of the unpaired electrons of two atoms to exchange. In the simplest case of two electronic spins-$\frac{1}{2}$, the exchange constant J is the difference between the energy of the antiferromagnetic singlet state and the ferromagnetic triplet state. The two electrons occupying the same orbital are forced into the singlet state. Through the admixture of this state onto the singlet state of two electrons bound to separate atoms, the energy of the latter is lowered compared to the triplet. This is known as kinetic exchange and is intrinsically antiferromagnetic. However, the Coulomb interaction energy coming from the charge distribution and wavefunction overlap is also different for the triplet and singlet, and lowers the energy of the triplet. This is known as direct exchange and is always ferromagnetic. There are also other possible contributions, such as polarization effects, that may be antiferromagnetic or ferromagnetic [47]. The final exchange constant J, may thus be positive or negative, and predicting that may prove difficult.

In ESR, the exchange interaction is only relevant in practice when at distances closer than about 1.5 nm. It may have an anisotropic component, but that is relevant only for distances shorter than 0.5 nm in most ESR experiments. In this work, such exchange coupled systems are investigated, but the strong exchange coupling is already included in a higher order approximation of the spin Hamiltonian, such as, treating the ground state manifold of two strongly exchange coupled spin $\frac{1}{2}$ particles as a spin 1 or 0 particle. For the weak exchange coupling directly included in the investigated Hamiltonians, it is assumed to be purely isotropic, and is referred to as the isotropic coupling [18, 45]. The Heisenberg exchange coupling Hamiltonian is:

$$\hat{H}_e = \hat{\boldsymbol{S}}^1 \boldsymbol{J} \hat{\boldsymbol{S}}^2 = J \left[\hat{S}_z^1 \hat{S}_z^2 + \hat{S}_x^1 \hat{S}_x^2 + \hat{S}_y^1 \hat{S}_y^2 \right] \tag{2.7}$$

The dipolar and exchange couplings can be separated from other interactions in ESR in a variety of ways [46], some of them discussed in 5.4. The same operators are involved in their quantum descriptions, so usually the separation is only possible by either rotation of a crystal sample, or angular selection in a disordered solution.

2.1.4 Hyperfine interaction

The hyperfine interaction between electron and nuclear spins is described by a tensor $\boldsymbol{A}$ and the following Hamiltonian:

$$\hat{H}_{HF} = \hat{\boldsymbol{S}} \cdot \boldsymbol{A} \cdot \hat{\boldsymbol{I}} \tag{2.8}$$

Where $\hat{\boldsymbol{I}}$ is the nuclear spin vector operator. The hyperfine interaction may provide a plethora of information about the spin system. Its source is a combination of the isotropic Fermi contact interaction between the electron and the nucleus and the fully anisotropic dipolar interaction, analogous to the one discussed above in case of two electron spins [18]. Note that the point-dipole approximation is usually invalid for an electron bound to the nucleus it interacts with and calculating the dipolar contribution to the hyperfine may become highly involved. In this work, sources of anisotropy and the nature of hyperfine interactions are not discussed in detail for any investigated samples, but hyperfine tensors with values obtained in the experiment are used in spin Hamiltonians.

If only the Zeeman terms and the hyperfine terms are present in the Hamiltonian, the latter modifies the transition frequency between states $\left|m_S = \frac{1}{2}, m_I\right\rangle$ and $\left|m_S = -\frac{1}{2}, m_I\right\rangle$ proportionally to the nuclear spin projection quantum number m_I, and it becomes $\omega + Am_I$, where ω is the Zeeman energy in frequency units[3].

2.1.5 Higher order terms

In spin-orbit coupled systems best characterized by a large total spin quantum number J, it might be necessary to include higher order terms in the spin Hamiltonian. Historically, there are two efficient ways to represent them, capturing their

[3]The transition effectively splits into $2I + 1$ separate ones.

rotational properties. The first are the irreducible spherical tensor (IST) operators $\hat{T}^k_q$. They satisfy the following commutation relations with the components of the angular momentum operator $\boldsymbol{J}$ [48]:

$$\begin{aligned}\left[\hat{J}_z, \hat{T}^k_q\right] &= q\hat{T}^k_q \\ \left[\hat{J}_\pm, \hat{T}^k_q\right] &= \sqrt{k(k+1) - q(q\pm 1)}\hat{T}^k_{q\pm 1}\end{aligned} \tag{2.9}$$

Where k is the order of the operator, and $q = -k, \ldots, +k$. The above commutation rules may be used recursively to efficiently calculate all the IST components of a given rank k. They are often use in magnetic resonance, because as a tensor analogue of spherical harmonics Y_{kq}, they transform identically to them under rotations. An IST operator rotated in 3 dimensions is a linear combination of same rank k ISTs, where the coefficients of this expansion are the elements of the rank k Wigner matrix:

$$\hat{\hat{R}}(\alpha, \beta, \gamma)\hat{T}^k_q = \sum_{q'=-k}^{k} \hat{T}^k_{q'} D^k_{q',q} \tag{2.10}$$

Where $\hat{\hat{R}}(\alpha, \beta, \gamma)$ is the rotation superoperator and $D^k_{q',q}$ are rank k Wigner functions. Expressing the spin Hamiltonian in terms of irreducible spherical tensor operators allows for easier and faster rotations, which is important when simulating powdered species, where the signal is a contribution from multiple orientations of the molecule. The details of how this is done are not important to this work however.

Another way to represent the higher order terms is through extended Stevens operators (ESO), $\hat{O}^q_k$. Unlike ISTs, which are spherical operators and analogues of the orbitals p_+, p_0, p_-, the ESOs are tesseral operators, analoguous to p_x, p_y, p_z. The positive q terms are the cosine tesseral terms, and the negative q terms are the sine tesseral operators. They are related to ISTs through:

$$\hat{O}^q_k = \begin{cases} \frac{c_{k,q}}{2}(\hat{T}^k_q + (-1)^q \hat{T}^k_{-q}) & \text{if } q \geq 0 \\ \frac{c_{k,q}}{2i}(\hat{T}^k_{-q} - (-1)^{-q}\hat{T}^k_q) & \text{if } q < 0 \end{cases} \tag{2.11}$$

Where $c_{k,q}$ are historical and not easily tabulated numerical coefficients.

The second rank ($k = 2$) terms are related to ZFS terms and may be used equivalently. The ESO Hamiltonian, capturing the higher order terms is:

$$\hat{H}_{ESO} = \sum_k \sum_{q=-k}^{k} B^q_k \hat{O}^q_k \tag{2.12}$$

Most typically, only the terms $k = 2, 4, 6$ (relevant to this work and listed in Table A.1) need to be used [43, 44].

2.2 Spin ensemble and thermal state

In pulsed ESR experiments, the sample is a disordered ensemble of spins, typically dissolved in a solvent. There are different modes of measurement that may involve a single molecule instead, like electrically detected magnetic resonance (EDMR) [49], or ESR-STM (scanning tunneling microscope) [50, 51].

To analyse the effect of any pulse sequence, we need to know the initial state of the system. In most cases, the initial state of the whole ensemble is given by the Boltzmann thermal state. If $\hat{H}_0$ is the laboratory frame Hamiltonian in frequency units, then the laboratory frame thermal state is described by the density matrix [18]:

$$\rho_0 = \frac{1}{Z} \exp\left(-\hat{H}\hbar/k_B T\right) \tag{2.13}$$

where division by the partition function $Z = \mathrm{Tr}\left(\exp\left(-\hat{H}\hbar/k_B T\right)\right)$ normalizes it to unit trace. If the Zeeman interaction dominates the Hamiltonian, so that $\hat{H} = \omega\hat{S}_z$, the thermal state can be approximated as:

$$\rho_0 \approx \frac{1}{d}\left(\mathbb{1} - \frac{\hbar\omega}{k_B T}\hat{S}_z\right) \tag{2.14}$$

where d is the dimension of the Hilbert space. Note that the factor $\frac{\hbar\omega}{k_B T}$ is usually small, for an X-band frequency 9.4 GHz and temperature 4.5 K, it is 0.1, which is considered a limit for this approximation [4]. At lower temperatures and higher frequencies, a more detailed approximation or a full expression may need to be used. The identity component and the multiplicative factor are often dropped, and the analysis of ESR pulse sequences is performed using the deviation density matrix $\rho_0 = -\hat{S}_z$. A general deviation density matrix is defined as the traceless part of the density matrix with arbitrary multiplicative component [34, 35]. In ESR (and NMR), the identity component of the density matrix is not measurable,

[4] A pure state $|1\rangle$ in a spin-$\frac{1}{2}$ system has a density matrix $\frac{1}{2}\mathbb{1} - \frac{1}{2}\hat{S}_z$, which shows that initial states in ensemble ESR are usually highly mixed.

because it is not affected by any unitary transformation, and the readout only measures polarizations. Without a single-shot readout capability, there is no practical difference whether the full or the deviation density matrix is analysed, except when the absolute spin count is important.

2.3 Pulsed ESR

The primary method of acquiring ESR data in this thesis is pulsed ESR. In pulsed ESR, a static magnetic field $\boldsymbol{B}_0$ is applied in z direction, while an oscillating magnetic field $\boldsymbol{B}_1$, oriented in x direction, interacts with the sample in the form of nanosecond-scale pulses. The operation of pulsed ESR is based on the assumption that the electron Zeeman terms dominate in the spin Hamiltonian and both $\boldsymbol{B}_0$ and $\boldsymbol{B}_1$ enter the Hamiltonian through them, but it is applicable also outside this regime. The pulsed ESR experiments are described by pulse sequences, which are the schematics of pulse amplitudes, durations and timings between them. During a pulse, the static Hamiltonian $\hat{H}$ acquires a field-dependent perturbation $\delta\hat{H}(\boldsymbol{B}_1)$, which may excite a transition between levels $|a\rangle$ and $|b\rangle$ of the static Hamiltonian if the matrix element:

$$\langle a|\,\delta\hat{H}(\boldsymbol{B}_1)\,|b\rangle \neq 0, \tag{2.15}$$

and the time dependence of $\delta\hat{H}(\boldsymbol{B}_1)$ includes frequency components corresponding to the transition energy.

The proper analysis of the effect of a pulse sequence requires quantum-mechanical treatment for systems with $S > \frac{1}{2}$. First, let us have a look at how the pulsed ESR spectrometer creates pulses, delivers them to the sample and acquires signal.

2.3.1 Pulse ESR instrumentation

The overall experimental setup of the modern pulsed ESR spectrometer is shown in Fig. 2.1. The two specific machines used exclusively to collect data presented in this work are Bruker ELEXSYS E580 and E680 spectrometers, operating at X-band (≈ 9.7 GHz) and Q-band (≈ 34 GHz) frequencies, and thus any quoted values refer to these two instruments. For a more in-depth explanation of the spectrometer

architecture, the reader is directed to the manual of a specific instrument [52]. Let us follow the path of the microwave pulse as it is programmed, created, amplified, resonates and interacts with the sample, and then the sample magnetization is detected and digitized.

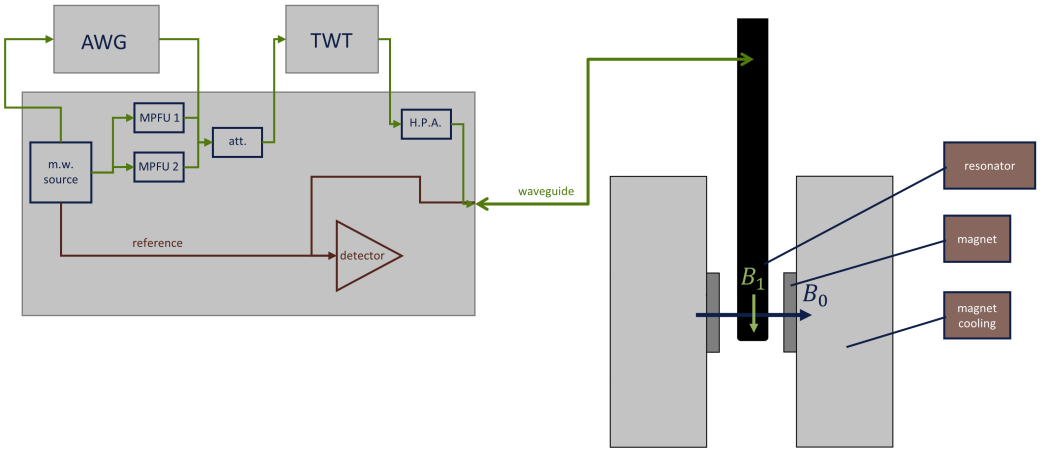


Figure 2.1: A simplified diagram of a pulsed ESR spectrometer. The arrows show the direction of meaningful pulse signal.

The microwave bridge

The microwave bridge has a twofold role: it creates the required microwave pulses and detects the signal coming from the resonator. The signal produced by a frequency-locked microwave oscillator passes through an MPFU (Microwave Pulse Forming Unit), consisting of several PIN (P-type Intrinsic N-type) diodes and phase shifters, to produce an oscillation with the required phase. Typical bridges have several MPFUs corresponding to different fixed $(+x, -x, +y, -y)$ and custom phases. After the MPFU, a short pulse is formed by passing through another PIN diode and a transmitter attenuator, to then be sent towards a TWT (Traveling Wave Tube) high-power amplifier [53]. The typical rise-fall times of pulses produced this way are of order 2 ns.

The detection part of the bridge consists of a preamplifier, a mixer separating the in-phase and quadrature components of the signal via comparison with the microwave signal that arrives at the detector from the source via the reference arm,

and the digitizer. The signals collected in the pulsed ESR experiment are of much lower amplitude than the pulses. Even with the most care taken, the pulses will have a reflected component, and ringdown from the resonator (discussed below), which will reach the detector. The reflected part of the pulse reaching the preamplifier could damage it, so to combat this effect, a defense pulse is implemented, during which the preamplifier is switched off. This creates a deadtime period after each pulse, where no signal may in principle be detected. The in-phase and quadrature voltages, corresponding to the magnetization detected in the resonator are then digitized into the real and imaginary channels of the recording device. The quadrature detection is followed by video amplification, with an adjustable gain and bandwidth, which is useful to reduce the noise and eliminate off-frequency responses from the sample, especially while working with multiple frequencies.

Arbitrary Waveform Generator

Alternatively to passing through an MPFU, the pulse might be generated with help of an Arbitrary Waveform Generator (AWG) unit, which through a combination of IQ-mixers may be able to produce pulses of variable shape and frequency, which may be even varied during the pulse (chirped pulse). The variation in frequency and shape is limited by the time resolution of the AWG, 0.5 ns for the device used here. The bridge still provides the local oscillator at the required frequency, and the AWG-produced signal is then mixed with it and sent to the TWT.

Traveling Wave Tube amplifier

The TWT is a high-power amplifier most commonly used in pulsed ESR [53]. A typical TWT has a power of about 1kW. The pulsed ESR needs a high power amplifier, because the loaded quality factor of the resonator, described next, needs to be relatively low to make the actual durations of the pulses interacting with the samples close to the programmed ones, and to keep the bandwidth large so multiple frequencies may be used. Unfortunately, the response of the TWT is not completely linear, but has diminishing gains as the amplitude of the incoming pulse increases. The TWT may be operated in the linear regime, which reaches about 50% of its

total power, which may be necessary in more complicated experiments involving pulses of multiple frequencies passing through each other [54]. The TWT can also be switched on only for 10 μs at once, which limits the duration and number of pulses sent in the sequence. This limit may be overcome by using two TWT gates, the minimum time between which is typically of order 300ns [52].

High Power Attenuator

The pulse is typically attenuated again after leaving the TWT through a high-power attenuator, which is also the only attenuator which levels are adjusted in a pulse experiment. Using it exclusively limits the impact of TWT's nonlinearity, as gate power may be adjusted predictably by setting appropriate attenuation. The attenuation affects the power, which is proportional to a square of the B_1 amplitude, so to reduce B_1 by half it needs to be increased by 6 dB.

Resonator

The pulse then reaches the resonator. There are a variety of resonators used in pulsed ESR experiments, such as loop-gap resonators, dielectric resonators and rectangular cavity resonators. As mentioned above, the loaded Q factor of the resonator needs to be low for the pulse experiment, and in practice values such as 100-200 are achievable by overcoupling. The same resonators used in a critically coupled (matched) mode may have Q factors as high as 4000-10000 [52]. The resonators are designed in such a way that the microwave mode of a target frequency has a magnetic field antinode at the position of the sample. The resulting oscillating $\boldsymbol{B_1}$ field is perpendicular to the static $\boldsymbol{B_0}$ field and reasonably homogenous in the space around the sample volume.

Spin coherence corresponding to a transition of frequency ω causes spin precession. This results in macroscopic magnetization vector $\boldsymbol{M}$, proportional to spin expectation values in the laboratory frame:

$$\boldsymbol{M} \propto \left[\langle \hat{S}_x \rangle, \langle \hat{S}_y \rangle, \langle \hat{S}_z \rangle\right] \tag{2.16}$$

oscillating at the frequency ω. If $\boldsymbol{M} \cdot \boldsymbol{B}_1 \neq 0$, the magnetization has a component corresponding to the oscillating modes of the resonator, the sample can re-radiate

into the resonator. The resulting signal then travels back to the bridge to be detected. As most commercial ESR resonators are engineered for the main working mode to have its magnetic field aligned with the vertical axis, typically labelled as x axis, this signal is in turn proportional to just $M_x \propto \langle \hat{S}_x \rangle$.

Magnet

The static magnetic field $\boldsymbol{B_0}$ is produced by an electromagnet. Magnets used for X-band and Q-band experiments need to be able to reach magnetic fields of about 1.5 T, which is possible without the use of superconducting components, necessary for higher frequency W-band ($\approx$ 95 GHz) and D-band ($\approx$ 130 GHz) spectrometers.

2.3.2 Quantum description of the spin state

The state of the quantum system in pulsed ESR is described using the density matrix formalism over the Hilbert space spanned by the spin states. The density operator is used firstly because the states tend to be highly mixed, and different spin packets in the ensemble all have slightly different Hamiltonians, and the density matrix approach helps capture their collective behaviour. As such, the evolution of the system during an experimental pulse sequence is described by the von Neumann formula:

$$i\frac{\partial \hat{\rho}}{\partial t} = \left[\hat{H}(t), \hat{\rho}\right] \tag{2.17}$$

For a time-independent Hamiltonian this results in a familiar expression for a propagator-based evolution:

$$\hat{\rho}(t) = \exp\left(-i\hat{H}t\right)\hat{\rho}(0)\exp\left(i\hat{H}t\right) \tag{2.18}$$

If the Hamiltonian is time-dependent, the time evolution is analyzed by discretizing it and treating it as a sequence of time-independent Hamiltonians. During the pulse sequence, the Hamiltonian shifts between the static Hamiltonian $\hat{H}_0$ and oscillating pulse Hamiltonians (described later in 2.3.5), and the final density matrix is obtained by applying the propagators in sequence.

2.3.3 Liouville space and product operators

A common way to describe magnetic resonance systems makes use of spin operators and their products, known as product operators. These are typically used in NMR teaching [55, 56]. For a two spin-$\frac{1}{2}$ system, there are 15 product operators. They are tensor products of the three Pauli operators and the identity $\sigma_x, \sigma_y, \sigma_z, \mathbb{1}_2$, scaled by a factor of $\frac{1}{2}$, to better represent physical spin observables. They are:

$$\begin{aligned} &\mathbb{1}_4, \hat{S}_x, \hat{S}_y, \hat{S}_z, \hat{I}_x, \hat{I}_y, \hat{I}_z, \\ &2\hat{I}_x\hat{S}_x, 2\hat{I}_x\hat{S}_y, 2\hat{I}_x\hat{S}_z, 2\hat{I}_y\hat{S}_x, 2\hat{I}_y\hat{S}_y, 2\hat{I}_y\hat{S}_z, 2\hat{I}_z\hat{S}_x, 2\hat{I}_z\hat{S}_y, 2\hat{I}_z\hat{S}_z \end{aligned} \tag{2.19}$$

Following the NMR convention, S and I represent different spins. The identity is typically dropped from the tensor products.

Product operators are a natural basis for computation of the quantum evolution in a (n^2-1)-dimensional Liouville space $\mathcal{L}$ instead of an n-dimensional Hilbert space $\mathcal{H}$. In Liouville space, the $n \times n$ density matrix [57, 58] becomes a vector of dimension (n^2-1), and its linear transformations are called superoperators [59, 60]. The superoperator and Liouville space formalisms are widely used in the study of open quantum systems, and are necessary to include effects of decoherence. In magnetic resonance, certain transformations are unitary when applied to just one quantum system, but become non-unitary if one wishes to describe their effect on an ensemble of non-identical quantum systems. The Liouville space is equipped with a trace inner product $(A|B) = \mathrm{tr}\left(A^\dagger B\right)$. The product operators as defined above form an orthonormal basis in respect to this product, as they are Hermitian, traceless, square to $\frac{1}{4}$ of identity and have the commutation relations inherited from Pauli matrices. In practice, the density matrix can be expressed as a sum of $\frac{1}{4}\mathbb{1}$ and a linear combination of the 15 product operators. This is an equivalent of the Bloch sphere in a 4-level system [61, 62].

Product operators also make it conceptually easy to construct and subsequently modify, unitary operations. The unitary evolution of a density operator $\hat{\rho}$ with

respect to a single product operator $\hat{A}$ is, starting from the von Neumann equation:

$$\begin{aligned} i\frac{\partial\hat{\rho}}{\partial t} &= \left[\hat{A},\hat{\rho}\right] \\ \hat{\rho}(t) &= \exp\left(-i\hat{A}t\right)\hat{\rho}(0)\exp\left(i\hat{A}t\right) \end{aligned} \tag{2.20}$$

Because $\hat{\rho}$ is written as a vector in the basis of product operators, we can simplify this further using the Baker-Campbell-Hausdorff formula [63]. If $\hat{B}$ is another product operator, then:

$$\exp\left(-i\hat{A}\phi\right)\hat{B}\exp\left(i\hat{A}\phi\right) = \begin{cases} \cos(\phi)\hat{A} - i\sin(\phi)\left[\hat{B},\hat{A}\right] & \text{if } \hat{B}\neq\hat{A} \\ \hat{A} & \text{if } \hat{B}=\hat{A} \end{cases} \tag{2.21}$$

which defines all the superoperator matrix elements in this basis. Of course, if the Hamiltonian is not diagonal or time dependent, either explicit exponentiation or Trotterization is still required, but the above is the convention used here whenever possible.

Alternative bases for the Liouville space of the two spins-$\frac{1}{2}$ include standard generators of the $\mathfrak{su}(4)$ algebra [61], or second rank irreducible spherical tensor operators [64], which become the most convenient whenever orientational averaging is involved. A spin Hamiltonian expressed in terms of irreducible spherical tensor operators may be efficiently converted to represent a specific orientation of a molecule through the Wigner-Eckhart theorem and Wigner matrix formalism. They are also the basis of choice when considering most relaxation theories [64]. The spin dynamics simulation engine Spinach [65] uses spherical tensors in Liouville space for most purposes.

2.3.4 Rotating frame and other interaction pictures

Microwave pulses in pulsed ESR interact with the spin sample through the Zeeman interaction. During the pulse, the spin Hamiltonian gains the additional term proportional to the oscillating magnetic field $\boldsymbol{B}_1 = [B_1\cos(\omega_{\text{mw}}t), 0, 0]$ at the sample position. For simplicity we will assume an isotropic g-tensor here, but in general this term arises from the tensor multiplication $\boldsymbol{B}_1\cdot\boldsymbol{g}\cdot\hat{\boldsymbol{S}}$:

$$\hat{H}_{\mathrm{mw}} = \frac{\mu_B}{\hbar} B_1 \cos(\omega_{\mathrm{mw}} t) g \hat{S}_x \tag{2.22}$$

The standard way of analyzing ESR experiments is to move to an interaction frame associated with $\hat{H}_0 = \omega_0 \hat{S}_z$. It is known as a rotating frame, because classically it corresponds to the frame in which the microwave field is static. In any interaction frame, the observables, the density operator and the reduced Hamiltonian $\hat{H} - \hat{H}_0$ transform in the following way:

$$\hat{A}_{\mathrm{int}} = \exp\left(i\hat{H}_0 t\right) \hat{A} \exp\left(-i\hat{H}_0 t\right) \tag{2.23}$$

if $\hat{A}$ is any operator[5]. All terms in the spin Hamiltonian (2.1) need to be transformed into the rotating frame using the above equation. Note that the resulting quantum state, described with a density matrix ρ_{rot} is not only a state of the spin, but also of the resonant magnetic field, and is known as a dressed state. As an illustration, let us assume the laboratory frame Hamiltonian only contains the Zeeman terms:

$$\hat{H}_{\mathrm{lab}} = \omega_0 \hat{S}_z + \omega_1 \cos(\omega_{\mathrm{mw}} t) \hat{S}_x \tag{2.24}$$

where $\omega_1 = \frac{\mu_B}{2\hbar} B_1 g$ is the microwave amplitude. Then in the rotating frame:

$$\hat{H}_{\mathrm{rot}} = (\omega_0 - \omega_{\mathrm{mw}}) \hat{S}_z + \omega_1 \hat{S}_x + \omega_1 \cos(2\omega_{\mathrm{mw}} t) \hat{S}_x \tag{2.25}$$

and the last term is dropped, because it rotates faster than the timescale of the experiment and averages to zero according to average Hamiltonian theory [66]. Any such time-dependent terms that cause Hamiltonians at different times to not commute with each other might cause additional resonant frequency shifts known as Bloch-Siegert shifts [67]. In this case, the Bloch-Siegert shift averages out to have an effect of a $-\frac{\omega_1^2}{2\omega_{\mathrm{mw}}} \hat{S}_z$ operator, which for most ESR experiments corresponds to a frequency shift of kHz order [18]. Its main effect is the shift in the classical microwave phase of the signal in more complicated experiments, depending on the order of applied pulses.

[5]It should be noted for completeness, that product operators (2.3.3), when used as a basis for a density matrix representation in Liouville space, do not transform into the interaction picture, because that would keep vector elements identical. Instead, the density matrix is transformed, and then evaluated in a basis of "naked" product operators.

Through the transformation into the rotating frame, the classical phase of the microwave signal ϕ transforms into the phase between the $\hat{S}_x$ and $\hat{S}_y$ operators:

$$\omega_1 \cos(\omega t - \phi)\hat{S}_x \rightarrow \omega_1 \cos(\phi)\hat{S}_x + \omega_1 \sin(\phi)\hat{S}_y + \text{quick.rot.terms} \tag{2.26}$$

The pulses with phase 0 are known as X pulses, and those with relative phase $\frac{\pi}{2}$ are known as Y pulses. The global microwave phase is not important, and when discussing the phase of the pulses, we need to remember it is relative, and only important in relation to other pulses in the sequence and to the detection. This is because the initial density matrix (2.2) does not contain any coherence; the coherence is created by the first pulse.

To understand how the rotating frame affects detection, we need to transform the rotating frame operators $\hat{S}_x$ and $\hat{S}_y$ back to the laboratory frame:

$$\begin{aligned} \langle \hat{S}_x \rangle_{\text{lab}} &= \left\langle \exp\left(-i\omega_{\text{mw}}\hat{S}_z t\right)\hat{S}_x \exp\left(i\omega_{\text{mw}}\hat{S}_z t\right)\right\rangle = \\ &= \cos\left(\omega_{\text{mw}} t\right)\langle \hat{S}_x \rangle_{\text{rot}} - \sin\left(\omega_{\text{mw}} t\right)\langle \hat{S}_y \rangle_{\text{rot}} = \text{Re}\left(\exp(i\omega_{\text{mw}} t)\langle \hat{S}_x + i\hat{S}_y \rangle_{\text{rot}}\right) \end{aligned} \tag{2.27}$$

In the laboratory frame $M \propto \langle \hat{S}_x \rangle$. The magnetization oscillating at ω_{mw} induces a microwave signal in the resonator. The signal travels back to the bridge and is split into the inphase and quadrature components, which are mixed down in frequency and digitized to the real and imaginary detection channels. The final detected signal is proportional to $\langle \hat{S}_x + i\hat{S}_y \rangle = \langle \hat{S}_+ \rangle$ in the rotating frame.

2.3.5 Pulses as operators

The action of each pulse is a unitary operation on the system's density matrix. The static terms remain in the pulse Hamiltonian during the pulse evolution, and the X pulse only acts as an X gate exactly on resonance. So far, the pulse was represented by switching the microwave radiation on and then off again, which corresponds to a rectangular pulse. The net propagator due to quantum evolution under such a pulse becomes:

$$\exp\left(-i\left[\Omega\hat{S}_z + \omega_1\hat{S}_x\right]t\right) \tag{2.28}$$

Where $\Omega = \omega_0 - \omega_{\mathrm{mw}}$ is the resonance offset. The product $\omega_1 t$ is the nominal turning angle of the pulse. Considering what happens away from resonance is important in most ESR experiments. The ESR lines are inhomogenously broadened, because of the angular dependence of the electron Zeeman interaction and other Hamiltonian terms. The pulses that only affect spin packets with certain transition frequencies corresponding to specific orientations of the molecule, are called orientationally selective. Orientation selection is specifically important in experiments reliant on dipolar interaction (2.1.2), due to its explicit orientational dependence.

Away from the resonance, if Ω is comparable with ω_1, the propagator does not correspond to the nominal rotation around the x axis, but to the rotation around the axis

$$\hat{n} = \frac{\Omega\hat{z} + \omega_1\hat{x}}{\sqrt{\Omega^2 + \omega_1^2}} \tag{2.29}$$

by the actual turning angle of the pulse:

$$\theta = t\sqrt{\Omega^2 + \omega_1^2} \tag{2.30}$$

All the spins in the ensemble are affected by the pulses, but to a different degree. It is characterized by the pulse's excitation profile, which can be approximately calculated by performing a Fourier Transform (FT) of the pulse's amplitude in time domain. For a rectangular pulse extending from $-t/2$ to $t/2$, the absolute value spectrum is:

$$P(\Omega) = \left|\frac{\sin(\Omega t/2)}{\Omega/2}\right| \tag{2.31}$$

The spectrum of such a pulse has a line width of $\Delta\nu = 1.207/t$, and its absolute value first reaches zero at points $\Omega = \pm 1/t$, leaving long oscillating tails on both sides. The FT is a linear operation, unlike the excitation response, so if exact excitation profile is needed, the propagators need to be explicitly calculated for each spin packet.

Of course, any electronic component used in a practical lab has a finite bandwidth, so a rectangular pulse is not actually possible to implement. In practice, the pulses are characterized by a short rise and fall times. Even more, the pulse's excitation

profile is further convoluted with the excitatation profile of the resonator (2.3.1), distorting the pulse further[6]. One may also want to purposefully modulate the amplitude of a pulse. If the amplitude of the actual B_1 field affecting the spin generates the frequency $\omega_1(t)$ at a given time, and the pulse extends from $-t_p/2$ to $t_p/2$, the nominal turning angle becomes given by:

$$\phi = \int_{-t_p/2}^{t_p/2} \omega_1(t) dt \tag{2.32}$$

Exactly on resonance, the rotating frame Hamiltonians at different times commute, so the propagator is easy to calculate. Off resonance however, the Hamiltonians at different times may not commute, and thus calculating the net propagator requires discretization.

One of the most commonly used alternative pulse shapes is a Gaussian pulse, because of its well behaved excitation profile. The FT of a Gaussian is a Gaussian, so the excitation profile of a Gaussian pulse lacks the long oscillating tail of a sinc function.

The pulses with equal nominal turning angles, but different bandwidths, affect the spins exactly on resonance in an identical way, but the larger bandwidth (shorter) pulse will affect a larger part of the spin ensemble. The small bandwidth pulses are more orientationally selective, because they select a smaller subpopulation or only affect certain transitions, whereas the pulses with larger bandwidth, would affect a larger subpopulation of spins or more transitions.

If selection rules allow the pulse to excite multiple transitions, and its excitation profile makes it reach these transitions, it is called a non-selective pulse. These pulses are usually extremely short, hard pulses. This nomenclature is a carry-over from NMR, where the transitions are typically sharper and the spin Hamiltonians are typically more isotropic.

[6]This effect may be analyzed, and used to optimize pulses to improve the precision of quantum operation [68].

2.3.6 Hahn Echo

The basic ESR experiment and a building block of more advanced ones is a Hahn spin echo [18, 69]. Each spin packet in the ensemble evolves according to a slightly different Hamiltonian. In case of a simple Zeeman Hamiltonian discussed above, this is just $(\omega_0 - \omega_{\mathrm{mw}})\hat{S}_z = \Delta\omega\hat{S}_z$ in the rotating frame. Due to the spread of $\Delta\omega$, the inhomogeneous broadening, the magnetization after the pulse quickly[7] becomes unmeasurable, as the signal contributions from different spin packets average to zero. The solution is to try and invert the evolution due to the unwanted parts of the Hamiltonian that contribute to this effect, which is most commonly done through the echo mechanism.

A $\frac{\pi}{2}$ pulse creates a coherence from the thermal state. The spins evolve for time τ, and then a π pulse is sent, inverting the evolved coherence. After another period of duration τ, the spins refocus and the total nonzero magnetization is observed again. The Hahn echo pulse sequence is shown in Fig. 2.2. Symbolically, expressing the density matrix in basis of spin operators:

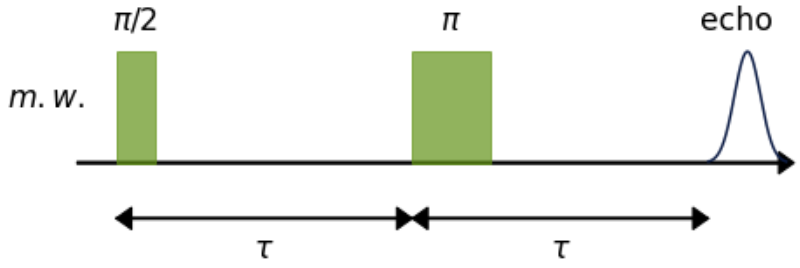


Figure 2.2: Pulse sequence corresponding to the Hahn echo experiment.

$$\hat{S}_z \xrightarrow{\frac{\pi}{2}\hat{S}_x} \hat{S}_y \xrightarrow{\hat{H}\tau} \cos(\Delta\omega\tau)\hat{S}_y - \sin(\Delta\omega\tau)\hat{S}_x \xrightarrow{\pi\hat{S}_x} -\cos(\Delta\omega\tau)\hat{S}_y - \sin(\Delta\omega\tau)\hat{S}_x \xrightarrow{\hat{H}\tau} -\hat{S}_y \tag{2.33}$$

In most experiments, the echo is a Gaussian-like shape which is then integrated. The echo integral is proportional to the number of affected spins and $\langle\hat{S}_+\rangle$.

[7] Quantified by the time T_2^* or the inhomogeneous linewidth Γ_{inh} [18].

In theoretical evaluations of ESR pulse sequences, it is usually assumed the pulses act as perfect operators, but actually the spins evolve according to their individual Hamiltonians. It is necessary to consider these out of resonance species to evaluate if the magnetization can be observed, in other words, if the state is refocused by the pulses. A refocused state is simply a state that does not depend on small individual differences in free Hamiltonians, such as the final state in the echo sequence. Such a state might be observed in echo-detected ESR.

The Hahn echo sequence $\frac{\pi}{2} - \tau - \pi - \tau - echo$ generates a primary echo. The pulses need not be nominal $\frac{\pi}{2}$ and π to generate an echo, two pulses of turning angles β_1 and β_2 generate an echo of amplitude propotional to

$$|\sin\beta_1| \sin^2\left(\frac{\beta_2}{2}\right) \tag{2.34}$$

from the disordered thermal state [18]. Due to the contribution of the off-resonant spins to the echo, the maximum of the echo occurs at about half the duration of the first pulse after the nominal end of the pulse sequence [70], in case of Hahn echo corresponding to 2τ after the first pulse.

In the practical experiment any two of possibly many pulses involved in the sequence will generate a secondary echo, even if the theoretical prediction for spins exactly on resonance says otherwise, due to the contribution of the off-resonant spins. In an experiment, such echoes may need to be supressed, which can be achieved for example through phase cycling [71].

2.4 Relaxation

Relaxation processes are a central part of ESR. They restrict the possible level of complication of an experiment, introducing errors, but may also be used constructively as a tool. Relaxation results from the interaction of the spin system with its environment and as such, cannot be described within a spin Hamiltonian, unitary operations and Hilbert space. It is however possible to capture the behaviour of various relaxation processes within a relaxation superoperator $\hat{\hat{R}}$ in Liouville space [18]. The density operator $\hat{\rho}$ captures the state of the system under relaxation,

and the von Neumann formula is modified, including the relaxation to thermal equilibrium state $\hat{\rho}_0$ [72]:

$$\frac{\partial}{\partial t}\hat{\rho} = -i\hat{\hat{H}}_0\hat{\rho} + \hat{\hat{R}}\left[\hat{\rho} - \hat{\rho}_0\right] \tag{2.35}$$

This adds one additional dimension to the problem, as $\hat{\hat{R}}\hat{\rho}_0$ can just be treated as a column vector of the same length as $\hat{\rho}$ in Liouville space.

Specific relaxation theories will not be discussed here, as they are not relevant for this work, but are included in many textbooks and publications [18, 73]. The simplest way to quantify relaxation is through longitudinal and transverse relaxation times, T_1 and T_2. Note that in a real experiment there usually are more relaxation pathways [73], and any experimentally measured parameters arise from the combination of all the contributions.

2.4.1 Longitudinal relaxation

Longitudinal relaxation, characterized by the time parameter T_1, is the process in which the spin relaxes to a state of a lower energy, usually through an interaction with phonons, either a direct emission of a phonon, or an absorption of a high energy phonon followed by a subsequent emission, i.e. a Raman process. In solids, this requires a lattice, so the longitudinal relaxation is also called a spin-lattice relaxation. Longitudinal relaxation is a process through which the system returns to thermal equilibrium.

In a spin-$\frac{1}{2}$ system, we may write:

$$\frac{d\langle\hat{S}_z\rangle}{dt} = \frac{\langle\hat{S}_z\rangle - \mathrm{Tr}\left(\hat{S}_z\rho_0\right)}{T_1} \tag{2.36}$$

The spin polarization thus exponentially decays to its equilibrium value.

The longitudinal relaxation is a mechanism ESR experiments rely on to reinitialize the system after a measurement. A rule of thumb is that after waiting $10T_1$, the system should be approximately in thermal equilibrium and the experiment may be repeated from the same starting point. If the T_1 is long compared to the time between subsequent repeats, it will result in saturation, and lowering

of the overall signal, as the system has not returned to equilibrium. In certain systems, this may altogether prevent measurement at low temperatures, where relaxation times are typically longer.

T_1 may be measured through an inversion recovery experiment. A single π pulse is applied to invert the thermal spin populations. After a variable time T, the polarization is measured with a Hahn echo. The signal follows an inverted exponential decay curve, whose time constant is taken as T_1.

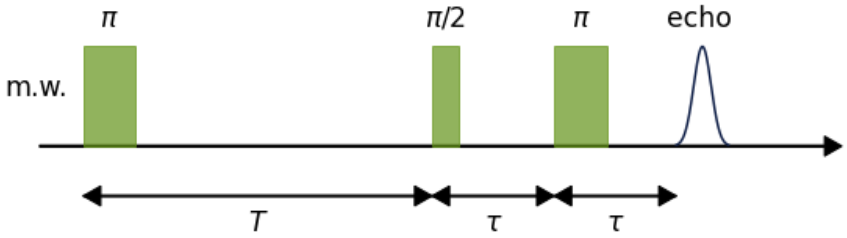


Figure 2.3: Pulse sequence of the inversion recovery experiment. The first pulse inverts the thermal spin population. The delay T is varied, and the echo signal recovers from negative to positive as T increases, following an inverted exponential decay curve.

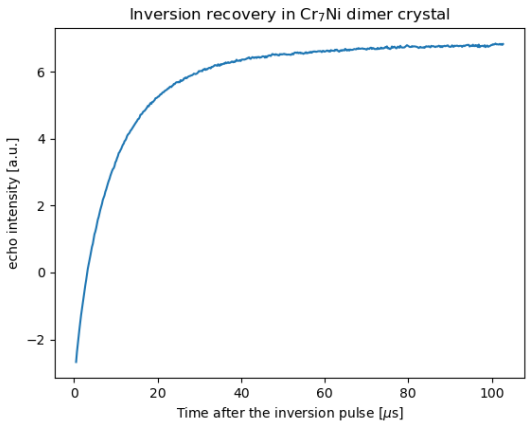


Figure 2.4: Example data from an echo detected inversion recovery experiment. These data were collected in the Cr_7Ni dimer crystal sample further discussed in 7.6.3 using the pulse sequence shown in Fig. 2.3 at temperature 3 K. The fitted T_1 value was 10.5 μs, which is typical for complexes of this type.

2.4.2 Transverse relaxation

Transverse relaxation is an energy-conserving process, in which the phase information and effectively the spin coherence is lost. The origin is broadly understood

uncontrolled $\boldsymbol{B}_0$ fluctuations, acting as $\hat{S}_z$ operators, shifting the phase of the coherence in inhomogeneous manner. A common mechanism is a nuclear flip-flop process, in which one spin flips from the higher energy to a lower energy state, providing the energy for the other spin to flip in the opposite direction, and that affects the field at the position of the coupled electron. It is thus called a spin-spin relaxation. If such processes occur with a rate T_2', the overall transverse relaxation time T_2 satisfies, according to Redfield relaxation theory [72]:

$$\frac{1}{T_2} = \frac{1}{T_2'} + \frac{1}{2T_1} \tag{2.37}$$

because any process causing longitudinal relaxation also contributes to a transverse relaxation.

In a spin-$\frac{1}{2}$ system, it causes the $\hat{S}_x$ and $\hat{S}_y$ to exponentially decay to 0 with characteristic time T_2. It is typically measured through a Hahn echo experiment, where the free evolution duration τ is varied. The echo signal decays exponentially to 0 as τ increases. The exponential decay curve will often have oscillatory contributions from other effects, such as proton Electron Spin Echo Envelope Modulation (ESEEM, resulting from hyperfine interaction) [74], or manifestation of the coupling between electrons in a multi-spin system. These topics are not investigated here, but in practice limiting the pulses' bandwidth may help eliminate these effects [75].

To avoid confusion and encompass all the dephasing mechanisms in a single parameter, a phase memory time T_m is sometimes used. The echo decay signal can be fitted with a phenomenological stretched exponential:

$$Y(2\tau) = Y(0)\exp(-(2\tau/T_m)^x) \tag{2.38}$$

where $Y(2\tau)$ is the echo amplitude, when the free evolution duration is τ, $Y(0)$ is echo signal extrapolated to $\tau = 0$ and x is a stretch parameter. The value of x is determined by the rate of the dominant dephasing process W relative to the duration of the experiment. If $W\tau \gg 1$, then $x = 1$. If $W\tau \ll 1$, x may be as large as $2 - 2.5$, and when the dominant dephasing process is comparable with the duration of the experiment, x as low as 0.5 could be observed [73].

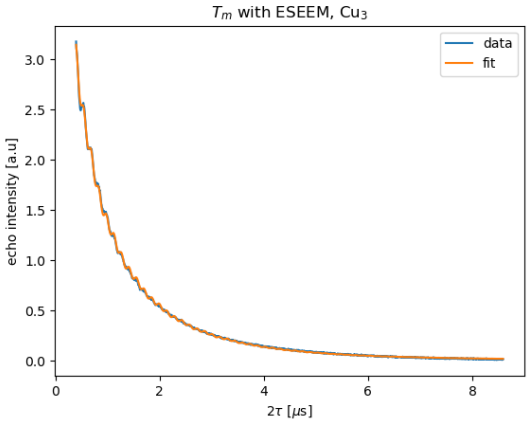


Figure 2.5: Example measurement of the phase memory time in Cu_3 complex. The stretched exponential decay with $T_m = 312$ ns and $x = 0.57$ includes an oscillation coming from proton ESEEM.

2.5 Selected pulsed ESR experiments

Several commonly performed ESR measurements are discussed below. A portion of experimental data and parameters presented in Chapters 6 and 7 rely on these.

2.5.1 Echo-detected field sweep

The echo-detected field sweep (EDFS) experiment is one of the methods of acquiring a B_0-dependent spectrum of the measured sample. A Hahn echo experiment is repeated with the same parameters, as B_0 is varied. The integrated echo amplitude follows the absorption spectrum of the sample. The EDFS signal will be affected by broadening resulting from short pulses exciting significant parts of the spectrum around the given B_0 position, so to resolve the finest features, longer pulses need to be used. In general, to resolve a feature of width $\Delta\omega$, expressed in angular frequency units, one needs to use an echo integration window of duration at least $\Delta t = 2\pi/\Delta\omega$. The collected absorption spectrum will also be dependent on the relaxation times and the choice of the τ parameter used, particularly if the relaxation times are orientation or otherwise field-dependent, or if the sample contains multiple species with different relaxation times. Several datasets from EDFS measurements are shown across Chapters 6 and 7.

2.5.2 Nutation and bandwidth measurement

The actual magnitude of the pulse, and thus the spin nutation frequency, Eq. 2.39, depends on the resonator's response to the particular frequency of the microwave field. The resonator's modes are shifted as a large sample is inserted, and typically the resonator needs to be overcoupled at the beginning of each measurement session. Thus the response of the resonator may be different each time, and needs to be measured, in order to calibrate the duration for π and $\frac{\pi}{2}$ pulses. A standard way of measuring the amplitude of the B_1 field in a simple system is through the echo detected transient nutation experiment. A pulse of varying duration t is sent first, followed by a delay $T \gg T_2$. The electron coherence decays during this delay, but the polarization may be measured with a Hahn echo sequence, which follows the delay. The full sequence is shown in Fig. 2.6. The trace resulting from the

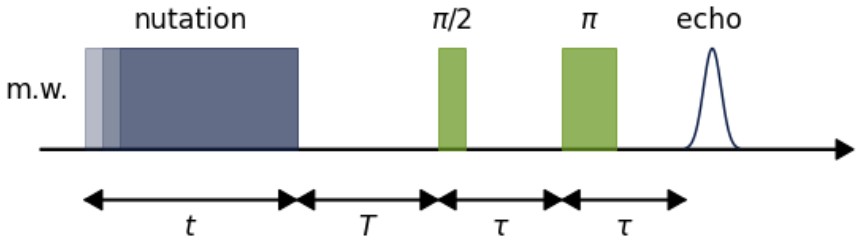


Figure 2.6: Pulse sequence of the echo detected transient nutation experiment. The delay between the nutation pulse T is fixed and large, the duration of the pulse t is varied. The echo sequence is used for detection.

echo integration at different values of t is a damped Rabi oscillation, or "nutation". The source of damping is the inhomogeneous broadening, more specifically B_1 inhomogeneity, but also the variation in the g-tensor across the participating spin packets and the spin-spin relaxation during the first pulse. The expected signal from single off-resonant spin packet is:

$$\langle \hat{S}_x \rangle(t) = \frac{\Omega^2 + \omega_1^2 \cos(\omega_{\text{eff}} t)}{\omega_{\text{eff}}^2} \tag{2.39}$$

Where $\omega_{\text{eff}}^2 = \Omega^2 + \omega_1^2$. Because ω_1 is proportional to B_1, the FT of the signal yields information about the B_1 magnitude at given ESR frequency. Repeating

the experiment at several frequencies yields an approximate response curve of the resonator, which may be useful in multi-frequency experiments.

This experiment helps quanitify the effect of $\boldsymbol{B}_1$ inhomogeneity. There are multiple pulse sequences that help minimize it by using composite pulses [76–79].

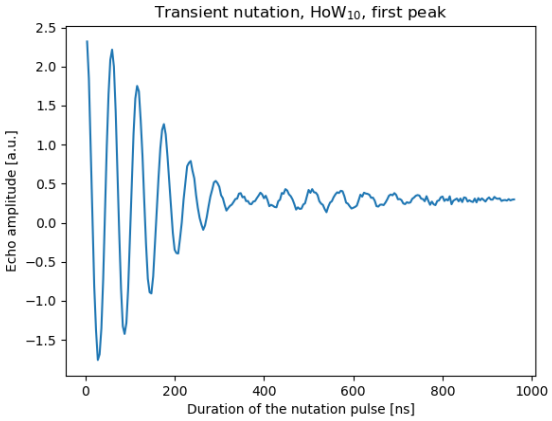


Figure 2.7: Example data from an echo detected transient nutation measurement. These data were collected using the pulse sequence shown in Fig. 2.6 on the HoW_{10} crystal sample, further discussed in 3.3 and 6.2.

2.5.3 Pulse calibration

The optimal duration of the $\frac{\pi}{2}$ and π pulses may be estimated using the above transient nutation experiment, measuring the interval between the peaks and troughs of the oscillation. In certain applications, π and $\frac{\pi}{2}$ pulses of the same excitation profiles need to be used, so the same spin packets are affected by each pulse. The duration of a pulse is fixed at a constant d, and the amplitude is calibrated instead in a modified echo experiment.

To calibrate the π pulse, the echo experiment is set up with a nominal $\frac{\pi}{2}$ pulse of duration $d/2$, and to calibrate the $\frac{\pi}{2}$ pulse, a nominal π pulse of duration $2d$ is used. The amplitude of both pulses in a given experiment is then varied continuously, either using an AWG or adjusting the attenuation. The amplitude of the echo follows Eq. 2.34, whose maximum corresponds to the optimal pulse amplitude in either case.

The maximum echo integral does not necessarily correspond to the nominal π or $\frac{\pi}{2}$ pulse, understood as the product $\omega_1 d$. The off-resonant spins have higher

effective turning angles, so the maximum for their contribution to the echo occurs at lower microwave pulse amplitude [80, 81].

2.6 Continuous Wave ESR

The traditional way of collecting ESR data is through a continuous wave (CW) experiment. Instead of using pulses, the microwave field $\boldsymbol{B}_1$ is applied continuously at a fixed frequency ν. The resonator is kept in a critically coupled mode, and the magnitude of the static magnetic field $\boldsymbol{B}_0$ is slowly swept through the selected range. Around the field positions, where ν corresponds to an allowed ESR transition in the sample, the resonance properties are modified. This leads to a detection of an absorption spectrum, which is a collection of peaks centred at resonance fields, whose width and shape depends on linewidths of the sample species.

2.6.1 Modulation

In most species, the changes in resonance properties that can be detected directly are small, and due to presence of multiple sources of noise, despite careful tuning, a direct detection of absorption spectrum becomes difficult. To solve this problem, a mechanism called phase-sensitive detection is employed. In addition to sweeping the magnetic field $\boldsymbol{B}_0$, a small oscillatory component is added to it, at frequencies of order 100 kHz and amplitudes of order 0.5 mT in X-band. The ESR spectrum will then also oscillate at the chosen frequency, enabling filtering out the noise components with different frequencies. An appropriately selected, small amplitude of this modulation will cause the collected ESR spectrum to look like a derivative of the true absorption spectrum.

The physics of CW ESR is in many ways more complicated[8] than the physics of pulsed ESR, but this topic is not explored here, as no datasets included in the final version of this thesis come from CW experiments. An interested reader is directed to textbooks [38–40].

[8]The CW experiment needs relaxation to work, and relaxation theories are complicated, as discussed in 2.4.

3

Molecular magnets as qubits

Contents

3.1 Molecular magnets and quantum computers 37
3.1.1 Well defined and scalable qubits 38
3.1.2 Operation and quantum gates 39
3.1.3 Initialization and readout 41
3.1.4 Relaxation and error correction 42
3.2 Properties of Cr_7Ni and Cr_7Mn molecular magnet rings 42
3.3 Properties of HoW_{10} crystals 44
3.3.1 Clock transitions and symmetry breaking in HoW_{10} crystals 47

In this chapter, we will move from a general overview of molecular magnets and their role within quantum-coherent nanoscience to the description of the properties of several important molecular systems investigated in this work.

3.1 Molecular magnets and quantum computers

One motivation for studying and engineering the properties of molecular nanomagnets is their potential application in a broadly defined field of quantum-coherent nanoscience [5]. Here, these properties and the current state-of-the-art will be reviewed using DiVincenzo's criteria for quantum computation as a framework [20]. Since DiVincenzo's proposal, the field has grown to encompass quantum simulation,

storage, information processing, communication and sensing [5, 19].

The research in present noisy intermediate-scale quantum (NISQ) [13] devices, based on superconducting circuits [6–8], spins in semiconductors [10–12] or trapped ions [9] is accelerating and approaching certain useful applications. The promise of quantum computers breaking encryption codes with Shor's algorithm [3] is however still far away, requiring millions of qubits, so it is sensible to keep considering alternative physical systems, such as molecular nanomagnets, and specific advantages they might provide.

For more systematic reviews of the field of quantum-coherent nanoscience [5] and the role of molecular magnets within it [19, 21], the reader is directed to the listed literature.

3.1.1 Well defined and scalable qubits

A qubit is a quantum system with at least two distinct energy levels, whose state during the computation remains in a subspace defined by these two levels. Such a two-level subspace may then be treated as a mathematical object, defined by the two basis states $|0\rangle$ and $|1\rangle$ [25]. Qubits are to quantum computation what bits are to classical computation. The alternative to a qubit is a qudit, which is defined analoguosly, but using not 2, but d levels instead.

One of the first proposals to use molecular magnets in quantum computation was to implement Grover's algorithm [2] in a single qudit system [16]. The molecular nanomagnets with the ground state $S = \frac{1}{2}$ can be considered qubits, and ones with higher total angular momentum J or nuclear spin I, are qudits, as they operate on $d = 2J + 1$ or $d = 2I + 1$ dimensional subspaces.

There are multiple strategies for scaling molecular magnets for quantum technologies. The first is scaling at the level of an individual molecule. This can be achieved by engineering higher angular momentum ground states, growing the dimension of each individual qudit. One of the first proposals [16] was based on using the large anisotropy (2.1.5) to lift the degeneracy of transitions in a qudit. Exploiting the hyperfine interaction between the electronic and nuclear spins modifies the

energy spacings between the states [24, 82]. In both cases, the transitions become addressable through different resonant frequencies. Alternatively, the advances in supramolecular chemistry may be leveraged to engineer structures composed of multiple molecular qubits linked together by thread molecules [29, 83]. This translates better to the standard circuit based quantum algorithms, as individual qubits are addressable by frequency, instead of different transitions within the same molecule, and the notion of entanglement makes sense.

The second way of scaling the molecular qubit architectures is to build individual quantum devices based around a single molecule and then link them together, engineering the interactions necessary to achieve a high-dimensional Hilbert space. Using molecular magnets for quantum technologies is a bottom-up approach [5], starting from intrinsic quantum properties such as electron spin. It may be contrasted with a top-down approach, where the qubit is an engineered unit, made to behave like a two-level quantum system through miniaturization and cooling, examples of which are the superconducting qubits and gate-defined quantum dots. These are naturally integrated with classical electronic elements needed to operate the devices. The molecular qubits are more challenging to fabricate in such a way, as they are significantly smaller in scale. However there are proposals to link molecular magnets with superconducting architectures [17, 84], and single devices were successfully built and operated [24]. A natural method is to use the power of chemical self-assembly to create devices that fabricate themselves from the bottom-up, for instance utilizing DNA nanotechnology [5, 85].

These strategies are not mutually exclusive, they can be and are pursued in tandem.

3.1.2 Operation and quantum gates

Electron Spin Resonance is the main method of operating magnetic molecules and performing quantum gates in relevant subspaces. A microwave pulse (2.3.5) is used to drive a transition between two magnetic energy states. Varying the duration or power of the pulse introduces Rabi oscillations, which may be used to calibrate

and implement single qubit rotations. The durations of these pulses need to be short compared to the phase memory time T_m, so that multiple operations can be performed before the system decoheres. In addition to single-qubit operations, a quantum gate set also requires two-qubit gates to be universal.

In systems based around a single molecular system, with multiple energy levels, the notion of a multi-qubit gate is meaningless[1]. For the gate set to be universal, it needs to be possible to create arbitrary coherences between different energy levels, through addressing each of the transitions in the system, directly or not. Implementing selective pulses becomes more challenging as the number of transitions increases, as their frequencies come closer to one another. For two transitions of frequencies ω_1 and ω_2 to be distinguishable in this way, a pulse needs to be at least $\frac{1}{|\omega_1-\omega_2|}$ long. If this starts approaching the decoherence time in the system, the universality of the gate set is threatened [21].

In weakly coupled systems, two-qubit gates may be realized through the terms of the static Hamiltonian describing the coupling. This is the topic of Chapter 7 of this work.

Due to frequency crowding, it would be beneficial to fabricate molecular architectures where each qudit can be addressable directly and separately from the others. Using microwave magnetic fields presents a challenge, as due to the scale of molecular magnets, which are already an order of magnitude smaller than superconducting circuits, a microwave magnetic field created from a current in a loop or coil will affect not only the selected molecule, but also its neighbours. In such a case, electric field control would be advantageous, as electric fields can be confined over smaller distances than magnetic fields. This is the topic of Chapters 4 and 6 of this work. Certain architectures of this type have been realized; a device based around a Tb^{3+} ion [24] uses the nuclear spin projection states $m_I = -\frac{3}{2}, -\frac{1}{2}, \frac{1}{2}, \frac{3}{2}$ as the basis for quantum operation. The hyperfine coupling with the electron

[1]In such systems it becomes challenging to implement quantum algorithms with measurements at intermediate steps, such as error correction based on stabilizer codes [86] or measurement based uncomputation [87], because even with projective measurement capabilities, the readout measures the state of the entire system, and these procedures require measurements of ancillary qubits while keeping the rest of the system coherent.

spin, remaining in the total angular momentum projection subspace $m_J = \pm 6$ shifts the transition frequencies significantly, so the transitions between them can be distinguished and realized through electric field microwave pulses. A simple instance of Grover's algorithm was already demonstrated in this system [88].

3.1.3 Initialization and readout

Quantum algorithms assume the system is initialized in a pure $|000\ldots0\rangle$ state. If a single shot projective readout is possible in the system, it is generally possible to initialize it by measurement. If the readout does not result in the ground state, it might be followed by a waiting period and another measurement, or manual rotation of the spin to the desired state. In the Tb^{3+} system mentioned above, the projective measurement is realized electrically. The electron spin is coupled to a gate defined quantum dot, whose conductance depends on the spin state. The static magnetic field is swept in this system, and the electronic spin may flip only at specific values of the field, dependent on the state of the nuclear spin projection. Thus the projective measurement is realized, and may also be used to initialize the system in any of the m_I states. In general, coupling to a quantum dot whose conductance is then measured electrically is a promising strategy for initialization and measurement of molecular magnet devices.

Without the single-shot measurement capabilities, the initialization may be done through cooling and waiting for system to return to the thermal equilibrium, which requires times longer than T_1. The purity of this thermal state is determined by the attainable temperature and the energy splitting, as explained in 2.2. For typical GHz transition frequencies, and mK temperatures achievable in dilution refrigerators, high purity initial states may be generated this way.

The measurement of the ensemble state is done under ESR principles, the electron coherence generates a signal oscillating at the frequency of the transition. Well-separated levels are thus again necessary for the operation.

3.1.4 Relaxation and error correction

The operation times in molecular magnets are meaningful when compared with relaxation rates (2.4). An accurate measurement of the intrinsic relaxation times may be challenging, as the decoherence times observed in an ensemble ESR experiment depend on the choice of the solvent [89]. The typical strategies to increase coherence times are based on removal of the sources of magnetic noise, and include embedding a paramagnetic specie in a crystal of a diamagnetic analogue [90], reducing the number of nuclear spins, or replacing the protons in the solvent with deuterium [89, 91]. The molecules may be engineered to encapsule the magnetic ion in a cage [92] or sandwich it between ligands [91], preventing spin diffusion. Another strategy is to employ an avoided level crossing to create a clock transition, where the transition frequency does not depend significantly on the magnetic field, and thus the transition's stability is improved [90, 93]. In general, the flexibility in the design of the molecular magnets allows experimenting with solvents, ligands and architectures to improve the relaxation times.

The present values of T_m reach from multiple μs up to 1 ms [94], compared to durations of microwave pulses of order 10 ns needed to drive the respective transitions. Specific examples are listed later in this chapter.

There are also proposals and realizations of certain basic quantum error correction protocols in molecular magnets [95, 96], which would further increase effective coherence times.

3.2 Properties of Cr_7Ni and Cr_7Mn molecular magnet rings

One particular family of molecular magnets investigated in this work are the Cr_7M wheels. The central part of these compounds is an antiferromagnetic ring of 8 Cr^{3+} ions ($S = \frac{3}{2}$), one of which has been substituted with a dopant ion (M in the general formula), either Mn^{5+} ($S = \frac{5}{2}$), or Ni^{2+} ($S = 1$) [89, 97]. The wheel is held together by carboxylate bridging ligands, and surrounds a cation, selected to counterbalance

the charge of the dopant ion. The structure is shown in Fig. 3.1. Different bridging ligands and cations may be utilized to influence the magnetic properties of the molecule [75]. The molecules were first synthesized [98] following a theoretical proposal predicting interesting magnetic properties of doped exchange coupled rings [99]. As a result of the doping, the rings exhibit well defined ground states corresponding to $S = \frac{1}{2}$ for Cr_7Ni and $S = 1$ for Cr_7Mn at temperatures below 50 K. Other possible dopant atoms include Zn, resulting in $S = \frac{3}{2}$ [100], Co, Cd or Fe [101].

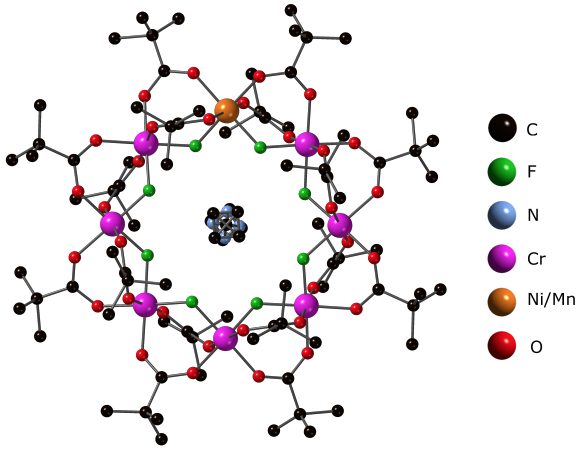


Figure 3.1: A possible structure of a Cr_7M ring molecule (M = Ni, Mn). The cation in the centre and the ligands may be varied, changing the properties of the molecule, such as phase memory times T_m [75].

The interest in these compounds escalated after long phase memory (2.4.2) times T_m were reported [75, 89] for Cr_7Ni and Cr_7Mn, of order 1 μs with stretch parameters x between 0.9 and 1.7, further increased by deuteration of the solvent and careful selection of carboxylate ligands, up to 15 μs. The main decoherence mechanism in these compounds is reported to be nuclear spin diffusion, where nuclear flip-flop processes destroy electronic phase coherence. It is the flexibility of these compounds, in relationship to a choice of ligands and cations, that kept the interest and hope to further increase decoherence times in molecular magnets. Single-qubit gates, represented by microwave pulses, may be realized on order 10 ns, so the Cr_7M rings were considered good candidates for qubits, satisfying some of the DiVincenzo's criteria (3.1).

The $S = \frac{1}{2}$ ground state of the Cr_7Ni molecule can be effectively described by a simple Zeeman spin Hamiltonian, with small g-tensor anisotropy and a g-strain resulting from unresolved hyperfine interactions and structural differences. On the other hand, the Cr_7Mn molecule with its $S = 1$ ground state, requires an inclusion of significant zero-field splitting and anisotropy terms, parametrized by D and E:

$$\hat{H} = \frac{\mu_B}{\hbar} g\boldsymbol{B} \cdot \hat{\boldsymbol{S}} + D\hat{S}_z^2 + E(\hat{S}_x^2 - \hat{S}_y^2) \tag{3.1}$$

where $\hat{S}_z^2, \hat{S}_x^2, \hat{S}_y^2$ are squares of relevant spin projection operators. In the 2007 study [89], $D = 21$ GHz and $E = 1.9$ GHz were found in addition to $g = 1.9$. This results in a much wider spectrum than the one observed from Cr_7Ni variety.

DiVincenzo's criteria require an universal set of quantum gates, which can be achieved with an addition of robust two-qubit gates to single qubit rotations. As a step towards this goal, several variations of dimers of Cr_7Ni molecules were synthesised and investigated [29]. The ground state of each ring results from strong exchange coupling between neighbouring ions, but the interaction of the two rings in a dimer, separated by distances between 1.6 and 3.1 nm depending on the variety, is weak and mostly dipolar. The strength and orientational selectability of this interaction were investigated and found sufficient to be a basis for a two-qubit gate using the interaction directly [2], with durations between 80 and 500 ns, relatively short compared to reported phase memory times ≈ 3 μs. The methods used are further discussed in 5.4 and the topic of two-qubit gates using the weak dipolar interactions in disordered spin-$\frac{1}{2}$ dimers is expanded upon in Chapter 7.

3.3 Properties of HoW_{10} crystals

Another interesting family of molecular magnets are the Ln $(W_5\ O_{18})_2$ complexes, where Ln is a lanthanide ion, (Ln = Gd, Tb, Dy, Ho and Er) [104, 105]. The ion is sandwiched between two polyoxometalate ligands. The sodium salts of these

[2] Directly, as opposed to using the interaction to mix and split the eigenstates and driving the two-qubit gate with selective pulses, which is possible in electron-nuclear coupled systems [32, 33] and more strongly coupled systems in general, for example in quantum architectures based on gate-defined quantum dots [102, 103].

complexes crystallize with a primitive P1 symmetry where each unit cell contains two molecules related by inversion symmetry, but the entrapment helps preserve the properties the ion has outside a crystal structure. The lanthanide ion has an approximate local D_{4d} symmetry, however there are individual differences between the angles and distances to the coordinated oxygens. This departure will prove crucial in the context of this work.

We will from now on focus on the holmium variant, as its unique properties lead to experimental results presented in later sections of this work.

All the molecules exhibit large spin orbit coupling, with $L = 6, S = 2$ and $J = 8$ in the ground state in the case of the holmium ion. The magnetic ground state of the HoW_{10} molecule has nuclear spin $I = \frac{7}{2}$ and can be described with the following spin Hamiltonian (2.1:

$$\hat{H} = \sum_{k=2,4,6} \sum_{q=-k}^{k} B_k^q \hat{O}_k^q + \hat{J} \cdot \mathbf{A} \cdot \hat{I} + \mu_B g_e \mathbf{B}_0 \cdot \hat{J} - \mu_N g_N \mathbf{B}_0 \cdot \hat{I} \tag{3.2}$$

where $\hat{O}_k^q$ are extended Stevens operators (2.1.5), $\mathbf{A}$ is the hyperfine tensor, g_e and g_N are respectively electronic and nuclear g-factors, and $\mathbf{B}_0$ is the static magnetic field, as usual. The only Stevens terms present in a Hamiltonian of a perfectly D_{4d} symmetric molecule would be the axial $B_2^0\hat{O}_2^0, B_4^0\hat{O}_4^0$ and $B_6^0\hat{O}_6^0$ terms. Because of the breaking of this symmetry, $q = 4$ terms are needed to describe effects of the tetragonal anisotropy. For the Ho molecule, the exact form of structural anisotropy is temperature dependent, but in general the skew angle θ between Ho-O bonds deviates from the D_{4d} ideal 45° by $2° - 3°$. The holmium ion is also shifted slightly, by $d = (h - h')/2$, towards one of the W_5O_{18} ligands (Fig. 3.2), where $d = (0.0023 \pm 0.0002)nm$, the exact value is temperature dependent. Previous studies [90, 105] used the following values to achieve agreement with the experimental data: $g_\parallel = 1.25$, (note it is equal to the Landé g-factor for $L = 6, S = 2, J = 8$ [105]), $A = 830$ MHz, $B_2^0 = 18.03$ GHz, $B_4^0 = 209$ MHz, $B_6^0 = -1.53$ MHz, $B_4^4 = 94.3$ MHz.

The above Hamiltonian results in the lowest energy states with $m_J = \pm 4$, separated from the closest $m_J = \pm 5$ by 20 cm^{-1}. ESR transitions between $m_J = 4$ and $m_J = -4$ should normally be forbidden, because the standard $\mu_B g_e B_1(\hat{J}_+ + \hat{J}_-)$

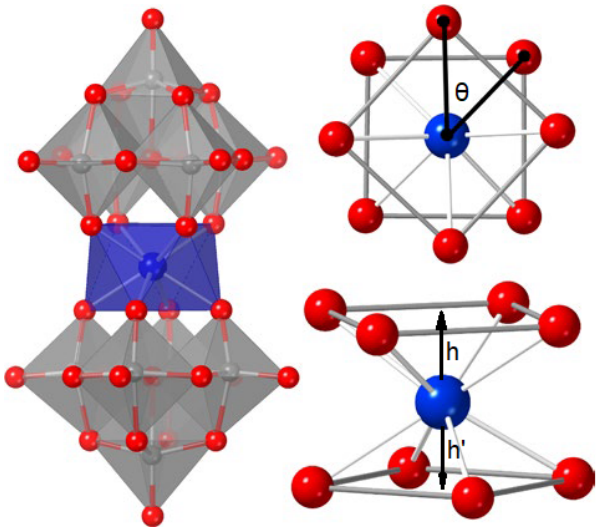


Figure 3.2: Approximate structure of the Ho $(W_5\ O_{18})_2$ complex. The crystal, including Na^+ ions and crystallization water, has general P1 symmetry, and includes two HoW_{10} molecules per unit cell, related by inversion. The coordination environment of the Ho ion itself has approximate D_{4d} symmetry, the departure from which can be parametrized by $d = (h - h')/2$ and θ, which would be 45° in a symmetric case.

term, originating from an oscillating magnetic field perpendicular to B_0, connects states with $\Delta m_J = \pm 1$, but the presence of the $\hat{O}_4^4 = \frac{1}{2}(J_+^4 + J_-^4)$ term mixes the $m_J = \pm 4$ states and enables parallel mode (where $\boldsymbol{B}_0 \parallel \boldsymbol{B}_1$) transitions between them to take place. It should be noted that in a standard ESR spectrometer architecture $\boldsymbol{B}_0$ and $\boldsymbol{B}_1$ are perpendicular. It was at first mysterious why any ESR experiment is possible with this sample. However, because of the axial symmetry of the molecule, for the $m_J = \pm 4$ doublet, the effective perpendicular g-factor, $g_\perp = 0.01$. This same effect also applies to the hyperfine tensor, i.e. $A_\perp \ll A_\parallel$. This implies the holmium electrons effectively only see magnetic field components parallel to the molecular axis. As the molecular axis is not parallel to any of the faces or edges of the physical crystal sample, in a practical experiment this axis is aligned with neither $\boldsymbol{B}_0$ nor $\boldsymbol{B}_1$, meaning both fields have components along it despite being perpendicular to each other and so, the parallel mode transitions become allowed. As a result, all the features in any field sweep ESR experiment are only dependent on the $B_0 \cos\alpha$, the longitudinal (parallel to molecular axis) component of the static magnetic field, instead of its total magnitude. The field sweep experiments conducted at different molecular orientations α_1, α_2 are related

to each other by the rescaling of the x-axis by a factor $\cos\alpha_1/\cos\alpha_2$, as confirmed by experiment [90, 105] and as a result an Echo Detected Field Sweep measurement may be used to determine this angle.

3.3.1 Clock transitions and symmetry breaking in HoW_{10} crystals

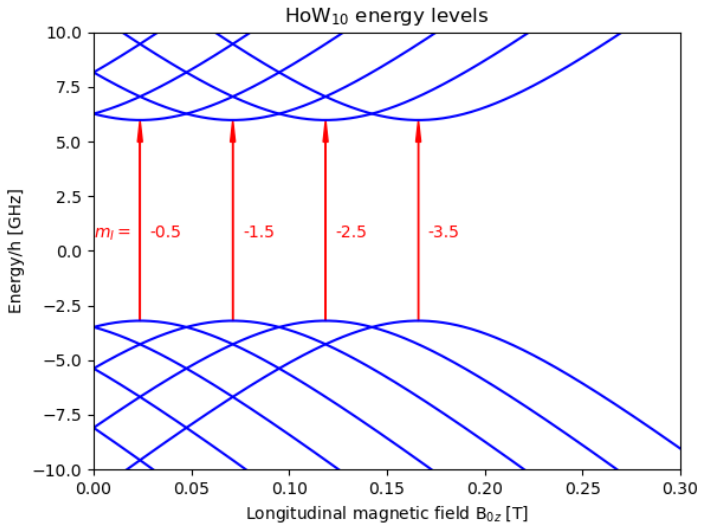


Figure 3.3: Low field energy level diagram of the HoW_{10} molecule. The red arrows represent clock transitions, each corresponding to a different nuclear spin projection m_I. The two states between which the transition takes place are superpositions of $m_J = 4, -4$ and to small degree also $m_J = 8, -8, 0$ quantum states. The avoided crossings appear as a result of broken tetragonal symmetry, parametrized in the Hamiltonian by the $B_4^4\hat{O}_4^4$ term.

The presence of the tetragonal anisotropy terms $B_4^4\hat{O}_4^4$ in the Hamiltonian produces avoided crossings between the energy levels, shown in the magnetic field dependent level diagram, Fig. 3.3. They are known as clock transitions (CT), because their ESR frequency is independent of small local variations in the B_0 field and fixed at about 9.15 GHz, which is close to the widely used X-band range of ESR frequencies. Because of the hyperfine interaction with the holmium nucleus, $I = \frac{7}{2}$, there are a total of 8 $\Delta m_I = 0$ CTs in the spectrum, each corresponding to a different m_I. The transition frequency around the crossing can be approximated as:

$$f = \Delta + \frac{\gamma_z}{\Delta}(B_{0z} - B_{\min}) \tag{3.3}$$

where $\Delta = 9.15$ GHz is the CT frequency,γ_z is the z component of the gyromagnetic ratio, B_{0z} the longitudinal component of B_0, and $B_{\min}$ the field at which the CT occurs. Because this turns the transition insensitive to magnetic noise in the first order, the decoherence times at the clock transitions increase significantly, to $5-8\mu$s at 5K compared to 1μs at elevated frequencies [90], which alone makes it an interesting molecular magnet. This is also where the name 'clock transitions' comes from, as a reference to atomic clocks, whose transition frequencies are insensitive to certain classes of fluctuations. Measuring the sample using higher frequencies results in a more traditional-looking ESR spectrum, a comparison is shown in Fig. 3.4.

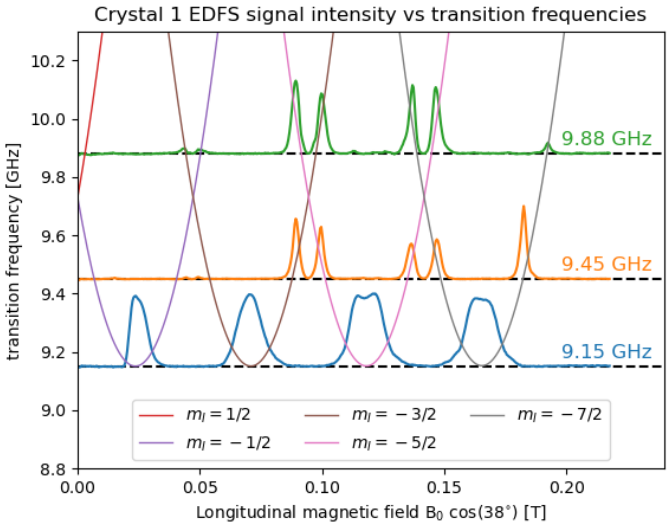


Figure 3.4: Echo Field Sweep spectra of the HoW_{10} with overlayed calculated transition frequencies corresponding to several nuclear spin projections m_I. At higher frequencies, the m_J become better quantum numbers, and one must be careful labelling the transitions with the nuclear spin projections m_I, as they switch places.

4
Electric fields and ESR

Contents

4.1 Motivation 49
4.2 Spin Electric Coupling Hamiltonians 50
4.2.1 The role of inversion symmetry 51
4.2.2 Breaking of chirality under electric fields 52
4.3 Detecting a Spin Electric Coupling using ESR 53
4.3.1 Continuous wave ESR 54
4.3.2 Pulsed ESR under static electric field 55
4.3.3 Using non-resonant E-field manipulation to enhance selectability in devices 59

In this chapter, several ways an external electric field may couple to electron spin in a molecular magnet are reviewed. Then, the methods of measuring the Spin-Electric Coupling (SEC) are discussed.

4.1 Motivation

Molecular magnets and their potential for creating quantum devices were introduced in Chapter 3. The electron spin in a molecular nanomagnet is one of the most natural, bottom-up candidates for a quantum bit, but to operate a device based upon it, individual qubits and interactions between them have to be controlled from outside. Spin naturally couples to magnetic fields, and controlling ensembles

of spins through oscillating magnetic fields is well established science [18]. At the nanometer scale of a single molecule, however, magnetic fields prove difficult to control, as they emerge from loops of current, and do not localise easily, not allowing a selection and control of one and one qubit only. Electric fields, on the other hand, emerge from electrical charges and using them to control individual magnetic qubits would make this task much easier technologically [22, 23, 106–108], but they do not naturally couple to spin. The challenge is then to research and engineer such molecular magnets, where a Spin-Electric Coupling (SEC) strong enough to facilitate building those quantum devices is introduced.

Quantum devices using E-field for quantum control already exist. Some are based on electron spins in gate-defined semiconductor quantum dots [10, 11, 22, 23]. Instead of applying an oscillating magnetic field using an antenna, a micromagnet is placed next to the quantum dot system, producing a magnetic field gradient. Then, the gate voltage itself may be driven at microwave frequency, causing the electron to move in the gradient and experience an oscillating magnetic field. This can be optimized and used to coherently implement quantum gates in these devices, and the E-field is used precisely for its better localizability.

Building such devices using molecular magnets with large SEC is thus a realistic goal [88, 109–114]. The only missing link are such molecular magnets themselves. In this chapter, we will look into ways molecular magnets might couple to E-fields, and what methods exist to measure and exploit these couplings. This will ultimately help us understand how to create molecular magnets with desirable properties.

4.2 Spin Electric Coupling Hamiltonians

The standard and effective way of describing spin systems is through low energy phenomenological spin Hamiltonians, which were summarized in 2.1. SEC would have to manifest itself in the Hamiltonian, as a modulation of one of its existing terms. Each of those terms arise because electron spins are embedded in a molecular structure, which modifies their properties. An external E-field might interact with the structure, deforming it, or interact directly with electron clouds, both of

which may potentially lead to changes in each of the above parameters, resulting in a SEC [115].

To illustrate the mechanism, one may look at a simple example of the axial anisotropy, or ZFS term, introduced in 2.1.5 and Eq. 3.1. In Mn defects in ZnO [116], the origin of the axial anisotropy $-D\hat{S}_z^2$ term are local crystal electric fields. An external electric field then modifies the D parameter, leading to a shift in transtion frequency ν between energy levels corresponding to different values of a square of the m_S spin projection quantum number.

Note that the aforementioned crystal electric fields are typically of order 10^9 V/m [116]. In the lab, it is possible to apply voltages of about $300-400$ V over the distance of $3-5$ mm, resulting in E-field of order 10^5 V/m. Any experiment aiming to measure resulting frequency shifts will need to be highly sensitive. Regardless of the origin of the SEC, it should be expected that the relative frequency shifts are small in most samples [117, 118].

4.2.1 The role of inversion symmetry

If one is interested in resonantly driving transitions using an external E-field, a linear SEC would be the most useful. Because the external E-field is usually much weaker compared to the internal, crystal field inside the molecule, a higher order coupling produces a much weaker frequency shift [119]. A linear SEC is however not allowed in molecular environments with local inversion symmetry. Inverting the direction of the E-field is equivalent to inverting the molecule, while keeping the E-field fixed. An E-field with the same magnitude and direction but opposite sign would cause the opposite first order effect in such an environment. However, in an inversion symmetric molecule, inverting the molecule causes no change, so the effect should also remain identical in the first order [120]. If $\hat{H}(\mathbf{E}) = \hat{H}_0 + \mathbf{E}\hat{H}_1$ is a Hamiltonian, where the $\hat{H}_0$ term is independent of the E-field, and the $\hat{H}_1$

linearly couples to the E-field, we have:

$$\begin{aligned} \hat{H}(-\mathbf{E}) &= \hat{H}(\mathbf{E}) \\ \hat{H}_0 - \mathbf{E}\hat{H}_1 &= \hat{H}_0 + \mathbf{E}\hat{H}_1 \\ \hat{H}_1 &= 0 \end{aligned} \tag{4.1}$$

Therefore an inversion symmetric system, or any system where inverting the sign of an applied E-field leads to the equivalent molecular environment, cannot have a first-order SEC.

This relationship was first used to investigate the symmetry of certain spin centres using ESR with E-field [119]. Centres related by inversion symmetry are magnetically identical, thus an experiment involving only magnetic fields will affect two spins related by inversion symmetry in the same way. Adding E-field helps distinguish them, and observing a linear SEC is evidence the inversion symmetry is broken [119, 120]. Nowadays, there exist more efficient methods of determining symmetries of spin centres, but broken inversion symmetry is an important marker of a molecule that may in principle exhibit linear SEC.

4.2.2 Breaking of chirality under electric fields

A particular example of inversion symmetry breaking was proposed by Trif et al. [107, 121]. The model molecule consists of three exchange-coupled spin-$\frac{1}{2}$ centres in an equilateral triangle geometry. The low-energy spin Hamiltonian of this system is:

$$\hat{H}_{\text{tr}} = J\left(\hat{\mathbf{S}}_1 \cdot \hat{\mathbf{S}}_2 + \hat{\mathbf{S}}_2 \cdot \hat{\mathbf{S}}_3 + \hat{\mathbf{S}}_3 \cdot \hat{\mathbf{S}}_1\right) \tag{4.2}$$

where J is the exchange coupling constant. When $J < 0$, the system is frustrated. Intuitively, the exchange coupling between each two spins would cause them to assume opposite projections in the ground state. However, this is not possible for all three pairs. As a result, the ground state multiplet splits into two degenerate manifolds: the higher energy $\left|S = \frac{3}{2}\right\rangle$ one, and the lower energy $\left|S = \frac{1}{2}\right\rangle$ one, generated by all the $|\uparrow\uparrow\downarrow\rangle$ and $|\uparrow\downarrow\downarrow\rangle$ symmetric configurations. The authors adopt

a chirality pseudospin C, with three operators $\hat{C}_z, \hat{C}_x, \hat{C}_y$ transforming like Pauli matrices, and use it to create a basis for the ground state multiplet:

$$\begin{aligned}\left|m_S = \frac{1}{2}, C_z = +1\right\rangle &= \frac{1}{\sqrt{3}}\left[|\uparrow\uparrow\downarrow\rangle + \exp(2i\pi/3)\,|\downarrow\uparrow\uparrow\rangle + \exp(4i\pi/3)\,|\uparrow\downarrow\uparrow\rangle\right] \\ \left|m_S = \frac{1}{2}, C_z = -1\right\rangle &= \frac{1}{\sqrt{3}}\left[|\uparrow\uparrow\downarrow\rangle + \exp(4i\pi/3)\,|\downarrow\uparrow\uparrow\rangle + \exp(2i\pi/3)\,|\uparrow\downarrow\uparrow\rangle\right]\end{aligned} \tag{4.3}$$

and analoguosly for $|m_2 = -1/2\rangle$. The authors demonstrate that within the model, E-field applied in molecular plane couples to the $\hat{C}_x, \hat{C}_y$ chirality pseudospin operators, and therefore induces transitions between the $\hat{C}_z$ eigenstates. This can also be intuitively understood as the planar E-field distorting the equilateral geometry, breaking the symmetry by elongating and shrinking the molecule, so that the chirality eigenstates are mixed. This is a direct model of how E-field may be used to drive transitions between quantum levels in a magnetic molecule, albeit with a nonstandard notion of spin. It is an important theoretical proposal, because it directly links the structural deformation of the molecule due to external electric field with specific modifications to its magnetic properties and postulates a very specific form of SEC. It has sparked experimental investigation, such as experiments with Fe_3 complexes [122, 123] and measurements of Cu_3 centres discussed later in 6.1.1, also published [37].

4.3 Detecting a Spin Electric Coupling using ESR

The tool most widely used for investigating molecular spin systems, and thus any SEC, is ESR [115, 117, 119]. Depending on the exact way the E-field enters the spin Hamiltonian, two kinds of manipulations on the underlying molecular spin system may be possible [115].

If the total Hamiltonian is

$$\hat{H} + \delta\hat{H}(\mathbf{E}) \tag{4.4}$$

where $\hat{H}$ is the static Hamiltonian, and $\delta\hat{H}(\mathbf{E})$ is the E-field dependent perturbation, resonant manipulation between energy levels $|0\rangle$ and $|1\rangle$ of the static Hamiltonian

$\hat{H}$ is possible whenever

$$\langle 0| \delta\hat{H}(\mathbf{E}) |1\rangle \neq 0 \tag{4.5}$$

An oscillating electric field of frequency $f = (E_0 - E_1)/h$, where energies E_0 and E_1 correspond to quantum levels $|0\rangle$ and $|1\rangle$, will then excite Rabi oscillations between those two levels, by Fermi's Golden Rule.

Alternatively, the E-field might modify the energy gap between the two levels. If the condition:

$$\langle 0| \delta\hat{H}(\mathbf{E}) |0\rangle \neq \langle 1| \delta\hat{H}(\mathbf{E}) |1\rangle \tag{4.6}$$

is satisfied, the transition frequency $f = (E_0 - E_1)/h$ is modified by presence of a static E-field. This transition needs to be an active magnetic transition, or otherwise be possible to be driven or detected. The shift in the frequency needs to be measured as a function of the applied static E-field to quantify the magnitude of the effect, which is known as non-resonant manipulation.

The detectability of different SEC Hamiltonian terms in both resonant and non-resonant manners were investigated theoretically by Troiani [115]. Importantly, a particular form of coupling might result in a possibility of either, both or none of these forms of manipulations. Finding an E-field dependence in the Hamiltonian through a non-resonant experiment does not imply a possibilty of a resonant control of quantum state with an E-field only. An allowed type of manipulation will still need to follow specific selection rules [124].

Here I discuss techniques of non-resonant manipulation using SEC in ESR.

4.3.1 Continuous wave ESR

A standard continuous wave (CW) experiment is used to observe the allowed magnetic transitions between the energy levels of the spin Hamiltonian, as explained in 2.6. Thus in principle, as E-field modifies the transition frequencies, it should be possible to perform this experiment under a static E-field to investigate how they are modified. Most of the time, the practically achievable shift in frequency is of order

of a few MHz [117, 119], which is less than the inhomogeneous broadening of the CW line corresponding to each transition. What is more challenging, if a significant effect is observed, is to determine whether a reduction in resonance intensity is coherent, or another type of decoherence caused by the aplication of the E-field.

Nevertheless, a recent study [122] attempts such an experiment. The researchers apply a static E-field to both a crystal sample and a powder ensemble of molecules based on an equilateral triangle of three Fe atoms, as proposed in [107]. They perform a standard CW ESR experiment, varying the magnitude of the external E-field. They find a small increase in the magnitude of the resonance, while its position is unchanged. This is consistent with the theoretical studies, which predict that a modification of the coupling between iron spins due to the in-plane external E-field would change the intensity of the transition, but the energy difference associated with the transition would not change.

A more sophisticated approach is to perform a CW experiment with slowly oscillating E-field acting as modulation. In a typical CW ESR experiment, there the static magnetic field is modulated, as explained in 2.6.1. It is possible to exploit the SEC by using the E-field as modulation instead. Then, the signal becomes proportional to the difference of the absorption at the extreme values of the magnitude of the E-field and thus is only visible if there is a SEC in the spin system. Fittipaldi et al. [124] perform such an experiment with molecular helices, where E-field is expected to modify the exchange coupling between electron spins via the interaction with the dipole moment.

4.3.2 Pulsed ESR under static electric field

An alternative to CW ESR is of course pulsed ESR (2.3). There exists a range of methods of measuring the SEC based on the Hahn echo sequence (2.3.6), with embedded E-field pulses. An application of DC voltage during parts of the quantum evolution modifies the underlying Hamiltonian, shifting the transition frequency by δf. If this voltage, or static E-field, is applied during the first half of the echo sequence for time t_E, it shifts the phase of the resulting echo by $-t_E \delta f$. If it is

applied during the second half, after the refocusing pulse, it corresponds to an opposite phase shift, $t_E \delta f$ [117, 119, 120]. Note that even if δf is not dependent on the voltage in any particular way, the rules of quantum dynamics guarantee that the phase shift is linear in time t_E.

The simplest pulse sequence utilizing this effect is to apply the E-field during the whole half duration of the experiment, either between the $\frac{\pi}{2}$ pulse and the π pulse, or following the π pulse up until or even beyond the echo. Due to technological constraints in 1976, this is how this experiment was performed initially [120]. This generates the maximum phase shift $\delta f \tau$, where τ is the duration of either of the free evolution periods in the Hahn echo sequence.

With the ability to switch the voltage on a faster scale, it is possible to improve this sequence. The duration t_E of the E-field pulse is varied, as shown in the diagram (Fig. 4.1), starting after the $\frac{\pi}{2}$ pulse and eventually extending all the way to the echo. The phase shift in the echo initially increases with t_E, and then starts decreasing as $t_E > \tau$, to finally reach 0 when the E-field pulse extends through the Hahn echo. The advantage here is to distinguish a coherent shift caused by SEC from a range of incoherent effects that may be associated with the voltage, which would not allow the echo to completely recover when $t_E = 2\tau$, as well as follow the evolution of the Hamiltonian under the E-field dependent term. If $\tau \geq \frac{2\pi}{\delta f}$, multiple oscillations will be observed in the data, enabling the use of a Fourier Transform to find the best fit for δf.

Alternative sequences may be used to distinguish a leading linear from a leading quadratic SEC. The value of a voltage applied for half the evolution might be swept, enabling the observation of how the frequency shift depends on it directly, as shown in Fig. 4.2.

Alternatively, bipolar voltage pulses may be used [117]. Two voltage pulses are applied during the Hahn echo sequence, with opposite polarity, as shown in Fig. 4.3, resulting in an opposite E-field. If both pulses have the same duration t_E and are applied during the first half of the evolution, and the frequency shift δf is linear in E-field amplitude, the overall phase shift at the echo will be $\delta f t_E - \delta f t_E = 0$.

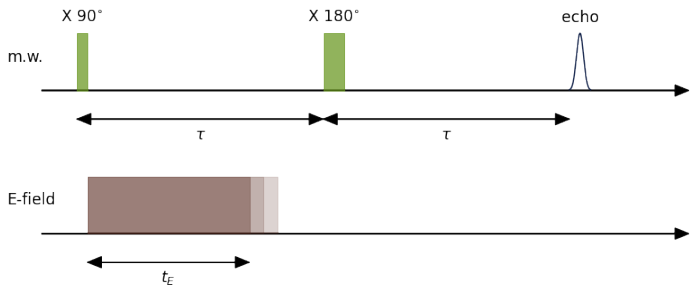


Figure 4.1: The pulse sequence used in the standard pulsed ESR investigation of the SEC. Based on the Hahn echo sequence, an E-field pulse of a varied duration t_E is inserted after the initial $\frac{\pi}{2}$ pulse. The final echo acquires a phase $-t_E\delta f$, where δf is the transition frequency shift due to the applied static E-field, when $t_E < \tau$. This phase shift increases linearly with the duration of the pulse until it reaches τ, at which point it starts decreasing as the evolution direction is reversed after the π pulse.

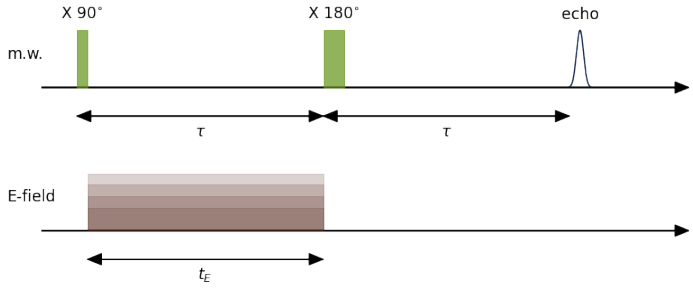


Figure 4.2: One way of investigating the linearity of the SEC is to vary the voltage that generates the E-field pulse. The phase shift $-t_E\delta f$ should increase while the voltage is increased, and the nature of this increase helps detemine the nature of the coupling.

If the SEC is quadratic, both pulses generate the same frequency shift, resulting in an overall $2\delta f t_E$ phase shift. The second voltage pulse might also be applied during the refocusing half of the Hahn echo sequence, in which case the quadratic phase shifts are refocused, but the linear ones are amplified.

If working with an ensemble of spins, even the simplest pulse sequence shown in Fig. 4.1 may allow distinguishing between linear and quadratic SEC. Spin centres related by inversion symmetry, as explained in 4.2.1, are magnetically equivalent but

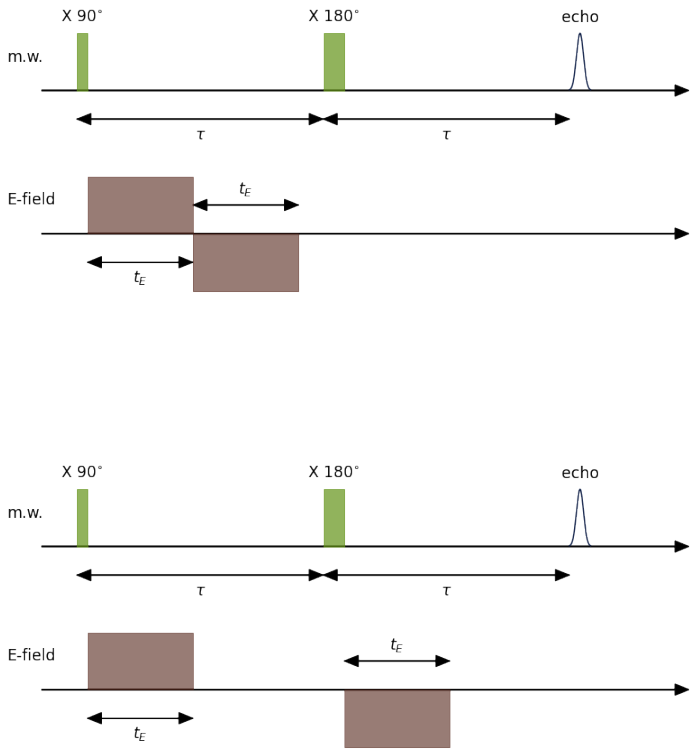


Figure 4.3: Pulse sequences that may be used to measure only the quadratic (top) or only the linear (bottom) part of the SEC. The inverted pulses signify E-field pulses of opposite polarity, but the same magnitude. They should generate an opposite frequency shift in case of a linear SEC and an identical one in case of a quadratic SEC [117].

experience opposite frequency shifts under external E-field if the leading contribution to the SEC is first order. The initial $\frac{\pi}{2}$ magnetic pulse places both spin centres in the same superposition state, but their contributions to the Hahn echo will be affected by opposite phase shifts. As a result, in the Hahn echo formed from all the affected spin centres in the ensemble, one will observe not a phase shift, but a decrease in magnitude of the echo by a factor of $\left(\exp(i\delta f t_E) + \exp(-i\delta f t_E)\right)/2 = \cos(\delta f t_E)$. If the SEC is second order, the frequency shifts are again identical for both spin centres, so a phase shift will be observed.

It is important to note that a clear phase shift in the data is not necessarily evidence of a non-linear SEC, if one failed to prevent predatory magnetic fields to emerge as a result of the application of the voltage pulse, for example from loops of

cables connecting to the electrodes that generate the E-field at the sample position.

4.3.3 Using non-resonant E-field manipulation to enhance selectability in devices

In a 1998 proposal of using P dopants in Si for quantum computation [106], Kane defines an A-gate. The hyperfine coupling between an electron and a nucleus, traditionally denoted with the letter 'A', may originate from the zero-contact interaction between them, as discussed in 2.1.4. Applying an external electric field to such a localized system inside a device, one may pull the electron away from the nucleus and thus modify the coupling. This in turn changes the transition frequency associated with the flip of the electron spin. This transition frequency then becomes targetable with the oscillating magnetic field, which no longer needs to be localized on one specific electron in a device constructed from many such electron-nucleus systems interacting via exchange (2.1.3). The transition frequencies of other electrons are not modified, so they do not interact with the applied oscillating magnetic field.

Even though the A-gates are not frequently used in present donor Si quantum devices [125], the idea of using the non-resonant E-field manipulation (Eq. 4.6) to allow selectability of a specific spin in a device without the need of localizing the $\boldsymbol{B}_1$ field could be one way to utilize weakly spin-electric coupled molecular magnets in devices. As long as it is possible to apply the E-field to one of the molecular magnets in the manufactured array and shift its frequency by $\Delta f > 1/d$, where d is the duration of the magnetic field pulse used to excite the relevant transition, it would be possible to selectably drive each molecular qudit without affecting the others.

5

Dynamics of dimer spin-$\frac{1}{2}$ systems

Contents

5.1 Mathematics of a two spin-$\frac{1}{2}$ system 62
5.1.1 Hamiltonian of a two spin-$\frac{1}{2}$ system 62
5.1.2 Rotating frames 62
5.2 Fidelity and an amount of entanglement as metrics . . 64
5.2.1 State fidelities 65
5.2.2 Process fidelity 67
5.2.3 Positive partial transpose and log-negativity 67
5.3 NMR quantum computing 68
5.3.1 Pure, pseudo-pure states and entanglement 69
5.3.2 Entangling gate 70
5.3.3 NMR readout and state tomography 72
5.4 Double Electron-Electron Resonance 73
5.4.1 DEER pulse sequences 74
5.4.2 DEER background 75
5.4.3 Orientational averaging of the dipolar interaction 76
5.4.4 Low temperature DEER 78

In this chapter selected concepts from mainstream pulsed ESR and NMR quantum computing will be presented, focusing on describing, probing, measuring and utilizing the interaction between two spin-$\frac{1}{2}$ particles, as well as quantifying the efficiency of implemented two-spin quantum gates.

To build a quantum computer, one needs robust qubits with long decoherence times, but also needs those qubits to interact with each other, so multi-qubit

gates may be implemented. As decoherence comes from the interaction with the environment, there is a common problem arising in most of the proposed quantum architectures. A qubit completely isolated from all quantum systems surrounding it will have long decoherence times, but will not be able to interact with other qubits. Design of quantum computers thus needs to walk this fine line, isolating the qubits just enough, but not too much. This is not an issue restricted to molecular magnets, ESR or NMR [12, 126, 127].

5.1 Mathematics of a two spin-$\frac{1}{2}$ system

In this section mathematics needed to describe a quantum system comprised of two interacting spin-$\frac{1}{2}$ particles is discussed in the context of a two electron system, however it does apply equally well to nuclear spins. The product operators (2.3.3) are used as a basis throughout.

5.1.1 Hamiltonian of a two spin-$\frac{1}{2}$ system

The spin Hamiltonian of a two-electron spin system contains two Zeeman terms corresponding to each electron and interaction terms. The interaction between two electrons is a sum of a dipolar (2.1.2) and exchange (2.1.3) interactions. For experiments and systems investigated in this work, the exchange interaction is taken to be isotropic, which is a common approximations for distances between spins larger than 1 nm [45, 46], and the dipolar interaction employs the point-dipole approximation. The form of the dipolar interaction term also assumes that the g-tensor is isotropic. Thus we have in frequency units:

$$\hat{H} = \frac{\mu_B B_0}{\hbar}\left(g_1\hat{S}_z^1 + g_2\hat{S}_z^2\right) + J\hat{\boldsymbol{S}}^1\cdot\hat{\boldsymbol{S}}^2 + D\left[\hat{\boldsymbol{S}}^1\cdot\hat{\boldsymbol{S}}^2 - 3\frac{1}{r^2}(\hat{\boldsymbol{S}}^1\cdot\boldsymbol{r})(\hat{\boldsymbol{S}}^2\cdot\boldsymbol{r})\right] \quad (5.1)$$

5.1.2 Rotating frames

We saw before in 2.3.4 why ESR experiments are usually considered in an interaction picture. With a two-electron system, there is a choice regarding appropriate interaction frames. When considering an idealized system, where pulses strictly interact

only with one electron each, it is useful to go to a doubly-rotating frame, which is an interaction frame with respect to a Hamiltonian $\hat{H}_0 = \frac{\mu_B B_0}{\hbar}\left(g_1\hat{S}_z^1 + g_2\hat{S}_z^2\right)$. On the other hand, when looking at the ensemble and investigating possible effects of the same pulse affecting both electrons, it is more convenient to use a single rotating frame with respect to a Hamiltonian corresponding to the pulse frequency ω.

Setting $\omega_1 = \frac{\mu_B B_0}{\hbar} g_1 - \omega$ and $\omega_2 = \frac{\mu_B B_0}{\hbar} g_2 - \omega$, an interaction picture transformation is performed with $\hat{H}_0 = \omega\left(\hat{S}_z^1 + \hat{S}_z^2\right)$, resulting in:

$$\hat{H}_1^R = \omega_1\hat{S}_z^1 + \omega_2\hat{S}_z^2 + \hat{H}_{\text{sec}} + \hat{H}_{\text{psec}} + \hat{H}_{\text{rotating}} \tag{5.2}$$

where

$$\hat{H}_{\text{sec}} = \left[J + D(1 - 3\cos^2(\theta))\right]\hat{S}_z^1\hat{S}_z^2 \tag{5.3}$$

$$\hat{H}_{\text{psec}} = \frac{1}{2}\left[J - \frac{1}{2}D(1 - 3\cos^2(\theta))\right]\left(\hat{S}_+^1\hat{S}_-^2 + \hat{S}_-^1\hat{S}_+^2\right) \tag{5.4}$$

and the last term of Eq. 5.2 is a sum of terms coming from the dipolar interaction, which acquire phase factors $e^{im\omega t}$, with $m = -2, -1, 1, 2$, where ω is of order 9 GHz. According to the average Hamiltonian theory [66] the effect of these terms can be ignored, as they average to small phase shift terms on the timescales associated with the evolution with respect to the rest of the Hamiltonian. The $\hat{H}_{\text{sec}}$ and $\hat{H}_{\text{psec}}$ terms are known as secular and pseudo-secular.

Let us now move further to the interaction picture with respect to $\hat{H}_0' = \omega_1\hat{S}_z^1 + \omega_2\hat{S}_z^2$:

$$\begin{aligned}\hat{H}_2^R = &\left[J + D(1 - 3\cos^2(\theta))\right]\hat{S}_z^1\hat{S}_z^2 + \\ &+ \left[\frac{1}{2}J - \frac{1}{4}D(1 - 3\cos^2(\theta))\right]\left(e^{i(\Delta\omega)t}\hat{S}_+^1\hat{S}_-^2 + e^{-i(\Delta\omega)t}\hat{S}_-^1\hat{S}_+^2\right)\end{aligned} \tag{5.5}$$

The pseudo-secular term acquires an explicit time dependence, but it is not clear if it may be dropped. According to the average Hamiltonian theory[1], it is necessary that $|\Delta\omega| = |\omega_1 - \omega_2| \gg \left[J - \frac{1}{2}D(1 - 3\cos^2(\theta))\right]$ to disregard it. For systems investigated in this study, the offset $|\omega_1 - \omega_2|$ used is typically over 65

[1]Employing the average Hamiltonian theory results in leftover (calculated using Eq. 26 from ref. [66] applied to $\hat{H}_2^R$ in Eq. 5.5) terms $\omega_B^2/\Delta\omega\left(\hat{S}_z^1 - \hat{S}_z^2\right)$ and $-2\omega_B^3/\Delta\omega^2\left(\hat{S}_+^1\hat{S}_-^2 + \hat{S}_-^1\hat{S}_+^2\right)$, where $\Delta\omega = \omega_1 - \omega_2$ and $\omega_B = \frac{1}{2}\left[J - \frac{1}{2}D(1 - 3\cos^2(\theta))\right]$. The first term is a Bloch-Siegert phase shift, and the second has the same form as the full pseudo-secular term.

MHz, whereas the dipolar constant D is of order 6 MHz, with J another order of magnitude smaller. The pseudosecular terms can generally be ignored in this case according to the literature [45, 46], but it is advised to confirm this each time while simulating the dynamics of the system.

If investigating the ensemble, we need to include the small frequency offsets due to g-factor anisotropy and inhomogeneous broadening. Here Ω_1 and Ω_2 are the individual Zeeman frequency offsets of the first and the second spin. Introducing $\omega_{ee}(\theta) = J + D(1 - 3\cos^2(\theta))$, the final dimer Hamiltonian becomes:

$$\hat{H}_{ee} = \Omega_1 \hat{S}_z^1 + \Omega_2 \hat{S}_z^2 + \omega_{ee}(\theta) \hat{S}_z^1 \hat{S}_z^2 \tag{5.6}$$

5.2 Fidelity and an amount of entanglement as metrics

Quantum gates are often described as unitary operations acting on a state of relatively small size. Quantum algorithms are then constructed using a quantum circuit model, where these idealized unitaries are applied to qubits in sequence. In practice, the operations implemented can never be perfect, and often are not even exactly unitary, due to interactions with the environment, which enlarges the actual Hilbert space. When implementing quantum gates in any hardware, it is important to have measures that help determine the usefulness of particular quantum operations in the context of a longer quantum algorithm or a process, as any scalable quantum hardware needs to be able to chain a number of gates and not decohere.

The first notion is fidelity, which quantifies how similar are two quantum states, gates or processes. [128, 129]. It can be used to quantify the amount of error in the implementation, both systematic, if the implemented gate or a process differs from the preferred one, and random, where low fidelity is caused by random noise present in the system.

The second notion is entanglement [130]. Two quantum systems are said to be entangled, if their quantum states cannot be described independently from each other. Mixed quantum states are defined to be entangled if their density operators

cannot be expressed as a statistical mixture of pure and separable states [131]. Entanglement is therefore a notion stronger than a classical correlation, and through Bell inequalities, a witness for quantum behaviour. In the context of quantum computation, entanglement is not as important as it is when two quantum systems are spacelike separated, but it is necessary, though not sufficient, for universal quantum computation [27, 28]. Without entanglement, each qubit can be described independently, which would make quantum computing no more powerful than probabilistic classical computing. There however exist specific protocols for efficient classical simulation of certain small subsets of entangled systems [27].

When constructing quantum hardware, one is concerned with a notion of entangling gates [26], which are gates that are able to maximally entangle nonentangled quantum states, thus enabling the access to the full Hilbert space. There exist methods for entanglement distillation [130, 132], which allow construction of a smaller amount of fully entangled states from a larger amount of states entangled to a lesser degree. To quantify the meaning of lesser or more entangled, we need a measure, ideally easy to calculate. Many such measures exist, and most of them behave the best in the context of a two qubit system [130, 133].

This section is not an exhaustive review of fidelity and entanglement measures, but a description of those relevant to work presented in Chapter 7, mostly regarding simulations.

5.2.1 State fidelities

The standard fidelity, applicable if at least one of the states ρ_1, ρ_2 is pure is given by[128]:

$$\mathcal{F}(\rho_1, \rho_2) = \mathrm{tr}(\rho_1 \rho_2) \tag{5.7}$$

The fidelity for two mixed states is more difficult to define [128] and many possible measures exist [134]. These expressions all satisfy the general notion of closeness inside a Hilbert space. That is, a system that is in a nearly maximally mixed state has near 1 fidelity with the maximally mixed state. This makes it

challenging to use these fidelity measures to compare deviation density matrices (2.2), which usually represent highly mixed states.

General desirable properties of mixed state fidelities were formulated by Jozsa [128]:

1. $0 \leq \mathcal{F}(\rho_1, \rho_2) \leq 1$ and $\mathcal{F}(\rho_1, \rho_2) = 1$ iff $\rho_1 = \rho_2$,
2. $\mathcal{F}(\rho_1, \rho_2) = \mathcal{F}(\rho_2, \rho_1)$,
3. $\mathcal{F}(\rho_1, \rho_2)$ equals pure state fidelity (Eq. 5.7) if one of the states is pure,
4. $\mathcal{F}(U\rho_1 U^\dagger, U\rho_2 U^\dagger) = \mathcal{F}(\rho_1, \rho_2)$ for a unitary U.

The formula satisfying all these conditions is:

$$\mathcal{F}(\rho_1, \rho_2) = \left(\mathrm{tr} \left(\sqrt{\sqrt{\rho_1}\rho_2\sqrt{\rho_1}} \right) \right)^2 \tag{5.8}$$

The above fidelity may be used if a full density matrix is found. In the analysis of magnetic resonance ensemble measurements, a measure based on the above conditions, but able to compare deviation density matrices, would be useful[2].

The procedure used to measure a density matrix of a mixed state is known as state tomography [25]. Equipped with a single-shot measurement capability and an ability to prepare multiple copies of an experimental density matrix, it is possible to perform the full tomography by measuring the system in different bases. The sampled results of these measurements are converted into probabilities of measuring the quantum system in specific states and used to reconstruct the density matrix. It has trace 1 by definition, as probabilities of distinct events sum to 1. A detailed description of this procedure is available in Nielsen's and Chuang's textbook, section 8.4.2 [25]. In the context of ensemble magnetic resonance, there is no single-shot readout. The tomography in NMR is described in section 5.3.3 and the tomography in ESR is one of the research topics investigated in this thesis and is discussed in Chapter 7.

[2]The only problematic condition is the third one, because it normalizes the fidelity, comparing it to a measure that explicitly looks at trace, and deviation density matrices are traceless.

5.2.2 Process fidelity

To analyze a trace preserving process $\mathcal{E}$, taking mixed states to mixed states, quantum process tomography may be utilized. The process is first applied to a set of prepared initial quantum states spanning the state space. State tomography is then performed on each of the results to obtain multiple density matrices, which are combined to obtain the general description of the quantum process $\mathcal{E}$ [25]. The process may be compared with a unitary gate U through average gate fidelity or quantum process fidelity, defined as:

$$\mathcal{F}(\mathcal{E}, U) = \int d\psi \, \langle\psi| \, U^\dagger \mathcal{E}(\psi) U \, |\psi\rangle \tag{5.9}$$

over a uniform measure $d\psi$, normalized to $\int d\psi = 1$. It can be shown [129] that if the quantum process $\mathcal{E}$ acts on a quantum system of dimension d, this fidelity can be expressed as

$$\mathcal{F}(\mathcal{E}, U) = \frac{\sum_j \mathrm{tr}\left(U U_j^\dagger U^\dagger \mathcal{E}(U_j)\right) + d^2}{d^2(d+1)} \tag{5.10}$$

where U_j are unitary operators that span the Liouville space (2.3.3) and $\mathrm{tr}\left(U_j^\dagger U_k\right) = \delta_{jk} d$. In case of dimer spin $\frac{1}{2}$ systems, $d = 4$ and the product operators already serve this role, but they need to be normalized properly. If $\hat{A}_j$ are product operators, then $\mathrm{tr}\left(\hat{A}_j \hat{A}_k\right) = \delta_{jk}$, thus:

$$\mathcal{F}(\mathcal{E}, U) = \frac{\sum_j \mathrm{tr}\left(U \hat{A}_j U^\dagger \mathcal{E}(\hat{A}_j)\right) + 4}{20} \tag{5.11}$$

5.2.3 Positive partial transpose and log-negativity

One of the first entanglement witnesses was the positive partial transform [131]. If a density matrix ρ_{AB}, describing two systems A and B, is separable, then a new matrix, ρ_{AB}^Γ, which is transposed in respect to one of the subsystems, that is:

$$\langle m, \mu| \, \rho_{AB}^\Gamma \, |n, \nu\rangle = \langle m, \nu| \, \rho_{AB} \, |n, \mu\rangle \tag{5.12}$$

has all eigenvalues positive. It can be visualized as dividing the large matrix describing both systems into blocks of the size corresponding to system B, and only transposing those, but keeping their position inside the large matrix fixed:

$$\rho_{AB} = \begin{pmatrix} B_{11} & B_{12} & \dots & B_{1k} \\ B_{21} & B_{22} & \dots & B_{2k} \\ \vdots & \vdots & \ddots & \vdots \\ B_{k1} & B_{k2} & \dots & B_{kk} \end{pmatrix} \rightarrow \rho_{AB}^{\Gamma} = \begin{pmatrix} B_{11}^T & B_{12}^T & \dots & B_{1k}^T \\ B_{21}^T & B_{22}^T & \dots & B_{2k}^T \\ \vdots & \vdots & \ddots & \vdots \\ B_{k1}^T & B_{k2}^T & \dots & B_{kk}^T \end{pmatrix} \tag{5.13}$$

where each entry B_{ij} represents a square matrix of a dimension corresponding to the size of system B. This condition is luckily both necessary and sufficient in systems of size 4, describing an entanglement of two qubits or two spin-$\frac{1}{2}$ particles. That is, if ρ_{AB} describes an entangled system, the matrix ρ_{AB}^{Γ} will have exactly one negative eigenvalue. For example, a Bell state $|\Psi^+\rangle = \frac{1}{\sqrt{2}}(|00\rangle + |11\rangle)$ is described by the following matrix:

$$\rho_{\Psi} = \begin{pmatrix} \frac{1}{2} & 0 & 0 & \frac{1}{2} \\ 0 & 0 & 0 & 0 \\ 0 & 0 & 0 & 0 \\ \frac{1}{2} & 0 & 0 & \frac{1}{2} \end{pmatrix} \rightarrow \rho_{\Psi}^{\Gamma} = \begin{pmatrix} \frac{1}{2} & 0 & 0 & 0 \\ 0 & 0 & \frac{1}{2} & 0 \\ 0 & \frac{1}{2} & 0 & 0 \\ 0 & 0 & 0 & \frac{1}{2} \end{pmatrix} \tag{5.14}$$

Each of the four 2×2 blocks of the original matrix has been transposed, and the new matrix has eigenvalues $\frac{1}{2}, \frac{1}{2}, \frac{1}{2}$ and $-\frac{1}{2}$.

Starting from the PPT, there is an easy to calculate entanglement monotone, called logarithmic negativity, which is also an upper limit on the amount of destillable entanglement [135]:

$$LN(\rho) = \log_2 \left(\left\| \rho^{\Gamma} \right\|_1 \right) \tag{5.15}$$

Where $\left\| \rho^{\Gamma} \right\|_1$ is a sum of absolute values of eigenvalues of ρ^{Γ}. The sum of eigenvalues of both the original and the PPT matrix is 1, so $\left\| \rho^{\Gamma} \right\|_1$ is only larger than 1 if some of the eigenvalues are negative. Logarithmic negativity is thus simple to calculate numerically if one has the density matrix.

5.3 NMR quantum computing

Here the techniques and properties of Nuclear Magnetic Resonance Quantum Computing relevant to this work, specifically to Chapter 7, will be reviewed. This

is not meant to be a comprehensive review of NMR QC. An interested reader is directed to reviews by Chuang and Jones [34, 35]. At their core, NMR and ESR are both techniques of spin magnetic resonance, and thus ideas explored in NMR quantum information research may require only slight alterations to be applied to electronic coupled systems.

This section will mostly follow the DiVincenzo's criteria for quantum computing introduced in 3.1; however there is not much to say about single-qubit gates. These were implemented by means of RF pulses of frequencies corresponding to transitions between spin energy levels, in exactly the same way it is done in pulsed ESR, just with a lower frequency.

5.3.1 Pure, pseudo-pure states and entanglement

Quantum information protocols require the state at the beginning to be initialized to a pure $|000\ldots0\rangle$. As explained in 2.2, an initial state of any magnetic resonance ensemble experiment is typically a Boltzmann thermal state. In NMR, the energy differences between the lowest states are too small for the thermal state to achieve any reasonable purity, as the thermal energy k_BT has to be much lower than $h\nu$ for the state to be significantly polarized [35]. There are attempts to circumvent this problem by utilizing parahydrogen [136] or transfering the polarization from the coupled electron spin state onto the nuclear spin, as electron spins are much more polarizable at the same magnetic field [33].

Instead, NMR quantum information protocols mostly used pseudo-pure states [34, 35, 137, 138], defined as:

$$\rho = (1-\epsilon)\frac{\mathbb{1}}{d} + \epsilon\,|\phi\rangle\langle\phi| \tag{5.16}$$

where $|\phi\rangle$ is a pure state, d a dimension of the Hilbert space and ϵ a small number. Because it is only possible to measure the deviation density matrix, the only difference between a pseudo-pure and a pure state in a practical experiment is the signal intensity, which is proportional to ϵ. Even though small polarizations are quite typical for most conventional experiments, a construction of a pseudo-pure

state on n qubits causes the signal to decrease proportionally to $\frac{n}{2^n}$ [35, 139], which limits the scalability of NMR quantum computing based on pseudo-pure states to about 10 qubits. To reliably construct a pseudo-pure state on multiple qubits, one needs to use multi-qubit gates [34].

There are practical limitations to using pseudo-pure states. There is however a more fundamental, philosophical problem. Entanglement is a quantity necessary to call a device truly quantum, as it is what makes the phenomenon not explainable using classical physics [25, 35, 130]. An amount of entanglement in a mixed state, which is what a pseudo-pure state ultimately is, is limited by the purity of that state. Applying the PPT criterion introduced in 5.2.3 it is found that all the states with $\epsilon < \frac{1}{3}$ are separable [131], and the typical values of ϵ are close to 10^{-5} [33].

5.3.2 Entangling gate

A coupled system of two nuclear spin-$\frac{1}{2}$ qubits can be approximated by a Hamiltonian analogous to Eq. 5.6:

$$\hat{H}_{12} = \Omega_1 \hat{I}_z + \Omega_2 \hat{S}_z + \omega_{12} \hat{I}_z \hat{S}_z \tag{5.17}$$

where $\hat{I}$ and $\hat{S}$ refer to nuclear spins now (NMR convention) [34]. The shortest pulse sequence producing entanglement between the two spins is two $\frac{\pi}{2}$ Y-pulses at frequencies corresponding to Ω_1 and Ω_2, followed by a period $t = \frac{\pi}{\omega_{12}}$ of free evolution. In the ideal circumstances of no frequency offset, the first two terms in the Hamiltonian may be ignored. At the temperature of 0K, both spins start aligned with the magnetic field in the $|00\rangle$ state. Here we use the quantum computing convention, according to which $|0\rangle$ and $|1\rangle$ are the eigenstates of the $\hat{S}_z$ ($\hat{I}_z$, or just Z) operator, and $|+\rangle = \frac{1}{\sqrt{2}}(|0\rangle + |1\rangle)$ and $|-\rangle = \frac{1}{\sqrt{2}}(|0\rangle - |1\rangle)$ are the eigenstates of the $\hat{S}_x$ ($\hat{I}_x$, or just X) operator [25].

The first two pulses act as a pseudo-Hadamard gate, and place the system in the state $|{+}{+}\rangle$. Evolution under the last term of the Hamiltonian for some time t can be understood as a rotation generated by the $2\hat{I}_z\hat{S}_z$ operator. Thus, the

state $|{+}{+}\rangle$ will evolve into:

$$\exp\left(-it\omega_{12}\hat{I}_z\hat{S}_z\right)|{+}{+}\rangle = \cos\left(\frac{t\omega_{12}}{4}\right)|{+}{+}\rangle - i\sin\left(\frac{t\omega_{12}}{4}\right)|{-}{-}\rangle \tag{5.18}$$

Setting $\frac{t\omega_{12}}{4} = \frac{\pi}{4}$ leads to:

$$\cos\left(\frac{\pi}{4}\right)|{+}{+}\rangle - i\sin\left(\frac{\pi}{4}\right)|{-}{-}\rangle = \frac{1}{\sqrt{2}}\left(|{+}{+}\rangle - i\,|{-}{-}\rangle\right) \tag{5.19}$$

which is evidently maximally entangled, and was created from a pure separable state, which means the gate is fully entangling [26].

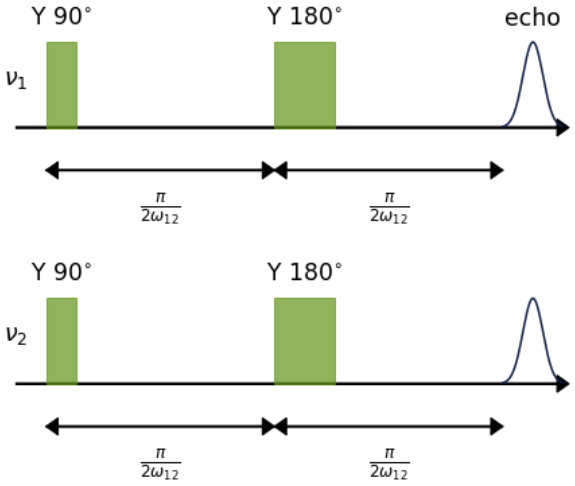


Figure 5.1: Pulse sequence of the entangling gate.

In systems with spectral width much larger than ω_{12}, the observables $\langle I_x\rangle, \langle S_x\rangle$ averaged over the range of resonance frequencies are zero. This makes the state at the end of the sequence to be hardly detectable. It may be prevented by employing a Hahn echo mechanism, introduced in section 2.3.6 [34, 35]. Two π Y-pulses are inserted in the middle of the free evolution period, that is $\frac{\pi}{2\omega_{12}}$ after the beginning of the $\frac{\pi}{2}$ pulse. The $2\hat{I}_y\hat{S}_y$ operator associated with that pulse anticommutes with each of the $\hat{I}_z, \hat{S}_z$ operators in the Hamiltonian, so it commutes with their product. As a result, the double π pulse refocuses the Zeeman terms, but not the interaction term, causing the end result of the gate to be identical up to a minus sign. The pulse sequence is shown in Fig. 5.1.

This is the gate implemented in an experiment with carbon-13 labelled chloroform in 1997 [34]. It is the simplest entangling gate possible in a quantum system based on magnetic resonance in an ensemble of dimers and a good place to start importing NMR quantum computing methods into ESR.

5.3.3 NMR readout and state tomography

A single readout data point in NMR QC experiment is a free induction decay (FID) signal collected by the spectrometer directly after the last pulse, which in a 2-spin system is proportional to [34]:

$$V(t) \propto \mathrm{tr}\left(e^{i\hat{H}t}\hat{\rho}e^{-i\hat{H}t}\left(\hat{I}_x + i\hat{I}_y + \hat{S}_x + i\hat{S}_y\right)\right) \tag{5.20}$$

The Fourier Transform of the above time domain signal exhibits 4 peaks grouped into 2 doublets, at $\Omega_1 \pm \frac{1}{2}\omega_{12}$ and $\Omega_2 \pm \frac{1}{2}\omega_{12}$. The magnitudes of these peaks depend on the density matrix ρ: the inphase coherences $\hat{S}_x, \hat{S}_y, \hat{I}_x, \hat{I}_y$ contribute positively to amplitudes of both peaks in their doublets, while the antiphase coherences $2\hat{I}_z\hat{S}_x, 2\hat{I}_z\hat{S}_y, 2\hat{I}_x\hat{S}_z, 2\hat{I}_y\hat{S}_z$ contribute positively to the first peak and negatively to the second peak in the doublet. The x coherences contribute to signal in the real, and y ones to the imaginary channel. Thus all 8 of these coherences may be estimated from a single measurement.

To measure the full deviation density matrix, the other 7 product operator amplitudes are needed. The state is modified by means of $\frac{\pi}{2}$ pulses before the FID is collected. The pulses each affect both transitions of one spin, thus are not fully selective. Their purpose is to transfer the coherence from the unobservable elements of the density matrix onto the observable ones. For example, a Y pulse at the spin S tranfers the coherence from the $2\hat{I}_x\hat{S}_x$ onto the $2\hat{I}_x\hat{S}_z$ antiphase coherence. By measuring the amplitude of the $2\hat{I}_x\hat{S}_z$ operator, the amplitude of the $2\hat{I}_x\hat{S}_x$ operator as a part of the initial density matrix is estimated.

In the standard protocol, 9 such measurements are performed, labelled after the phases of the pulses. There are three options for each frequency, X, Y, or sending no pulse (I) [30, 31, 34, 35]. For example, an IY measurement uses a single Y

pulse at the spin S, and no pulse at spin I. Each measurement retrieves 8 numbers, corresponding to magnitudes of 8 product operators in the original density matrix. Each product operator appears in multiple measurements, results of which are then combined using least squares fitting to retrieve the full density matrix. It has been employed successfully in NMR experiments [34, 140–142] as well as an ESR experiment with an electron-nuclear hyperfine-coupled system [143].

Note that the single-spin pulses can only transform single spin orders into single spin orders, and 2-spin orders into 2-spin orders, that is, no pulse can turn a 2-spin order like $2\hat{I}_x\hat{S}_y$ into for example $\hat{S}_x$ [26, 144]. The ability to read out the antiphase coherences like $2\hat{I}_z\hat{S}_x$ is crucial for the tomography process to work, as it enables the estimation of all the 2-spin order expectation values.

Additional comments on the tomography procedure as well as several worked through examples are available in Appendix B.1.

5.4 Double Electron-Electron Resonance

Dipolar coupling exhibits an inverse cubic dependence on the distance between two electron spins. This simple observation is a basis of a growing field motivated by understanding protein chemistry. Electron spin labels, typically nitroxide centres, are attached to the protein at certain selected points. An ESR experiment is then conducted, measuring the distribution of strenghts of the dipolar interaction between these electron spin labels, which is then converted to a distance distribution, which helps determine, confirm or reject a proposed protein shape [46, 54, 145]. Several techniques were created within that field to understand, separate and measure the dipolar interaction between two electrons spins. In this part, I will review some of these, which proved useful in this work, specifically in the dimer entanglement project described in Chapter 7.

The most popular approaches to separating dipolar coupling are measuring double quantum coherences through an echo experiment [146], refocusing all the other interactions (SIFTER) [147], and the two-frequency technique known as Double Electron-Electron Resonance (DEER) [46, 54, 145, 148], which I will focus on here.

5.4.1 DEER pulse sequences

The two main DEER pulse sequences are 3-pulse DEER and 4-pulse DEER. The simpler of them consists of two pulses creating a Hahn echo at the frequency resonant with the first spin, known as the detection frequency, and the third pulse between the other two, at the frequency resonant with the second spin, known as the pump pulse. The echo is created and integrated to retrieve the signal. The interval τ between the two detection pulses is constant, and the interval T between the initial $\frac{\pi}{2}$ pulse and the pump pulse is varied [45, 148]. The sequence is shown in Fig. 5.2.

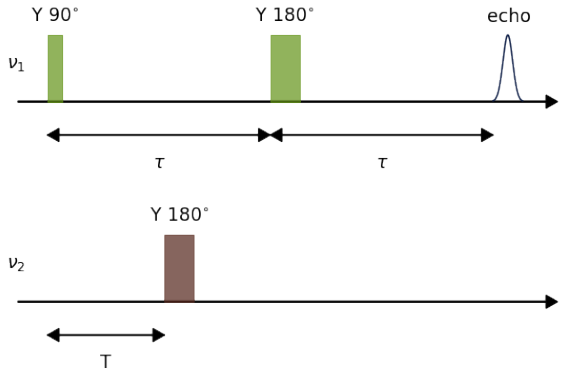


Figure 5.2: 3-pulse DEER pulse sequence. The ν_1 detection pulses create a coherent Hahn echo, the ν_2 pump pulse inverts the other spin in the dimer to modulate the echo. The τ parameter is fixed, the T parameter is varied. The echo is integrated between points corresponding to its full width at half maximum.

The pump pulse can be understood as a flip of the second spin, changing the sign of the magnetic field produced by it at the position of the first, influencing its evolution. Mathematically, the sequence is equivalent to a unitary rotation with respect to the $2\hat{S}_z^1\hat{S}_z^2$ operator, by an angle $\omega_{ee}T$. Only the first spin is refocused and generates the echo. Any coherence in the second spin is defocused[3].

Starting from the thermal $\hat{S}_z^1$ state, the density matrix at the echo position is $-\cos(\omega_{ee}T)\,\hat{S}_x^1 - 2\sin(\omega_{ee}T)\,2\hat{S}_y^1\hat{S}_z^2$. As T is varied, the echo amplitude, generated

[3]The sequence generates a $\Omega_B(2T-2\tau)$ rotation through the $\hat{S}_z^2$ operator, which should average to 0 in the ensemble.

by the observable $\hat{S}_x^1$ term, is modulated by $\cos(\omega_{ee}T)$. The frequency $\omega_{ee}(\theta)$ depends both on the distance between the spins and the orientation of the dimer, so the observed trace is is a sum of multiple oscillatory contributions, and becomes less resolved as T increases. Fixing the parameter τ allows to disregard the effect of relaxation on the shape of the data, as the total duration of the experiment is constant. Choosing the value of τ is a trade-off between signal sensitivity and resolution of the dipolar coupling [45]. Essentially, the longer the τ, the more periods of oscillation will be visible in the data, but increased duration of the experiment results in a lower signal to noise ratio.

Due to the averaging of the frequency contributions, the most interesting and useful part of the data typically corresponds to small values of T. However, experimentally it is problematic to send pulses of two frequencies too close to one another. If the pulse bandwidths overlap, the associated Bloch-Siegert phase shift will be opposite for sequences where the pump pulse is sent before the first $\frac{\pi}{2}$ pulse [54]. Also, if an amplifier, such as TWT, briefly described in section 2.3.1, is nonlinear, care must be taken when crossing the pulses of different frequencies. It is possible to move the pump pulse through the first $\frac{\pi}{2}$ and even through the π pulse, towards the end of the sequence, but it requires additional calibration [54].

A more popular way to counteract this problem is a 4-pulse DEER experiment, where another detection π pulse is inserted into the sequence to refocus the initial $\frac{\pi}{2}$ and enable the pump pulse be positioned around the $T = 0$ point [45, 46]. The sequence is shown in Fig. 5.3.

The additional refocusing lengthens the entire experiment, increasing the effects of relaxation, but it allows for a better resolution at those most crucial parts of the trace.

5.4.2 DEER background

The experimental trace is a combination of a form factor and a background factor. It can be shown [149], that the background seen in the DEER data originates from the interactions between different dimers in the solution, which also interact dipolarly.

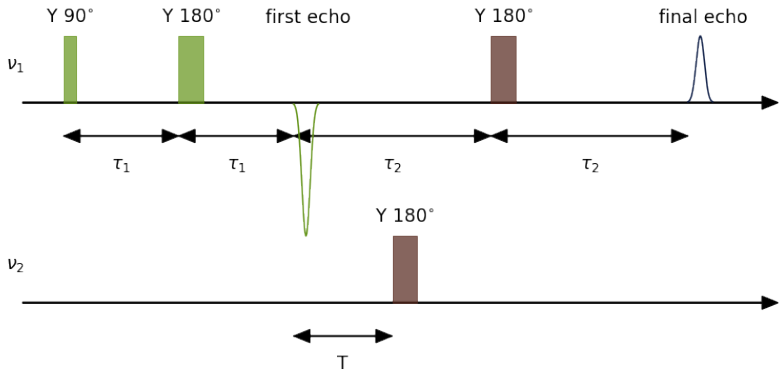


Figure 5.3: 4-pulse DEER pulse sequence. The echo created by the first two detection ν_1 pulses is refocused again after additional duration τ_2. The parameters τ_1 and τ_2 are fixed, the parameter T takes positive and negative values as the pump ν_2 pulse moves between the two $\nu_1\pi$ pulses.

For the uniform D-dimensional distribution of these dimers, the background function is proportional to $\exp\left(-kT^{\frac{D}{3}}\right)$, where k is a constant. For most experiments $D = 3$, resulting in simple exponentially decaying background. The form factor itself does not decay to 0, but to a positive value $(1 - \Delta)$, which is a consequence of the insufficient modulation by the pump pulse [46]. In other words, the pump frequency does not excite all the spins paired up with the spins affected by the detection frequency. The ensemble includes dimers, whose one spin is resonant with the detection frequency, but the other spin is not resonant with the pump frequency. The signal coming from them is a basic Hahn echo. There are ways to increase the modulation depth, for example through chirp pump pulses [150], where frequency is varied during the pulse. All these factors contribute to a typical shape of DEER data looking like a small, rapidly decaying oscillation of top of large background. Example data are shown in Fig. 5.4.

5.4.3 Orientational averaging of the dipolar interaction

The distance distribution of the dipolarly coupled dimers is one factor that contributes to the averaging of the DEER oscillatory signal, but it is not the only one.

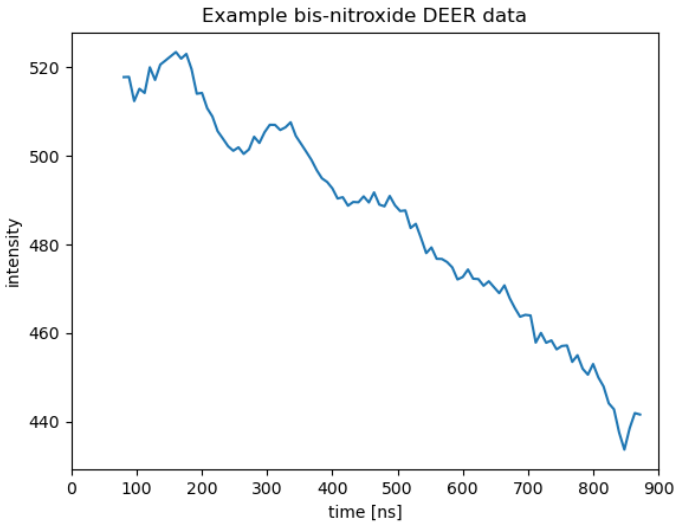


Figure 5.4: Example 3-pulse DEER data, collected from a DEER standard bis-nitroxide molecule, as a part of experiment discussed in 7.6.2. Typical DEER trace is a decaying oscillation on top of large background due to inter-dimer interactions.

The dipolar interaction has an explicit dependence on the angle θ between the z direction and the axis connecting the two spins. In a disordered solution, many orientations contribute to the DEER signal. Assumming a fixed D, so no distance distribution, and that all the molecules oriented between some two colatitudes θ_1 and θ_2 are included in the signal, the $\cos(\omega_{ee}T)$ becomes:

$$\int_{\theta_1}^{\theta_2} \cos\left[\left(D(1-3\cos^2\theta)+J\right)T\right]d\theta = \\ = \sqrt{\frac{\pi}{6DT}}\left[\cos((D+J)T)\mathrm{FrC}\left(\sqrt{\frac{6DT}{\pi}}\cos\theta\right)+\sin((D+J)T)\mathrm{FrS}\left(\sqrt{\frac{6DT}{\pi}}\cos\theta\right)\right]_{\theta_1}^{\theta_2} \tag{5.21}$$

where FrC and FrS are Fresnel special cosine and sine integrals, respectively [151]. If signal proportional to $\sin(\omega_{ee}T)$ for an individual molecule is measured, its orientational average will become:

$$\int_{\theta_1}^{\theta_2} \sin\left[\left(D(1-3\cos^2\theta)+J\right)T\right]d\theta = \\ = \sqrt{\frac{\pi}{6DT}}\left[\sin((D+J)T)\mathrm{FrC}\left(\sqrt{\frac{6DT}{\pi}}\cos\theta\right)-\cos((D+J)T)\mathrm{FrS}\left(\sqrt{\frac{6DT}{\pi}}\cos\theta\right)\right]_{\theta_1}^{\theta_2} \tag{5.22}$$

The typical DEER data, especially from a rigid molecule with narrow distance distribution, would follow this pattern. In highly orientationally averaged data, these analytic expressions help distinguish between contributions from the dipolar and exchange coupling, however they are the easiest to use when one manages to excite all the orientations equally, since then the bounds become just 0 and $\frac{\pi}{2}$.

5.4.4 Low temperature DEER

The above description of a typical DEER experiment assumes the initial state to be a thermal $\hat{S}_z^1$ state. However, ESR experiments are able to reach higher purity initial states, especially if higher magnetic fields and lower temperatures are employed. In the laboratory frame, the Hamiltonian can be approximated with $\hat{H} = \omega\hat{S}_z^1 + \omega\hat{S}_z^2$, because for the purposes of the calculation of the thermal state the spin-spin interaction is much weaker than the Zeeman interaction and $|\omega_1 - \omega_2| \ll \omega_1, \omega_2$. The thermal state is calculated as described in section 2.2:

$$\rho_{thermal} = \exp\left(-\frac{\hat{H}\hbar}{k_B T}\right) \tag{5.23}$$

and then normalized to unit trace:

$$\rho_{\text{thermal}} = \frac{1}{4}\mathbb{1} + \frac{1}{2}\frac{\sinh\gamma}{\cosh\gamma+1}\hat{S}_z^1 + \frac{1}{2}\frac{\sinh\gamma}{\cosh\gamma+1}\hat{S}_z^2 + \frac{\cosh\gamma-1}{\cosh\gamma+1}\hat{S}_z^1\hat{S}_z^2 \tag{5.24}$$

where $\gamma = \frac{\hbar\omega}{k_B T}$. Applying the 3-pulse DEER sequence to this initial state yields the two focused observable operators:

$$\cos(\omega_{ee}T)\,\frac{\sinh\gamma}{\cosh\gamma+1}\hat{S}_x^1 + \sin(\omega_{ee}T)\,\frac{\cosh\gamma-1}{\cosh\gamma+1}\hat{S}_y^1 \tag{5.25}$$

Thus we expect an additional oscillation, behaving like the Fresnel sine integral (Eq. 5.22) to appear 90° out of phase in respect to the usual DEER oscillation. This experiment was performed with biradical samples at magnetic fields exceeding 6 T and temperatures below 5 K by Marko et al [152], confirming this general behaviour. The behaviour of the real signal does not depend on temperature, but a signal in the imaginary channel, translated about a quarter of a period, appears and grows relatively to the real channel, as the temperature is lowered. The authors

suggest such an experiment might be used to achieve better modulation depths and understand the structures of biomolecules better, but it is also a piece of evidence that the DEER sequence can help probe the purity of the initial state by comparing the magnitudes of the two oscillatory signals.

6

Investigation of the Spin Electric Coupling in molecular magnets

Contents

6.1 Spin Electric Coupling in exchange coupled systems . 82
6.1.1 Spin Electric Coupling in Cu_3 complexes 82
6.1.2 Spin Electric Couplings in Cr_7Ni and Cr_7Mn rings . . . 86
6.2 Spin Electric Coupling in the HoW_{10} complex 88
6.2.1 Experimental setup 89
6.2.2 Origins of Spin Electric Coupling 91
6.2.3 Orientational dependence of Spin Electric Coupling . . . 93
6.2.4 Implementing an A-gate using the SEC in the HoW_{10} complex 96
6.3 Future directions 98

In this chapter, original research into the SEC of several molecular magnets and its origins is presented. This project was conducted in collaboration with Dr Junjie Liu, with molecules supplied by Dr Grigore Timco, (Dr) Benjamin Kintzel, Prof. Winfried Plass, Yan Duan, Dr José Baldoví, Prof. Eugenio Coronado, and with theoretical assistance of Dr Alejandro Gaita Ariño and Aman Ullah. Research described here was published [36, 37, 118] and this chapter is largely a reproduction of these publications with some new data and insights.

6.1 Spin Electric Coupling in exchange coupled systems

In 4.2.2, a mechanism proposed by Trif et al [107, 121] for the emergence of SEC in antiferromagnetic exchange coupled systems was discussed. Such complexes, additionally lacking inversion symmetry, are good candidates for experimental investigation of E-field sensitivities in spin Hamiltonians. E-field modifying the molecular structure would affect exchange couplings and may lead to significant shifts in ESR transition frequencies, enabling nonresonant manipulation of their spin states.

The two kinds of antiferromagnetically coupled molecules reported here were triangle Cu systems directly equivalent to the geometry discussed in the aforementioned proposal, and rotaxane Cr_7Ni and Cr_7Mn, discussed in 3.2.

All measurements were performed in the Centre for Advanced Electron Spin Resonance (CÆSR) on Bruker Elexsys 580 and 680 X-band pulsed ESR spectrometers with ^{4}He flow cryostats. The dissolved samples were contained in a standard 3mm probe equipped with two parallel wires, at a distance of 1.8mm held together by a piece of tape, see Fig. 6.1. An external generator Avtech AVR-4-B created voltage up to 180 V between the wires, which acted as a capacitor, giving rise to a nonuniform electric field. The probe was oriented for the E-field to be perpendicular to the microwave magnetic field $\boldsymbol{B}_1$. The wires were shorted above by a 50Ω resistor for a purpose of impedance matching. All measurements, unless stated otherwise, were performed using frozen, diluted ensembles of investigated molecules at the temperature of 3 K and used the pulse sequence introduced in Fig. 4.1, comprising a Hahn echo experiment with fixed pulse separation τ and pulses of d.c. voltage of variable duration t_E, starting just after the $\frac{\pi}{2}$ microwave pulse and eventually covering the whole sequence until the Hahn echo.

6.1.1 Spin Electric Coupling in Cu_3 complexes

The first investigated species were chosen because of their similarity to the molecules discussed in the earlier theoretical proposal, described in 4.2.2. The Cu_3 triangles

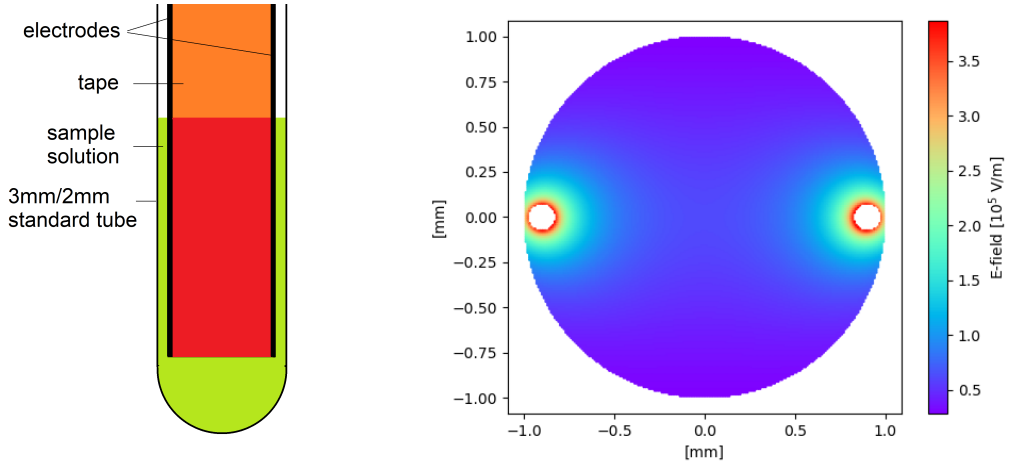


Figure 6.1: Probe geometry for E-field measurements with solution samples. Left: A diagram of the probe contained within a standard ESR glass tube with an internal diameter of 2mm. Right: Top view of the distribution of E-field magnitudes in the probe for 180V voltage applied between the wires. This distribution arises from assuming that the electrodes are uniformly charged, infinitely long cylinders. In reality, the wires were not perfectly straight. The inhomogeneity of the E-field was taken into account in the process to retrieve the magnitude of SEC in investigated samples, by assuming the sample is uniformly distributed in the tube and the measured Hahn echo is a sum of contributions of all the molecules in the solution experiencing inhomogeneous E-fields shown here.

($[Cu_3(saltag)(py)_6]ClO_4$) [36] behave like a spin $\frac{1}{2}$ below 50 K due to their strong antiferromagnetic interactions. The molecular structure is shown in Fig. 6.2.

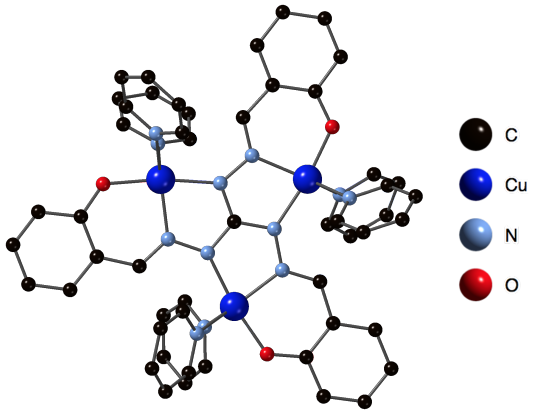


Figure 6.2: Molecular structure of $Cu_3(saltag)(py)_6$. The pyridine groups dynamically exchange with the solvent pyridine molecules. The triangular geometry of this antiferromagnetically coupled complex helps investigate the ideas described in 4.2.2.

The pulse sequence described and shown in Fig. 4.1 is used to investigate the

SEC in a disordered ensemble of these molecules. They were dissolved in pyridine, which exchanges with the ligands of the molecules rapidly in the solution. Later, deuterated pyridine was used instead to increase coherence times by removing the interactions with proton spins. We find the evidence of coherent, linear SEC through an observation of echo decay and recovery, when the duration of the E-field pulse t_E is increased, as detailed in 4.3.2. There is no overall phase shift between the in-phase and out-of-phase spectrometer channels, indicating no quadratic SEC. With an applied voltage of 150 V between the two cable electrodes, we find the echo amplitude decrease to 0.85 ± 0.03 of its value in the absence of E-field, when $t_E = 5$ μs $= \tau$, the delay between the pulses used in the experiment. The data were fit taking into account the inhomogeneity of E-field shown in Fig. 6.1. If $E(x, y)$ is the E-field magnitude at position (x, y) inside the tube, and S is the cross section of the sample tube, as shown on the right of Fig. 6.1, the magnitude of the echo should follow:

$$Y(t_E) = \iint_S \cos\left[E(x,y)a\left(\tau + |t_E - \tau|\right)\right] dxdy \tag{6.1}$$

where $Y(t_E)$ is a unnormalized echo amplitude where the duration of the E-field pulse is t_E and a is the average SEC magnitude. The argument of the cosine takes into account the reversion of the phase accumulation when $t_E = \tau$. The best fit for the orientationally averaged SEC factor yields $a = 1.8 \pm 0.2$ Hz m V^{-1}. The typical data are shown in Fig. 6.3, all data collected at the temperature 3 K.

One possible interpretation of these results is to assume the SEC arises through the mechanism proposed by Trif et al [107, 121], discussed in 4.2.2. However, the observed effect is quite small, on a similar order as the Stark effect observed in phosphorus donors in silicon [117], where the coupling modifies the hyperfine interaction, even though it is observed to be quadratic. It is therefore a sensible hypothesis that we observed a Stark effect [153] in Cu atoms, and it had little to do with the triagonal geometry [37].

To provide additional evidence about the most likely origin of the coupling in these complexes, additional experiments were conducted on another molecule, differing from the Cu_3 triangle only by substitution of the two out of three copper

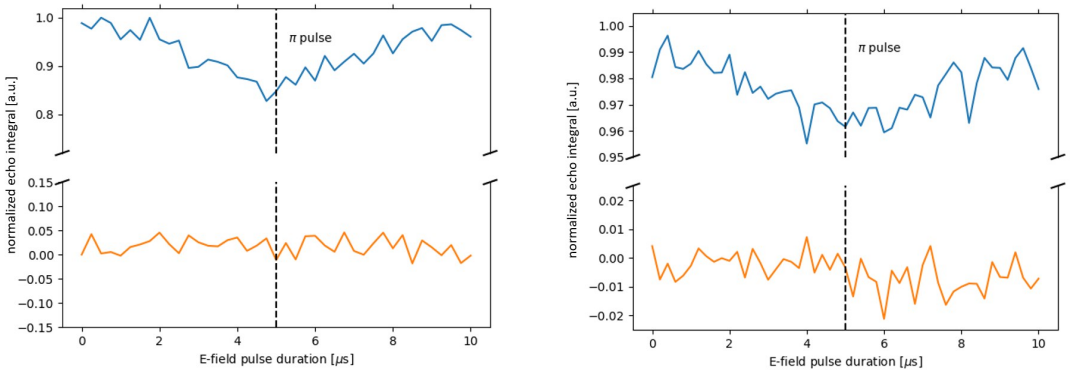


Figure 6.3: Data from the SEC detection measurements on Cu triangles. Integrated echo amplitude as a function of the duration of the E-field pulse. The temperature is 3 K. Left: Cu_3 triangles, 150 V, right: $CuZn_2$ triangles, 200 V. The top panels show the in phase, and the bottom panel the out of phase components of the integrated echos. Both components behave in the way indicative of a linear SEC in a disordered ensemble. There is no overall phase shift, but instead the magnitude of the echo decays until the duration of the E-field pulse t_E reaches $\tau = 5$ μs and then recovers. The reduction in the magnitude of the echo is $8 - 10$ times smaller in the $CuZn_2$ species, indicative of the 3 times smaller SEC, compared to Cu_3 triangles.

ions with zinc ions. This $CuZn_2$ triangle has a ground spin $\frac{1}{2}$, this time resulting from the single unpaired Cu electron. There is no triangular exchange geometry in this complex, so any effect observed there could not be attributed to the proposed mechanism.

The measurement of the $CuZn_2$ centres reveals a small SEC, with average magnitude 0.6 ± 0.2 Hz m V^{-1}. With an applied voltage of 200 V and an equivalent experimental setup, the magnitude of the echo achieves a minimum of 0.97 ± 0.01 of its maximum value when $t_E = \tau$. The measurement has all the previously discussed qualities indicating the linearity and coherence of the E-field effect. Such a small SEC is difficult to measure accurately, and it is smaller than in the case of the Cu_3 triangle. However, it would be enough evidence to claim that the mechanism based on geometry is at least not the only source of SEC. Most likely, due to interactions with the molecular environment, the investigated triangles are not sufficiently equilateral, and the E-field does not break the symmetry. It has to be noted, though, that a possibility of the sample contamination with the Cu_3 species cannot be confidently rejected due to methods used in synthesis. In such

a case, $CuZn_2$ triangles might not exhibit any SEC.

6.1.2 Spin Electric Couplings in Cr_7Ni and Cr_7Mn rings

The other investigated exchange coupled species, where broken inversion symmetry (4.2.1) allows linear SEC, are the rotaxane molecules introduced in 3.2. These complexes, due to antiferromagnetic interactions between metal ions, behave like spin $\frac{1}{2}$ (Cr_7Ni) and spin 1 (Cr_7Mn) particles respectively below 10 K [89]. They were dissolved in deuterated toluene, to increase coherence times. The same experimental procedure was used as in the case of the triangle molecules to investigate the SEC in disoriented ensembles of these complexes. The typical data are shown in Fig. 6.4.

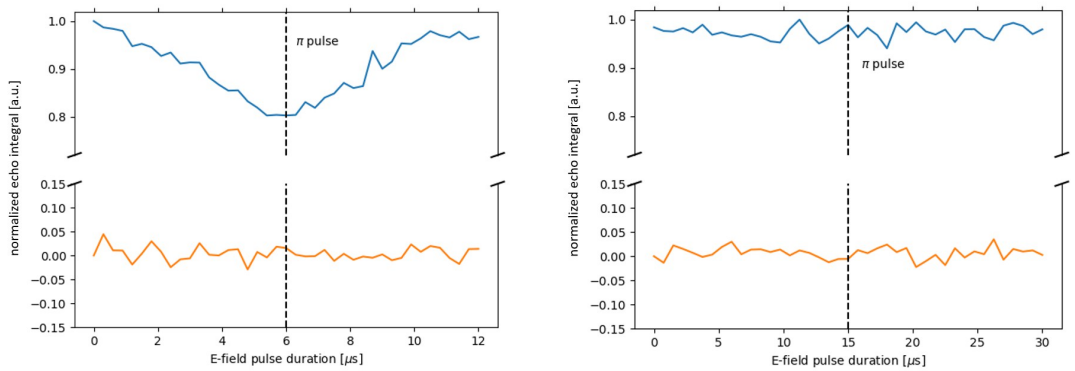


Figure 6.4: Typical data from the SEC detection experiment in Cr_7Ni/Mn rings, conducted using the pulse sequence shown in Fig. 4.1. Integrated echo amplitude as a function of the duration of the E-field pulse. The temperature is 3 K. Right: Cr_7Mn, $\tau = 6$ μs, V = 180 V, data showing significant decrease and recovery of the Hahn echo due to the applied E-field pulse. Left: Cr_7Ni, $\tau = 15$ μs, V = 150 V, data showing no significant effect on the echo, despite a much longer duration of the experiment.

We find that with a voltage of 180 V applied between the electrodes, and the duration of the E-field pulse $t_E = 6$ μs, the echo amplitude in Cr_7Mn decreases to 0.79 ± 0.02 of its original value. Following the same fitting process as in the case of Cu_3, the best fit for the SEC is 1.9 ± 0.2 Hz m V^{-1}. Cr_7Ni molecules exhibit no significant effect, despite longer E-field pulse durations, up to 30 μs, enabled by the longer T_2 coherence time. The two molecules are exactly identical, the only difference between them is the different atom substituted for one of the chromiums in the ring, which breaks the inversion symmetry. The $S = 1$ Cr_7Mn rotaxanes do

exhibit an axial and rhombic anisotropy, or zero-field splitting, lacked by the Cr_7Ni complexes. The data are indicative that it is this interaction that might be a source of SEC in these molecules, as discussed in 4.2 and found in Mn defects in ZnO [116].

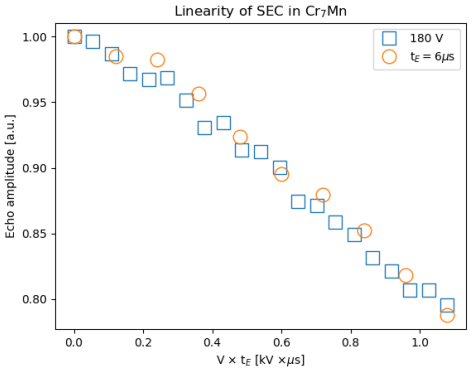


Figure 6.5: Voltage and time dependence of the echo magnitude in Cr_7Mn rings. In both measurements, the $\tau = 6\mu$s. The squares denote the reduction in echo amplitude as a result of increasing the duration of the E-field pulse, but keeping the applied voltage constant and equal to 180 V. The circles denote such a reduction resulting from keeping the duration of the E-field pulse at a fixed value $t_E = 6$ μs, but varying the voltage.

The SEC in Cr_7Mn molecules was investigated further. The pulse sequence introduced in Fig. 4.2 was used to confirm that its leading contribution is first order in E-field magnitude. The voltage was varied, while the duration of the E-field pulse was fixed at $t_E = \tau = 6$ μs. The data reveal the echo reduction was proportional to the applied voltage and only depends on the product $t_E \times V$, as shown in Fig. 6.5. The absorption spectrum of the ring, collected at 9.5 GHz, extends significantly, from 0.35 T up to 1 T, as a result of the anisotropy terms needed to describe its ground $S = 1$ state, Eq. 3.1 [89].

To gain insight into the origins of SEC in this molecule, we perform the experiment at several B_0 values. As discussed in 3.2, the Hamiltonian of Cr_7Mn is characterized by large anisotropies D and E (Eq. 3.1. This enables the B_0 values to select different orientations of the molecule and through that, different m_S subpopulations of states, that could couple to E-field to different degrees. However, the data (shown in Fig. 6.6) suggest no to low dependence between the SEC and the field values, indicating that the SEC most likely does arise from a modification to the g-factor or the hyperfine interaction. Due to the small size of the induced

phase shift, and limited sensibility in the experiment, the precise form of coupling in this molecule, and whether or not it affects these terms, cannot be determined.

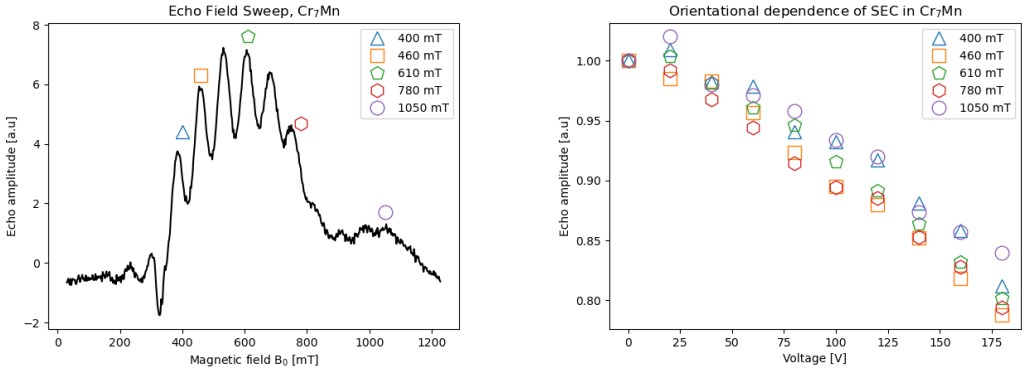


Figure 6.6: Magnetic field and voltage dependence of SEC in Cr_7Mn complexes. Left: Cr_7Mn absorption spectrum collected through an Echo Field Sweep experiment with $\tau = 2$ μs. The SEC measurements were conducted at 5 distinct field values. Right: Echo magnitude under an E-Field pulse covering half the echo sequence, $t_E = \tau = 6$ μs, dependent on the static magnetic field and applied voltage.

Regardless of the origin of the SEC in the above exchange-coupled cluster molecules, the magnitude of the effect observed is not sufficient for any form of resonant manipulation of the spin state using oscillating E-fields. However, in a single molecule device, it would be possible to apply an E-field of the magnitude of the order 10^8 Vm^{-1}, as already done in several architectures of this kind [24, 154], shifting the transition frequency of the Cr_7Mn molecule by about 30 MHz. Such a shift would enable selective excitation of neighbouring molecules, and effectively realize an A-gate, as postulated by Kane [22, 106], and it would only require a microwave pulse as long as 30 ns, which is of order typically used in ESR experiments. The microwaves would no longer need to be spatially localized on a specific molecule, because its neighbours would be forced out of resonance through the application of the E-field.

6.2 Spin Electric Coupling in the HoW_{10} complex

The largest linear Spin Electric Couplings were observed in the HoW_{10} crystal, whose physics was discussed in 3.3. The initial decision to investigate this complex

was motivated by the origins of the clock transitions it exhibited [90]. It was hypothesised that the $B_4^4\hat{O}_4^4$ giant spin approximation term (discussed in 2.1.5), responsible for the emergence of the anti-crossing in the spin spectrum, enters the spin Hamiltonian as a result of the structural distortion, which also causes breaking of inversion symmetry of the molecule. It was hoped that the magnitude of this term is connected to internal electric fields present in the molecule and thus it is possible to modify it together with the structural distortion, with an external electric field. Operating the HoW_{10} molecule at the clock transition (3.3.1) also increases the decoherence times because it lowers the sensitivity to magnetic noise. This makes it a good candidate for this experiment, requiring long evolution times, as well as for quantum information processing applications in general.

6.2.1 Experimental setup

The HoW_{10} crystal samples were placed inside a standard quartz ESR tube of 1.6 mm outer diameter, which was mounted inside a capacitor consisting of two metallic plates separated by 2 mm and connected to the AVTECH pulse generator. The entire sample setup was mounted in a Bruker MD5 resonator. This design allowed for independent rotation of the sample and the electrodes. Bruker ELEXSYS 580 and 680 spectrometers were used to conduct the measurements. The macro crystal sample faces or edges do not correspond to any crystallographic direction, so it was challenging to determine the molecular orientation.

In practice, the angle between the main molecular axis and the static magnetic field B_0 was found by rotating the sample around the vertical axis and conducting Echo Field Sweep measurements. Because the positions of the clock transitions depend only on the static magnetic field along the magnetic easy axis [90, 105], as discussed in 3.3, it was possible to determine the orientation with good precision by locating the maximum of this projection. Because the targeted transition involving the $m_J = 4$ and $m_J = -4$ quantum levels can only be excited with microwave fields which are also parallel to the magnetic easy axis, the orientation of the crystal directly corresponds to the achievable signal to noise ratio, and needed to be optimized.

In all the measurements here, the magnetic easy axis was oriented as close as possible to the direction of B_0. This is the main source of variation between collected data sets, as the crystals obtained from separate batches could not be mounted in the identical way. After the initial determination of the optimal crystal orientation, the electrodes could be rotated independently, so that the electric field could be applied at a variable angle ϕ to B_0.

The pulse sequence discussed in 4.3.2 with 32 ns long $\frac{\pi}{2}$ pulse and 64 ns long π pulse was used for most of the measurements described here, with the exception of the experiment described later in 6.2.4. The crystal contains two copies of the HoW_{10} molecule per unit cell, related by inversion symmetry. Their magnetic properties are identical, but their electric field sensitivities are opposite, thus the quadrature signals originating from either copy are expected to cancel. Therefore, even though the sample is a crystal, the linear SEC would still cause the quadrature channel signal to be zero.

Typical data are shown in Fig. 6.7. There universally is a prominent, decaying oscillation in the echo integrated signal, fully recovering for durations of the E-field pulse longer than τ. The decay is caused by the E-field inhomogeneity, and its recovery confirms this effect is coherent. As expected, there is no oscillation in the out of phase channel, suggesting the linearity of the effect and lack of parasitic magnetic fields. The magnitude of the E-field effect itself is calculated from the peak FT frequency, and the associated full width at half maximum gives the uncertainty. This allows partial mapping of the SEC and serves as a lower bound on its maximum value, as not all orientations are accesible in a single experiment.

A separate experiment, with the duration of the E-field pulse fixed at exactly τ and its voltage varied, is then conducted at the ϕ corresponding to the maximum frequency shift to confirm the linearity of the SEC, exactly as in Cr_7Mn. The value recovered from the fit is 11.4 ± 0.3 Hz m V^{-1}.

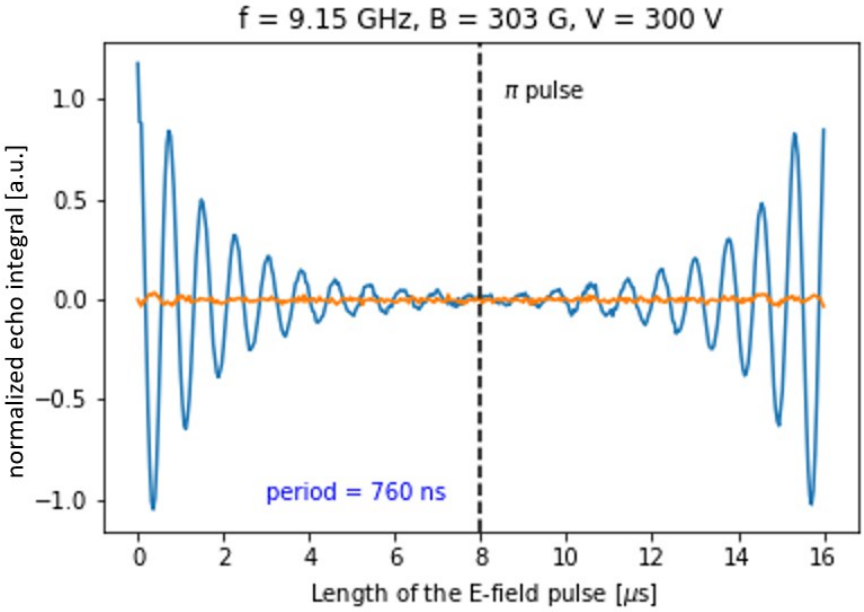


Figure 6.7: Data from the SEC detection measurements in HoW_{10} complex, in-phase and quadrature channels. Again, integrated echo amplitude is plotted against the duration of the voltage pulse. The pulse durations are 32 ns and 64 ns, the delay between them is $\tau = 8\mu$s. The oscillation in the in-phase channel is caused by the Spin Electric Coupling, no oscillation in the out-of-phase channel is indicative of the linearity of the coupling.

6.2.2 Origins of Spin Electric Coupling

The clock transition frequency in this complex is fixed at 9.15 GHz and defined by the departure from the tetragonal symmetry, manifesting through the B_4^4 term in the Hamiltonian. In particular, the frequency does not depend on the g-factor or the hyperfine tensor A in first order, thus any modulation of these parameters by the external E-field may not affect the data collected exactly at the clock transition frequency. To explore the possibility of SEC through these other parameters, the experiments were performed using two additional frequencies; other than the clock transition frequency 9.15 GHz, 9.45 GHz and 9.88 GHz were also investigated. At these frequencies, we expect the effect due to the modification in the B_4^4 parameter to be smaller, because it affects the transition frequency the most at the exact point of the anti-crossing.

Reference to the energy level diagram of this complex (Fig. 3.3) shows that the magnetic field values at which these needed to be conducted also need to

change, so Echo-Detected Field Sweep measurements were conducted to find the field values of these transitions. The frequency shift induced by the E-field pulse is the same within uncertainty for all the peaks at the clock transition, as expected. At the higher frequencies, the shifts start to differ, indicating that a portion of the coupling affects the g-factor or the hyperfine tensor. The data collected from two crystals are summarized in Fig. 6.8.

Through simple diagonalization of Hamiltonians the best fit for the value of the shift in the B_4^4 parameter, δB_4^4, due to the external electric field, can be determined. The frequency shifts corresponding to four clock transition peaks recovered from the simulation are almost identical, assuming that the B_4^4 is the only affected parameter. At this frequency, the shifts due to changes in g or A are approximately three orders of magnitude smaller than those due to the changes in B_4^4. The direct diagonalization also confirms that the clock transition frequency is not affected by fluctuations in the static magnetic field B_0, which was previously quoted as the origin of long coherence times in this molecule [90]. At the elevated frequencies, the contributions from other parameters of the Hamiltonian become more significant, as expected, and it is possible to fit specific values explaining the experimental results in both crystals. However, due to a small number of remaining degrees of freedom, these values should not be overinterpreted.

Of course, the parameters only tell a part of the story. The actual origin of the Spin Electric Coupling is most likely due to a structural distortion associated with the application of the external E-field. Density Functional Theory calculations may be performed to aid in understanding the exact way the E-field distorts the molecular structure and thus modifies the spin Hamiltonian. To support our publication about this complex [118], such calculations were performed by collaborators at the University of Valencia using a normal vibrational modes expansion of the structural displacements. Each normal mode has a force constant κ_i, a reduced mass μ_i and an associated frequency $\omega_i = \sqrt{\kappa_i/\mu_i}$. An applied E-field causes a displacement Δx_i in this mode, which in turn modifies the electric dipole moment $\mathbf{p}$ by $\Delta\mathbf{p}$. The dipole moment may thus be calculated depending on the applied

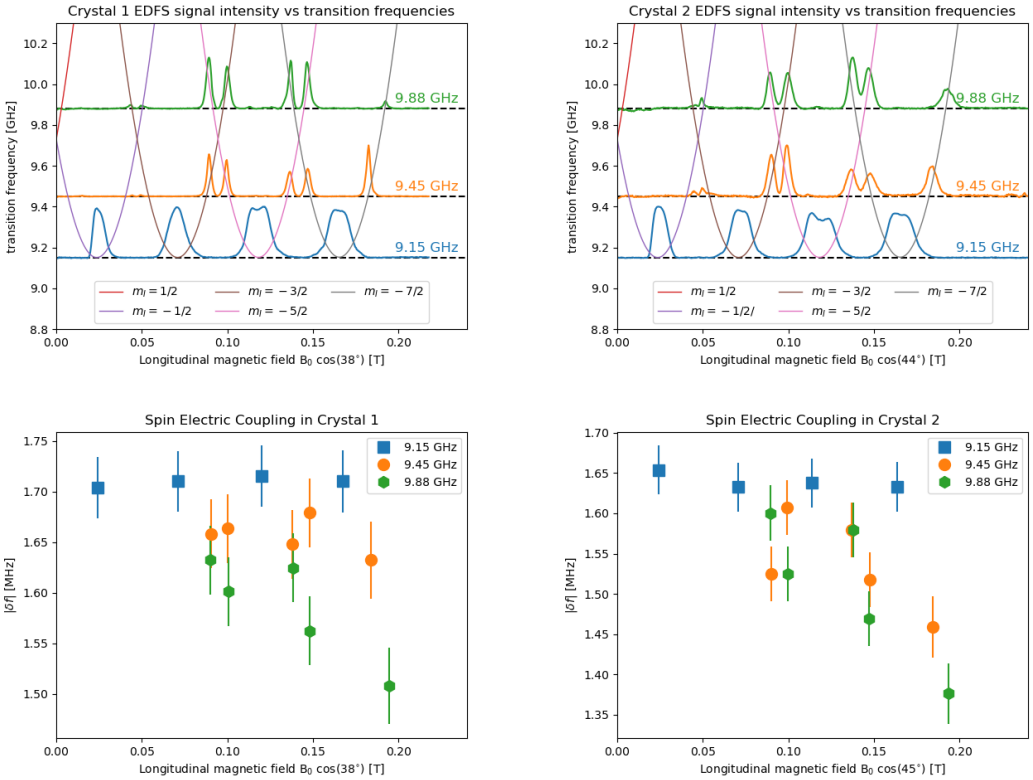


Figure 6.8: Field and frequency dependence of the Spin Electric Coupling in the HoW_{10} complex. Left: crystal 1. Right: crystal 2. For consistency, the x-axes are rescaled to correspond to the longitudinal static magnetic field, by a factor cos(38°) and cos(44°) respectively. Top: Echo Field Sweep spectra with overlayed calculated transition frequencies corresponding to several nuclear spin projections m_I. Bottom: frequency shift due to the Spin Electric Coupling corresponding to different field values and frequencies with applied voltage of 300 V. In both crystals, the shift δf at the clock transition is the highest and the most consistent, as modifications in the g-factor and hyperfine tensor due to E-field does not impact the transition frequency there. We observe higher variance between the peaks at the elevated frequencies, suggesting that while the modification to the tetragonal anisotropy terms is the highest, the overall effect of the E-field is more complex.

E-field. Then, the modes responsible for causing the kinds of distortions that could lead to significant modifications of tetragonal asymmetry nearby the Ho atom may be identified and their effect investigated.

6.2.3 Orientational dependence of Spin Electric Coupling

Working with the crystal allows for the opportunity to investigate the dependence of the Spin Electric Field on the relative orientations of the molecule, E-field

and the B_0-field. This study is still restricted by the inability to rotate the crystal in all the directions once it is mounted. However it reveals interesting properties of the molecule.

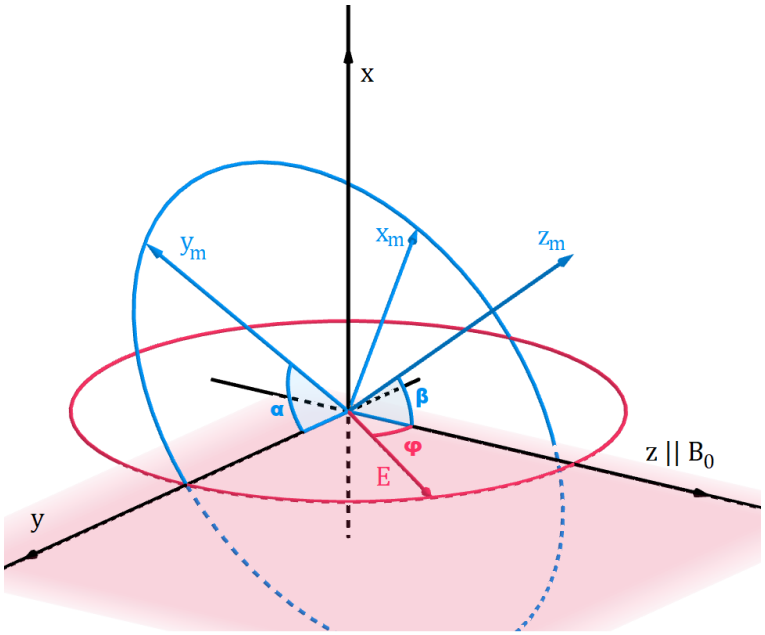


Figure 6.9: A summary of the angles used to describe the relationship between the molecular frame and the laboratory frame in the measurement of SEC in HoW_{10} crystal. The axes x_m, y_m, z_m describe the internal molecular frame, the angles α, β transform this to the laboratory frame. The crystal is rotated around the laboratory x axis so that the angle β between z and z_m is minimal, which eliminates one Euler angle.

The direction of the B_0 field is traditionally chosen to be the z-axis of the laboratory frame. The direction of the microwave B_1 field, vertical in the same frame, represents the x-axis (Fig 6.9). In the experiment, we are able to rotate the mounted sample around the x-axis, or in the $y-z$ plane. The E-field direction can be rotated independently around the same axis, and it stays perpendicular to the x-axis[1]. In the experiment, the molecular axis of the molecule is first rotated so that the angle β it forms with the z-direction is minimized. This occurs when it is contained within the vertical $x-z$ plane. This may be achieved through repeated Echo Field Sweep experiments, as described in 6.2.1. For the orientational

[1]The alternative strategy is to attach the the electrodes to the sample holder, and rotate them together, against the direction of the B_0 field. In this configuration, the field position of the first clock transition peak changed, but the magnitude of the Spin Electric Coupling observed was extremely consistent, independent of the angle of rotation.

dependence investigation, we restricted ourselves to the lowest field clock transition only for simplicity. At this field position, the frequency shift caused by the external E-field is only due to the changes in the B_4^4 parameter, simplifying the analysis.

The direction of the E-field is parametrized by the angle ϕ between the E-field vector and the B_0. At each position, the magnitude of the Spin Electic Coupling is calculated by Fourier transforming the data from the measurement described in 4.3.2.

In general, the orientational dependence of the Spin Electric Coupling could be described by a rank 2 tensor coupling between the E-field vector and whichever term in the Hamiltonian is affected by it. In this sample, however, we find that a simple model explains the data from multiple experimental runs particularly well.

The frequency shift due to applied E-field is equal to:

$$\delta f = \mathbf{A}_m \cdot \mathbf{E} \tag{6.2}$$

Where $\mathbf{A}_m$ is a coupling vector in the molecular frame, whose direction and magnitude may depend on the ESR frequency. However, since we are performing the measurements at the clock transition, the transition frequency is not affected by B_0 misalignment, so it will not depend on the laboratory frame orientation of the crystal. In other words, we find that there is a direction in the crystal, such that only the electric field component along this direction contributes to the magnitude of the coupling. To turn this model into a measurable hypothesis, an angle α is introduced. This is the angle the molecule would need to be rotated by around its easy axis so the vector $\mathbf{A}_m$ is in the $x-z$ plane in the laboratory frame. This vector defines the molecular $x-z$ plane and the angles α and β are used to parametrize the transformation to the laboratory frame by the rotation matrix:

$$R_m = \begin{pmatrix} \cos\alpha\cos\beta & -\sin\alpha & -\cos\alpha\sin\beta \\ \sin\alpha\cos\beta & \cos\alpha & -\sin\alpha\sin\beta \\ \sin\beta & 0 & \cos\beta \end{pmatrix} \tag{6.3}$$

The parametrization of frames and vectors is summarized in Fig. 6.9.

Because $\mathbf{A}_m = [A_{m,x}, 0, A_{m,z}]$ in the molecular frame, and $\mathbf{E} = [0, E\sin\phi, E\cos\phi]$ in the laboratory frame, we obtain:

$$\begin{aligned} \delta f = \mathbf{A}_m \cdot \mathbf{E} = [A_{m,x}, 0, A_{m,z}] R_m \mathbf{E} = \\ = -E A_{m,x} \sin\alpha \sin\phi + E\left(A_{m,z}\cos\beta - A_{m,x}\cos\alpha\sin\beta\right)\cos\phi \end{aligned} \tag{6.4}$$

This parametrization is chosen, because the angle β is directly measurable from the EFS spectrum, however the angle α needs to be fitted to the experimental data. The data collected from two crystals, with the Eq. 6.4 best fit, is shown in Fig 6.10. The best fit parameters are $A_{m,x} = 9.8$ Hz V^{-1} m, $A_{m,z} = 6.1$ Hz V^{-1} m, $\alpha_1 = -45°$, $\alpha_1 = 88°$. For these crystals $\beta_1 = 38°$ and $\beta_2 = 45°$ were found using the EFS measurement. We recover the angle $\tan^{-1}\left(\frac{A_{m,x}}{A_{m,z}}\right) \approx 58°$ between the vector $\mathbf{A}_m$ and the molecular easy axis.

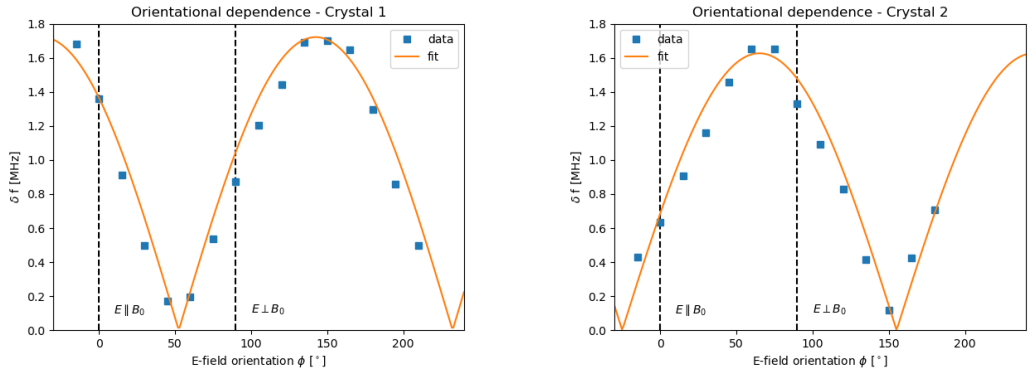


Figure 6.10: Orientational dependence of the Spin Electric Coupling in the HoW_{10} complex. Data collected from two crystals. The coupling is proportional to $|\cos(\phi - \phi_0)|$ in both crystals. It is not possible to determine the true sign of the coupling, because there are two inversion symmetry related molecules per unit cell of the crystal. The offsets are dependent on the crystal orientation. The fit follows Eq. 6.4. The Spin Electric Coupling vector parameters are fitted to be the same for both crystals.

6.2.4 Implementing an A-gate using the SEC in the HoW_{10} complex

In this complex, the Spin Electric Coupling is strong enough to be used to address different molecular subpopulations. More precisely, we are able to distinguish molecular partners related by inversion symmetry, which is not possible with magnetic fields alone. As discussed above, the E-field has an exact opposite effect on the Hamiltonians, and consequently, frequencies of allowed transitions in these two copies of the molecule. Magnetic fields, on the other hand, have exactly the same effect. In principle, localizable electric fields may be used to shift the frequencies of the transitions in the two copies of the molecule away from each other, so that

an oscillating magnetic field may be used to drive the transition in one molecule independently of the other one, which behaves like an A-gate discussed in 4.3.3.

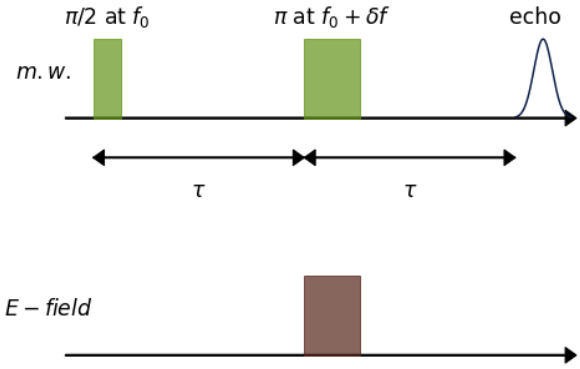


Figure 6.11: Pulse sequence used for the E-field addressability experiment. A 400 ns long $\frac{\pi}{2}$ pulse at the frequency f_0 selectively excites two narrow subpopulations of spins. An E-field pulse applied during a 800 ns long π pulse modifies the underlying static Hamiltonian, thanks to which, a coherence in either subpopulation is only refocused if the shifted $f_0 + \delta f$ ESR frequency corresponds to the modified transition frequency.

This possibility is investigated in the HoW_{10} crystal using a modified pulse sequence shown in Fig. 6.11. The $\frac{\pi}{2}$ pulse at the clock transition frequency $f_0 = 9.15$ GHz creates coherence in both subpopulations. The E-field pulse applied only during the inversion pulse shifts the clock transition frequency by δf, so an inversion pulse at either $f_0 - \delta f$ or $f_0 + \delta f$ only inverts one of the subpopulations, resulting in an echo of halved intensity. To achieve this effect, however, the microwave pulses need to be more frequency selective, which is achieved by significantly increasing their duration in respect to preceding experiments, to 400 ns $\left(\frac{\pi}{2}\right)$ and 800 ns (π), so that their bandwidth is reduced. Specifically, it is necessary that the pulse duration $d > \frac{1}{|2\delta f|}$ to achieve the required resolution.

The frequency of the inversion pulse is swept through f_0 for each value of the applied voltage, which is varied from 0 V to 400 V. The results are shown in Fig. 6.12. The offsets evolve linearly with the voltage and are in agreement with the Spin Electric Coupling present in this system found in the previous experiments. They are placed symmetrically in respect to f_0, and are clearly distinct for voltages higher than 150 V. The amplitudes of the collected echos are identical on both sides at each step of the experiment, confirming that we managed to access the targeted molecules.

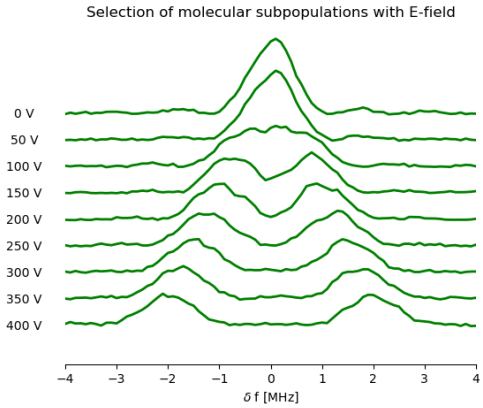


Figure 6.12: Selecting a molecular subpopulation using the E-field. The electric field is applied during the π pulse of the standard Hahn echo sequence. The π pulse itself has a frequency modified by δf. As the voltage of the E-field pulse increases, we observe separation of the two echo components corresponding to the two inversion symmetry related copies of the molecule. The intensities of each component are identical, their position is symmetric around the $\delta f = 0$ point, and changes linearly as higher voltages are used.

6.3 Future directions

The research into SEC in molecular magnets continues. The potential high-SEC molecules need to have broken inversion symmetry, they should exhibit high electrical polarizability and be mechanically soft. The electronic properties should be sensitive to changes in the molecular structure, which provides a pathway for the E-field to couple to spin. This is the case in the HoW_{10} molecule described above, and was the main point of the theoretical argument predicting the SEC in copper triangles [107, 121], see 4.2.2. Usually, the successful candidates should also have long decoherence times, allowing for the effect to be measured, and later utilized in a quantum device.

Following these criteria, we have began investigating the SEC in VO molecular magnets [91], which lack inversion symmetry and exhibit unusually long phase memory times of order 100 μs. We have found a small effect, but the research in its origins is ongoing.

Another possible direction of this project is to further explore the properties of the HoW_{10} nanomagnet, by driving its transitions coherently with E-field. Assuming the E-field only modifies the B_4^4 coefficient and does so linearly, causes the relevant matrix

element (Eq. 4.5) at the clock transition to be 0, disallowing the resonant driving with electric field. The transition fortunately becomes allowed at higher frequencies.

The design of a standard ESR resonator places the sample at the antinode of the magnetic field of the relevant resonant mode, and attempts to make the $\boldsymbol{B}_1$ field there homogeneous. To drive the transition resonantly with E-field, the opposite design strategy is needed, and thus a completely new resonator will need to be constructed. A resonator, based on a rhumbatron double-klystron resonator [155] geometry would be suitable for modelling using finite element analysis [156], providing an E-field antinode at the sample position.

7

Two-qubit entangling gate in a molecular dimer system using ESR

Contents

7.1 Definition of the problem 102
7.2 Building blocks of the entangling gate 103
7.2.1 Initial state 104
7.3 Tomography 105
7.3.1 DEER-assisted tomography 106
7.3.2 Tomography of the thermal state 112
7.3.3 Fidelity in the high-temperature regime 112
7.4 Simulations of the physical gate fidelity 114
7.4.1 Methodology 114
7.4.2 Effects of the physical interaction 115
7.4.3 Effects of the imperfect gate phases and amplitudes . . 119
7.4.4 Effects of finite pulse durations 123
7.4.5 Effects of decoherence 129
7.5 Full Spinach simulations of the experiment 130
7.5.1 Methodology 130
7.5.2 Simulation structure 132
7.5.3 Recovering the density matrix from the simulated and experimental time traces 133
7.5.4 Simulation parameters and results 136
7.6 Entanglement experiments 142
7.6.1 Calibration procedures 143
7.6.2 DEER standard measurements 143
7.6.3 Cr_7Ni ring dimer crystals measurements 149
7.7 Future directions 155

In this chapter we will move from the most abstract mathematical definition of the system in consideration, the gate and its tomography, through simulation steps including various complications, towards the experimental realization of the procedure.

This project was possible thanks to insight provided by Dr Alice Bowen and Edmund Little, samples prepared by Dr Grigore Timco, and support of Prof Eric McInnes and Prof Richard Winpenny. The Cr_7Ni rings experiments were performed in collaboration with Edmund Little.

7.1 Definition of the problem

The system in consideration is a thermal ensemble of dimer paramagnetic molecules, as described in section 5.1. Each end of the molecule is a spin $\frac{1}{2}$ particle, and there is a weak interaction between the two ends. The physical nature of this interaction and the double rotating frame transformation are described in section 5.1 and result in a simple Ising Hamiltonian, Eq 5.6. Like in 5.4, $\hat{S}^1$ corresponds to one end of the molecule and $\hat{S}^2$ corresponds to another.

$$\hat{H} = \Omega_1 \hat{S}_z^1 + \Omega_2 \hat{S}_z^2 + \omega_{ee} \hat{S}_z^1 \hat{S}_z^2 \tag{7.1}$$

where Ω_1 and Ω_2 are resonant frequency offsets from respective frequencies for an individual representant molecule and ω_{ee} is the strength of the interaction. The Hilbert space for this system is a four-dimensional complex vector space with usual vector inner product.

The main goal is to establish universal experimental control over such a molecular system in ESR, that is, enable ourselves to use multi-frequency ESR to apply any unitary transformation to this system, or to get as close as possible to being able to do that. Only once this is achieved, it is possible to build any architecture based on molecular qubits.

A set of all single spin rotation gates with any entangling gate forms a universal set of quantum gates [26]. If the coupling was stronger, and individual transitions targetable with microwave pulses, entangling gates, like CNOT, could be created with pulses alone [32, 33, 102, 103]. As mentioned before in 5.1, here we operate in the limit of weak interaction, which means individual pulses act as single spin operators and thus do not impact the amount of entanglement in the system [144], as described in 5.2. They act as single qubit rotations. Here, the interaction terms in the static Hamiltonian have to be utilized to implement an entangling gate, but the exact type of this entangling gate is less important - any single fully entangling gate can be used to implement any other entangling gate by means of single spin rotations. The choice of a particular gate to implement will be dictated by experimental efficiency, measured in the number and duration of necessary pulses.

7.2 Building blocks of the entangling gate

The entangling gate implemented here is a $\frac{\pi}{2}ZZ$ rotation, identical to the NMR case described in 5.3.2. The echo version needs to be used, with two π pulses in the middle, because the frequency offsets Ω_1 and Ω_2 of the two spins involved in the measurement are much larger than the inverse of the evolution time, which necessitates the use of the echo to detect the state at the end of the sequence. That is, the observables $\langle S_x^1 \rangle$ averaged over the range of frequency offsets, are zero.

The echo version is shown in fig. 7.1 and generates a state $\frac{1}{\sqrt{2}}(|{+}{+}\rangle - i\,|{-}{-}\rangle)$ if starting from $|00\rangle$, where the states $|0\rangle, |1\rangle, |+\rangle$ and $|-\rangle$ are again defined according to quantum computing convention, summarized in 5.3.2. The evolution time can be increased by a factor or $3, 5$ or 7, resulting in a $\frac{3}{2}\pi$, $\frac{5}{3}\pi$ or a $\frac{7}{2}\pi ZZ$ rotation respectively. All these are perfect entanglers in the ideal case, but the $\frac{3}{2}\pi$ and $\frac{7}{2}\pi$ variations result in an orthogonal $\frac{1}{\sqrt{2}}(|{+}{+}\rangle + i\,|{-}{-}\rangle)$ state instead if starting from $|00\rangle$.

In general, any useful gate on the ensemble will need to result in a focused state. A focused state is a state that does not depend on small variations in Ω_1 and Ω_2, and therefore all or the majority of spins affected by the pulses are rotating together and contributing to measurable magnetization. Of course, the spins not

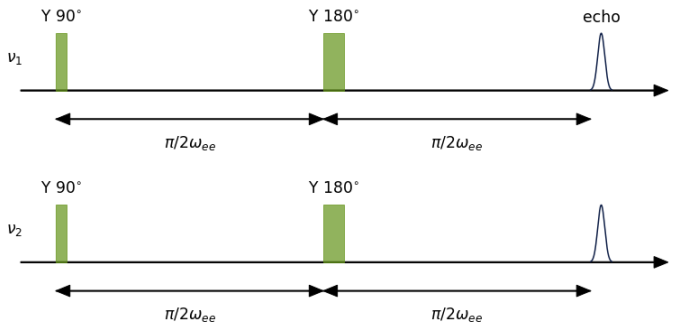


Figure 7.1: Pulse sequence of the entangling gate. The two $\frac{\pi}{2}$ pulses create coherence, and the two π pulses refocus the Zeeman offsets part of the Hamiltonian. Application of both π pulses simultaneously inverts the interaction part of the Hamiltonian twice, so at the end its effect is not reversed. Choosing an appropriate duration τ creates the entanglement at the echo position.

exactly on resonance experience slightly different operators when the pulses are applied and this affects the overall entanglement of the ensemble. This is one of the imperfections further discussed in section 7.5.

This state is fully entangled, according to any entanglement measure such as logarithmic negativity explored in 5.2. Such entanglement can however only be reached at low temperatures, beyond the applicability of the standard ESR approximation, according to which the thermal state can be approximated by the sum of $\hat{S}_z^1 + \hat{S}_z^2$ operators, as discussed in 5.3.1. In ESR, it is within practical capabilities of magnets, spectrometers and cryostats to reach that limit, because the energy gap between the two Zeeman-split energy levels is large enough, unlike in NMR, where the solution required the use of the pseudopure states.

7.2.1 Initial state

The initial state for this exeriment is a low temperature thermal state, described by Eq. 5.24. It is transformed into:

$$\rho_{\text{gate}} = \frac{1}{4}\mathbb{1} + \frac{\sinh\gamma}{\cosh\gamma+1}\hat{S}_y^1\hat{S}_z^2 + \frac{\sinh\gamma}{\cosh\gamma+1}\hat{S}_z^1\hat{S}_y^2 + \frac{\cosh\gamma-1}{\cosh\gamma+1}\hat{S}_x^1\hat{S}_x^2 \tag{7.2}$$

where $\gamma = \frac{\hbar\omega}{k_B T}$. As the temperature increases, the magnitude of the last $\hat{S}_x^1 \hat{S}_x^2$ term decreases in comparison to the other two. The presence of this term is what makes the final state pure and therefore, entangled, so it can be said that for this experiment, the entanglement resides in the $\hat{S}_x^1 \hat{S}_x^2$ double coherence.

In a high temperature approximation, we will be expecting the state at the end of the gate to be $\hat{S}_y^1 \hat{S}_z^2 + \hat{S}_z^1 \hat{S}_y^2$ with some small proportionality factor and nearly maximally mixed.

7.3 Tomography

In the NMR quantum computing quantum state tomography (5.3.3), the expected values corresponding to each of the product operators were measured through a combination of single spin pulses with varied phases, and then used to reconstruct the density matrix. It relies on the ability to measure the antiphase coherence operators, such as $2\hat{S}_x \hat{I}_z$, which contribute positively to one half of the doublet, but negatively to the other one. However, these two peaks are only distinguishable if the coupling strength is larger than the linewidth of the transition. In electronic coupled systems considered here, the linewidth is significantly larger than in most nuclear spin systems because of inhomogeneous broadening, hence the need for an echo. The two peaks merge, thus making the antiphase coherence undetectable directly. If there was another way for these coherences to be measured, the NMR density matrix tomography procedure could be replicated in ESR in a mathematically equivalent way.

The tomography procedure should be applicable in case of a homoelectronic dimer, where both spins have the same orientationally averaged spectrum, because of practical reasons such as limited bandwidth of the resonators and available samples. Even in case of heteroelectronic samples, the orientational distribution of dipolar couplings (2.1.2, later discussed in 7.4.2) forces orientational selection in powder and glass samples. Consequently, the density operator will be defined by the bandwidths of the used pulses - species excited by ν_1 are labelled Spin 1, and species excited by ν_2 are labelled Spin 2. The working ensemble is the collection of

dimers where one end belongs to the Spin 1 category and the other belongs to the Spin 2 category. Unfortunately, if the spectra of both ends of the molecule overlap, the majority of the signal will be generated by the molecules where one, or both electrons fall into the Spin 1 category, and no electrons are in the Spin 2 category. This is an origin of the large background in the DEER experiment, discussed in 5.4.2. A successful tomography scheme needs to effectively remove or disregard that signal, as it does not correspond to our working ensemble.

Of course, the ensemble is not split into the electrons that feel a perfect π pulse and those that are completely unaffected. Instead, an effect of each pulse is different on each electron and ranges continuously, as seen in Eqs. 2.29 and 2.30. That said, it will be shown in the following sections that a density matrix can be reconstructed, and corresponds closely to the theoretical predictions of the idealized case.

7.3.1 DEER-assisted tomography

The following approach to the density operator tomography is based on the DEER experiment, described in 5.4. The inspiration was the low temperature DEER experiment (described in 5.4.4), where the second trace, shifted in phase by 90°, appeared and became more significant at lower temperatures. If it is possible to distinguish it from the regular DEER oscillation and use it to identify the temperature of the state, it may also be possible to use that to identify a more general initial state.

The DEER-assisted tomography manages to solve both problems presented above, it enables the measurement of the expectation values of all the product operators, and select the working ensemble effectively.

Let us first consider what happens if a part of the DEER sequence is attached at the end of another pulse sequence, which ends with an arbitrary focused state. The theoretical result of any pulses and timings applied before does not depend on the frequency offsets Ω_1 and Ω_2 and it may or may not generate an echo. The pulse sequence is shown in Fig. 7.2.

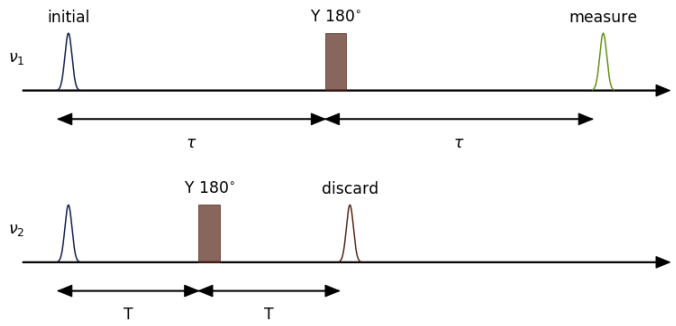


Figure 7.2: DEER-assisted tomography sequence. The initial state may be any focused ensemble state - it can be generated from the thermal equilibrium by a pulse or an echo refocused by preceding pulses. It is followed by two DEER π pulses, transforming the $2\hat{S}_y^1\hat{S}_z^2$ and $2\hat{S}_x^1\hat{S}_z^2$ antiphase coherences, unobservable in the large linewidth and weak coupling limit, into detectable $\hat{S}_x^1$ and $\hat{S}_y^1$ coherences. The τ parameter is fixed, T is varied from 0 to τ, resulting in the oscillating trace proportional to the initial $\langle 2\hat{S}_y^1\hat{S}_z^2\rangle$ and $\langle 2\hat{S}_x^1\hat{S}_z^2\rangle$ in the real and imaginary channels respectively.

At variable time T a π pump Y-pulse at frequency ν_2 is sent. Then, at a fixed time τ a π detection Y-pulse at frequency ν_1 is sent. The echo appears after another time interval τ passes and then is integrated as a function of T, with detection tuned to ν_1. The variable T ranges from 0 to τ. The pump pulse cannot be sent earlier, like in the 4p DEER experiment, because the focused state might be created or modified by a pulse of frequency ν_2. The roles of the two frequencies may be switched, but the fixed duration τ always describes the detection frequency sequence, and the variable duration T - the other one.

This part of the DEER sequence is equivalent to a rotation generated by the $2\hat{S}_z^1\hat{S}_z^2$ operator by the angle $T\omega_{ee}$ and a rotation generated by the $\hat{S}_z^2$ operator by the angle $\Omega_B(2T-2\tau)$, as discussed in 5.4.1. Those two commute with each other, and the only effect of the latter is defocusing of the second spin, which at the end of the sequence averages to 0 over the ensemble. Thus the only measurable observables are $\langle\hat{S}_x^1\rangle$ and $\langle\hat{S}_y^1\rangle$. Because of the construction of product operators (2.3.3), we know that the only observables of the initial focused state contributing to the signal are $\hat{S}_x^1, \hat{S}_y^1$ as well as $[\hat{S}_x^1, 2\hat{S}_z^1\hat{S}_z^2] = -2\hat{S}_y^1\hat{S}_z^2$ and $[\hat{S}_y^1, 2\hat{S}_z^1\hat{S}_z^2] = 2\hat{S}_x^1\hat{S}_z^2$.

The part of the density operator of the initial state associated with those four operators evolves in the following way:

$$\begin{aligned} a\hat{S}_x^1 + b\hat{S}_y^1 + 2c\hat{S}_y^1\hat{S}_z^2 + 2d\hat{S}_x^1\hat{S}_z^2 \rightarrow \\ a\cos(\omega_{ee}T)\hat{S}_x^1 - 2a\sin(\omega_{ee}T)\hat{S}_y^1\hat{S}_z^2 + \\ b\cos(\omega_{ee}T)\hat{S}_y^1 + 2b\sin(\omega_{ee}T)\hat{S}_x^1\hat{S}_z^2 + \\ 2c\cos(\omega_{ee}T)\hat{S}_y^1\hat{S}_z^2 + c\sin(\omega_{ee}T)\hat{S}_x^1 + \\ 2d\cos(\omega_{ee}T)\hat{S}_x^1\hat{S}_z^2 - d\sin(\omega_{ee}T)\hat{S}_y^1 \end{aligned} \tag{7.3}$$

All the other operators present in the initial density operator evolve to unmeasurable observables or do not evolve at all. If the phase of the detection is tuned so that the in-phase (real) channel of the spectrometer corresponds to the $\langle\hat{S}_x^1\rangle$ observable and the quadrature (imaginary) channel of the spectrometer corresponds to the $\langle\hat{S}_y^1\rangle$ observable, the resulting echo at the end of the sequence is going to be proportional to $[a\cos(\omega_{ee}T) + c\sin(\omega_{ee}T)] + i\,[b\cos(\omega_{ee}T) - d\sin(\omega_{ee}T)]$. Therefore, provided that it is possible to distinguish between the cosine and the sine in the collected data, it is also possible to measure the observables associated with the antiphase operators $2\hat{S}_x^1\hat{S}_z^2$ and $2\hat{S}_y^1\hat{S}_z^2$ of the initial state by performing this procedure. These are simply the numbers $-d$ and c. Thus, in theory, it is possible to recreate the NMR state tomography by following exactly the same procedure, but replacing the measurement at the end with the DEER-assisted echo measurement.

To recreate the procedure one more element is necessary, the single spin rotations. At time 0, single spin filter $\frac{\pi}{2}$ pulses may be applied. If the initial state is created by previously applied pulses, the modifying pulses should be aligned with them (the impact of pulse misalignment is investigated later in 7.4). Like in NMR tomography, these pulses are phased to correspond to an X or Y rotation on the spin they affect. There are three options for either frequency: no pulse (I), X pulse or a Y pulse, thus 9 possible measurements. Note that the DEER-based tomography is not symmetric in respect to frequencies ν_1 and ν_2, so switching the roles they play in the experiment generates another 9 measurements. Then, the results of all the 18 measurements are combined, taking phases and errors into account. Like in the

NMR case, this allows the measurement of the full deviation density matrix, as the identity operator is undetectable in ESR for the same reasons.

As demonstrated in Eq. 7.3, the coherences $\hat{S}_x^1, \hat{S}_y^1, 2\hat{S}_x^1\hat{S}_z^2$ and $2\hat{S}_y^1\hat{S}_z^2$ present in the density operator describing the state after the filter $\frac{\pi}{2}$ pulses generate the real cosine, imaginary cosine, imaginary sine and real sine oscillations in the collected trace. The reconstruction of the density matrix requires tracing these coherences back to the corresponding element of the original density operator, depending on the pulse phases and detection frequency. Table 7.1 contains the summary of all the measurements and which product operators may be measured through identification and separation of which components of the signal. Each measurement in the tomography procedure will be referred to by its name, shown in the first column of this table.

name	detection	ν_1 phase	ν_2 phase	real cos	real sin	imag cos	imag sin
1II	ν_1	no pulse	no pulse	$-\langle\hat{S}_x^1\rangle$	$2\langle\hat{S}_y^1\hat{S}_z^2\rangle$	$\langle\hat{S}_y^1\rangle$	$2\langle\hat{S}_x^1\hat{S}_z^2\rangle$
1IX	ν_1	no pulse	X	$-\langle\hat{S}_x^1\rangle$	$2\langle\hat{S}_y^1\hat{S}_y^2\rangle$	$\langle\hat{S}_y^1\rangle$	$2\langle\hat{S}_x^1\hat{S}_y^2\rangle$
1IY	ν_1	no pulse	Y	$-\langle\hat{S}_x^1\rangle$	$-2\langle\hat{S}_y^1\hat{S}_x^2\rangle$	$\langle\hat{S}_y^1\rangle$	$-2\langle\hat{S}_x^1\hat{S}_x^2\rangle$
1XI	ν_1	X	no pulse	$-\langle\hat{S}_x^1\rangle$	$-2\langle\hat{S}_z^1\hat{S}_z^2\rangle$	$-\langle\hat{S}_z^1\rangle$	$2\langle\hat{S}_x^1\hat{S}_z^2\rangle$
1XX	ν_1	X	X	$-\langle\hat{S}_x^1\rangle$	$-2\langle\hat{S}_z^1\hat{S}_y^2\rangle$	$-\langle\hat{S}_z^1\rangle$	$2\langle\hat{S}_x^1\hat{S}_y^2\rangle$
1XY	ν_1	X	Y	$-\langle\hat{S}_x^1\rangle$	$2\langle\hat{S}_z^1\hat{S}_x^2\rangle$	$-\langle\hat{S}_z^1\rangle$	$-2\langle\hat{S}_x^1\hat{S}_x^2\rangle$
1YI	ν_1	Y	no pulse	$-\langle\hat{S}_z^1\rangle$	$2\langle\hat{S}_y^1\hat{S}_z^2\rangle$	$\langle\hat{S}_y^1\rangle$	$2\langle\hat{S}_z^1\hat{S}_z^2\rangle$
1YX	ν_1	Y	X	$-\langle\hat{S}_z^1\rangle$	$2\langle\hat{S}_y^1\hat{S}_y^2\rangle$	$\langle\hat{S}_y^1\rangle$	$2\langle\hat{S}_z^1\hat{S}_y^2\rangle$
1YY	ν_1	Y	Y	$-\langle\hat{S}_z^1\rangle$	$-2\langle\hat{S}_y^1\hat{S}_x^2\rangle$	$\langle\hat{S}_y^1\rangle$	$-2\langle\hat{S}_z^1\hat{S}_x^2\rangle$
2II	ν_2	no pulse	no pulse	$-\langle\hat{S}_x^2\rangle$	$2\langle\hat{S}_z^1\hat{S}_y^2\rangle$	$\langle\hat{S}_y^2\rangle$	$2\langle\hat{S}_z^1\hat{S}_x^2\rangle$
2IX	ν_2	no pulse	X	$-\langle\hat{S}_x^2\rangle$	$-2\langle\hat{S}_z^1\hat{S}_z^2\rangle$	$-\langle\hat{S}_z^2\rangle$	$2\langle\hat{S}_z^1\hat{S}_x^2\rangle$
2IY	ν_2	no pulse	Y	$-\langle\hat{S}_z^2\rangle$	$2\langle\hat{S}_z^1\hat{S}_y^2\rangle$	$\langle\hat{S}_y^2\rangle$	$2\langle\hat{S}_z^1\hat{S}_z^2\rangle$
2XI	ν_2	X	no pulse	$-\langle\hat{S}_x^2\rangle$	$2\langle\hat{S}_y^1\hat{S}_y^2\rangle$	$\langle\hat{S}_y^2\rangle$	$2\langle\hat{S}_y^1\hat{S}_x^2\rangle$
2XX	ν_2	X	X	$-\langle\hat{S}_x^2\rangle$	$-2\langle\hat{S}_y^1\hat{S}_z^2\rangle$	$-\langle\hat{S}_z^2\rangle$	$2\langle\hat{S}_y^1\hat{S}_x^2\rangle$
2XY	ν_2	X	Y	$-\langle\hat{S}_z^2\rangle$	$2\langle\hat{S}_y^1\hat{S}_y^2\rangle$	$\langle\hat{S}_y^2\rangle$	$2\langle\hat{S}_y^1\hat{S}_z^2\rangle$
2YI	ν_2	Y	no pulse	$-\langle\hat{S}_x^2\rangle$	$-2\langle\hat{S}_x^1\hat{S}_y^2\rangle$	$\langle\hat{S}_y^2\rangle$	$-2\langle\hat{S}_x^1\hat{S}_x^2\rangle$
2YX	ν_2	Y	X	$-\langle\hat{S}_x^2\rangle$	$2\langle\hat{S}_x^1\hat{S}_z^2\rangle$	$-\langle\hat{S}_z^2\rangle$	$-2\langle\hat{S}_x^1\hat{S}_x^2\rangle$
2YY	ν_2	Y	Y	$-\langle\hat{S}_z^2\rangle$	$-2\langle\hat{S}_x^1\hat{S}_y^2\rangle$	$\langle\hat{S}_y^2\rangle$	$-2\langle\hat{S}_x^1\hat{S}_z^2\rangle$

Table 7.1: Each experiment produces a trace consisting of a sine and cosine parts in real and imaginary channels. The amplitude of each of the four oscillations corresponds to an expected value of a specific product operator of the state being reconstructed. The name of each measurement consists of the number of the readout frequency, and the choice of the phases of the two operators applied, where I, identity, means no pulse is sent.

An oscillating signal is observed on top of a large, exponentially decaying background. Just like in a conventional DEER experiment, the background will come from the molecules where only one end is excited by one of the frequencies used in the experiment, and the oscillation part will correspond to the molecules for which both ends are excited, as discussed in 5.4.2. Therefore the coefficients recovered from this measurement will correspond to the density operator of the working subensemble defined in section 7.3. Thus, this procedure in principle solves both problems introduced in ESR (compared to NMR) and enables full state tomography, such as the state after the entangling gate. Note that what it effectively does is to disentangle the state and show (through the existence of the out-of-phase traces) that it must have been entangled at the end of the gate sequence. The full pulse sequence used in the experiments is shown in Fig. 7.3. The expected results of the tomography of the entangling gate are summarized in Table 7.2. Worked through examples of this tomography procedure applied to pure $|{+}{+}\rangle$, entangled $\frac{1}{\sqrt{2}}(|00\rangle + |11\rangle)$ states, as well as a low-temperature version of the main experiment are available in Appendix B.1.

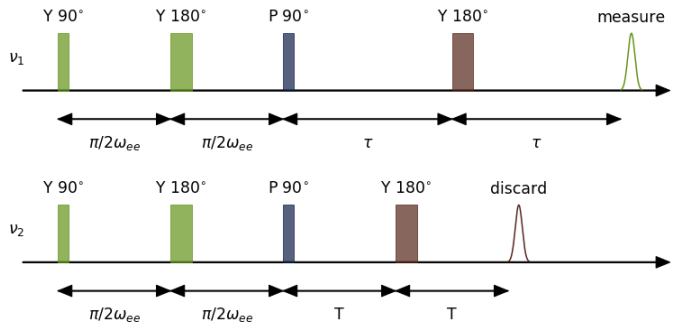


Figure 7.3: The entangling gate sequence followed by full tomography. "P" corresponds to either X, Y, or not sending a pulse.

The sequence as a whole bears similarity to other experments, like SIFTER [147] or Double Quantum [157], but it is philosophically different, as its key feature are variable phases on the central pulses allowing the full tomography of the density

measurement	state after pulses	real channel	imaginary channel
1II	$2\hat{S}_y^1\hat{S}_z^2 + 2\hat{S}_z^1\hat{S}_y^2$	$+\sin(\omega_{ee}T)$	no oscillation
1IX	$2\hat{S}_y^1\hat{S}_y^2 - 2\hat{S}_z^1\hat{S}_z^2$	no oscillation	no oscillation
1IY	$-2\hat{S}_y^1\hat{S}_x^2 + 2\hat{S}_z^1\hat{S}_y^2$	no oscillation	no oscillation
1XI	$-2\hat{S}_z^1\hat{S}_z^2 + 2\hat{S}_y^1\hat{S}_y^2$	no oscillation	no oscillation
1XX	$-2\hat{S}_z^1\hat{S}_y^2 - 2\hat{S}_y^1\hat{S}_z^2$	$-\sin(\omega_{ee}T)$	no oscillation
1XY	$2\hat{S}_z^1\hat{S}_x^2 + 2\hat{S}_y^1\hat{S}_y^2$	no oscillation	no oscillation
1YI	$2\hat{S}_y^1\hat{S}_z^2 - 2\hat{S}_x^1\hat{S}_y^2$	$+\sin(\omega_{ee}T)$	no oscillation
1YX	$2\hat{S}_y^1\hat{S}_y^2 + 2\hat{S}_x^1\hat{S}_z^2$	no oscillation	$+\sin(\omega_{ee}T)$
1YY	$-2\hat{S}_y^1\hat{S}_x^2 - 2\hat{S}_x^1\hat{S}_y^2$	no oscillation	no oscillation
2II	$2\hat{S}_y^1\hat{S}_z^2 + 2\hat{S}_z^1\hat{S}_y^2$	$+\sin(\omega_{ee}T)$	no oscillation
2IX	$2\hat{S}_y^1\hat{S}_y^2 - 2\hat{S}_z^1\hat{S}_z^2$	no oscillation	no oscillation
2IY	$-2\hat{S}_y^1\hat{S}_x^2 + 2\hat{S}_z^1\hat{S}_y^2$	$+\sin(\omega_{ee}T)$	no oscillation
2XI	$-2\hat{S}_z^1\hat{S}_z^2 + 2\hat{S}_y^1\hat{S}_y^2$	no oscillation	no oscillation
2XX	$-2\hat{S}_z^1\hat{S}_y^2 - 2\hat{S}_y^1\hat{S}_z^2$	$-\sin(\omega_{ee}T)$	no oscillation
2XY	$2\hat{S}_z^1\hat{S}_x^2 + 2\hat{S}_y^1\hat{S}_y^2$	no oscillation	$+\sin(\omega_{ee}T)$
2YI	$2\hat{S}_y^1\hat{S}_z^2 - 2\hat{S}_x^1\hat{S}_y^2$	no oscillation	no oscillation
2YX	$2\hat{S}_y^1\hat{S}_y^2 + 2\hat{S}_x^1\hat{S}_z^2$	no oscillation	no oscillation
2YY	$-2\hat{S}_y^1\hat{S}_x^2 - 2\hat{S}_x^1\hat{S}_y^2$	no oscillation	no oscillation

Table 7.2: Expected signal in each measurement of the tomography procedure, if applied to the state after the entangling gate in the high temperature limit. The gate should generate the mixed state $\rho = 2\hat{S}_y^1\hat{S}_z^2 + 2\hat{S}_z^1\hat{S}_y^2$, which leads to above oscillating part of the signal in the tomography procedure measurements. If the global classical electronics phase and the origin position are incorrect or unreliable, we can treat them as free parameters and still retrieve the most important behaviour, based on which measurements exhibit oscillations, and which do not, as well as the relative 0°, 90° and 180° phases of the signal from these measurements. The low temperature version is detailed in Table B.7.

matrix of any preceding state to be performed. Note that the final echo in this sequence comes from both the first pulse, refocused twice, and the third pulse, refocused once. This is a feature of this experiment, and not a problem, because we aim to recover the full density matrix. If it has a $\hat{S}_z^1$ component, it will be recovered.

The above procedure provides enough data points to accurately reconstruct the density matrix, but allows to conduct the experiments in limited time. However, to increase precision of the tomography, one might want to incorporate pulses of variable phases between X and Y. If the phase of the pulses is inaccurate or unreliable, one might want to include a selection of equally spaced phases in the experiment and then fit the results instead of trusting the pulse generation

method to provide the correct phase. The full table of the extended phase-variant tomography is in the Appendix B.2.

7.3.2 Tomography of the thermal state

The tomography procedure inspired by NMR shares one of the flaws of the original, it only recovers the deviation density matrix, because all the observables are measured up to an unknown proportionality factor, which depends on experimental parameters, the classical electronics, number of dimers in the sample and the resonator's bandwidth. In other words, the state exists in a 15-dimensional analogue of the Bloch sphere [61, 62] and the direction of the vector corresponding to the quantum state can be measured, but not its length. If the objective is to demonstrate real entanglement, this can only be done if the full density matrix is measured, because entanglement in a mixed state requires certain purity treshold, as explained in 5.2.

One solution is to apply the tomography procedure directly to the low temperature thermal state (Eq. 5.24), using the same experimental setup and parameters as the entangling gate tomography experiment. The strategy is to find expectation values of $\langle \hat{S}_z^1 \rangle$, $\langle \hat{S}_z^2 \rangle$ and $\langle 2\hat{S}_z^1 \hat{S}_z^2 \rangle$, and then combine them through hyperbolic identities to find the value of γ, to then find the proportionality factor and normalize the state to trace 1. The same proportionality factor can then be used to normalize the state after the entangling gate, as long as all the experimental parameters are kept the same, because it deppends only on those parameters.

Note that the thermal state tomography is essentially the low temperature DEER experiment described in 5.4.4 [152].

7.3.3 Fidelity in the high-temperature regime

Various fidelity measures were introduced in 5.2.1 and 5.2.2. In the high temperature regime, only a deviation density matrix may be measured, and the above thermal state tomography procedure cannot be implemented, due to low sensitivity. Even if retrieving the full density matrix was possible, it represents an almost maximally mixed state both before and after the gate, and most fidelity measures would be

equal to 1 regardless of the quality of the gate. The process fidelity formula 5.11 was proposed [129] as a way to experimentally measure the quality of quantum gates, but to efficiently do that, it requires high purity states as input to the gate and does not solve this problem.

A quantitative measure is still needed, but the important property is the direction in the generalized Bloch sphere to which the state is rotated. Product operators (2.3.3) may be used as a basis for this representation. Each quantum state is thus a vector in the generalized Bloch sphere [61, 62] and we may just calculate the cosine of the angle between the two vectors:

$$\mathcal{F}_{\text{angle}} = \cos\angle(\rho_1, \rho_2) = \frac{\sum \alpha_k \alpha_j}{\sqrt{\left(\sum \alpha_k^2\right)\left(\sum \alpha_j^2\right)}}$$

Where $\alpha_1, \alpha_2, \ldots, \alpha_{15}$ are expected values of the product operators in some order. Note that this is equivalent to:

$$\frac{\text{tr}(\rho_1\rho_2) - \frac{1}{4}}{\sqrt{\left(\text{tr}(\rho_1^2) - \frac{1}{4}\right)\left(\text{tr}(\rho_2^2) - \frac{1}{4}\right)}}$$

making it the most similar to the geometric mean Hilbert-Schmidt fidelity [134], but it explicitly does not satisfy most of the Jozsa's requirements [128], except for $\mathcal{F}_{\text{angle}}(\rho_1, \rho_1) = 1$, $\mathcal{F}_{\text{angle}}(\rho_1, \rho_2) = \mathcal{F}_{\text{angle}}(\rho_2, \rho_1)$ and, importantly:

$$\mathcal{F}_{\text{angle}}\left(U\rho_1 U^\dagger, U\rho_2 U^\dagger\right) = \mathcal{F}_{\text{angle}}(\rho_1, \rho_2) \tag{7.4}$$

where U is a unitary gate of an appropriate dimension. Because the above expression decribes the angle between two vectors in the generalized Bloch sphere, it should at least generalize to the pure state fidelity if both states are pure. For two pure states the fidelity $\mathcal{F} = \text{tr}(\rho_1\rho_2)$, and the purities $\text{tr}(\rho_1^2), \text{tr}(\rho_2^2)$ will both be 1. In this limit, our formula currently gives

$$\mathcal{F}_{\text{angle}} = \cos\angle(\rho_1, \rho_2) = \frac{4}{3}\left(\text{tr}(\rho_1\rho_2) - \frac{1}{4}\right)$$

So we can modify it by setting

$$\mathcal{F}_{\text{ps}} = \frac{3}{4}\cos\angle(\rho_1, \rho_2) + \frac{1}{4} \tag{7.5}$$

where 'ps' refers to 'pseudo'-fidelity. Note that while the maximum value of the above is still 1 and other previously satisfied conditions are still satisfied, the minimum value is $-\frac{1}{2}$. This is because not every state inside the generalized Bloch sphere is physical [61, 62], and so not every state with $\mathrm{tr}(\rho^2) = 1$ is pure. For example, a state $\rho = \frac{1}{4}\mathbb{1} + \varepsilon\hat{S}_z^1 + \varepsilon\hat{S}_z^2$ can never be pure, because for $\mathrm{tr}(\rho^2) = 1$, the $\varepsilon = \sqrt{\frac{3}{8}}$, which would mean the expected value of the spin projection is $\sqrt{\frac{3}{8}} > \frac{1}{2}$.

This formula should not be used in general, but it is useful when comparing deviation density matrices in the high temperature limit. Note that because the condition in Eq. 7.4 is satisfied, this formula may be used to compare the effect of the non-ideal process mimicking a unitary to the effect of that unitary, which is exactly what it is needed for here.

The rest of this chapter is devoted to simulating this experiment with realistic parameters and increasing number of sources of imperfections taken into account, such as the physics of the interaction, imperfections in microwave pulses, temperature, decoherence, and ensemble averaging.

7.4 Simulations of the physical gate fidelity

7.4.1 Methodology

The goal of this project can be interpreted in two ways: one is to create a robust entangling gate that can be used as a part of a longer sequence and applied to any initial state, producing predictable results; the less ambitious subgoal is to create and demonstrate entanglement in the system. Both goals are interesting, but slightly different. When examining the robustness of the gate, we will use the average gate fidelity (Eq. 5.11) with the ideal unitary operation. Whenever a specific initial state is mentioned, we will also examine the amount of entanglement produced by the gate, using logarithmic negativity, introduced in section 5.2.3. Finally, the robustness of the tomography procedure will be examined using the same Eq. 5.11, treating is this time as fidelity of a process, which in the ideal case acts as identity on the state, that is, recovers exactly the state fed into it.

The simulations are divided into multiple parts. First, the coefficient ω_{ee} was broken down into its dipolar and exchange components, and the effect of the angular averaging on the gate efficiency was examined analytically using a Python `sympy` package. Next, the small errors of the phases and rotation angles of the pulses as well as effects of decoherence were simulated using a Python `scipy` and `numpy` packages. In those sections, fidelities are calculated separately for the gate and the reconstruction procedure. They are distinct quantum operations, so it is important to consider them on their own, however experimentally there is no access to the density matrix produced after the gate, only to the reconstructed one.

Finally, a full simulation of the pulsed experiment, including the ensemble effects coming from nonisotropic g-factors, physical gate lenghts comparable with the length of the delay between the gates, different molecular g-tensors in case of the dipolar coupling, was performed using a MATLAB Spinach library [65].

7.4.2 Effects of the physical interaction

The two-spin interaction can be broken down into a dipolar (section 2.1.2), dominating in the ESR systems investigated here, and exchange (section 2.1.3) terms. The duration of the free evolution is directly proportional to ω_{ee}, and $\omega_{ee}(\theta) = D(1 - 3\cos^2\theta) + J$, where D and J are dipolar and exchange interaction constants respectively, and thus depends heavily on the angle between the molecular axis and the B_0 magnetic field θ. Suppose there is no further anisotropy in the Hamiltonian, and the two spins belong to different species with different resonant frequencies and can be affected independently. Then, in a disordered ensemble, all the orientations are affected by pulses in the same way, and the optimal delay becomes difficult to determine, as the amplitude of the anisotropic component changes from D to $-2D$[1]. In most ESR species however orientational selection techniques allow to only excite a fraction of the spin packets involved, as discussed in 2.3.5. The variation in $\omega_{ee}(\theta)$ will be reduced under these circumstances, what will lead to a more robust gate. Here we will explore how this affects the amount of entanglement the gate can

[1] And if $D > \frac{1}{2}J$, the total interaction strength will cross 0 at magic angle, where the delay would need to be infinite

produce, and how that informs the experimental strategy and desired properties of molecular systems. This simple model concentrates just on the interaction, disregarding other physical effects of finite durations and bandwidths of used pulses, and treats the latter as instantaneous.

The overall effect of the gate described above is a ZZ-rotation by an angle $\phi = \omega_{ee}(\theta)t$, where t is the total gate duration. This rotation can be written as a Liouville-space superoperator $\hat{\hat{R}}$ that acts on the density operator $\hat{\rho}$:

$$\hat{\hat{R}}\hat{\rho} = \exp\left(-\frac{\phi}{2}\hat{S}_z^1\hat{S}_z^2\right)\hat{\rho}\exp\left(\frac{\phi}{2}\hat{S}_z^1\hat{S}_z^2\right) \tag{7.6}$$

The superoperator becomes a matrix R in the product operator basis. The only elements of this matrix are 1, 0, $\cos\phi$ and $\pm\sin\phi$:

$$R = \begin{bmatrix}
1 & 0 & 0 & 0 & 0 & 0 & 0 & 0 & 0 & 0 & 0 & 0 & 0 & 0 & 0 & 0 \\
0 & 1 & 0 & 0 & 0 & 0 & 0 & 0 & 0 & 0 & 0 & 0 & 0 & 0 & 0 & 0 \\
0 & 0 & \cos(\phi) & 0 & 0 & 0 & 0 & -\sin(\phi) & 0 & 0 & 0 & 0 & 0 & 0 & 0 & 0 \\
0 & 0 & 0 & \cos(\phi) & 0 & 0 & -\sin(\phi) & 0 & 0 & 0 & 0 & 0 & 0 & 0 & 0 & 0 \\
0 & 0 & 0 & 0 & 1 & 0 & 0 & 0 & 0 & 0 & 0 & 0 & 0 & 0 & 0 & 0 \\
0 & 0 & 0 & 0 & 0 & 1 & 0 & 0 & 0 & 0 & 0 & 0 & 0 & 0 & 0 & 0 \\
0 & 0 & 0 & \sin(\phi) & 0 & 0 & \cos(\phi) & 0 & 0 & 0 & 0 & 0 & 0 & 0 & 0 & 0 \\
0 & 0 & \sin(\phi) & 0 & 0 & 0 & 0 & \cos(\phi) & 0 & 0 & 0 & 0 & 0 & 0 & 0 & 0 \\
0 & 0 & 0 & 0 & 0 & 0 & 0 & 0 & \cos(\phi) & 0 & 0 & 0 & 0 & -\sin(\phi) & 0 & 0 \\
0 & 0 & 0 & 0 & 0 & 0 & 0 & 0 & 0 & \cos(\phi) & 0 & 0 & \sin(\phi) & 0 & 0 & 0 \\
0 & 0 & 0 & 0 & 0 & 0 & 0 & 0 & 0 & 0 & 1 & 0 & 0 & 0 & 0 & 0 \\
0 & 0 & 0 & 0 & 0 & 0 & 0 & 0 & 0 & 0 & 0 & 1 & 0 & 0 & 0 & 0 \\
0 & 0 & 0 & 0 & 0 & 0 & 0 & 0 & 0 & -\sin(\phi) & 0 & 0 & \cos(\phi) & 0 & 0 & 0 \\
0 & 0 & 0 & 0 & 0 & 0 & 0 & 0 & \sin(\phi) & 0 & 0 & 0 & 0 & \cos(\phi) & 0 & 0 \\
0 & 0 & 0 & 0 & 0 & 0 & 0 & 0 & 0 & 0 & 0 & 0 & 0 & 0 & 1 & 0 \\
0 & 0 & 0 & 0 & 0 & 0 & 0 & 0 & 0 & 0 & 0 & 0 & 0 & 0 & 0 & 1
\end{bmatrix} \tag{7.7}$$

In general, the relationship between the angle θ and the orientation of either spin centre of the dimer is complicated, especially if the molecule is soft, that is, has a degree of freedom that lets both spin centres rotate or vibrate individually. To simplify this analysis, let's assume that a fraction $f(\theta)$ of molecules, at angles between θ and $\theta + d\theta$ are perfectly excited by both pulses. The density operator at the end of the gate, averaged over all the included orientations, is simply

$$\hat{\rho} = \frac{\int_{\theta_1}^{\theta_2} f(\theta)\hat{\hat{R}}\sin\theta d\theta}{\int_{\theta_1}^{\theta_2}\sin\theta d\theta}\hat{\rho}_0 \tag{7.8}$$

where θ_1 and θ_2 are colatitudes below and above which no molecules are affected by the pulses. This can be further simplified by removing the $f(\theta)$ factor, and just assuming all the molecules between colatitudes θ_1 and θ_2 are perfectly excited and

participating in the gate. In such a case, the integrals evaluate analytically, as discussed in section 5.4.3, in particular all the $\cos\phi$ terms integrate to

$$\sqrt{\frac{\pi}{6DT}}\left[\cos((D+J)T)\mathrm{FrC}\left(\sqrt{\frac{6DT}{\pi}}\cos\theta\right)+\sin((D+J)T)\mathrm{FrS}\left(\sqrt{\frac{6DT}{\pi}}\cos\theta\right)\right]_{\theta_1}^{\theta_2} \tag{7.9}$$

where FrC is a Fresnel special cosine integral, and FrS - special sine integral, and all the sine terms integrate to similar expressions with special Fresnel integrals switched.

Starting from a pure or thermal initial state, the above superoperator is applied on the density operator, followed by a calculation of log-negativity (discussed in 5.2.3), measuring the amount of entanglement in the system. This is possible to calculate analytically, but is not practical due to methods involved[2]. Instead, several examples are presented below.

These calculations do not include any noise or decoherence, and thus are a good starting point to discuss the importance of the interaction strength distribution on the amount of entanglement produced by the gate. All the other sources of noise can only reduce the amount of entanglement.

The parameters of this model are the two colatitudes θ_1 and θ_2, a $\frac{1}{\gamma}=\frac{k_BT}{\hbar\omega}$ factor, and the ratio between J and D. Any J-dominated system can reach full entanglement at $T=0$ and remains entangled in higher temperatures. The same thing happens with D-dominated systems, if the two colatitudes are close together - there is no averaging. However, in a D-dominated system with full averaging the entanglement is much lower. When the factor $\frac{1}{\gamma}$ reaches around 1.13 in a J-dominated system or around 0.5 in a D-dominated one, all entanglement is lost. These values correspond to about 1.8 K and 0.8 K respectively for a Q-band system, with frequency $f=33$GHz. The maximum, $T=0K$ value of log-negativity in a J-dominated system is 1, in a D dominated one it is about 0.4, and the interaction time at which these maxima occur also changes. Note that these values depend

[2]As logarithmic negativity is calculated from eigenvalues of a 4×4 PPT matrix (5.12), this analytical formula would require solving a general polynomial of degree 4 through Cardano's formulas.

only on fundamental physical constants and the kind of interaction there is in the system. This is shown in Fig 7.4.

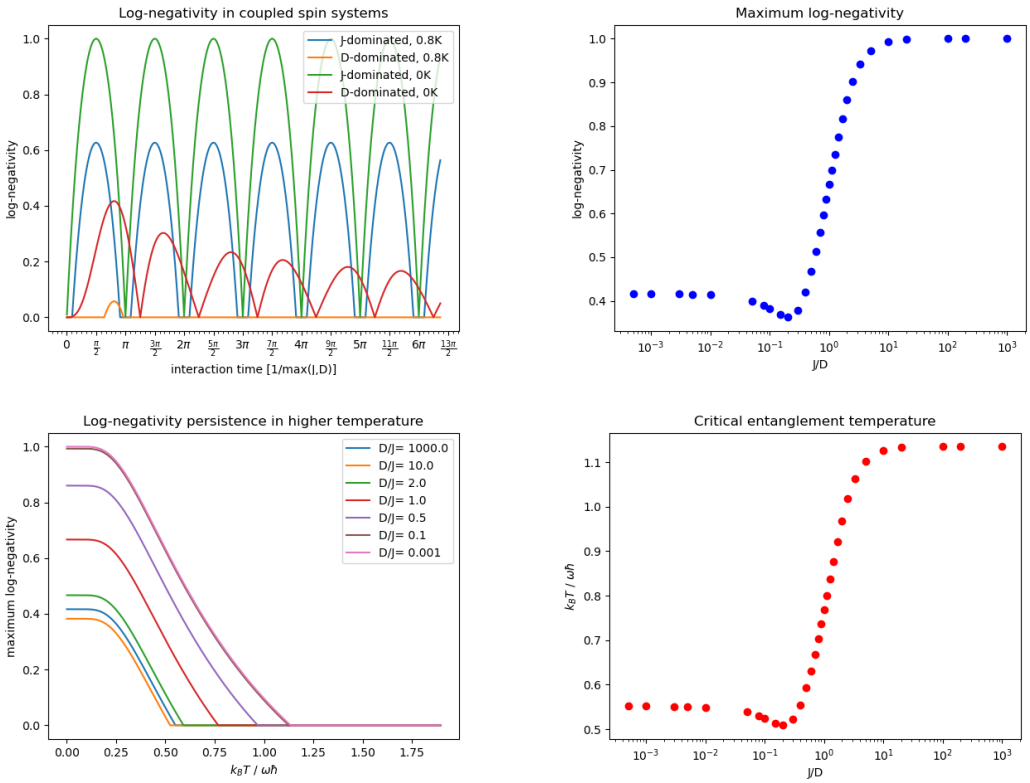


Figure 7.4: Calculations of entanglement properties in dimer spin $\frac{1}{2}$ systems. **Top-left**: Amount of entanglement in the system after the entangling gate depending on the ZZ-interaction time. The time axis scales linearly with overall strength of the interaction. At absolute zero, the log-negativity at subsequent local maxima decreases as a consequence of the broadening in interaction strengths. At higher temperatures, entanglement disappears faster in dipolar-dominated systems compared to exchange-dominated ones. **Bottom-left**: Persistence of the log-negativity measure of entanglement depending on thermal energy in the system. Effectively maxima of functions plotted on the top left. The ratio between J and D is a distinguishing factor. **Top-right**: Maximum attainable entanglement as a function of J/D. Effectively positions where the functions from the bottom left graph cross the y-axis. **Bottom-right**: Critical temperature/thermal energy at which entanglement disappears as a function of J/D. Effectively positions where the functions from the bottom left graph cross the x-axis.

Note that as we move from a D-dominated to a J-dominated system, the log-negativity dips slightly before increasing. The average across all the orientations includes the magic angle, that is the position where $D(1 - 3\cos^2\theta) + J = 0$. As J increases, the magic angle moves towards the equator, and more dimers exhibit

much weaker interaction strengths. As J increases even further and the magic angle is eliminated, the entanglement is almost at maximum.

This problem will reemerge in later sections, regarding full gate simulations and experiments. The conclusion here is, to achieve entanglement, full angular averaging should be avoided in dimers where dipolar interaction dominates.

7.4.3 Effects of the imperfect gate phases and amplitudes

In the previous sections single spin rotations were considered ideal $\frac{\pi}{2}$ or π gates. In practice, these gates are implemented by means of microwave pulses, as discussed in section 2.3.5. In ESR, a common source of error is a systematic error in the rotation angle, resulting from the fact that the sample occupies space inside the resonator and the B_1 field mode is not completely uniform across this space. A number of pulse sequences were devised in NMR to solve this problem [79, 158], they all need to use an increased number of pulses to account for it, which is costly in most ESR systems. There were also several attempts at characterization and correction of those pulse errors in ESR. [159, 160].

Another common source of error are phases of the pulses. Importantly, the first pulse of any particular frequency interacting with the sample can be considered to have an arbitrary phase. In practice, if using an AWG (2.3.1) to construct pulses of several frequencies, the phases of the subsequent pulses need to be adjusted to account for the time passed between them. This can never be done perfectly, as waveform generation is done in discrete steps and the phasing of the pulses is never ideal. This is important mostly for the operations which are part of a longer sequence, and the phases need to be adjusted throughout. A 5° systematic phase error is not uncommon in the commercial ESR spectrometers.

This part was performed using the `sympy` package, in the product operator formalism (2.3.3). An explicit formula for the superoperator representing each experiment, including the imperfections in its duration, amplitudes and phases of all the pulses involved, was calculated. The full rotating frame free evolution Hamiltonian (Eq. 7.1) was used, but the gates were taken to be instantaneous.

Variations in 9 parameters, 4 amplitudes, 4 phases and the τ were included in this analysis. They are summarized in Fig. 7.5.

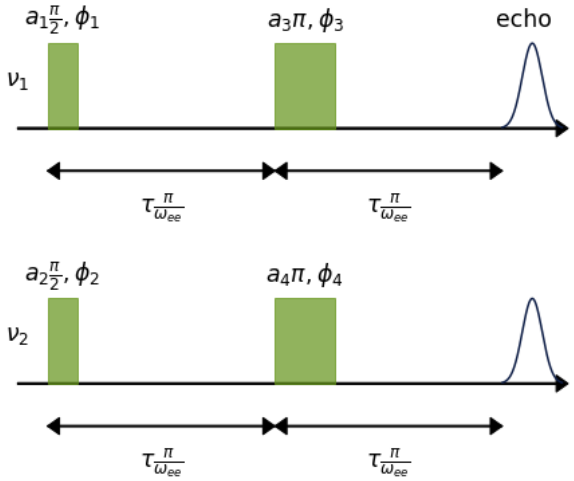


Figure 7.5: Parameters of the gate varied in this section. a_1, a_2, a_3, a_4 are amplitudes, and $\phi_1, \phi_1, \phi_3, \phi_4$ phases of corresponding pulses.

The process fidelity $\mathcal{F}^{\mathrm{g}}$ was calculated from Eq. 5.11, using product operators as the basis U_j and the ideal $\frac{\pi}{2}$ ZZ rotation gate as U. The full analytic formula is too long for a human being to gain any insight from, as it was handled by a computer program. However from the experimental point of view, it is interesting how these parameters affect the fidelity relative to one another. Thus, the fidelity may be expanded into a Taylor series around the point corresponding to no imperfections, that is $\tau = a_1 = a_2 = a_3 = a_4 = 1$, $\phi_1 = \phi_2 = \phi_3 = \phi_4 = \frac{\pi}{2}$:

$$\begin{aligned}\mathcal{F}^{\mathrm{g}} \approx 1 &- \frac{\pi}{10}(\Delta\phi_1)^2\Delta a_1 + \frac{\sqrt{2}\pi}{10}(\Delta\phi_1)^2\Delta a_3 - \frac{2}{5}(\Delta\phi_1)^2 + \frac{\pi}{5}\Delta\phi_1\Delta\phi_3\Delta a_1 + \\ &+ \frac{4}{5}\Delta\phi_1\Delta\phi_3 - \frac{\pi}{10}(\Delta\phi_2)^2\Delta a_2 + \frac{\sqrt{2}\pi}{10}(\Delta\phi_2)^2\Delta a_4 - \\ &- \frac{2}{5}(\Delta\phi_2)^2 + \frac{\pi}{5}\Delta\phi_2\Delta\phi_4\Delta a_2 + \frac{4}{5}\Delta\phi_2\Delta\phi_4 - \frac{4}{5}(\Delta\phi_3)^2 - \\ &- \frac{4}{5}\Delta\phi_4^2 - \frac{\pi^2}{20}(\Delta a_1)^2 - \frac{\sqrt{2}\pi^2}{10}\Delta a_1\Delta a_3 - \frac{\pi^2}{20}(\Delta a_2)^2 - \\ &- \frac{\sqrt{2}\pi^2}{10}\Delta a_2\Delta a_4 - \frac{\pi^2}{5}(\Delta a_3)^2 - \frac{\pi^2}{5}(\Delta a_4)^2 - \frac{\pi^2}{20}(\Delta\tau)^2\end{aligned} \tag{7.10}$$

where Δx is a deviation from the optimal value of x. The quadratic errors in Ising gates were discussed before in the context of NMR and several methods have been proposed to minimize them [161, 162]. These constructions are effective in

reducing this error, but they use a vastly increased number of pulses, which would be suboptimal in most ESR systems due to ensemble averaging and decoherence. The above results are shown here for comparison and completeness.

The phases of the pulses have no effect on the amount of entanglement. Thus, an important example is the rate of change of fidelity and entanglement if identical systematic error affects all pulse amplitudes, caused by inhomogeneity in the B_1 magnetic field across the resonator. The entanglement loss can be compared to the loss caused by temperature. For example, 10% systematic B_1 error corresponds to $\frac{1}{\gamma} = 0.25$, or roughty $0.4K$ in a Q-band system, as shown in Fig. 7.6. In general, because the logarithmic negativity is logarithmic in nature, the losses due to different effects tend to combine linearly to a good approximation.

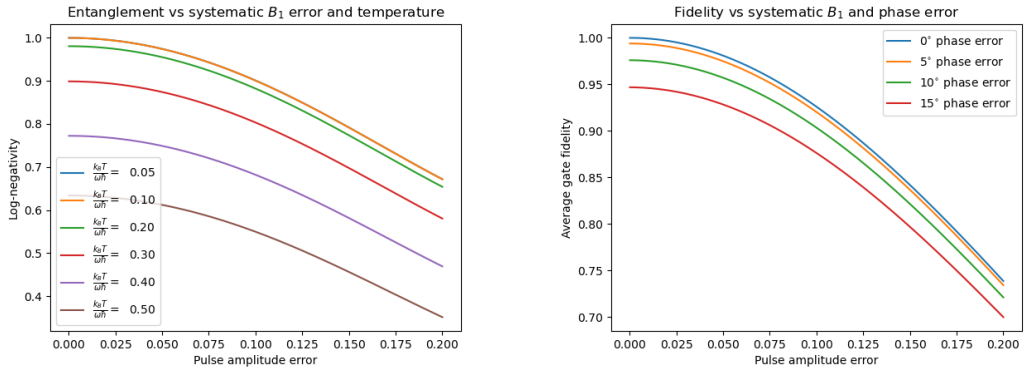


Figure 7.6: Effects of a systematic B_1 error on the entangling gate. **Left**: Log-negativity at the end of an imperfect gate experiencing a systematic pulse amplitude error, compared with loss of entanglement due to temperature of the initial state. Phases of pulses have no effect on entanglement. **Right**: Average gate fidelity of an imperfect gate experiencing both a systematic pulse amplitude and phase error. Phase errors become important if the gate is used as a part of a longer sequence.

The tomography procedure was analyzed analogously. Each of the 18 tomography measurement sequences was turned into a superoperator, assuming instantaneous pulses, with parametric amplitudes and phases shown in Fig. 7.7. As described earlier in 7.3.1, each measurement recovers 4 numbers; any state evolved through this operator acquires four detectable terms, two in $\hat{S}_x$ and two in $\hat{S}_y$, proportional to $\cos(\omega_{ee})$ and $\sin(\omega_{ee})$. Coefficients of these four terms were extracted symbolically and then used to recover the full density matrix using Table 7.1. This process is

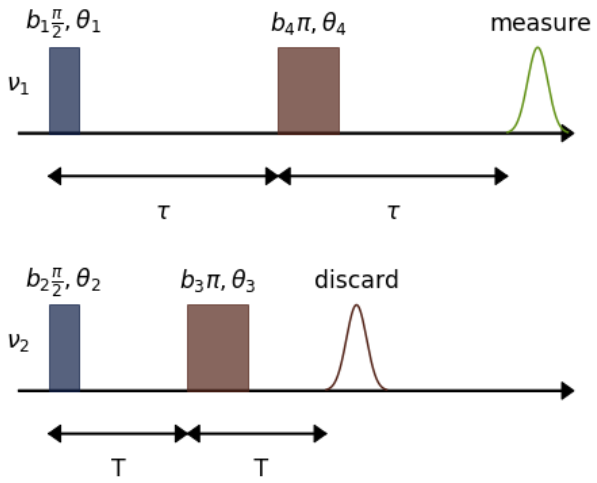


Figure 7.7: Parameters of the tomography sequence varied in this part. b_1, b_2, b_3, b_4 are amplitudes, and $\theta_1, \theta_1, \theta_3, \theta_4$ phases of corresponding pulses. The delay duration τ does not influence the result of the tomography, and the parameter T is used to recover the final state.

linear in the initial state, so the Eq. 5.11 may be used again to calculate the average fidelity of the entire process $\mathcal{F}^{\mathrm{t}}$, generating an analytic expression[3]. To compare the different sources of errors, it is expanded as a Taylor series:

$$\begin{aligned}\mathcal{F}^{\mathrm{t}} \approx 1 &- \frac{\pi}{8}(\Delta\theta_1)^2\Delta b_1 - \frac{21}{40}(\Delta\theta_1)^2 + \frac{\pi}{8}\Delta\theta_1\Delta\theta_4\Delta b_1 + \\ &+ \frac{1}{2}\Delta\theta_1\Delta\theta_4 - \frac{\pi}{8}(\Delta\theta_2)^2\Delta b_2 - \frac{21}{40}(\Delta\theta_2)^2 + \frac{\pi}{8}\Delta\theta_2\Delta\theta_4\Delta b_2 + \\ &+ \frac{1}{2}\Delta\theta_2\Delta\theta_4 - 3(\Delta\theta_4)^2 - \frac{11\pi^2}{160}(\Delta b_1)^2 - \frac{11\pi^2}{160}(\Delta b_2)^2 - \\ &- \frac{9\pi^2}{40}(\Delta b_3)^2 - \frac{3\pi^2}{8}(\Delta b_4)^2\end{aligned} \tag{7.11}$$

The phase of the pump pulse is the only parameter not affecting the fidelity up to third order. Its only function of is the inversion on the second spin, just like in the DEER experiment where it originates, so the phase should not be important[4].

Nevertheless, the tomography process is more sensitive to the pulse phases than the gate. Note that a systematic phase error in either frequency, consistent

[3] Again, in full too complicated for a human to gain any insight from.

[4] A perfect π pulse of an arbitrary phase may be decomposed into a Y π pulse followed by a Z phase rotation, described by the $\hat{S}_z^2$ operator, which commutes with the ν_1 pulse, the free Hamiltonian, and does not affect the detection, which only looks at $\hat{S}_x^1$ and $\hat{S}_y^1$. The deviation in this phase only matters when the amplitude of the π pump pulse is non-ideal, and thus appears first in the $(\Delta\phi_3)^2(\Delta b_3)^2$ fourth order term.

across both gate and tomography, may be corrected at the detection by adjusting the global phase at the end of the full experimental sequence. Amplitude errors cannot be corrected so easily. An example calculation of the fidelity in typical experimental conditions is shown in Fig. 7.8.

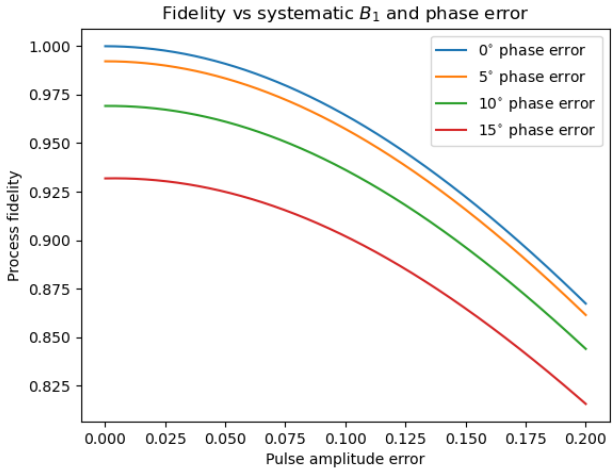


Figure 7.8: Effects of a systematic B_1 and phase error on the tomography procedure. Phase errors are important and more significant here, as the tomography process is always performed at the end of an experimental sequence.

These small imperfections do not have a large effect on the gate nor the tomography process. Most of the time, there is an experimental procedure that should be followed to calibrate the pulse amplitudes and phases, and the overall errors can be minimized to about 1% / 1° with careful calibration. This corresponds to changes in fidelity of order 10^{-4}, which would be significant in most quantum computing architectures, but here are small compared to interaction anisotropy and thermal effects.

7.4.4 Effects of finite pulse durations

So far, the microwave pulses were treated as instantanteous single qubit gates, and we have looked into imperfections in certain parameters of these gates, their phase and turning angle. Physically, the pulses have certain duration and shape, as explained in 2.3.5. The most popular pulse shapes in ESR are square and Gaussian pulses. The square pulses are easier to simulate and analyze, and in a

multi-frequency experiment Gaussian pulses will have less band overlap with the other frequency used, limiting one source of error.

The longer the pulse is the more defined its frequency, so it is important to ensure that $|\nu_1 - \nu_2|$ is larger than the pulse bandwidth. Otherwise, the ν_1 pulse will significantly interact with the spins resonant with the frequency ν_2. However, the longer the pulse is compared to the length of the gate, the less defined the gate operation. This is because the Hamiltonian experienced by the sample during the pulse still contains the $\omega_{ee}\hat{S}_z^1\hat{S}_z^1$ term, which does not commute with the $\hat{S}_y$ terms used to describe the action of the pulse. Here this effect will be analyzed separetely, to quantify the loss of fidelity due to square pulse's duration, without considering any ensemble effects yet.

One of the goals for this analysis was to establish whether to implement the gate as a $\frac{3}{2}\pi$, $\frac{5}{2}\pi$ or even $\frac{7}{2}\pi$ ZZ rotation. All of these gates are perfect entanglers and therefore serve the purpose of this project. Of course, longer gates would suffer more from the anisotropy of the interaction described in 7.4.2 and decoherence analyzed in 7.4.5. It would be a reasonable assumption that these longer variants might make better gates, because the free evolution period is longer compared to the duration of the pulse. In the end, it will be a trade-off, but will it be a deal worth taking?

The calculations for this part have been performed using the same Python code including the `sympy`, `numpy` and `scipy` libraries as the previous ones described here. During the double pulses, the Hamiltonian was taken to be

$$\hat{H}_{\text{pulse}} = A\hat{S}_y^1 + A\hat{S}_y^2 + \omega_{ee}\hat{S}_z^1\hat{S}_z^2 \tag{7.12}$$

and the time t under this Hamiltonian was adjusted so that At was equal to the nominal pulse rotation angle. All pulses have the same duration, but differ by amplitude, which is also how the majority of experiments are conducted, to ensure that bandwidths of all the pulses include the same spin packets. The interval between the beginning of the first and the second pulse, as well as the interval after the beginning of the second pulse, is equal to τ. All the time variables are in units of $\frac{\pi}{\omega_{ee}}$, to keep this analysis general.

First, the gate is analyzed. The fidelity is again calculated from Eq. 5.11, to quantify the distance between the implemented gate and the ideal $\frac{1}{2}\pi$ and $-\frac{1}{2}\pi$ ZZ rotations, which are both perfect entanglers. The log-negativity is calculated for each set of parameters. As the duration of pulses increases, the optimal τ increases by slightly more than a half of the duration of the pulse, making the duration of the optimal gate increase by slightly more than one pulse duration. Note that because for instantaneous pulses, the optimal $\tau = \frac{1}{2}\frac{\pi}{\omega_{ee}}$, for $t > \frac{\pi}{\omega_{ee}}$ the gate is effectively no longer possible to be implemented, since pulses take the entire duration of the experiment and the free evolution period is eliminated. The maxima of entanglement and fidelity occur at roughly the same points, the respective values at these maxima decrease with the duration of a pulse, as shown in Fig. 7.9. The maximum fidelities of $\frac{1}{2}\pi, \frac{3}{2}\pi, \frac{5}{2}\pi$ and $\frac{7}{2}\pi$ nominal ZZ rotation versions of the gate are close, so in most cases it is not recommended to use the longer versions instead. When the gate is applied to a specific initial state, however, the $\frac{7}{2}\pi$ results in the highest entanglement, although it becomes significant only for pulses longer than $0.4\frac{\pi}{\omega_{ee}}$. The entanglement stays robust, varying by less than 10^{-4} until the $0.2\frac{\pi}{\omega_{ee}}$ point.

Fidelity and entanglement may be improved by adjusting the amplitude of the pulses. Another calculation was performed, where amplitudes were modified by -15% to 15%, the results of which are summarized in Fig. 7.10. The effect is small even for long pulses. In case of log-negativity, in all the cases explored in this simple model, it was possible to bring it up to 1, indicating maximum entanglement.

In the second step, the tomography procedure was analyzed. The coefficients standing before $\cos(\omega_{ee}T)$ and $\sin(\omega_{ee}T)$ in the observable components of states generated by all 18 measurements are retrieved and compiled using the Table 7.1. Interestingly, the finite durations of pulses cause the maximum fidelity (calculated using Eq.5.11) to be attained if the origin of this oscillation is shifted slightly forward by some T_0, resulting in $\cos(\omega_{ee}(T - T_0))$ and $\sin(\omega_{ee}(T - T_0))$ playing the roles of cosine and sine oscillations. Optimally, T_0 is about 20% of the pulses' duration in this simple model. An example of tomography trace is shown in Fig. 7.11 and the summary of its overall fidelity is shown in Fig. 7.12.

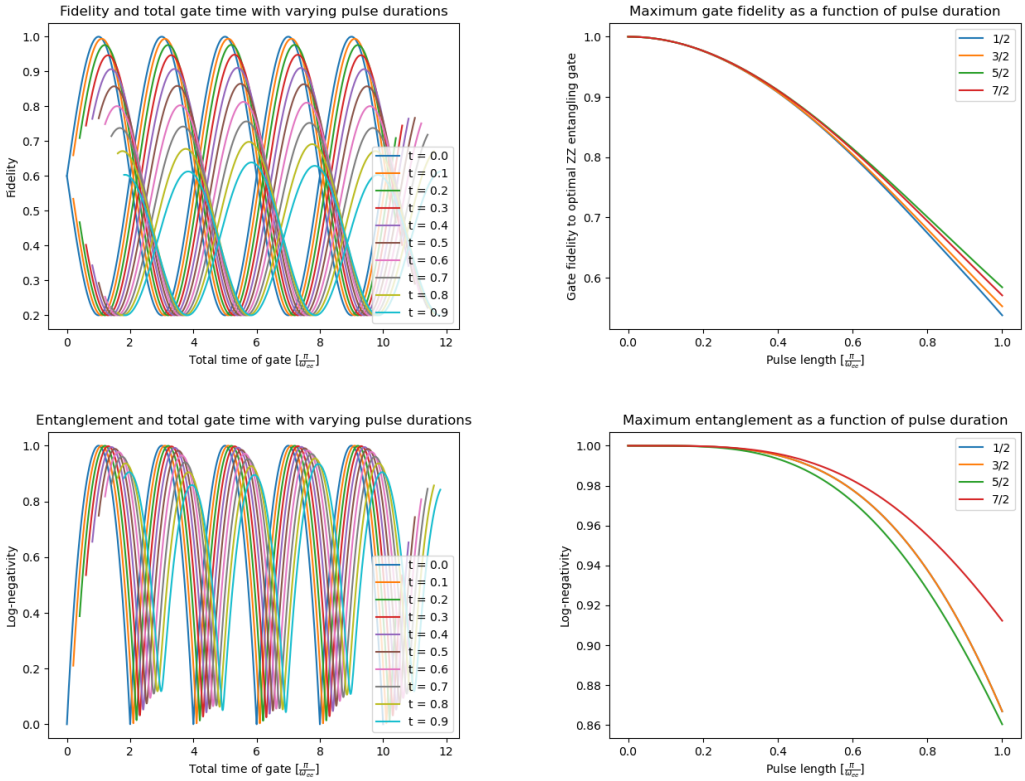


Figure 7.9: Fidelity and log-negativity of the entangling gate as a function of pulse and overall gate duration. **Upper left**: Example fidelity with ideal $\frac{1}{2}\pi$ and $-\frac{1}{2}\pi$ ZZ rotations as a function of total gate duration 2τ, for several selected values of pulse duration t. The consecutive peaks correspond to $\frac{1}{2}\pi$, $\frac{3}{2}\pi$, $\frac{5}{2}\pi$, $\frac{7}{2}\pi$ and $\frac{9}{2}\pi$ rotations. As the pulse duration increases, the maxima shift to the right and their value decreases. The shift to the right is equal to slightly more than t. **Upper right**: The maxima of fidelity for 4 first peaks as a function of pulse duration. There is no significant difference between the gate variations. **Lower left**: Logarithmic negativity for the same selected values of t, as a function of total gate duration $2(t+\tau)$. The maxima occur at roughly the same points. **Lower right**: The maxima of log-negativity at the 4 first peaks. The amount of entanglement in the system does not significantly decrease until about $0.2\frac{\pi}{\omega_{ee}}$.

The overall effect is significant given the experimental constraints, especially the nonlinearity and the power of the amplifier (2.3.1), but also the bandwidth problem discussed earlier. The pulses used in the experiments, described later in this chapter, correspond to about $0.15\frac{\pi}{\omega_{ee}}$, which is caused by the amplifier reaching its limits, mostly due to the need to send pulses simultaneously. Even in this simple model, not including the ensemble effects, the gate fidelity reaches about 0.985. The tomography, assuming it is possible to correct for the origin of the oscillation, has fidelity of approximately 0.983, dropping the overall fidelity to about

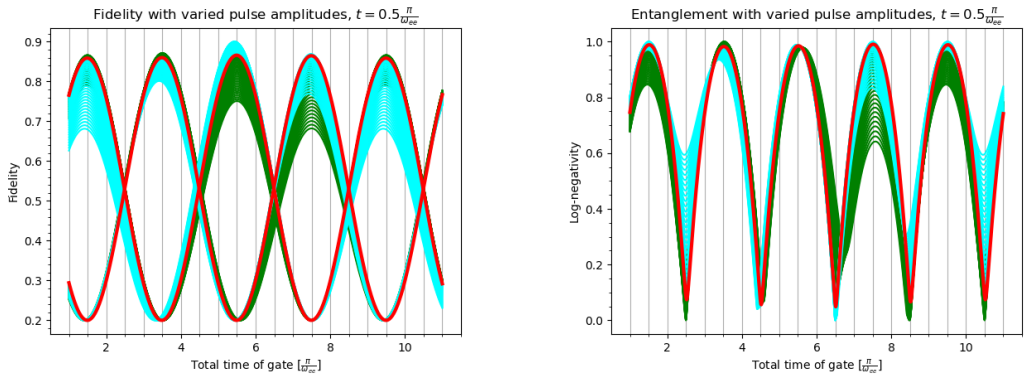


Figure 7.10: Fidelity and log-negativity of the entangling gate as a function of pulse and overall gate duration and changes to pulse amplitudes. The pulse duration is equal to $0.5\frac{\pi}{\omega_{ee}}$. The thick red line corresponds to nominal amplitude of the pulses, analyzed earlier. The dark green lines are simulations where the amplitude of pulses was increased, and the cyan lines correspond to those where it was decreased. **Left:** Gate fidelity. **Right:** Log-negativity of the state after the gate.

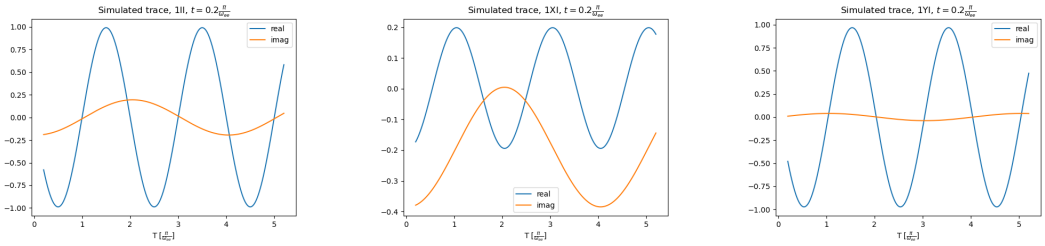


Figure 7.11: Example calculated time traces from a tomography process with finite duration $t = 0.2\frac{\pi}{\omega_{ee}}$ pulses. The state at the beginning of the tomography is the pure state $\frac{1}{\sqrt{2}}(|{+}{+}\rangle - i\,|{-}{-}\rangle)$. Left: 1II. Centre: 1XI. Right: 1YI. In the ideal case the left and right time traces would be a real $-\sin(\omega_{ee}T)$ with 0 in the imaginary channel, and the centre trace would be 0 in both channels. The long pulses introduce additional signal, additional oscillation the frequency $\frac{1}{2}\omega_{ee}$ and an offset in the oscillation's phase.

0.97. Fortunately, if one is only interested in producing entanglement, it should not decrease significantly with the pulse durations used in a typical experiment, provided that all the parameters are appropriately adjusted.

Of course, the specific numbers presented in this analysis will not correspond exactly to the experimental ones, where the response of the resonator and the ensemble effects play a role. The goal here is to quantify the order of magnitude of this effect and stress the need for it needing attention in the experiment. Other effects of pulse durations and ways to calibrate parameters experimentally will be discussed in the full simulation (section 7.5) and experiment (section 7.6) parts.

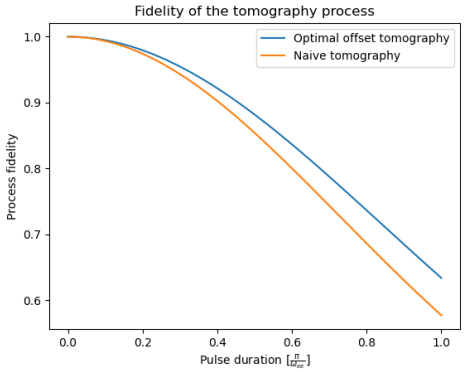


Figure 7.12: Process fidelity of the tomography with long pulses, as a function of pulse duration. The naive tomography does not take into account an offset in the oscillation caused by the pulses, equal to about 0.2 of the pulse duration. The optimal tomography includes it and corresponds to the maximum fidelity as a function of the time shift in the time traces.

In all the above calculations, the dimer Hamiltonian was approximated without the pseudosecular part, introduced in Eq. 5.4. The conclusions of this section give insight on whether or not this is justified. If the spin system is such that the pseudosecular terms should not be dropped, there will be more significant deviations from the ideal gate and the tomography process as a result of that. The pulse duration should satisfy:

$$t_{\text{pulse}} < 0.2\frac{\pi}{\omega_{ee}}$$

to avoid lowering the fidelity. On the other hand, the pulse bandwidth needs to be smaller than the separation of the two frequencies ν_1 and ν_2. Otherwise, the pulse excitation bands will overlap and significantly affect the opposite spins. Thus:

$$\frac{1}{t_{\text{pulse}}} < \left|\frac{1}{2\pi}\omega_1 - \frac{1}{2\pi}\omega_2\right|$$

Where $\nu_1 = \frac{1}{2\pi}\omega_1$ and $\nu_2 = \frac{1}{2\pi}\omega_2$. Combining the inequalities and eliminating t_{pulse} we obtain:

$$\omega_{ee} < 0.1\,|\omega_1 - \omega_2|$$

The factor 0.1 is not exact, but it specifies the order of magnitude required for this experiment to avoid both errors associated with lengths of pulses and the

pulse bandwidths. This is also enough to disregard the pseudosecular part of the Hamiltonian [46].

7.4.5 Effects of decoherence

In any attempt at quantum control or computing, relaxation times are of utmost importance; the longer they are, the more gates can be constructed and the longer the potential computation (2.4). Usually, the desired decoherence times are as long as possible. A T_1 several orders of magnitude longer than T_2 in these systems might prevent state reinitialization, if relying on this mechanism.

The effect of relaxation in this experiment is twofold. First, the decoherence can modify the gate itself, reducing the gate's fidelity. Second, it may affect the tomography process. The longer the tomography sequence, the more peaks and troughs will be measured, hence increasing the precision of the whole process, but significant relaxation, which is a random process, will introduce a random error in the signal. This section should help us understand if relaxation causes only this random error, which may be counteracted by performing more shots, or does it also cause some systematic error that changes the description of the recovered state.

As discussed previously in section 2.4, there are multiple realistic models for relaxation in ESR that can be utilized if one has access to relaxation data, and their parameters in general depend on the properties of the molecule and the solvent. Here the simplest possible model, only including diagonal terms corresponding to longitudinal and transverse relaxation times T_1 and T_2 will be considered, to provide the most general overview of the effect the relaxation would have in a molecular magnet dimer.

Thus, the relaxation superoperator introduced in Eq. 2.35 was constructed with only diagonal relaxation rates. Longitudinal terms relax with rate $\frac{1}{T_1}$, transverse - $\frac{1}{T_2}$ and product terms with relaxation rates equal to sums of relevant rates, which is a common approximation. This part was performed symbolically and numerically using `sympy`, `numpy` and `scipy` Python packages again, by explicitly exponentiating the matrices in a product operator basis in Liouville space, with

one additional dimension to account for the thermal state. Like in 7.4.4, the time variables are in units of $\frac{\pi}{\omega_e e}$.

Multiple T_1/T_2 models were considered, here two limiting ones are presented: infinite T_1 with varying T_2 and $T_2 = 2T_1$. Physically T_2 cannot be longer than $2T_1$, because with only longitudinal relaxation, the transverse terms still relax at half the rate. The conclusion of this calculation is that for the entangling gate, T_2 is more important, which should not be surprising, because entanglement after gate resides in the $\hat{S}_x^1\hat{S}_x^2$ double coherence, which decays the fastest.

For the tomography sequence, in this simple model the relaxation does not introduce any systematic errors. In the experiment, the in-phase channel signal corresponds to $\langle S_x\rangle$ and the quadrature channel to $\langle S_y\rangle$. From each trace, two numbers are recovered, one corresponding to cosine amplitude, and the other to the sine amplitude. Those oscillatory signals have frequency $\frac{\omega_{ee}}{2\pi}$. The simulation shows that all these features, including the frequency, the phase and relative amplitudes of these components, are maintained. The overall signal in each of the 18 measurements decreases by a constant factor, which depends on the total duration of the tomography sequence, T_2 and T_1. However, since there already is a multiplicative factor in the experiment, this has no effect on the final recovered state, as it needs to be normalized regardless. An example is shown in Fig. 7.13. Note that by symmetry, in the rotating frame coherences associated with those two operators must relax at the same rate, and so must the expectation values of the $\hat{S}_y^1\hat{S}_z^2$ and $\hat{S}_x^1\hat{S}_z^2$. The tomography sequence is a back-and-forth ZZ rotation, so unless there is complicated cross-relaxation between these operators, the tomography sequence should be robust.

7.5 Full Spinach simulations of the experiment

7.5.1 Methodology

The last unexplored source of error are the effects of the ensemble. Those cannot be captured without also considering durations, and possibly shapes of pulses, because the pulse bandwidth determines what part of the ensemble is participating in the experiment and to what degree. These effects were investigated using Spinach [65]

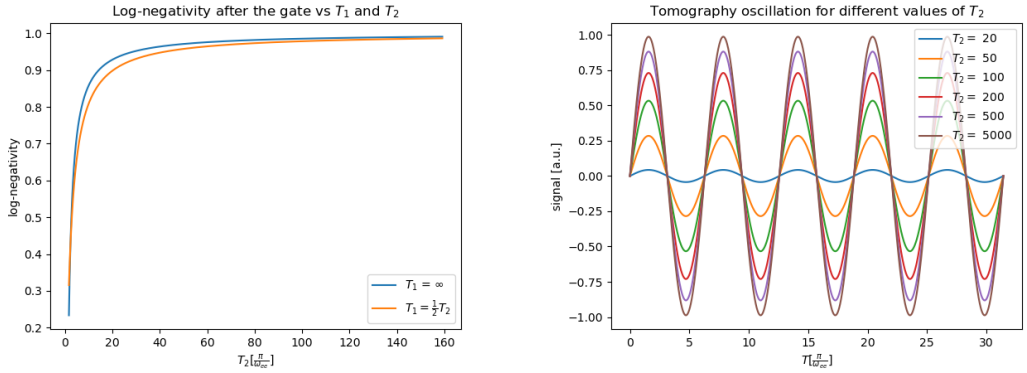


Figure 7.13: Calculations of the systematic effect of the characteristic relaxation times T_1 and T_2, at $0K$. The characteristic times are in units of $\frac{\pi}{\omega_e e}$. Left: Log-negativity at the end of the gate, with two T_1/T_2 models. T_1 has little effect on entanglement, and log-negativity of 0.9 can be achieved for $\omega_{ee}T_2 = 50$. Right: Examlpe effect of T_2 on the trace in the tomography sequence, if the total length of that sequence is $20\frac{\pi}{\omega_{ee}}$. All the relevant time traces remain in phase and their magnitude decreases by the same factor, introducing no systematic error to the tomography process. The total duration of the sequence is an experimental trade-off between seeing more peaks and troughs in the oscillation and maximizing signal to noise ratio. In contrast, the gate sequence has to have a very specific duration to result in a correct unitary operation.

spin dynamics simulation library for MATLAB. Spinach performs quantum evolution calculations in Liouville space, using spherical tensors as basis and supports fast angular averaging over a predefined grid. These simulations imitate the way the actual experiment is performed. An ensemble of spins is illuminated with a sequence of microwave pulses of certain shapes and frequencies, a Hahn echo is formed and then integrated. The result of a single simulation is a trace, corresponding to echo amplitudes for different values of the parameter T. In all the simulations described in this section, the fundamental pulse sequence is the entangling gate followed by the tomography process, shown in Fig. 7.3.

A crucial characteristic of this entire project is that it is difficult to properly define a density matrix in systems of this kind, due to large bandwidths. In the simulations and calculations described above in section 7.4, Spin 1 and Spin 2 were defined explicitly as 2-level quantum systems and the density matrix was defined in a natural way, what made it possible to examine said density matrix at any point during the calculation, for example just after the entangling gate. Here, we are moving away from this possibility and into the territory of experimental

undefinedness. Even though of course the simulations are following the mathematical rules of quantum mechanics and are performed using a density operator formalism, those density operators are just simulation tools. The density matrix describing the part of the system we can interact with will only emerge at the end, from the tomography procedure, as described before in section 7.3. This is why here the sequence is examined as a whole.

7.5.2 Simulation structure

Spinach uses a Liouville space formalism based on spherical tensor operators, and processes evolution according to the von Neumann equation with a Hamiltonian commutation superoperator, as discussed in 2.3.3. For a typical powder simulation, the user specifies the type of spins, associated g-tensors and couplings, parameters for a chosen relaxation theory, as well as experimental parameters, magnetic field, and optionally temperature. The pulse sequence, and all the parameters associated with it, also need to be supplied. In case of a pulse sequence ending with an echo, the density matrix is evolved in discrete steps at the end of the sequence and the expected value of the readout observable proportional to the magnetization seen by the resonator, in our case $\langle \hat{S}_+^1 + \hat{S}_+^2 \rangle$ is calculated at each point. All the steps are repeated for all the grid points, with extensive parallelization, and the magnetization is added together, to average to a Hahn echo oscillating at the detection frequency. This signal is then shifted in frequency and integrated.

Spinach uses a single rotating frame for most of the evolution simulations. Using the lab frame is impractical due to required sampling at the readout, and using a doubly rotating frame does not allow for including the way the microwave pulse interacts with all the spins in the molecule, which is an effect we are specifically interested in, without introducing unnecessary time dependence into the Hamiltonian.

During a single-frequency pulse, the Hamiltonian is shifted to the rotating frame associated exactly with the microwave frequency, given by Eq. 5.2. The pseudosecular (Eq. 5.4) terms may be included in the simulation or dropped.

Including them increases the time needed to complete a simulation significantly, as the free evolution Hamiltonian is no longer diagonal, but it could lead to more accurate results. As discussed at the end of 7.4.4, the pseudosecular term may be dropped in the investigated regime due to interplay between pulse durations and bandwidth overlaps, which would introduce more significant issues. In the simulations, the pseudosecular part was included for several simulations from each set and it did not modify the results in a detectable way, so it was dropped for the results presented here.

Unfortunately, moving to the exact rotating frame associated with the pulse frequency is only efficient if there is only one simultaneous pulse. With two frequencies, a pulse Hamiltonian will always have an explicit time dependence. During the double pulse, the frequency of the rotating frame was taken to be an average of the two frequencies and the Hamiltonian was discretized. The stepsize was lowered until there was no detectable change in the result of a simulation for a given pair of frequencies and a spin system. When synthesizing pulses of this kind, it is important to remember to track evolution time, and adjust the phases of all pulses and the appropriate detection accordingly. Spinach does not support multiple frequencies of pulses or time and phase tracking by itself, some of its functions needed to be modified to allow it[5].

7.5.3 Recovering the density matrix from the simulated and experimental time traces

The tomography procedure consists of not just the pulse sequences and data collection, but also the analysis of these data that leads to the recovered deviation density matrix. The trace recovered from each individual tomography measurement has all the properties of a DEER experiment trace, discussed in 5.4, which complicates the process of recovering the components of the density matrix. This includes the large background, and the fact that with anisotropic coupling present in the system, the sinusoidal oscillation changes into Fresnel integral oscillation. Using

[5]My code can be found on GitHub [163].

these functions in the fitting process exactly would however break the tomography procedure, as these functions do not have a well defined phase variable. Instead, the sine and cosine functions with an exponential decay envelope, with a decay parameter $-1/t_3$ were used as an approximation providing high fit quality. The same choice was made for the experimental data.

Unlike in the traditional analysis of DEER data [46, 54], here the fitting function includes background added to the signal, and not multiplied. Separating the background in such a way represents removing the signal coming from molecules not part of the selected subensemble. The ratio of the background to the oscillatory signal heavily depends on the choice of pulses, and thus treating the background additively is in this case more appropriate, as it enables comparison between oscillatory magnitudes between the measurements.

The parameters used in the fit may be divided into local and global. Local parameters correspond to a specific data set, and global parameters correspond to all the datasets simulated or measured with the same settings, and differing only by durations of the free evolution periods and temperature.

Python's `scipy.optimize.curvefit` nonlinear least squares fitting function was used to fit a

$$A\sin(\omega_{ee}T+\phi)+B\cos(\omega_{ee}T+\phi)+C \tag{7.13}$$

function to time traces obtained from exchange-coupled systems, and

$$e^{-\frac{T}{t_3}}\left[A\sin(\omega_{ee}T+\phi)+B\cos(\omega_{ee}T+\phi)\right]+C+DT \tag{7.14}$$

function to time traces obtained from systems with anisotropic coupling. A and B are signal amplitudes, which are then used to recover the corresponding density matrix components, according to Table 7.1. C and D are background parameters, where a linear expansion of a slow exponential decay (5.4.2) was used for efficiency. In the simulation, the background does not decay, because experimentally it is a result of interactions between dimers which were not included in the simulation. A, B, C, D are local parameters, and are fitted individually to each of the 18 time traces.

The parameters t_3 and ω_{ee} are global parameters, and are fitted to all time traces in the set at once. The frequency of oscillation depends on the coupling strength, so for simulations with isotropic coupling it did not need to be fitted. In the simulations with anisotropic coupling, the oscillation frequency depended not only on the underlying system, but also the parameters of the pulses used to orientationally select a part of the ensemble. When fitting experimental data, these parameters were obtained from a previous calibration experiment.

The parameter ϕ corresponds to the shift in the origin of the oscillation due to finite durations of pulses, discussed in 7.4.4, and it is a global parameter. There are three more global parameters, α, β and λ. The first two are the global microwave phases corresponding to the time traces collected with frequencies ν_1 and ν_2 respectively. The parameter λ describes the normalization ratio between amplitudes of time traces collected with different frequencies[6]. All three may be fitted as global parameters using a global least squares fit. The details of this procedure are in the Appendix B.3. Intuitively, this fitting disregards the global phases and recovers the density matrix from the phase differences between measured time traces.

In the experiment, these parameters may be calibrated. This was done using a 4-pulse DEER experiment, which is identical to a Hahn echo followed by the 1II step of the tomography. Two 4-pulse DEER experiments are performed, one per each frequency, and the relative phases, origins of oscillation and amplitudes are fitted for each detection frequency.

In the high-temperature limit, the angle-fidelity introduced in Eq. 7.5 was calculated. The process fidelity (Eq. 5.10) proved useful in the examination of the tomography procedure performed in the previous section. In this part, the density matrix is defined by the bandwidths of the pulses, and not by the natural linewidth of the sample, however. Thus, using this formula is only reasonable if we prepare a set of initial states spanning the Liouville space [129] using the pulses, that is,

[6]The reasons these global phases need to be corrected for include Bloch-Siegert shifts (2.3.4), including these caused by the presence of the pseudo-secular terms (5.1.2) and phase errors in π pulses discussed in 7.4.3. The normalization ratio is needed mostly due to the resonator's response differing for frequencies ν_1 and ν_2; in the simulations the λ parameter is close to 1.

fully simulate an experimental attempt. Crucially, such a set includes entangled states like the one created by our entangling gate. Thus preparing, analyzing and benchmarking the entangling gate is a necessary step that needs to be completed before the tomography procedure is analyzed in general terms.

7.5.4 Simulation parameters and results

With good experimental data, the natural approach to the simulation would be to extract the molecular parameters from the data, and using them, only explore the space of the frequencies, gate shapes and sequence parameters. However, because the experimental data were unsatisfactory and it was unclear what the reasons for that were, I decided to test different hypothetical molecules instead. I chose parameters corresponding to possible dimers with certain, desireable or not, properties, that could exist but do not have a specific physical counterparts. This kind of search cannot be exhaustive because of the number of parameters and the time it takes to complete a single simulation. Unlike in other sections, the bounds discovered here are not fundamental and might possibly be improved without modyfing the pulse sequence. However, these simulations are easy to run if a successful experiment is performed, and provide interesting insights using the hypothetical parameters.

Most of the simulations in this section were performed using the high-temperature limit, to help understand the actual experiment that was possible to run at the time. The temperature degree of freedom is added to this simulation at the end. For all the simulations, the B_0 variable was set to 0.345 T. All the pulses used in all the simulations were set to 20 ns, and other time and frequency parameters were adjusted instead.

For each parameter set, 18 simulations were performed in Spinach, the entangling gate followed by all the experiments listed in Table 7.1, and then analyzed using the method described in the previous section.

First, the coupling was assumed to be isotropic to isolate the ensemble effects coming from the g-tensor anisotropy. To also reduce the effect of the pulse durations, the coupling was assumed to be orders of magnitude smaller than one typically

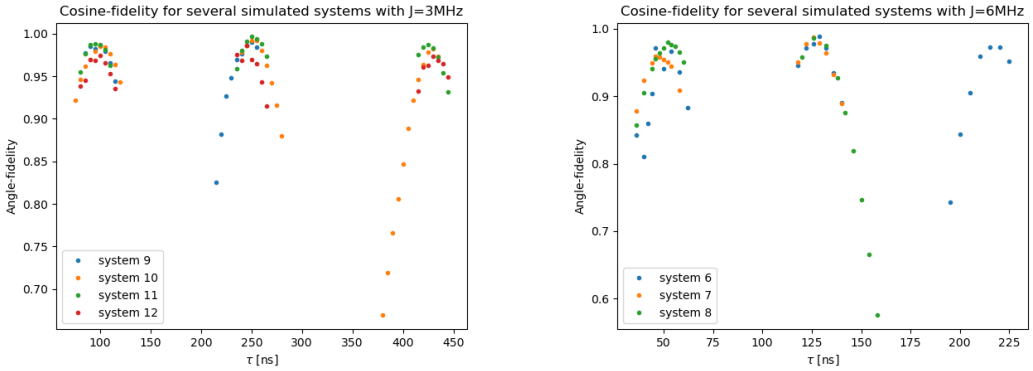


Figure 7.14: Fidelities of several simulated systems with isotropic exchange coupling, grouped by the value of the coupling. The numbers correspond to systems specified in Table A.2. The fidelities depend on the underlying ensemble systems, but the positions of their maxima are consistent with the results of the analysis in 7.4.4 and only depend on the coupling strength.

encountered in such systems, with J = 20 kHz. Five sets of parameters were investigated, together with τ values corresponding to the first entangling angle, to find which duration implements the gate the best.

Next, the effect of pulse lengths compared to the coupling strength was also taken into the account, by increasing the coupling to more realistic values of J = 6MHz and J = 3MHz. All these parameter sets are included in Table A.2 and the results are shown in Fig. 7.14. Some of the simulated time traces are shown in Fig. 7.15 for context.

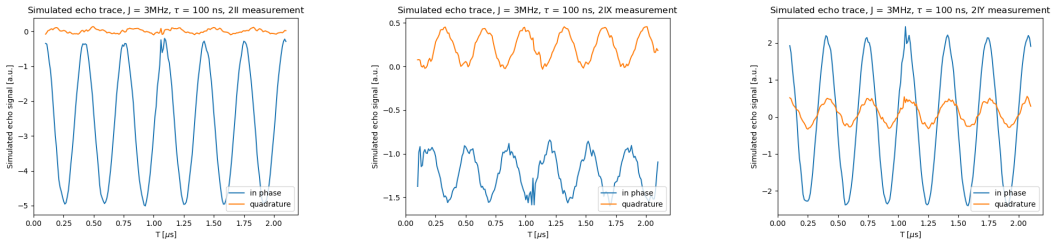


Figure 7.15: Example time traces from the simulation of one of the exchange coupled sets of parameters, analogous to time traces shown in Fig. 7.11. The parameter $\tau = 100$ ns. Left: 2II Centre: 2IX Right: 2IY. In the ideal case the left and right time traces would be a real $-\sin(\omega_{ee}T)$ with 0 in the imaginary channel, and the centre trace would be 0 in both channels. Additional signal is introduced as a result of long pulses and ensemble effects. The signal is a Fourier transformed integral of an echo, which itself is a sum of 1024 grid components. The noise arises as a result of magnifying the floating point precision error.

In general, the fidelities depend on the underlying spin ensemble parameters, because of the differences in how the pulse bandwidths overlap with the spectrum of the molecule, but are consistently at about 0.98 at a maximum. The positions of the maxima of these fidelities are consistent with the analysis in section 7.4.4. For J equal to 3MHz (6MHz), the optimal gate τ-s should be 83 ns (42 ns) for the $\frac{\pi}{2}$ variation of the gate, and 3 and 5 times longer for the respective longer variations. In all cases these maxima are shifted by about 10 ns forward, which is about half the duration of the microwave pulses used in the experiment, appearing at, 92 ± 2 ns and 52 ± 2 ns respectively.

Next, a dipolar, anisotropic coupling was investigated. All the dimers were homo-systems, created from two identical spin-$\frac{1}{2}$ molecules. Several coupling strengths and gate durations were included. An obvious complication in an anisotropically coupled system is the dependence of the coupling strength on the frequencies, and thus subpopulations, chosen, as explained in 7.4.2.

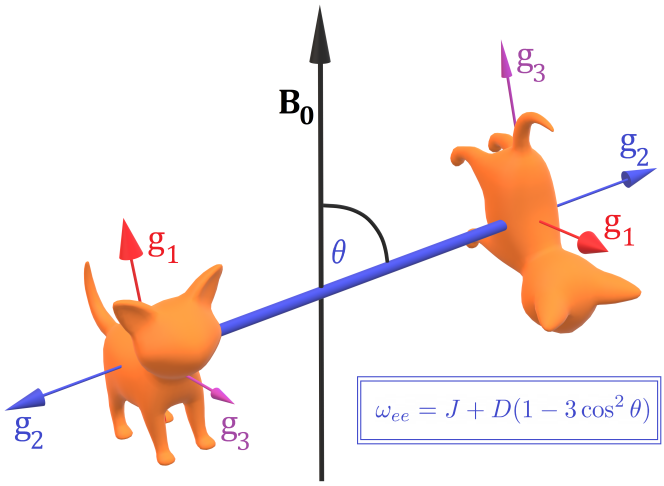


Figure 7.16: The magic dimer model. Two identical, but perpendicular spin centres connected by a rigid thread interact dipolarly. The principal values of the g-tensor satisfy $g_1 > g_2 > g_3$. The directions of g_1 and g_3 are perpendicular to the inter-molecular axis (blue).

The last investigated dimer was examined to test an idea of what would be a preferred geometry for a dipolarly coupled homo system. A model is shown in Fig. 7.16. The parts of the spectrum corresponding to the extreme values of the g-factor are easily identifiable at the edges of the spectrum. Whenever one

spin centre is resonant at the frequency corresponding to the maximum value of the g-factor, the molecule must be oriented such that the inter-molecular axis is close to the $x - y$ plane, and the other end of the dimer is resonant with the minimum frequency. Choosing these two frequencies as ν_1 and ν_2 would have two effects. Firstly, the coupling strength $\omega_{ee}(\theta)$ would be more consistent across the selected molecules, as the angle $\theta = \frac{\pi}{2}$:

$$\omega_{ee}\left(\frac{\pi}{2}\right) = D(1 - 3\cos^2\frac{\pi}{2}) = D$$

and

$$\left.\frac{\partial \omega_{ee}}{\partial \theta}\right|_{\theta=\frac{\pi}{2}} = 0$$

Secondly, the background should significantly decrease, as the number of molecules at resonance with just one frequency is reduced.

The point of this particular set of simulations was to provide evidence that making such a rotated dimer is a reasonable idea for this project, to provide synthetic chemists with a simple set of conditions to satisfy when preparing samples. The main reason no molecules were ever synthesised was the outbreak of the COVID-19 pandemic.

For dipolar coupling, Spinach requires the point-dipole distance as a parameter, and it was set to 3 nm for this parameter set. The g-tensor primary values were set to 2.0123, 1.9774 and 2.0322 for each end. The frequencies used were $\nu_1 = 9.6$ GHz and $\nu_2 = 9.76$ GHz. The oscillation period fitted to simulated echo data was 515 ns, and the oscillation decay rate was fitted to be 2.4μs. The strategy seems to have worked: despite the dipolar coupling, a selection is possible. The maximum fidelity is similar to the exchange case, with maxima at about 0.98. The maxima occur at 160 ns, 380 ns, and 680 ns, and are displaced with respect to expected values of 129 ns, 386 ns, and 644 ns respectively for $\frac{1}{2}\pi$, $\frac{3}{2}\pi$ and $\frac{5}{2}\pi$ variations of the gate. This displacement is variable, which suggests that because the oscillation is described by a Fresnel integral function, calibrating the gate duration based on the oscillation period is a good initial guess, which should be improved upon in

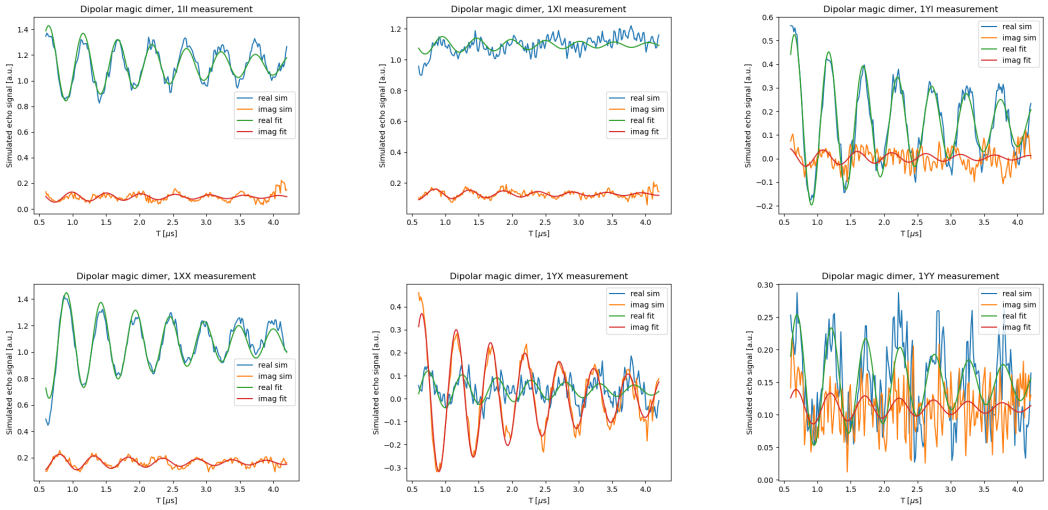


Figure 7.17: Example simulated time traces of the dipolar magic dimer set of parameters, analogous to time traces shown in Fig. 7.11. The $\tau = 160$ ns, which corresponded to maximum fidelity. Top left: 1II, top centre: 1IX, top right: 1IY, bottom left: 1XX, bottom centre: 1YX, bottom right: 1YY. In the ideal case, for this particular state, the top left and right tiime traces would be a real $-\sin(\omega_{ee}T)$ with 0 in the imaginary channel, and the top centre trace would be 0 in both channels. At the bottom, the left trace should be $+\sin(\omega_{ee}T)$ in the real channel, the centre trace should be $-\sin(\omega_{ee}T)$ in the imaginary channel and the bottom right trace should be zero in both channels. Note that the actual functional form of this trace is the Fresnel integral, but it can be fitted with a simple sine or cosine, if an exponential decay envelope is included. The time traces are shifted due to finite lengths of pulses and ensemble dynamics, but their relationships to one another are consistent with the expectations. Some of the time traces also exhibit signs of cross-excitation of pulses of frequencies ν_1 and ν_2, manifesting as a small predatory echo added to the main echo when T approaches $\tau - \frac{\pi}{2\omega_{ee}}$.

subsequent experiments. Some of the simulated time traces are shown in Fig. 7.17 and the fidelity results are summarized in Fig. 7.18.

The simulated time traces reveal another interesting effect. There are small variations in the signal at the end of some of the experimental time traces, as shown in Fig. 7.17, which are indicative of cross-excitation of pulses of frequencies ν_1 and ν_2. The excitation band of the pump π pulse overlaps with the excitation band of the first $\frac{\pi}{2}$ pulse, and so the echo is created, which travels forward as the parameter T is increased. When the pump pulse nears the detection π pulse, so the parameter T approaches $\tau - \frac{\pi}{2\omega_{ee}}$, the cross-excitation echo starts overlaping with the targeted echo and causes a small change in the integrated signal. Fortunately, because the band overlap is small, the predatory echo is orders of magnitude smaller than the

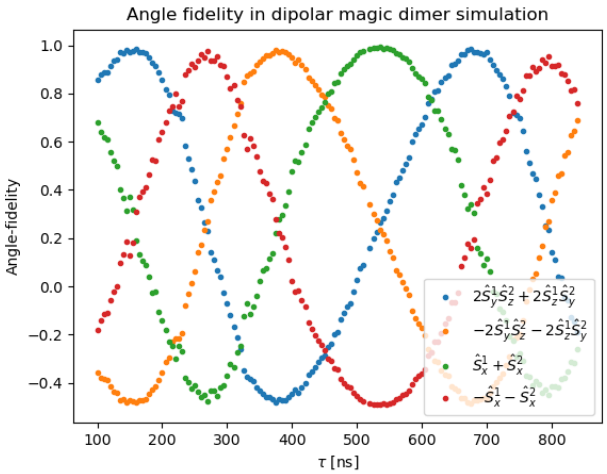


Figure 7.18: Fidelities of the final state in the magic dimer system as a function of τ. The fitted oscillation period is 515 ns. Blue and orange dots correspond to fidelities with the $2\hat{S}_y^1\hat{S}_z^2 + 2\hat{S}_z^1\hat{S}_y^2$ states, red and green dots correspond to fidelities with the $\hat{S}_x^1 + \hat{S}_x^2$ states. The system oscillates between these two states, as expected.

main integrated echo. These variations can be and have been ignored in fitting, the results are promising even then. They may be eliminated by phase cycling the pump π pulse, as its phase is otherwise unimportant for the tomography procedure. In general however, it should be aimed that in the experiment, bandwidths of the pulses are actually smaller than $|\nu_1 - \nu_2|$ so this effect does not occur. It is however expected to be observed in the experimental data as well, if this phase cycling is not employed.

The final part of the Spinach simulations included temperature effects. The sets of parameters corresponding to one exchange-coupled system (number 12 in Table A.2) and the dipolarly-coupled magic dimer at the respective maxima of their fidelity were given the initial state temperature. The thermal state was recalculated for each laboratory frame Hamiltonian resulting from the points in the averaging grid and used as an initial state for that point. The expectation here is that, according to Eq. 7.2, the state after the gate has three components: $2\hat{S}_y^1\hat{S}_z^2$, $2\hat{S}_z^1\hat{S}_y^2$ and $2\hat{S}_x^1\hat{S}_x^2$. Normalizing the traceless part of this state such that the coefficients of the first two terms are 1, we get:

$$\rho_{\text{traceless}}(\gamma) = \hat{S}_y^1\hat{S}_z^2 + \hat{S}_z^1\hat{S}_y^2 + \frac{\cosh\gamma - 1}{\sinh\gamma}\hat{S}_x^1\hat{S}_x^2 \tag{7.15}$$

where $\gamma = \frac{\hbar\omega}{k_B T}$. The simplest way to verify the results is to look at the $\langle 2\hat{S}_x^1\hat{S}_x^2\rangle$, normalizing all the components by the magnitude of $\langle 2\hat{S}_y^1\hat{S}_z^2\rangle$, and check whether it follows the above relationship. In all the cases, it does, with the best fit ω between the measurement frequencies $2\pi\nu_1$ and $2\pi\nu_2$, as shown in Fig. 7.19. There is only minimal change in other density matrix components when the temperature is varied[7]. It suggests that most of the $2\hat{S}_z^1\hat{S}_z^2$ spin order of the thermal initial state is correctly transfered to the $2\hat{S}_x^1\hat{S}_x^2$ spin order after the gate.

It is worth noting that the realistic limit for a Q-band system with a flow cryostat corresponds to $\nu = 34$ GHz and $T = 2.5$ K, which would imply $\langle \hat{S}_x^1\hat{S}_x^2\rangle = -0.31\langle \hat{S}_y^1\hat{S}_z^2\rangle$, which would be detectable. Unfortunately, a low-temperature entanglement experiment was not possible to be performed with existing samples.

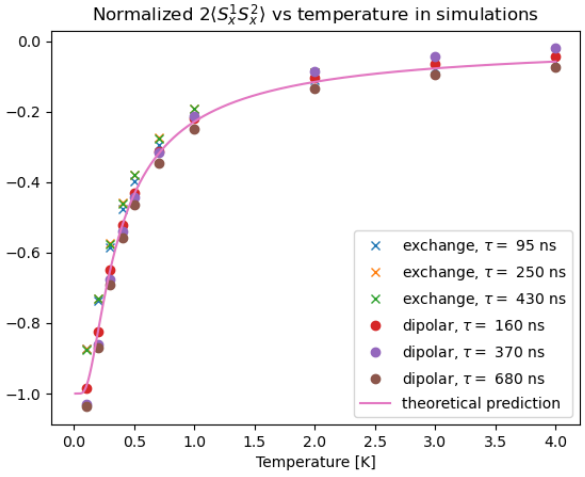


Figure 7.19: Normalized expected value $\frac{2\langle \hat{S}_x^1\hat{S}_x^2\rangle}{\langle \hat{S}_y^1\hat{S}_z^2\rangle + \langle \hat{S}_z^1\hat{S}_y^2\rangle}$ in selected simulations with low temperature parameters. The parameter $\omega = 2\pi \times (9.68$ GHz) in the theoretical curve $\frac{\cosh\gamma - 1}{\sinh\gamma}$ shown in the graph corresponds to the average value between the two frequencies used in the simulations of the dipolarly coupled system.

7.6 Entanglement experiments

Several experimental runs were performed to realize this procedure. They were preceded by DEER (5.4) and other experiments needed for calibration on the

[7]Even though this simulation just recovers the parameter fed into it, it is still reassuring to see exactly 4 of the 18 measurements to be affected by this parameter, and in the predicted way.

related samples. All experiments were performed in CAESR Oxford, and used a Bruker E580 commercial spectrometer with an Arbitrary Waveform Generator, used for creation of the off-frequency pulses, and the Q-band range of frequencies, between 33 GHz and 34.2 GHz.

7.6.1 Calibration procedures

The first calibration step is to determine the frequencies ν_1 and ν_2 to use in the final experiment. The most important criteria are signal to noise at both frequencies and the size of the subensemble selected.

First, the bandwidth of the resonator with the inserted sample was probed using a nutation experiment (2.5.2). Then, amplitudes of single π and $\frac{\pi}{2}$ pulses at promising frequencies were calibrated (2.5.3). Two DEER experiments were conducted at each pair of frequencies, optimizing for the signal and modulation depth. First, where ν_1 is detection and ν_2 is pump, and the second, where the roles were reversed.

Then, with the pair of frequencies used for the experiment determined, the double π and $\frac{\pi}{2}$ pulses' amplitudes needed to be recalibrated in an iterative procedure, because of the amplifier's non-linearity (2.3.1). The amplitude of the half of the double pulse corresponding to current detection is increased, while the off-frequency amplitude is fixed. Then, the frequencies are switched and the process repeated until it converges. The sequence is shown in Fig. 7.20. The $\frac{\pi}{2}$ double pulses were calibrated analogously, but in practice due to their lower amplitude, the TWT operated in its linear regime, so the process concluded after the first iteration.

Finally, one more 4-pulse DEER experiment was conducted, and the phase of the detection was adjusted to the phase of the echo. The following set of 9 experiments then used these parameters. The 4-pulse DEER measurement was later used for normalization, as described in 7.5.3.

7.6.2 DEER standard measurements

The first experiments were conducted using a bis-nitroxide molecule shown in Fig. 7.21. The free electrons are shared between the nitrogen and oxygen atoms at

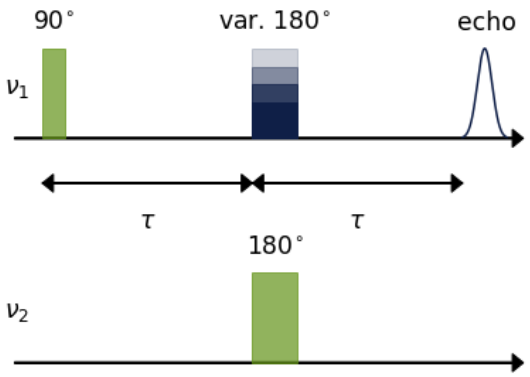


Figure 7.20: Calibrating the amplitude of a double π pulse. A $\frac{\pi}{2}$ pulse only excites spins resonant at ν_1, and the π pulse attempts to invert them in a presence of a ν_2 π pulse. The pulse interacting with the sample should have the same amplitude as in the case of a single π pulse, however the pulse sent needs to have higher relative amplitude because of the amplifier non-linearity.

the ends of the molecule, which is used as a DEER standard, due to its well-defined inter-spin distance and satisfaction of the point-dipole approximation, which results in clean oscillations. This sample was selected, as these properties, making a sample suitable for the DEER experiment, also make it suitable for the tomography experiments, because the tomography sequence is a modified DEER sequence. The T_1 time in this molecule at helium temperatures unfortunately does not allow for any repeated shot experiments in that range, as the time needed for the state reinitialization becomes prohibitively long. This is why all experiments with this sample were conducted either temperatures where the tomography process recovers the high-temperature state.

DEER experiment is time consuming, if one wishes for a good resolution, and collecting the tomography traces requires performing a similar measurement 18 separate times. With limited availability of spectrometers, it was only possible to conduct the full experiment several times, each with all the parameters, such as the duration of the gate, fixed. It took 36 hours of spectrometer time to obtain an analogue of a single point in Fig. 7.18.

The data from two best experimental runs are presented here. All the early experiments suffered from the AWG phase errors described earlier in 7.4.3, and were

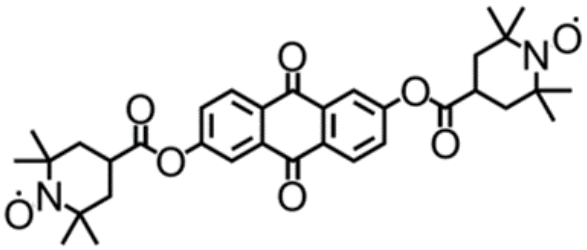


Figure 7.21: A standard DEER sample, bis-nitroxide double radical.

analyzed using a slightly modified tomography process described in Appendix B.2 and the fitting procedure described in 7.5.3. The state components, or measured product operator expectation values, are normalized so that the trace norm is 2.

The first of these runs was the first test of the tomography procedure. Before looking at entangling gates, the tomography was applied to a simpler state created by a simple one-frequency Hahn echo experiment. The state after a single Hahn echo in ν_1 should be proportional to $-\hat{S}_x^1 - \hat{S}_z^2$. The first spin acquires coherence in a normal echo sequence, and the other one is unaffected, as the effect of the interaction part of the static Hamiltonian is refocused. The full pulse sequence is shown in Fig. 7.22.

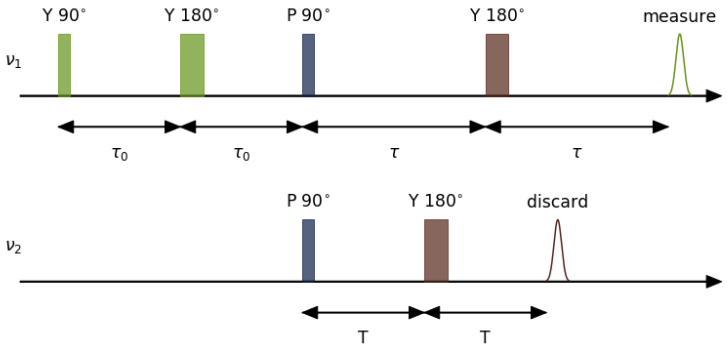


Figure 7.22: A Hahn echo sequence at one frequency followed by full tomography. The "P" pulses are each 3 possibilities - no pulse, X pulse or Y pulse.

The frequencies used were $\nu_1 = 33.705$ GHz, $\nu_2 = 33.77$ GHz, the data were collected using $B_0 = 1.202$ T. The spectrum of the bis-nitroxide sample, obtained from an echo field sweep experiment, with the two frequencies used marked is shown

in Fig. 7.23. It is a typical choice in DEER experiments to use the frequency corresponding to the highest peak of the spectrum as the pump frequency, so this decision was made here as well. The $\frac{\pi}{2}$ pulses and single π pulses were 16 ns long, the double π pulse needed to be longer, at 24 ns, to realize the π rotation at the limit of the amplifier. Note that because $\frac{1}{16\text{ns}} = 62.5$ MHz, and $|\nu_1 - \nu_2| = 65$ MHz, we do expect the bandwidths of the two pulses to overlap, however the main peak of the excitation band of one pulse should correspond to the zero of the other pulse's band, as these are approximately given by sinc functions, see 2.3.5. The DEER oscillation period was fitted to be 165 ± 5 ns for these two frequencies. The time $\tau = 46$ ns was used in the entangling gate, aiming for about a quarter of the oscillation period. Note that 2×46 ns $\times 65$ MHz $= 5.98$, which is close to an integer and it means the systematic phase offset, which at the time was not being corrected, was about $-7°$. For the Hahn echo, the τ should not affect the final state, but it was set to be $\tau = 60$ ns.

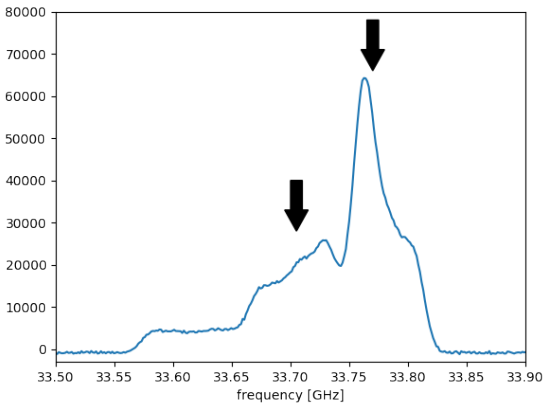


Figure 7.23: Absorption spectrum of the bis-nitroxide sample at $B_0 = 1.202$ T obtained from echo-detected field sweep at frequency 33.77 GHz. The arrows show approximate positions of the frequencies used in the experiment.

The time traces obtained in the Hahn echo tomography experiment were consistent with the predictions, which is not surprising, since several measurements with ν_1 detection are identical to 4-pulse DEER experiments which were earlier used for calibration. Measurements with ν_2, like 2IY, are similar to a 3-pulse DEER with additional pump frequency pulses. What is more, the expected density matrix

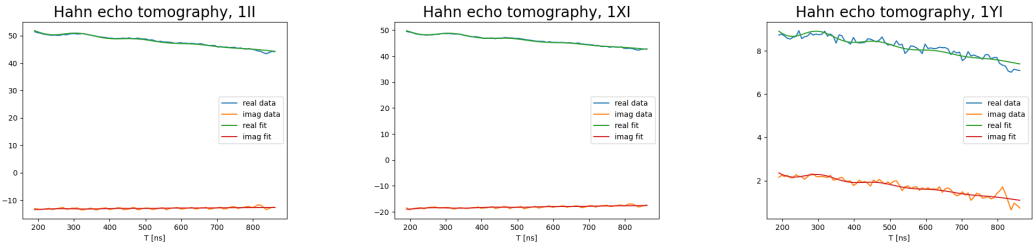


Figure 7.24: Selected time traces from the Hahn echo tomography experiment. Left: 1II, Centre: 1IX, Right: 1IY. In this experiment we expect a real $-\cos(\omega_{ee}T)$ oscillation in the left and centre trace, and no oscillation in the right trace.

component $\langle \hat{S}_x^1 \rangle$ should only influence the results of the measurements with ν_1 detection, and the component $\langle \hat{S}_z^2 \rangle$ only those with ν_2 detection. In the latter case, the phase of the ν_1 $\frac{\pi}{2}$ pulse also should not be relevant, resulting in many measurements which are supposed to and look identical. These time traces are shown in Fig. 7.24. Incorporating the normalization factors, the tomography results are as follows (Fig. 7.25):

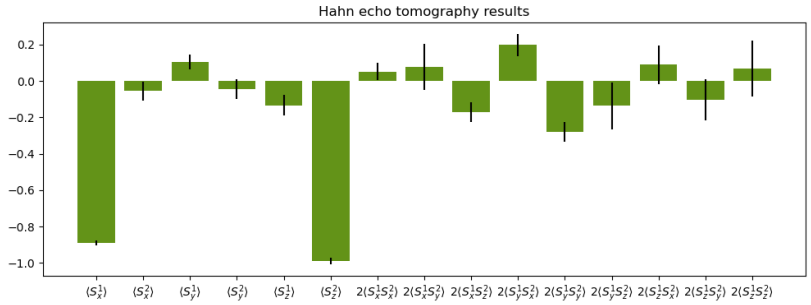


Figure 7.25: Results of the tomography process applied to the to the single Hahn echo in frequency ν_1 at high temperature. For this experiment, the expected result was to measure $-\hat{S}_x^1 - \hat{S}_z^2$, that is, these two operators were expected to be measured as -1, and the rest as 0.

The fidelity (Eq. 7.5) of this result is 0.95. The tomography procedure succeeds to read out this simple density matrix.

Note that all the expected components of the signal in the Hahn echo tomography experiments correspond to cosines in Table 7.1, whereas the components expected in the entangling gate experiment correspond to sines. This means we should be able to directly compare the time traces generated in these two processes, as they should be shifted in oscillation phase by about a quarter of a period, as shown in Fig. 7.26.

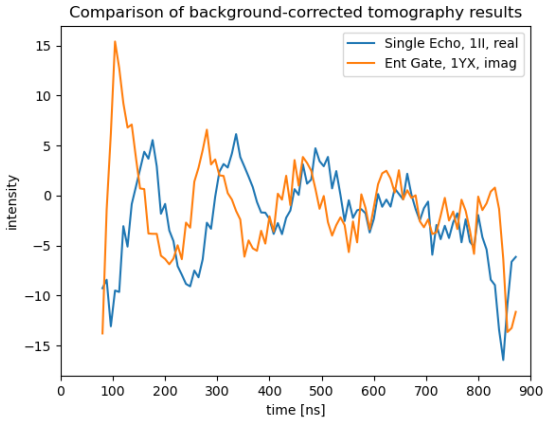


Figure 7.26: Comparison between time traces collected in two tomography experiments. The entangling gate tomography expects all the most significant oscillation traces to be sines, and the Hahn echo tomography expects them all to be cosines. Raw data from the two measurements, collected with otherwise all the parameters fixed, are shifted by about a quarter of a period in respect to each other. The small bumps at the end of traces come from cross-excitation, also seen in the simulation described in 7.5.4.

The time traces obtained in the entangling gate tomography experiment followed the expectations, discussed earlier in detail. For comparison with the simulation, some time traces are shown in Fig. 7.27. The background is significant, and the data are noisy, especially the data collected with detection at ν_2, which exhibit a sawtooth pattern, most likely originating from the AWG or other equipment issues, which were resolved by the time subsequent experiments on this project were conducted. Nevertheless, some of the time traces show clear oscillations, which may be used to recover the final state in the tomography process, shown at the top half of Fig. 7.28.

Most of the coherence is correctly transfered to $2\hat{S}_y^1\hat{S}_z^2$ and $2\hat{S}_z^1\hat{S}_y^2$, with some leaked to $2\hat{S}_x^1\hat{S}_z^2$. We can also see some residing in the single spin orders. The overall fidelity (Eq. 7.5) of these results is 0.9. These results were a good proof of concept of the tomography procedure.

The other set of data was collected with different calibration parameters. A decision has been made to try to make the two frequencies more symmetric in terms of the underlying spectrum and thus the echo intensity. The magnetic field $B_0 = 1.2045$ T, $\nu_1 = 33.84$ GHz and $\nu_2 = 33.775$ GHz, with the same difference 65 MHz. This time, a slightly longer $\tau = 48$ ns was selected. Note that 2×48 ns $\times 65$

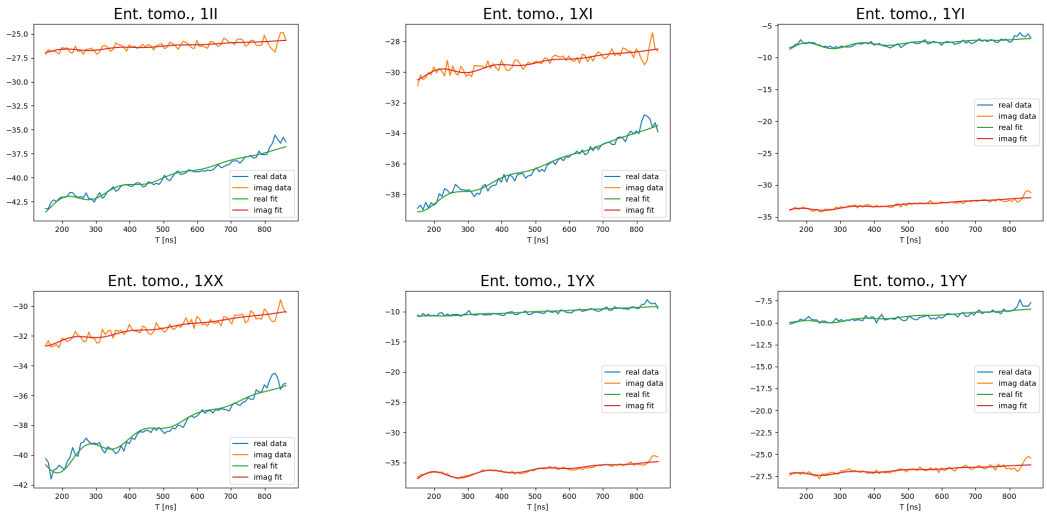


Figure 7.27: Time traces from the entangling gate tomography experiment with the bis-nitroxide sample. Selection is analogous to the one in Fig. 7.17. The real data from this sample has a significantly larger background and is quite noisy, but the oscillations are featured in correct measurements. The fitting process is robust enough to use this data to reconstruct a state, whose angle-fidelity with the expected one is 0.9. The total echo amplitudes are not comparable between the subplots, as it mostly comes from unwanted background, which behaves differently under readout $\frac{\pi}{2}$ pulses. The amplitudes of the oscillations in these time traces are directly comparable. Some background-corrected time traces are shown in Fig. 7.26. The bumps at the end of the traces come from excitation band overlap, as discussed in 7.5.4.

MHz = 6.24, which is far from an integer and thus generated a large phase error in the off-frequency $\frac{\pi}{2}$ pulses. Nevertheless, knowing that, it is possible to extract the density matrix from the data. The durations of the pulses were the same as in the first run, 16 ns for all the pulses but the double π pulse, whose duration was 24 ns. The results are shown in the bottom half of Fig. 7.28.

The fidelity (Eq. 7.5) of these results is 0.92. This time, there is a rotation into $2\hat{S}_z^1\hat{S}_x^2$. These problems are most likely a consequence of ensemble dynamics.

7.6.3 Cr_7Ni ring dimer crystals measurements

An inspiration for this project was a previous experiment involving dimers of molecular ring magnets Cr_7Ni [29], discussed earlier in 3.2. In that system, because of its wide spectrum, a high degree of angular selection, necessary to obtain a robust interaction strength, was possible. However, after selecting such a small part of

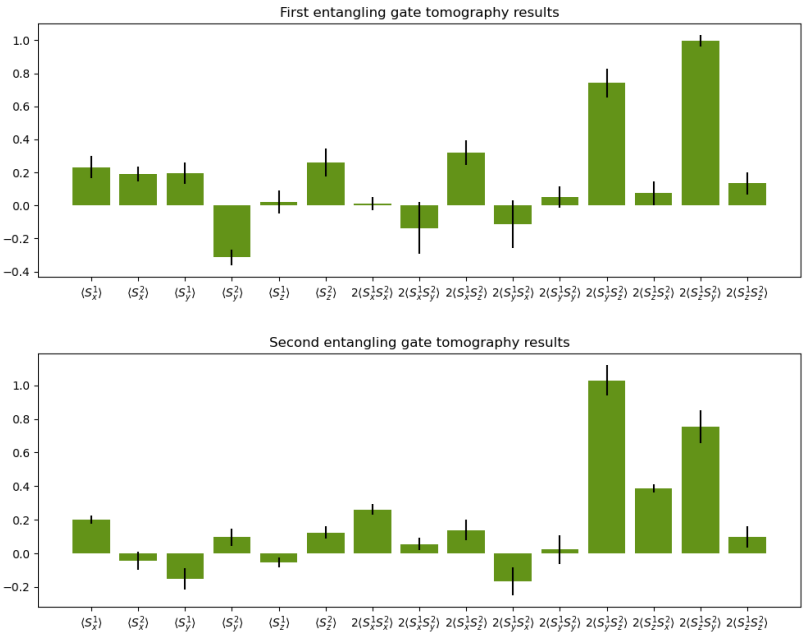


Figure 7.28: Results of the tomography procedure applied to the entangling gate at high temperature. Top: $\tau = 46$ ns, bottom: $\tau = 48$ ns. $\nu_1 - \nu_2 = 65$ MHz in both cases. Both states come close to the expected $2\hat{S}_y^1\hat{S}_z^2 + 2\hat{S}_z^1\hat{S}_y^2$ high temperature state, but there is some rotation to other coefficients due to ensemble dynamics.

the subensemble, the signal become extremely weak and needed multiple hours of averaging. A solution to this are crystals. More specifically, a dimer Cr_7NiF_8 rotaxane molecule embedded in a crystal of diamagnetic Ti_7GaO_8 dimers, at 0.1% concentration to suppress the intermolecular dipolar couplings.

Each dimer consists of two parallel Cr_7Ni rings, connected by a rigid molecular thread, so that the molecule has an approximate axial symmetry. There are two molecules per unit cell of this crystal, rotated by 95°. The intermolecular axes of the two copies of a dimer define a plane. The molecular structure is shown in Fig. 7.29. As confirmed by XRD measurements, the largest face of the macroscopic single crystal roughly corresponds to this plane. The crystals come as small, thin squares, facilitating their orientation in the experiment. For the ESR measurements, a single crystal was mounted at the end of a 1 mm (1.6 mm) diameter glass rod, which was placed inside a 2 mm (3 mm) external diameter sample tube. The B_0 field was in plane of the crystal. The crystal could be rotated so that the magnetic field vector remained in plane, but changed its orientation in respect to

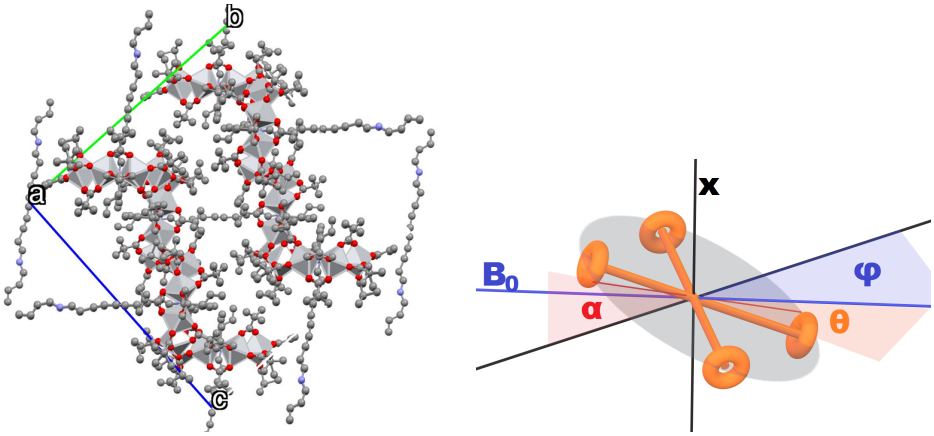


Figure 7.29: The structure of the Cr_7Ni/Ti_7Ga rotaxane crystal. There are two copies of a dimer per unit cell, rotated by 95°. Each dimer consists of two Cr_7Ni rings and a thread. Left: The full molecular enviroment. Right: Schematic of the molecule. The angle φ is the angle that can be controlled in situ by rotating the sample tube once the crystal is mounted. The angle α is the tilt angle between the plane of the two copies of the dimer and the horizontal, z-y plane. The angle θ is the angle between the molecular axis and the B_0 field, which determines the strength of the dipolar coupling. θ can be varied indirectly by varying φ, but its minimum value depends on α.

both inter-molecular axes. A simple mechanical goniometer was used to measure the angle. In practice, this alignment was not perfect; the flat face of the crystal did not exactly correspond to the plane defined by inter-molecular axes, and was later tested through an angle-dependent echo-detected field sweep measurement.

In the case of ideal alignment, we would expect the EFS data to have an approximate 90° symmetry. This would also allow access to interaction strengths $\omega_{ee}(\theta)$ corresponding to $\theta = 0$, where B_0 is parallel to the inter-molecular axis. If the crystal plane is tilted, this position may not be accessible.

In three separate runs the goal was to collect angle-dependent DEER traces, showing angular dependence of the oscillation period, and then perform the tomography experiment. The XRD experiment aiming to orient the crystal was performed at the first run, however the same piece of crystal could not be used in ESR experiments, because the crystals need to stay moist in order to remain crystalline, and the investigated sample dried out. All experiments were conducted using Bruker E580 pulsed spectrometer, with microwave frequencies between 34 GHz to 34.2 GHz and two resonators, a loop-gap QD2 and a rectangular QT2. The temperature was

maintained at 3K using a liquid Helium cryostat. The data presented come from the last experimental run, using the loop-gap resonator and smaller sample sizes.

To test the crystal orientation, angle resolved EFS experiments were performed, in 5° steps, covering the full 0°-360° range. The frequency used was 34.1465 GHz. The data were modelled as coming from two copies of an axially symmetric molecule, at the 95° angle to each other, but tilted from the $z - x$ plane by an angle α and broadening coming from individual differences and unresolved hyperfine coupling. The best fit parameters were $g_{\|} = 1.755$ and $g_{\perp} = 1.787$ and $\alpha = 35° \pm 5°$. This α would also be the smallest possible θ, when the sample is rotated. The EFS data and the fit is shown in Fig. 7.30. Assuming there are 2, 3 or more crystals in the sample, all characterized by the same g-tensors, but at different orientations, does not improve the quality of the fit significantly, despite increasing the number of parameters.

The memory time of this sample was found to be 395 ns with stretch parameter $\chi = 1.26$ according to the Eq. 2.38. This allowed to use $\tau = 600 - 1000$ ns for the DEER experiments.

The aim was to perform DEER experiments at orientations corresponding to $\theta = 0°, 45°, 90°$. The $\theta = 45°$ position should be accessible at the angle where the EFS is the narrowest, as the spectra of both molecules coincide there. Then, the other two should be accessible as the right and left peaks in the spectrum collected 45° away. In this data set, the narrowest spectrum seemed to be the one with $\alpha = 315°$, and the widest spectra were ones corresponding to $\alpha = 285°$ and 350°, so these three were selected for the subsequent measurements. Then, the 4-pulse DEER experiments were conducted at several field positions. A selection of the results is shown in Fig. 7.31.

The DEER data were collected using detection and pump frequencies of 34.12 GHz and 34.2 GHz for first initial experiments, and then 34.12 GHz and 34.185 GHz for later experiments. All the pulses were 16ns long, with π pulses at about 28 % and 38 % of power, what would allow the double pulses needed for the entangling gate to be produced. The data presented in Fig 7.31 are only the 4-pulse DEER

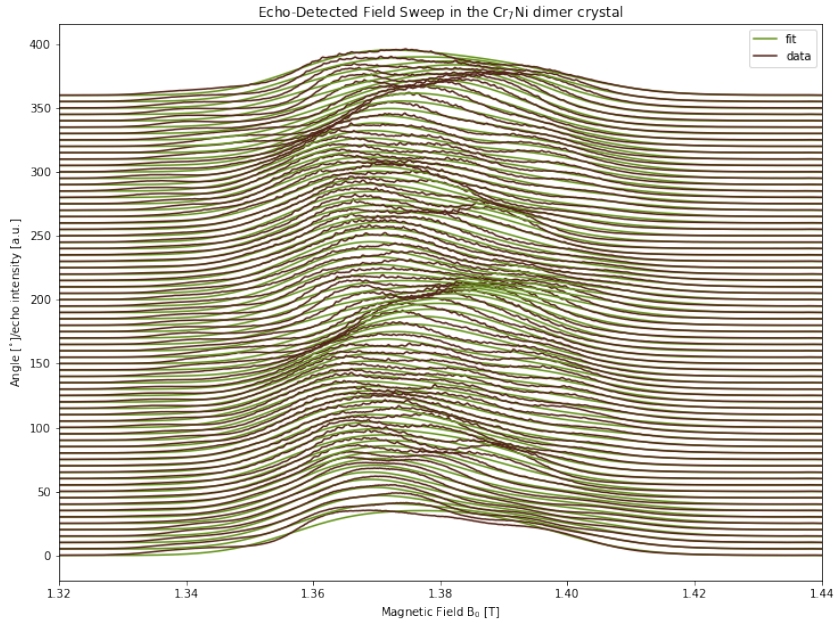


Figure 7.30: Angle-resolved echo-detected field sweep data collected from the Cr_7Ni dimer system, together with a global fit. Each trace corresponds to the angle denoted at the y-axis. All the data were fitted together, assuming they come from the same crystal system, rotated as indicated. The data have clear 180° period, which is just a consequence of the g-tensor symmetry, but their expected 95° symmetry is much weaker, suggesting the two copies of the dimer are not in-plane. The best fit parameter for the tilt angle is $35° \pm 5°$.

traces. Some 3-pulse DEER traces were also collected, but they have no oscillation visible. All the data sets were τ-averaged [45, 46], varying the τ parameter with 8 steps of 4 ns to, as discussed in 5.4, remove contribution of unwanted interactions.

An analysis of angularly selective DEER data may be as simple as fitting a cosine and a background function to the data (7.5.3). For the later tomography experiment to be successful, the 3-pulse DEER data needs to exhibit such an oscillation, because the tomography $\frac{\pi}{2}$ pulses are placed at the position of the first 3-pulse DEER pulse. Even though there is some oscillation in the 4-pulse DEER data sets, Fourier transforming the time traces that exhibit it, namely 285° at 1363 mT and 1355 mT, 315° at 1355 mT and 350° at 1378.1 mT, reveals the oscillation is all of the same frequency, around 18 MHz, what suggests it actually comes from proton ESEEM present in the system [29]. Unfortunately, the corresponding 3-pulse

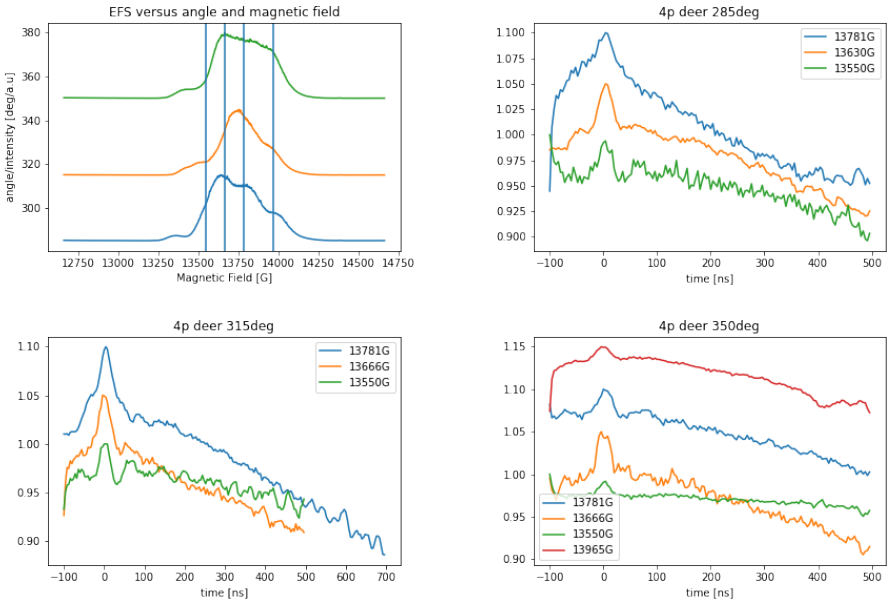


Figure 7.31: Selected results of the DEER experiment on the Cr_7Ni dimer crystal. Top left: EFS spectra at angle positions where DEER measurements were performed, with 4 field positions marked. Others: DEER measurements conducted at each rotation angle. Different colours correspond to different field positions, same colours correspond to the same field positions. The field positions are marked in the top left EFS spectra for comparison.

DEER traces are flat, so they cannot be used as a tomography tool.

There are clear differences in the data sets collected at the same field positions but different angles, confirming the sample was a crystal. The zero-point peaks in the 4-pulse DEER data have similar height and width within in the data collected at different field positions, but the same angle, than ones collected at same field positions and different angles. However it is easy to overfit the models to these data. Most of DEER analysis software, including neural nets [164], are used to fit data that is angularly nonselective and the results gained from those are unphysical.

In the 2015 DEER experiment with Cr_7Ni dimers [29], the oscillation with highest modulation came from the low field DEER, corresponding to molecules parallel to B_0. It seems like we were not able to access these orientations in any of the three measurements of this crystal. In a powder solution, this orientation was possible to be selected by adjusting the field or frequency, however the signal to noise ratio would be too low for the tomography to be possible. Working with

a crystal, one may completely lock oneself out of accessing it, if the sample is not mounted perfectly. The pandemic situation has made it challenging to collect data, and the project involving these crystals has been passed to our collaborators now.

7.7 Future directions

In this chapter we have explored a type of an entangling gate and the tomography sequence that may be used in specific conditions to recover a density matrix of the state directly preceding it. We have established that to succesfully perform this experiment, we need a spin-$\frac{1}{2}$ dimer sample, with a selectable subpopulation where each spin is addressable by pulses of separate frequency, Spin 1 by ν_1 and Spin 2 by ν_2. This implies that the pulse durations t_{pulse} used have to be longer than $\frac{1}{|\nu_1-\nu_2|}$. The coupling strengths $\omega_{ee}(\theta)$ in this subpopulation should be as uniform as possible, which may be achieved by specialized selection in a powder of dipolarly coupled dimers, or by synthesis of a crystal. These couplings need to be weak enough so that the gate is possible to be implemented, namely, the pulse duration $d < 0.2\frac{\pi}{\omega_{ee}}$. In typical conditions, this would correspond to dipolar coupling at a distance of at least 2.5 nm between the spins. A high modulation, angularly selective DEER experiment needs to be possible to be performed, with several peaks and troughs before the signal to noise ratio renders the experiment impossible due to relaxation.

If all the above conditions are satisfied, the gate may be implemented according to the sequence shown in Fig. 7.1, with the distance between pulses adjusted by about half of the pulse duration for the optimal entangling gate, and the full deviation density matrix tomography may be used to confirm the successful implementation. Overall, this experiment is challenging, but definitely possible.

Our collaborators in Manchester, Edmund Little and Dr Alice Bowen, continue working on this project, utilizing the new nitroxide dimers similar to the one investigated, but with longer inter-spin distance of about 3nm, synthesized by Ciaran Rogers, resulting in a weaker interaction. New Cr_7Ni dimers and crystals are synthesized by Dr Grigore Timco to be utilized in future research in this area.

Appendices

A
Tables

Contents

A.1 Extended Stevens Operators 159
A.2 Simulation parameters for isotropic coupled entangling gate tomography 159

This Appendix contains several Tables of data and parameters that did not fit in the main text.

A.1 Extended Stevens Operators

A.2 Simulation parameters for isotropic coupled entangling gate tomography

k	q	$\hat{O}_k^q$
2	0	$3\hat{S}_z^2 + s\mathbb{1}$
	±1	$\frac{c_\pm}{2}\left\{\hat{S}_z, \hat{S}_+ \pm \hat{S}_-\right\}$
	±2	$c_\pm\left(\hat{S}_+^2 \pm \hat{S}_-^2\right)$
4	0	$35\hat{S}_z^4 - (30s-25)\hat{S}_z^2 + (3s^2-6s)\mathbb{1}$
	±1	$\frac{c_\pm}{2}\left\{7\hat{S}_z^3 - (3s+1)\hat{S}_z, \hat{S}_+ \pm \hat{S}_-\right\}$
	±2	$\frac{c_\pm}{2}\left\{7\hat{S}_z^2 - (s+5)\mathbb{1}, \hat{S}_+^2 \pm \hat{S}_-^2\right\}$
	±3	$\frac{c_\pm}{2}\left\{\hat{S}_z, \hat{S}_+^3 \pm \hat{S}_-^3\right\}$
	±4	$c_\pm\left(\hat{S}_+^4 \pm \hat{S}_-^4\right)$
6	0	$213\hat{S}_z^6 - (315s-735)\hat{S}_z^4 + (105s^2-525s+294)\hat{S}_z^2 - (5s^3-40s^2+60s)\mathbb{1}$
	±1	$\frac{c_\pm}{2}\left\{33\hat{S}_z^5 - (30s-15)\hat{S}_z^3 + (5s^2-10s+12)\hat{S}_z, \hat{S}_+ \pm \hat{S}_-\right\}$
	±2	$\frac{c_\pm}{2}\left\{33\hat{S}_z^4 - (18s+123)\hat{S}_z^2 + (s^2+10s+102)\mathbb{1}, \hat{S}_+^2 \pm \hat{S}_-^2\right\}$
	±3	$\frac{c_\pm}{2}\left\{11\hat{S}_z^3 - (3s+59)\hat{S}_z, \hat{S}_+^3 \pm \hat{S}_-^3\right\}$
	±4	$\frac{c_\pm}{2}\left\{11\hat{S}_z^2 - (s+38)\mathbb{1}, \hat{S}_+^4 \pm \hat{S}_-^4\right\}$
	±5	$\frac{c_\pm}{2}\left\{\hat{S}_z, \hat{S}_+^5 \pm \hat{S}_-^5\right\}$
	±6	$c_\pm\left(\hat{S}_+^6 \pm \hat{S}_-^6\right)$

Table A.1: Extended Stevens Operators for $k = 2, 4, 6$. The curly braces $\left\{\hat{A}, \hat{B}\right\}$ denote an anticommutator $\hat{A}\hat{B} + \hat{B}\hat{A}$, $c_+ = 1/2, c_- = 1/2i$ and $s = S(S+1)$. The superscript at the spin operators $\hat{S}_z, \hat{S}_+, \hat{S}_-$ is an exponent in this context.

n	J [kHz]	g_1^1	g_2^1	g_3^1	α^1	β^1	γ^1	g_1^2	g_2^2	g_3^2	α^2	β^2	γ^2	ν_1	ν_2
1	2	2.127	2.123	2.135	30	0	120	2.017	2.013	2.025	30	0	120	9.748	10.28
2	2	2.125	2.123	2.135	30	0	150	2.011	2.013	2.001	30	0	150	9.702	10.276
3	2	2.105	2.123	2.135	45	75	155	2.05	2.013	2.001	30	0	150	9.724	10.252
4	2	2.075	2.08	2.086	0	20	20	2.05	2.054	2.066	0	10	30	9.93	10.047
5	2	2.065	2.08	2.096	0	20	40	2.04	2.051	2.066	0	10	120	9.908	10.048
6	6000	2.075	2.08	2.086	0	20	20	2.05	2.054	2.066	0	10	30	9.93	10.047
7	6000	2.125	2.123	2.135	30	0	150	2.011	2.013	2.001	30	0	150	9.702	10.276
8	6000	2.127	2.123	2.135	30	0	120	2.017	2.013	2.025	30	0	120	9.729	10.262
9	3000	2.075	2.08	2.086	0	20	20	2.05	2.054	2.066	0	10	30	9.93	10.047
10	3000	2.125	2.123	2.135	30	0	150	2.011	2.013	2.001	30	0	150	9.702	10.276
11	3000	2.127	2.123	2.135	30	0	120	2.017	2.013	2.025	30	0	120	9.748	10.28
12	3000	2.022	2.012	1.987	0	0	0	2.022	2.012	1.987	90	90	90	9.625	9.722

Table A.2: Parameters used in Spinach simulations of exchange coupled dimers. Listed are the g-tensor principal values g_1, g_2, g_3 for each spin and the corresponding Euler angles α, β, γ, as well as the coupling strength J and the two frequencies used ν_1 and ν_2.

B

Miscellaneous topics in ESR tomography

Contents

B.1 Examples of the NMR and ESR tomography 161
B.1.1 General comments 161
B.1.2 Pure state $|{+}{+}\rangle$ 164
B.1.3 Pure Bell state $\frac{1}{\sqrt{2}}(|00\rangle + |11\rangle)$ 167
B.1.4 Entangling the thermal state 170
B.2 Variable phase tomography equations 173
B.2.1 Evolution equations with variable phase pulses 173
B.2.2 Systematic phase error tomography 174
B.3 Least squares fitting of the parameters in the tomography procedure 175

B.1 Examples of the NMR and ESR tomography

This section contains several fully worked through examples of NMR and ESR tomography, applied to pure and mixed states.

B.1.1 General comments

As the only difference between the NMR and my ESR tomography procedures is the way the 8 spin orders used to reconstruct the density matrix are detected, each worked example will follow the common part of the two procedures before

they diverge, and then the two detection cases will be treated separately. The procedures applied are the same, regardless of the state at the beginning, because the tomography is supposed to detect the state so it should not depend on what it is. This also means the worked examples in this appendix will be extremely similar to one another and the reader who need not be convinced that the tomography procedure is correct, may want to skip some of them.

Generally, the tomography procedure can only detect the traceless part of the density matrix, the deviation density matrix. It also operates explicitly on the product operator basis in the Liouville space. A pure state $|\psi\rangle$ or mixed state ρ expressed as a Hilbert space density matrix should first be translated to this basis by calculating quantum expectation values of each product operator. When all 15 of these expectation values are calculated, they provide the full description of the state, no information is lost at this stage. For each product operator, we calculate:

$$\langle\hat{O}\rangle = \langle\psi|\,\hat{O}\,|\psi\rangle = \mathrm{tr}\left(\hat{O}\,|\psi\rangle\,\langle\psi|\right) = \mathrm{tr}\left(\hat{O}\rho\right) \tag{B.1}$$

And then we write:

$$\rho = \frac{1}{4}\mathbb{1} + \sum_{\text{prodops}} \langle\hat{O}\rangle\hat{O} \tag{B.2}$$

Which is guaranteed because product operators are normalized to be orthonormal.

The first step of the tomography is the application of $\frac{\pi}{2}$ pulses of various phases, to modify the state. An ideal X pulse at frequency ν_1 acts on the density matrix as $\exp\left(-i\hat{S}^1_x\frac{\pi}{2}\right)\hat{\rho}\exp\left(i\hat{S}^1_x\frac{\pi}{2}\right)$. Analogously, a Y pulse at frequency ν_1 uses the $\hat{S}^1_y$ operator instead. The X and Y pulses at frequency ν_2 use $\hat{S}^2_x$ and $\hat{S}^2_y$ operators respectively. Of course, we are making an assumption here each pulse only interacts with one end of the dimer. Due to this assumption, we can assume the pulses sent at different frequencies commute and consider their action in any order. The state we are trying to recover is already expressed in terms of product operators, so we can use the Eq. 2.21 to find out how each term in it evolves. It simplifies to just the commutator $-i\left[\hat{B},\hat{A}\right]$, because $\phi = \frac{\pi}{2}$. As $-i\left[\hat{S}^1_x,\hat{S}^1_y\right] = \hat{S}^1_z$, $-i\left[\hat{S}^1_y,\hat{S}^1_z\right] = \hat{S}^1_x$ and $-i\left[\hat{S}^1_z,\hat{S}^1_x\right] = \hat{S}^1_y$, we find that:

1. Under $\frac{\pi}{2}$ X pulse: $\hat{S}_x \to \hat{S}_x, \hat{S}_y \to -\hat{S}_z, \hat{S}_z \to \hat{S}_y$

2. Under $\frac{\pi}{2}$ Y pulse: $\hat{S}_x \to \hat{S}_z, \hat{S}_y \to \hat{S}_y, \hat{S}_z \to -\hat{S}_x$

In the NMR tomography, the product operators $\hat{S}^1_x, \hat{S}^1_y, \hat{S}^2_x, \hat{S}^2_y, 2\hat{S}^1_y\hat{S}^2_z, 2\hat{S}^1_x\hat{S}^2_z, 2\hat{S}^1_z\hat{S}^2_y, 2\hat{S}^1_z\hat{S}^2_x$ can be measured directly. In the Fourier transformed signal collected after the pulses, we are expecting to see up to 4 peaks, their positions given by $\nu_1 - \frac{1}{2}J$, $\nu_1 + \frac{1}{2}J$, $\nu_2 - \frac{1}{2}J$, $\nu_2 - \frac{1}{2}J$, where J is the exchange coupling. Typically $J \ll \nu_1, \nu_2$, so the peaks are grouped into pairs, or doublets. Each peak will also have a real and imaginary component. The real channel corresponds to $\hat{S}_x$ observables. The amplitudes of each peak correspond to some combination of one inphase and one antiphase term, as detailed in Table B.1.

operator	1r	1i	2r	2i	3r	3i	4r	4i
$\hat{S}^1_x$	1	0	1	0	0	0	0	0
$\hat{S}^1_y$	0	1	0	1	0	0	0	0
$\hat{S}^2_x$	0	0	0	0	1	0	1	0
$\hat{S}^2_y$	0	0	0	0	0	1	0	1
$2\hat{S}^1_x\hat{S}^2_z$	1	0	-1	0	0	0	0	0
$2\hat{S}^1_y\hat{S}^2_z$	0	1	0	-1	0	0	0	0
$2\hat{S}^1_z\hat{S}^2_x$	0	0	0	0	1	0	-1	0
$2\hat{S}^1_z\hat{S}^2_y$	0	0	0	0	0	1	0	-1

Table B.1: Peak amplitudes corresponding to unit inphase and antiphase single quantum coherences in NMR tomography procedure. The number in the top row corresponds to the peak number in the Fourier Transform of the data, from low to high frequency. The letters "r" and "i" denote real and imaginary components of these peaks respectively. Other tables in this Appendix follow this convention.

In the ESR DEER-based tomography, these 8 single quantum coherence terms generate the following oscillating signals in the echo detected trace, dependent on the T parameter:

- $\hat{S}^1_x$ - real cosine in ν_1 detection measurements
- $\hat{S}^1_y$ - imaginary cosine in ν_1 detection measurements
- $\hat{S}^2_x$ - real cosine in ν_2 detection measurements

- $\hat{S}_y^1$ - imaginary cosine in ν_2 detection measurements
- $2\hat{S}_y^1\hat{S}_z^2$ - real sine in ν_1 detection measurements
- $2\hat{S}_x^1\hat{S}_z^2$ - imaginary sine in ν_1 detection measurements
- $2\hat{S}_z^1\hat{S}_y^2$ - real sine in ν_2 detection measurements
- $2\hat{S}_z^1\hat{S}_x^2$ - imaginary sine in ν_2 detection measurements

Note that the antiphase coherence $2\hat{S}_x^1\hat{S}_z^2$ in ESR DEER tomography manifests itself through the inphase coherence $\hat{S}_y^1$ it evolves into under the $\omega_{ee}\hat{S}_z^1\hat{S}_z^2$ term in the Hamiltonian, so it is seen in the imaginary channel, but in NMR it is seen together with $\hat{S}_x^1$ in the real channel. Other antiphase coherences are similarly switched.

B.1.2 Pure state $|{+}{+}\rangle$

The state $|{+}{+}\rangle$ is not entangled and corresponds to both spins in a $|{+}\rangle = \frac{1}{\sqrt{2}}(|0\rangle + |1\rangle) = \frac{1}{\sqrt{2}}(|\uparrow\rangle + |\downarrow\rangle)$ state. The product operator density matrix expansion of this state is simple to calculate, because it is a fully separable, pure state, so expectations of tensor products of operators acting on opposite spins are products of expectation values of constituent operators. For example, we have $\langle 2\hat{S}_x^1\hat{S}_x^2\rangle = 2\langle\hat{S}_x^1\rangle \times \langle\hat{S}_x^2\rangle$. This is not true for the entangled states.

Thus

$$\langle\hat{S}_x^1\rangle = \langle{+}{+}|\,\hat{S}_x^1\,|{+}{+}\rangle = \frac{1}{2}\langle{+}{+}|{+}{+}\rangle = \frac{1}{2} \tag{B.3}$$

As $|{+}{+}\rangle$ is an eigenstate of $\hat{S}_x^1$ with eigenvalue $\frac{1}{2}$. But:

$$\begin{aligned}\langle\hat{S}_y^1\rangle &= \langle{+}{+}|\,\hat{S}_y^1\,|{+}{+}\rangle = -i\frac{1}{2}\langle{+}{+}|{-}{+}\rangle = 0\\ \langle\hat{S}_z^1\rangle &= \langle{+}{+}|\,\hat{S}_z^1\,|{+}{+}\rangle = \frac{1}{2}\langle{+}{+}|{-}{+}\rangle = 0\end{aligned} \tag{B.4}$$

Analogously:

$$\begin{aligned}\langle\hat{S}_x^2\rangle &= \langle{+}{+}|\,\hat{S}_x^2\,|{+}{+}\rangle = \frac{1}{2}\langle{+}{+}|{+}{+}\rangle = \frac{1}{2}\\ \langle\hat{S}_y^2\rangle &= \langle{+}{+}|\,\hat{S}_y^2\,|{+}{+}\rangle = -i\frac{1}{2}\langle{+}{+}|{+}{-}\rangle = 0\\ \langle\hat{S}_z^2\rangle &= \langle{+}{+}|\,\hat{S}_z^2\,|{+}{+}\rangle = \frac{1}{2}\langle{+}{+}|{+}{-}\rangle = 0\end{aligned} \tag{B.5}$$

Thus the only double spin order with a non-zero coefficient is $2\hat{S}_x^1\hat{S}_x^2$, with a coefficient of $2 \times \frac{1}{2} \times \frac{1}{2} = \frac{1}{2}$. The density matrix for this state can be expressed as

$$|{+}{+}\rangle\langle{+}{+}| = \frac{1}{4}\mathbb{1} + \frac{1}{2}\hat{S}_x^1 + \frac{1}{2}\hat{S}_x^2 + \hat{S}_x^1\hat{S}_x^2 \tag{B.6}$$

The tomography procedure will be able to recover the $\frac{1}{2}\hat{S}_x^1 + \frac{1}{2}\hat{S}_x^2 + \hat{S}_x^1\hat{S}_x^2$ part, up to a proportionality constant.

Let us calculate the state after each of the 9 possible pairs of pulses:

pulses	state after	1r	1i	2r	2i	3r	3i	4r	4i
II	$\frac{1}{2}\hat{S}_x^1 + \frac{1}{2}\hat{S}_x^2 + \hat{S}_x^1\hat{S}_x^2$	$\frac{1}{2}$	0	$\frac{1}{2}$	0	$\frac{1}{2}$	0	$\frac{1}{2}$	0
IX	$\frac{1}{2}\hat{S}_x^1 + \frac{1}{2}\hat{S}_x^2 + \hat{S}_x^1\hat{S}_x^2$	$\frac{1}{2}$	0	$\frac{1}{2}$	0	$\frac{1}{2}$	0	$\frac{1}{2}$	0
IY	$\frac{1}{2}\hat{S}_x^1 + \frac{1}{2}\hat{S}_z^2 + \hat{S}_x^1\hat{S}_z^2$	1	0	0	0	0	0	0	0
XI	$\frac{1}{2}\hat{S}_x^1 + \frac{1}{2}\hat{S}_x^2 + \hat{S}_x^1\hat{S}_x^2$	$\frac{1}{2}$	0	$\frac{1}{2}$	0	$\frac{1}{2}$	0	$\frac{1}{2}$	0
XX	$\frac{1}{2}\hat{S}_x^1 + \frac{1}{2}\hat{S}_x^2 + \hat{S}_x^1\hat{S}_x^2$	$\frac{1}{2}$	0	$\frac{1}{2}$	0	$\frac{1}{2}$	0	$\frac{1}{2}$	0
XY	$\frac{1}{2}\hat{S}_x^1 + \frac{1}{2}\hat{S}_z^2 + \hat{S}_x^1\hat{S}_z^2$	1	0	0	0	0	0	0	0
YI	$\frac{1}{2}\hat{S}_z^1 + \frac{1}{2}\hat{S}_x^2 + \hat{S}_z^1\hat{S}_x^2$	0	0	0	0	1	0	0	0
YX	$\frac{1}{2}\hat{S}_z^1 + \frac{1}{2}\hat{S}_x^2 + \hat{S}_z^1\hat{S}_x^2$	0	0	0	0	1	0	0	0
YY	$\frac{1}{2}\hat{S}_z^1 + \frac{1}{2}\hat{S}_z^2 + \hat{S}_z^1\hat{S}_z^2$	0	0	0	0	0	0	0	0

Table B.2: Density matrix of the state after the two initial pulses and the peak amplitudes in each NMR tomography measurement, applied to a pure $|{+}{+}\rangle$ state.

Because the X pulses do not modify this particular state, many of the measurements here will look identical. In the NMR tomography, the FID signal is collected just after these pulses and Fourier transformed. In measurements II, IX, XI, XX we expect to see the in-phase, real doublets at both ν_1 and ν_2, so four real, positive peaks. In measurements IY, XY, the antiphase doublet generated by $2\hat{S}_x^1\hat{S}_z^2$ cancels at the second peak with the inphase doublet at ν_1, and the other frequency peaks do not appear. The same effect, but at ν_2, occurs in measurements YI and YX. Finally, we expect to see nothing in measurement YY.

In ESR DEER - based tomography, we are measuring the same observables, but through different means. Because of the usage of the DEER sequence, the experiment becomes asymmetric and needs to be performed twice as many times. The first symbol denotes the detection frequency, only the product operators

associated with that frequency can be read out. The state after the pulses, but before the DEER sequence, is the same as in the NMR case.

The Table B.3 below shows the expected signal measured in each of the 18 measurements. The $\hat{S}_x^1$ coherence translates into a real cosine signal in 6 measurements, and the $2\hat{S}_x^1\hat{S}_z^2$ generates an imaginary sine signal in 2 measurements. The echo inversion adds a minus sign to it. We can also detail what conclusions

measurement	state after pulses	real channel	imaginary channel
1II	$\frac{1}{2}\hat{S}_x^1 + \frac{1}{2}\hat{S}_x^2 + \hat{S}_x^1\hat{S}_x^2$	$-\cos(\omega_{ee}T)$	no oscillation
1IX	$\frac{1}{2}\hat{S}_x^1 + \frac{1}{2}\hat{S}_x^2 + \hat{S}_x^1\hat{S}_x^2$	$-\cos(\omega_{ee}T)$	no oscillation
1IY	$\frac{1}{2}\hat{S}_x^1 + \frac{1}{2}\hat{S}_z^2 + \hat{S}_x^1\hat{S}_z^2$	$-\cos(\omega_{ee}T)$	$-\sin(\omega_{ee}T)$
1XI	$\frac{1}{2}\hat{S}_x^1 + \frac{1}{2}\hat{S}_x^2 + \hat{S}_x^1\hat{S}_x^2$	$-\cos(\omega_{ee}T)$	no oscillation
1XX	$\frac{1}{2}\hat{S}_x^1 + \frac{1}{2}\hat{S}_x^2 + \hat{S}_x^1\hat{S}_x^2$	$-\cos(\omega_{ee}T)$	no oscillation
1XY	$\frac{1}{2}\hat{S}_x^1 + \frac{1}{2}\hat{S}_z^2 + \hat{S}_x^1\hat{S}_z^2$	$-\cos(\omega_{ee}T)$	$-\sin(\omega_{ee}T)$
1YI	$\frac{1}{2}\hat{S}_z^1 + \frac{1}{2}\hat{S}_x^2 + \hat{S}_z^1\hat{S}_x^2$	no oscillation	no oscillation
1YX	$\frac{1}{2}\hat{S}_z^1 + \frac{1}{2}\hat{S}_x^2 + \hat{S}_z^1\hat{S}_x^2$	no oscillation	no oscillation
1YY	$\frac{1}{2}\hat{S}_z^1 + \frac{1}{2}\hat{S}_z^2 + \hat{S}_z^1\hat{S}_z^2$	no oscillation	no oscillation
2II	$\frac{1}{2}\hat{S}_x^1 + \frac{1}{2}\hat{S}_x^2 + \hat{S}_x^1\hat{S}_x^2$	$-\cos(\omega_{ee}T)$	no oscillation
2IX	$\frac{1}{2}\hat{S}_x^1 + \frac{1}{2}\hat{S}_x^2 + \hat{S}_x^1\hat{S}_x^2$	$-\cos(\omega_{ee}T)$	no oscillation
2IY	$\frac{1}{2}\hat{S}_x^1 + \frac{1}{2}\hat{S}_z^2 + \hat{S}_x^1\hat{S}_z^2$	no oscillation	no oscillation
2XI	$\frac{1}{2}\hat{S}_x^1 + \frac{1}{2}\hat{S}_x^2 + \hat{S}_x^1\hat{S}_x^2$	$-\cos(\omega_{ee}T)$	no oscillation
2XX	$\frac{1}{2}\hat{S}_x^1 + \frac{1}{2}\hat{S}_x^2 + \hat{S}_x^1\hat{S}_x^2$	$-\cos(\omega_{ee}T)$	no oscillation
2XY	$\frac{1}{2}\hat{S}_x^1 + \frac{1}{2}\hat{S}_z^2 + \hat{S}_x^1\hat{S}_z^2$	no oscillation	no oscillation
2YI	$\frac{1}{2}\hat{S}_z^1 + \frac{1}{2}\hat{S}_x^2 + \hat{S}_z^1\hat{S}_x^2$	$-\cos(\omega_{ee}T)$	$-\sin(\omega_{ee}T)$
2YX	$\frac{1}{2}\hat{S}_z^1 + \frac{1}{2}\hat{S}_x^2 + \hat{S}_z^1\hat{S}_x^2$	$-\cos(\omega_{ee}T)$	$-\sin(\omega_{ee}T)$
2YY	$\frac{1}{2}\hat{S}_z^1 + \frac{1}{2}\hat{S}_z^2 + \hat{S}_z^1\hat{S}_z^2$	no oscillation	no oscillation

Table B.3: Expected signal in each measurement of the tomography procedure, if applied to the state $|{+}{+}\rangle$

about the initial state would be drawn from each measurement, if it was perfect. We use the Table 7.1 for that purpose.

- 1II $\langle\hat{S}_x^1\rangle = \frac{1}{2}, \langle\hat{S}_y^1\rangle = 0, 2\langle\hat{S}_y^1\hat{S}_z^2\rangle = 0, 2\langle\hat{S}_x^1\hat{S}_z^2\rangle = 0$
- 1IX $\langle\hat{S}_x^1\rangle = \frac{1}{2}, \langle\hat{S}_y^1\rangle = 0, 2\langle\hat{S}_y^1\hat{S}_y^2\rangle = 0, 2\langle\hat{S}_x^1\hat{S}_y^2\rangle = 0$
- 1IY $\langle\hat{S}_x^1\rangle = \frac{1}{2}, \langle\hat{S}_y^1\rangle = 0, 2\langle\hat{S}_y^1\hat{S}_x^2\rangle = 0, 2\langle\hat{S}_x^1\hat{S}_x^2\rangle = \frac{1}{2}$
- 1XI $\langle\hat{S}_x^1\rangle = \frac{1}{2}, \langle\hat{S}_z^1\rangle = 0, 2\langle\hat{S}_z^1\hat{S}_z^2\rangle = 0, 2\langle\hat{S}_x^1\hat{S}_z^2\rangle = 0$

- 1XX $\langle\hat{S}_x^1\rangle = \frac{1}{2}, \langle\hat{S}_z^1\rangle = 0, 2\langle\hat{S}_z^1\hat{S}_y^2\rangle = 0, 2\langle\hat{S}_x^1\hat{S}_y^2\rangle = 0$
- 1XY $\langle\hat{S}_x^1\rangle = \frac{1}{2}, \langle\hat{S}_z^1\rangle = 0, 2\langle\hat{S}_z^1\hat{S}_x^2\rangle = 0, 2\langle\hat{S}_x^1\hat{S}_x^2\rangle = \frac{1}{2}$
- 1YI $\langle\hat{S}_z^1\rangle = 0, \langle\hat{S}_y^1\rangle = 0, 2\langle\hat{S}_y^1\hat{S}_z^2\rangle = 0, 2\langle\hat{S}_z^1\hat{S}_z^2\rangle = 0$
- 1YX $\langle\hat{S}_z^1\rangle = 0, \langle\hat{S}_y^1\rangle = 0, 2\langle\hat{S}_y^1\hat{S}_y^2\rangle = 0, 2\langle\hat{S}_z^1\hat{S}_y^2\rangle = 0$
- 1YY $\langle\hat{S}_z^1\rangle = 0, \langle\hat{S}_y^1\rangle = 0, 2\langle\hat{S}_y^1\hat{S}_x^2\rangle = 0, 2\langle\hat{S}_z^1\hat{S}_x^2\rangle = 0$
- 2II $\langle\hat{S}_x^2\rangle = \frac{1}{2}, \langle\hat{S}_y^2\rangle = 0, 2\langle\hat{S}_z^1\hat{S}_y^2\rangle = 0, 2\langle\hat{S}_z^1\hat{S}_x^2\rangle = 0$
- 2IX $\langle\hat{S}_x^2\rangle = \frac{1}{2}, \langle\hat{S}_z^2\rangle = 0, 2\langle\hat{S}_z^1\hat{S}_z^2\rangle = 0, 2\langle\hat{S}_z^1\hat{S}_x^2\rangle = 0$
- 2IY $\langle\hat{S}_z^2\rangle = 0, \langle\hat{S}_y^2\rangle = 0, 2\langle\hat{S}_z^1\hat{S}_y^2\rangle = 0, 2\langle\hat{S}_z^1\hat{S}_z^2\rangle = 0$
- 2XI $\langle\hat{S}_x^2\rangle = \frac{1}{2}, \langle\hat{S}_y^2\rangle = 0, 2\langle\hat{S}_y^1\hat{S}_y^2\rangle = 0, 2\langle\hat{S}_y^1\hat{S}_x^2\rangle = 0$
- 2XX $\langle\hat{S}_x^2\rangle = \frac{1}{2}, \langle\hat{S}_z^2\rangle = 0, 2\langle\hat{S}_y^1\hat{S}_z^2\rangle = 0, 2\langle\hat{S}_y^1\hat{S}_x^2\rangle = 0$
- 2XY $\langle\hat{S}_z^2\rangle = 0, \langle\hat{S}_y^2\rangle = 0, 2\langle\hat{S}_y^1\hat{S}_y^2\rangle = 0, 2\langle\hat{S}_y^1\hat{S}_z^2\rangle = 0$
- 2YI $\langle\hat{S}_x^2\rangle = \frac{1}{2}, \langle\hat{S}_y^2\rangle = 0, 2\langle\hat{S}_x^1\hat{S}_y^2\rangle = 0, 2\langle\hat{S}_x^1\hat{S}_x^2\rangle = \frac{1}{2}$
- 2YX $\langle\hat{S}_x^2\rangle = \frac{1}{2}, \langle\hat{S}_z^2\rangle = 0, 2\langle\hat{S}_x^1\hat{S}_z^2\rangle = 0, 2\langle\hat{S}_x^1\hat{S}_x^2\rangle = \frac{1}{2}$
- 2YY $\langle\hat{S}_z^2\rangle = 0, \langle\hat{S}_y^2\rangle = 0, 2\langle\hat{S}_x^1\hat{S}_y^2\rangle = 0, 2\langle\hat{S}_x^1\hat{S}_z^2\rangle = 0$

Thus we recover the state we started with, $\frac{1}{2}\hat{S}_x^1 + \frac{1}{2}\hat{S}_x^2 + \hat{S}_x^1\hat{S}_x^2$, in practice up to a proportionality factor.

B.1.3 Pure Bell state $\frac{1}{\sqrt{2}}(|00\rangle + |11\rangle)$

Let us compare this to a pure entangled state, like a $\frac{1}{\sqrt{2}}(|00\rangle + |11\rangle)$.

After an analogous calculation, left as an exercise, we find that the density matrix for this state can be expressed as

$$\rho_{\text{Bell}} = \frac{1}{4}\mathbb{1} + \hat{S}_x^1\hat{S}_x^2 - \hat{S}_y^1\hat{S}_y^2 + \hat{S}_z^1\hat{S}_z^2 \tag{B.7}$$

Which is a well known fact, as Bell states are eigenstates of XX, YY and ZZ operators [25]. The tomography procedure will be able to recover the $\hat{S}_x^1\hat{S}_x^2 - \hat{S}_y^1\hat{S}_y^2 + \hat{S}_z^1\hat{S}_z^2$ part, up to a proportionality constant.

Let us calculate the state after each of the 9 possible pairs of pulses: This is

pulses	state after	1r	1i	2r	2i	3r	3i	4r	4i
II	$\hat{S}_x^1\hat{S}_x^2 - \hat{S}_y^1\hat{S}_y^2 + \hat{S}_z^1\hat{S}_z^2$	0	0	0	0	0	0	0	0
IX	$\hat{S}_x^1\hat{S}_x^2 + \hat{S}_y^1\hat{S}_z^2 + \hat{S}_z^1\hat{S}_y^2$	0	$\frac{1}{2}$	0	$-\frac{1}{2}$	0	$\frac{1}{2}$	0	$-\frac{1}{2}$
IY	$\hat{S}_x^1\hat{S}_z^2 - \hat{S}_y^1\hat{S}_y^2 - \hat{S}_z^1\hat{S}_x^2$	$\frac{1}{2}$	0	$-\frac{1}{2}$	0	$-\frac{1}{2}$	0	$\frac{1}{2}$	0
XI	$\hat{S}_x^1\hat{S}_x^2 + \hat{S}_y^1\hat{S}_z^2 + \hat{S}_z^1\hat{S}_y^2$	0	$\frac{1}{2}$	0	$-\frac{1}{2}$	0	$\frac{1}{2}$	0	$-\frac{1}{2}$
XX	$\hat{S}_x^1\hat{S}_x^2 - \hat{S}_z^1\hat{S}_z^2 + \hat{S}_y^1\hat{S}_y^2$	0	0	0	0	0	0	0	0
XY	$\hat{S}_x^1\hat{S}_z^2 + \hat{S}_z^1\hat{S}_y^2 - \hat{S}_y^1\hat{S}_x^2$	$\frac{1}{2}$	0	$-\frac{1}{2}$	0	0	$\frac{1}{2}$	0	$-\frac{1}{2}$
YI	$\hat{S}_z^1\hat{S}_x^2 - \hat{S}_y^1\hat{S}_y^2 - \hat{S}_x^1\hat{S}_z^2$	$-\frac{1}{2}$	0	$\frac{1}{2}$	0	$\frac{1}{2}$	0	$-\frac{1}{2}$	0
YX	$\hat{S}_z^1\hat{S}_x^2 + \hat{S}_y^1\hat{S}_z^2 - \hat{S}_x^1\hat{S}_y^2$	0	$\frac{1}{2}$	0	$-\frac{1}{2}$	$\frac{1}{2}$	0	$-\frac{1}{2}$	0
YY	$\hat{S}_z^1\hat{S}_z^2 - \hat{S}_y^1\hat{S}_y^2 + \hat{S}_x^1\hat{S}_x^2$	0	0	0	0	0	0	0	0

Table B.4: Density matrix of the state after the two initial pulses and the peak amplitudes in each NMR tomography measurement, applied to a pure entangled $\frac{1}{\sqrt{2}}(|00\rangle + |11\rangle)$ state.

very different from the previous case. We are not expecting any signal from the II, XX and YY measurements. In each of the other 6, we expect to detect the out-of-phase coherence at both frequencies, which would manifest as two peaks with opposite magnitude in each doublet.

In ESR DEER - based tomography, again the observables split between measurements with different detection frequency.

The Table B.5 below shows the expected signal measured in each of the 18 measurements. Note that because all the product operators present in the density matrix are two-spin orders, all the expected traces should exhibit a sine, and no cosine oscillation. We can also detail what conclusions about the initial state would be drawn from each measurement, if it was perfect. We use the Table 7.1 for that purpose.

- 1II $\langle\hat{S}_x^1\rangle = 0, \langle\hat{S}_y^1\rangle = 0, 2\langle\hat{S}_y^1\hat{S}_z^2\rangle = 0, 2\langle\hat{S}_x^1\hat{S}_z^2\rangle = 0$
- 1IX $\langle\hat{S}_x^1\rangle = 0, \langle\hat{S}_y^1\rangle = 0, 2\langle\hat{S}_y^1\hat{S}_y^2\rangle = -\frac{1}{2}, 2\langle\hat{S}_x^1\hat{S}_y^2\rangle = 0$

measurement	state after pulses	real channel	imaginary channel
1II	$\hat{S}_x^1\hat{S}_x^2 - \hat{S}_y^1\hat{S}_y^2 + \hat{S}_z^1\hat{S}_z^2$	no oscillation	no oscillation
1IX	$\hat{S}_x^1\hat{S}_x^2 + \hat{S}_y^1\hat{S}_z^2 + \hat{S}_z^1\hat{S}_y^2$	$-\sin(\omega_{ee}T)$	no oscillation
1IY	$\hat{S}_x^1\hat{S}_z^2 - \hat{S}_y^1\hat{S}_y^2 - \hat{S}_z^1\hat{S}_x^2$	no oscillation	$-\sin(\omega_{ee}T)$
1XI	$\hat{S}_x^1\hat{S}_x^2 + \hat{S}_y^1\hat{S}_z^2 + \hat{S}_z^1\hat{S}_y^2$	$-\sin(\omega_{ee}T)$	no oscillation
1XX	$\hat{S}_x^1\hat{S}_x^2 - \hat{S}_z^1\hat{S}_z^2 + \hat{S}_y^1\hat{S}_y^2$	no oscillation	no oscillation
1XY	$\hat{S}_x^1\hat{S}_z^2 + \hat{S}_z^1\hat{S}_y^2 - \hat{S}_y^1\hat{S}_x^2$	no oscillation	$-\sin(\omega_{ee}T)$
1YI	$\hat{S}_z^1\hat{S}_x^2 - \hat{S}_y^1\hat{S}_y^2 - \hat{S}_x^1\hat{S}_z^2$	no oscillation	$\sin(\omega_{ee}T)$
1YX	$\hat{S}_z^1\hat{S}_x^2 + \hat{S}_y^1\hat{S}_z^2 - \hat{S}_x^1\hat{S}_y^2$	$-\sin(\omega_{ee}T)$	no oscillation
1YY	$\hat{S}_z^1\hat{S}_z^2 - \hat{S}_y^1\hat{S}_y^2 + \hat{S}_x^1\hat{S}_x^2$	no oscillation	no oscillation
2II	$\hat{S}_x^1\hat{S}_x^2 - \hat{S}_y^1\hat{S}_y^2 + \hat{S}_z^1\hat{S}_z^2$	no oscillation	no oscillation
2IX	$\hat{S}_x^1\hat{S}_x^2 + \hat{S}_y^1\hat{S}_z^2 + \hat{S}_z^1\hat{S}_y^2$	$-\sin(\omega_{ee}T)$	no oscillation
2IY	$\hat{S}_x^1\hat{S}_z^2 - \hat{S}_y^1\hat{S}_y^2 - \hat{S}_z^1\hat{S}_x^2$	no oscillation	$\sin(\omega_{ee}T)$
2XI	$\hat{S}_x^1\hat{S}_x^2 + \hat{S}_y^1\hat{S}_z^2 + \hat{S}_z^1\hat{S}_y^2$	$-\sin(\omega_{ee}T)$	no oscillation
2XX	$\hat{S}_x^1\hat{S}_x^2 - \hat{S}_z^1\hat{S}_z^2 + \hat{S}_y^1\hat{S}_y^2$	no oscillation	no oscillation
2XY	$\hat{S}_x^1\hat{S}_z^2 + \hat{S}_z^1\hat{S}_y^2 - \hat{S}_y^1\hat{S}_x^2$	$-\sin(\omega_{ee}T)$	no oscillation
2YI	$\hat{S}_z^1\hat{S}_x^2 - \hat{S}_y^1\hat{S}_y^2 - \hat{S}_x^1\hat{S}_z^2$	no oscillation	$-\sin(\omega_{ee}T)$
2YX	$\hat{S}_z^1\hat{S}_x^2 + \hat{S}_y^1\hat{S}_z^2 - \hat{S}_x^1\hat{S}_y^2$	no oscillation	$-\sin(\omega_{ee}T)$
2YY	$\hat{S}_z^1\hat{S}_z^2 - \hat{S}_y^1\hat{S}_y^2 + \hat{S}_x^1\hat{S}_x^2$	no oscillation	no oscillation

Table B.5: Expected signal in each measurement of the tomography procedure, if applied to the state $\frac{1}{\sqrt{2}}(|00\rangle + |11\rangle)$

- 1IY $\langle\hat{S}_x^1\rangle = 0, \langle\hat{S}_y^1\rangle = 0, 2\langle\hat{S}_y^1\hat{S}_x^2\rangle = 0, 2\langle\hat{S}_x^1\hat{S}_x^2\rangle = \frac{1}{2}$
- 1XI $\langle\hat{S}_x^1\rangle = 0, \langle\hat{S}_z^1\rangle = 0, 2\langle\hat{S}_z^1\hat{S}_z^2\rangle = \frac{1}{2}, 2\langle\hat{S}_x^1\hat{S}_z^2\rangle = 0$
- 1XX $\langle\hat{S}_x^1\rangle = 0, \langle\hat{S}_z^1\rangle = 0, 2\langle\hat{S}_z^1\hat{S}_y^2\rangle = 0, 2\langle\hat{S}_x^1\hat{S}_y^2\rangle = 0$
- 1XY $\langle\hat{S}_x^1\rangle = 0, \langle\hat{S}_z^1\rangle = 0, 2\langle\hat{S}_z^1\hat{S}_x^2\rangle = 0, 2\langle\hat{S}_x^1\hat{S}_x^2\rangle = \frac{1}{2}$
- 1YI $\langle\hat{S}_z^1\rangle = 0, \langle\hat{S}_y^1\rangle = 0, 2\langle\hat{S}_y^1\hat{S}_z^2\rangle = 0, 2\langle\hat{S}_z^1\hat{S}_z^2\rangle = \frac{1}{2}$
- 1YX $\langle\hat{S}_z^1\rangle = 0, \langle\hat{S}_y^1\rangle = 0, 2\langle\hat{S}_y^1\hat{S}_y^2\rangle = -\frac{1}{2}, 2\langle\hat{S}_z^1\hat{S}_y^2\rangle = 0$
- 1YY $\langle\hat{S}_z^1\rangle = 0, \langle\hat{S}_y^1\rangle = 0, 2\langle\hat{S}_y^1\hat{S}_x^2\rangle = 0, 2\langle\hat{S}_z^1\hat{S}_x^2\rangle = 0$
- 2II $\langle\hat{S}_x^2\rangle = 0, \langle\hat{S}_y^2\rangle = 0, 2\langle\hat{S}_z^1\hat{S}_y^2\rangle = 0, 2\langle\hat{S}_z^1\hat{S}_x^2\rangle = 0$
- 2IX $\langle\hat{S}_x^2\rangle = 0, \langle\hat{S}_z^2\rangle = 0, 2\langle\hat{S}_z^1\hat{S}_z^2\rangle = \frac{1}{2}, 2\langle\hat{S}_z^1\hat{S}_x^2\rangle = 0$
- 2IY $\langle\hat{S}_z^2\rangle = 0, \langle\hat{S}_y^2\rangle = 0, 2\langle\hat{S}_z^1\hat{S}_y^2\rangle = 0, 2\langle\hat{S}_z^1\hat{S}_z^2\rangle = \frac{1}{2}$

- 2XI $\langle\hat{S}_x^2\rangle = 0, \langle\hat{S}_y^2\rangle = 0, 2\langle\hat{S}_y^1\hat{S}_y^2\rangle = -\frac{1}{2}, 2\langle\hat{S}_y^1\hat{S}_x^2\rangle = 0$
- 2XX $\langle\hat{S}_x^2\rangle = 0, \langle\hat{S}_z^2\rangle = 0, 2\langle\hat{S}_y^1\hat{S}_z^2\rangle = 0, 2\langle\hat{S}_y^1\hat{S}_x^2\rangle = 0$
- 2XY $\langle\hat{S}_z^2\rangle = 0, \langle\hat{S}_y^2\rangle = 0, 2\langle\hat{S}_y^1\hat{S}_y^2\rangle = -\frac{1}{2}, 2\langle\hat{S}_y^1\hat{S}_z^2\rangle = 0$
- 2YI $\langle\hat{S}_x^2\rangle = 0, \langle\hat{S}_y^2\rangle = 0, 2\langle\hat{S}_x^1\hat{S}_y^2\rangle = 0, 2\langle\hat{S}_x^1\hat{S}_x^2\rangle = \frac{1}{2}$
- 2YX $\langle\hat{S}_x^2\rangle = 0, \langle\hat{S}_z^2\rangle = 0, 2\langle\hat{S}_x^1\hat{S}_z^2\rangle = 0, 2\langle\hat{S}_x^1\hat{S}_x^2\rangle = \frac{1}{2}$
- 2YY $\langle\hat{S}_z^2\rangle = 0, \langle\hat{S}_y^2\rangle = 0, 2\langle\hat{S}_x^1\hat{S}_y^2\rangle = 0, 2\langle\hat{S}_x^1\hat{S}_z^2\rangle = 0$

Thus in the ideal case we would recover the deviation density matrix of the initial state $\hat{S}_x^1\hat{S}_x^2 - \hat{S}_y^1\hat{S}_y^2 + \hat{S}_z^1\hat{S}_z^2$.

B.1.4 Entangling the thermal state

Let us now move on to the state Chapter 7 is focused on, the result of the entangling gate applied to the thermal state in ESR introduced in Eq. 7.2. As the tomography procedure may only recover the deviation density matrix up to a proportionality constant, we can express it as $2A\hat{S}_y^1\hat{S}_z^2 + 2A\hat{S}_z^1\hat{S}_y^2 + 2B\hat{S}_x^1\hat{S}_x^2$, where A and B are some constants. In low temperature B/A tends to 1, in high temperature it tends to 0, so we can recover the high temperature result by setting $B = 0$.

Let us calculate the state after each of the 9 possible pairs of pulses: This

pulses	state after	1r	1i	2r	2i	3r	3i	4r	4i
II	$2A\hat{S}_y^1\hat{S}_z^2 + 2A\hat{S}_z^1\hat{S}_y^2 + 2B\hat{S}_x^1\hat{S}_x^2$	0	A	0	$-A$	0	A	0	$-A$
IX	$2A\hat{S}_y^1\hat{S}_y^2 - 2A\hat{S}_z^1\hat{S}_z^2 + 2B\hat{S}_x^1\hat{S}_x^2$	0	0	0	0	0	0	0	0
IY	$-2A\hat{S}_y^1\hat{S}_x^2 + 2A\hat{S}_z^1\hat{S}_y^2 + 2B\hat{S}_x^1\hat{S}_z^2$	B	0	$-B$	0	A	0	$-A$	0
XI	$-2A\hat{S}_z^1\hat{S}_z^2 + 2A\hat{S}_y^1\hat{S}_y^2 + 2B\hat{S}_x^1\hat{S}_x^2$	0	0	0	0	0	0	0	0
XX	$-2A\hat{S}_z^1\hat{S}_y^2 - 2A\hat{S}_y^1\hat{S}_z^2 + 2B\hat{S}_x^1\hat{S}_x^2$	0	$-A$	0	A	0	$-A$	0	A
XY	$2A\hat{S}_z^1\hat{S}_x^2 + 2A\hat{S}_y^1\hat{S}_y^2 + 2B\hat{S}_x^1\hat{S}_z^2$	B	0	$-B$	0	A	0	$-A$	0
YI	$2A\hat{S}_y^1\hat{S}_z^2 - 2A\hat{S}_x^1\hat{S}_y^2 + 2B\hat{S}_z^1\hat{S}_x^2$	0	A	0	$-A$	B	0	$-B$	0
YX	$2A\hat{S}_y^1\hat{S}_y^2 + 2A\hat{S}_x^1\hat{S}_z^2 + 2B\hat{S}_z^1\hat{S}_x^2$	A	0	$-A$	0	B	0	$-B$	0
YY	$-2A\hat{S}_y^1\hat{S}_x^2 - 2A\hat{S}_x^1\hat{S}_y^2 + 2B\hat{S}_z^1\hat{S}_z^2$	0	0	0	0	0	0	0	0

Table B.6: Density matrix of the state after the two initial pulses and the peak amplitudes in each NMR tomography measurement, applied to the $2A\hat{S}_y^1\hat{S}_z^2 + 2A\hat{S}_z^1\hat{S}_y^2 + 2B\hat{S}_x^1\hat{S}_x^2$ state.

time, it is possible to directly measure this state, even without any pulses. It should be noted that the thermal state purity in NMR is such that $B \ll A$, so it would be challenging to read out exactly what is detailed above in Table B.6. Again, in each measurement that yields any signal, we expect to detect the antiphase coherence at both frequencies, which would manifest as two peaks with opposite magnitude in each doublet.

The Table B.7 below shows expected results of the ESR DEER-based tomography of this state. Again, because all the product operators present in the density matrix are two-spin orders, all the expected traces should exhibit a sine, and no cosine oscillation. Again, the following conclusions about the initial state under

measurement	state after pulses	real channel	imaginary channel
1II	$2A\hat{S}_y^1\hat{S}_z^2 + 2A\hat{S}_z^1\hat{S}_y^2 + 2B\hat{S}_x^1\hat{S}_x^2$	$+A\sin(\omega_{ee}T)$	no oscillation
1IX	$2A\hat{S}_y^1\hat{S}_y^2 - 2A\hat{S}_z^1\hat{S}_z^2 + 2B\hat{S}_x^1\hat{S}_x^2$	no oscillation	no oscillation
1IY	$-2A\hat{S}_y^1\hat{S}_x^2 + 2A\hat{S}_z^1\hat{S}_y^2 + 2B\hat{S}_x^1\hat{S}_z^2$	no oscillation	$-B\sin(\omega_{ee}T)$
1XI	$-2A\hat{S}_z^1\hat{S}_z^2 + 2A\hat{S}_y^1\hat{S}_y^2 + 2B\hat{S}_x^1\hat{S}_x^2$	no oscillation	no oscillation
1XX	$-2A\hat{S}_z^1\hat{S}_y^2 - 2A\hat{S}_y^1\hat{S}_z^2 + 2B\hat{S}_x^1\hat{S}_x^2$	$-A\sin(\omega_{ee}T)$	no oscillation
1XY	$2A\hat{S}_z^1\hat{S}_x^2 + 2A\hat{S}_y^1\hat{S}_y^2 + 2B\hat{S}_x^1\hat{S}_z^2$	no oscillation	$-B\sin(\omega_{ee}T)$
1YI	$2A\hat{S}_y^1\hat{S}_z^2 - 2A\hat{S}_x^1\hat{S}_y^2 + 2B\hat{S}_z^1\hat{S}_x^2$	$+A\sin(\omega_{ee}T)$	no oscillation
1YX	$2A\hat{S}_y^1\hat{S}_y^2 + 2A\hat{S}_x^1\hat{S}_z^2 + 2B\hat{S}_z^1\hat{S}_x^2$	no oscillation	$+A\sin(\omega_{ee}T)$
1YY	$-2A\hat{S}_y^1\hat{S}_x^2 - 2A\hat{S}_x^1\hat{S}_y^2 + 2B\hat{S}_z^1\hat{S}_z^2$	no oscillation	no oscillation
2II	$2A\hat{S}_y^1\hat{S}_z^2 + 2A\hat{S}_z^1\hat{S}_y^2 + 2B\hat{S}_x^1\hat{S}_x^2$	$+A\sin(\omega_{ee}T)$	no oscillation
2IX	$2A\hat{S}_y^1\hat{S}_y^2 - 2A\hat{S}_z^1\hat{S}_z^2 + 2B\hat{S}_x^1\hat{S}_x^2$	no oscillation	no oscillation
2IY	$-2A\hat{S}_y^1\hat{S}_x^2 + 2A\hat{S}_z^1\hat{S}_y^2 + 2B\hat{S}_x^1\hat{S}_z^2$	$+A\sin(\omega_{ee}T)$	no oscillation
2XI	$-2A\hat{S}_z^1\hat{S}_z^2 + 2A\hat{S}_y^1\hat{S}_y^2 + 2B\hat{S}_x^1\hat{S}_x^2$	no oscillation	no oscillation
2XX	$-2A\hat{S}_z^1\hat{S}_y^2 - 2A\hat{S}_y^1\hat{S}_z^2 + 2B\hat{S}_x^1\hat{S}_x^2$	$-A\sin(\omega_{ee}T)$	no oscillation
2XY	$2A\hat{S}_z^1\hat{S}_x^2 + 2A\hat{S}_y^1\hat{S}_y^2 + 2B\hat{S}_x^1\hat{S}_z^2$	no oscillation	$+A\sin(\omega_{ee}T)$
2YI	$2A\hat{S}_y^1\hat{S}_z^2 - 2A\hat{S}_x^1\hat{S}_y^2 + 2B\hat{S}_z^1\hat{S}_x^2$	no oscillation	$-B\sin(\omega_{ee}T)$
2YX	$2A\hat{S}_y^1\hat{S}_y^2 + 2A\hat{S}_x^1\hat{S}_z^2 + 2B\hat{S}_z^1\hat{S}_x^2$	no oscillation	$-B\sin(\omega_{ee}T)$
2YY	$-2A\hat{S}_y^1\hat{S}_x^2 - 2A\hat{S}_x^1\hat{S}_y^2 + 2B\hat{S}_z^1\hat{S}_z^2$	no oscillation	no oscillation

Table B.7: Expected signal in each measurement of the tomography procedure, if applied to the state $2A\hat{S}_y^1\hat{S}_z^2 + 2A\hat{S}_z^1\hat{S}_y^2 + 2B\hat{S}_x^1\hat{S}_x^2$

tomography would be drawn, using Table 7.1:

- 1II $\langle\hat{S}_x^1\rangle = 0, \langle\hat{S}_y^1\rangle = 0, 2\langle\hat{S}_y^1\hat{S}_z^2\rangle = A, 2\langle\hat{S}_x^1\hat{S}_z^2\rangle = 0$
- 1IX $\langle\hat{S}_x^1\rangle = 0, \langle\hat{S}_y^1\rangle = 0, 2\langle\hat{S}_y^1\hat{S}_y^2\rangle = 0, 2\langle\hat{S}_x^1\hat{S}_y^2\rangle = 0$

- 1IY $\langle \hat{S}_x^1 \rangle = 0, \langle \hat{S}_y^1 \rangle = 0, 2\langle \hat{S}_y^1 \hat{S}_x^2 \rangle = 0, 2\langle \hat{S}_x^1 \hat{S}_x^2 \rangle = B$
- 1XI $\langle \hat{S}_x^1 \rangle = 0, \langle \hat{S}_z^1 \rangle = 0, 2\langle \hat{S}_z^1 \hat{S}_z^2 \rangle = 0, 2\langle \hat{S}_x^1 \hat{S}_z^2 \rangle = 0$
- 1XX $\langle \hat{S}_x^1 \rangle = 0, \langle \hat{S}_z^1 \rangle = 0, 2\langle \hat{S}_z^1 \hat{S}_y^2 \rangle = A, 2\langle \hat{S}_x^1 \hat{S}_y^2 \rangle = 0$
- 1XY $\langle \hat{S}_x^1 \rangle = 0, \langle \hat{S}_z^1 \rangle = 0, 2\langle \hat{S}_z^1 \hat{S}_x^2 \rangle = 0, 2\langle \hat{S}_x^1 \hat{S}_x^2 \rangle = B$
- 1YI $\langle \hat{S}_z^1 \rangle = 0, \langle \hat{S}_y^1 \rangle = 0, 2\langle \hat{S}_y^1 \hat{S}_z^2 \rangle = A, 2\langle \hat{S}_z^1 \hat{S}_z^2 \rangle = 0$
- 1YX $\langle \hat{S}_z^1 \rangle = 0, \langle \hat{S}_y^1 \rangle = 0, 2\langle \hat{S}_y^1 \hat{S}_y^2 \rangle = 0, 2\langle \hat{S}_z^1 \hat{S}_y^2 \rangle = A$
- 1YY $\langle \hat{S}_z^1 \rangle = 0, \langle \hat{S}_y^1 \rangle = 0, 2\langle \hat{S}_y^1 \hat{S}_x^2 \rangle = 0, 2\langle \hat{S}_z^1 \hat{S}_x^2 \rangle = 0$
- 2II $\langle \hat{S}_x^2 \rangle = 0, \langle \hat{S}_y^2 \rangle = 0, 2\langle \hat{S}_z^1 \hat{S}_y^2 \rangle = A, 2\langle \hat{S}_z^1 \hat{S}_x^2 \rangle = 0$
- 2IX $\langle \hat{S}_x^2 \rangle = 0, \langle \hat{S}_z^2 \rangle = 0, 2\langle \hat{S}_z^1 \hat{S}_z^2 \rangle = 0, 2\langle \hat{S}_z^1 \hat{S}_x^2 \rangle = 0$
- 2IY $\langle \hat{S}_z^2 \rangle = 0, \langle \hat{S}_y^2 \rangle = 0, 2\langle \hat{S}_z^1 \hat{S}_y^2 \rangle = A, 2\langle \hat{S}_z^1 \hat{S}_z^2 \rangle = 0$
- 2XI $\langle \hat{S}_x^2 \rangle = 0, \langle \hat{S}_y^2 \rangle = 0, 2\langle \hat{S}_y^1 \hat{S}_y^2 \rangle = 0, 2\langle \hat{S}_y^1 \hat{S}_x^2 \rangle = 0$
- 2XX $\langle \hat{S}_x^2 \rangle = 0, \langle \hat{S}_z^2 \rangle = 0, 2\langle \hat{S}_y^1 \hat{S}_z^2 \rangle = A, 2\langle \hat{S}_y^1 \hat{S}_x^2 \rangle = 0$
- 2XY $\langle \hat{S}_z^2 \rangle = 0, \langle \hat{S}_y^2 \rangle = 0, 2\langle \hat{S}_y^1 \hat{S}_y^2 \rangle = 0, 2\langle \hat{S}_y^1 \hat{S}_z^2 \rangle = A$
- 2YI $\langle \hat{S}_x^2 \rangle = 0, \langle \hat{S}_y^2 \rangle = 0, 2\langle \hat{S}_x^1 \hat{S}_y^2 \rangle = 0, 2\langle \hat{S}_x^1 \hat{S}_x^2 \rangle = B$
- 2YX $\langle \hat{S}_x^2 \rangle = 0, \langle \hat{S}_z^2 \rangle = 0, 2\langle \hat{S}_x^1 \hat{S}_z^2 \rangle = 0, 2\langle \hat{S}_x^1 \hat{S}_x^2 \rangle = B$
- 2YY $\langle \hat{S}_z^2 \rangle = 0, \langle \hat{S}_y^2 \rangle = 0, 2\langle \hat{S}_x^1 \hat{S}_y^2 \rangle = 0, 2\langle \hat{S}_x^1 \hat{S}_z^2 \rangle = 0$

Thus in the ideal case we recover the deviation density matrix of the initial state $2A\hat{S}_y^1\hat{S}_z^2 + 2A\hat{S}_z^1\hat{S}_y^2 + 2B\hat{S}_x^1\hat{S}_x^2$. Note that B appears in 4 measurements, but is supposed to only modify one element of the reconstructed density matrix. An experiment or a simulation, in which this is the case, should be a strong argument that the whole tomography procedure works.

As a closing remark, note that the contents of this Appendix relate to a perfect readout. In practice, there are additional steps required to reconstruct the density

matrix, namely least squares fitting of the parameters obtained from different measurements, estimation or calibration of some parameters, that are described in 7.5.3 and Appendix B.3.

B.2 Variable phase tomography equations

This Appendix contains lengthy formulas arising when the tomography procedure is extended to include $\frac{\pi}{2}$ pulses of variable phase.

B.2.1 Evolution equations with variable phase pulses

In the basic tomography procedure, only X or Y $\frac{\pi}{2}$ pulses are used. One may want to increase the number of measurements to include pulses of other phases. If the phase is unreliable, this method might allow to fit it to the data instead of trusting the generation mechanism. The tomography sequence following the $\frac{\pi}{2}$ pulses will still exhibit oscillations with frequency ω_{ee} which can be broken down into 4 components, real and imaginary sines and cosines. To recover the original density matrix from before the $\frac{\pi}{2}$ pulses, The arbitrary density matrix is evolved symbolically using Python's `sympy` package, first through the pulses, and then through the tomography sequence. The observed signal is proportional to the $\hat{S}_x^1$ component of resulting density matrix in the real channel and to its $\hat{S}_y^1$ component in the imaginary channel. These components are recovered, and the coefficient standing before $\cos(\omega_{ee}T)$ is taken to be the cosine signal and the one before $\sin(\omega_{ee}T)$ - the sine signal.

Three general cases are shown here. 1PI is sending a ν_1 pulse with phase θ_1 and not sending a pulse in ν_2, 1IP is sending a ν_2 pulse with phase θ_2 and not sending a pulse in ν_1, and finally 1PP is sending a ν_1 pulse with phase θ_1 and a ν_2 pulse with phase θ_2. These compare to the basic tomography procedure by assuming X pulses have phase 0 and Y pulses have phase $\frac{\pi}{2}$. The cases where ν_2 is the detection frequency, so 2IP, 2PI and 2PP are analogous, but all the labels 1 and 2 need to be switched there.

1PI	real cos	$-S_x^1 \cos^2(\theta_1) - \frac{1}{2}S_y^1 \sin(2\theta_1) - S_z^1 \sin(\theta_1)$
1PI	real sin	$S_x^1 S_z^2 \sin(2\theta_1) + 2S_y^1 S_z^2 \sin^2(\theta_1) - 2S_z^1 S_z^2 \cos(\theta_1)$
1PI	imag cos	$\frac{1}{2}S_x^1 \sin(2\theta_1) + S_y^1 \sin^2(\theta_1) - S_z^1 \cos(\theta_1)$
1PI	imag sin	$2S_x^1 S_z^2 \cos^2(\theta_1) + S_y^1 S_z^2 \sin(2\theta_1) + 2S_z^1 S_z^2 \sin(\theta_1)$

Table B.8: Signal in the experiment with ν_1 detection, a variable phase θ_1 in ν_1 and no pulse in ν_2.

1IP	real cos	$-S_x^1$
1IP	real sin	$-2S_x^2 S_y^1 \sin(\theta_2) + 2S_y^1 S_y^2 \cos(\theta_2)$
1IP	imag cos	S_y^1
1IP	imag sin	$-2S_x^1 S_x^2 \sin(\theta_2) + 2S_x^1 S_y^2 \cos(\theta_2)$

Table B.9: Signal in the experiment with ν_1 detection, no pulse in ν_1 and a variable phase θ_2 in ν_2.

Now multiple elements of the original density matrix are involved in each measurement, so reconstructing it requires more than one measurement and to fit the coefficients using the tables B.9, B.8 and B.10.

B.2.2 Systematic phase error tomography

One common way a basic tomography experiment may fail, is if one forgets or is unsuccessful at correctly implementing the phases on the tomography $\frac{\pi}{2}$ pulses. If using the AWG, it takes the detection frequency, and mixes the secondary oscillation on top of it, arriving at the secondary frequency. In the entangling gate sequence, where there is an initial $\frac{\pi}{2}$ sent in the secondary frequency, the tomography $\frac{\pi}{2}$ pulse needs to have its phase aligned manually. If it is not corrected, the phase error $\theta = 4\pi\tau(\nu_2 - \nu_1)$ will accumulate and affect the tomography. The phase of

1PP	real cos	$-S_x^1 \cos^2(\theta_1) - \frac{1}{2}S_y^1 \sin(2\theta_1) - S_z^1 \sin(\theta_1)$
1PP	real sin	$\frac{1}{2}S_x^1 S_x^2 (-\cos(2\theta_1 - \theta_2) + \cos(2\theta_1 + \theta_2)) + 2S_x^1 S_y^2 \sin(\theta_1)\cos(\theta_1)\cos(\theta_2)$ $-2S_x^2 S_y^1 \sin^2(\theta_1)\sin(\theta_2) + 2S_x^2 S_z^1 \sin(\theta_2)\cos(\theta_1) + 2S_y^1 S_y^2 \sin^2(\theta_1)\cos(\theta_2)$ $-2S_y^2 S_z^1 \cos(\theta_1)\cos(\theta_2)$
1PP	imag cos	$\frac{1}{2}S_x^1 \sin(2\theta_1) + S_y^1 \sin^2(\theta_1) - S_z^1 \cos(\theta_1)$
1PP	imag sin	$-2S_x^1 S_x^2 \sin(\theta_2)\cos^2(\theta_1) + 2S_x^1 S_y^2 \cos^2(\theta_1)\cos(\theta_2)$ $+\frac{1}{2}S_x^2 S_y^1 (-\cos(2\theta_1 - \theta_2) + \cos(2\theta_1 + \theta_2)) - 2S_x^2 S_z^1 \sin(\theta_1)\sin(\theta_2)$ $+2S_y^1 S_y^2 \sin(\theta_1)\cos(\theta_1)\cos(\theta_2) + 2S_y^2 S_z^1 \sin(\theta_1)\cos(\theta_2)$

Table B.10: Signal in the experiment with ν_1 detection, a variable phase θ_1 in ν_1 and a variable phase θ_2 in ν_2.

the ν_2 pulse in the ν_1 detection measurements shifts by θ and the phase of the ν_1 pulse in the ν_2 detection measurements shifts by $-\theta$. The resulting traces are thus proportional to different elements of the density matrix than originally expected. Table B.11 shows the new expectation in such an experiment.

name	real cos	real sin	imag cos	imag sin
1II	$-S_x^1$	$2S_y^1S_z^2$	S_y^1	$2S_x^1S_z^2$
1IX	$-S_x^1$	$-2S_x^2S_y^1\sin(\theta)+2S_y^1S_y^2\cos(\theta)$	S_y^1	$-2S_x^1S_x^2\sin(\theta)+2S_x^1S_y^2\cos(\theta)$
1IY	$-S_x^1$	$-2S_x^2S_y^1\cos(\theta)-2S_y^1S_y^2\sin(\theta)$	S_y^1	$-2S_x^1S_x^2\cos(\theta)-2S_x^1S_y^2\sin(\theta)$
1XI	$-S_x^1$	$-2S_z^1S_z^2$	$-S_z^1$	$2S_x^1S_z^2$
1XX	$-S_x^1$	$2S_x^2S_z^1\sin(\theta)-2S_y^2S_z^1\cos(\theta)$	$-S_z^1$	$-2S_x^1S_x^2\sin(\theta)+2S_x^1S_y^2\cos(\theta)$
1XY	$-S_x^1$	$2S_x^2S_z^1\cos(\theta)+2S_y^2S_z^1\sin(\theta)$	$-S_z^1$	$-2S_x^1S_x^2\cos(\theta)-2S_x^1S_y^2\sin(\theta)$
1YI	$-S_z^1$	$2S_y^1S_z^2$	S_y^1	$2S_z^1S_z^2$
1YX	$-S_z^1$	$-2S_x^2S_y^1\sin(\theta)+2S_y^1S_y^2\cos(\theta)$	S_y^1	$-2S_x^2S_z^1\sin(\theta)+2S_y^2S_z^1\cos(\theta)$
1YY	$-S_z^1$	$-2S_x^2S_y^1\cos(\theta)-2S_y^1S_y^2\sin(\theta)$	S_y^1	$-2S_x^2S_z^1\cos(\theta)-2S_y^2S_z^1\sin(\theta)$
2II	$-S_x^2$	$2S_y^2S_z^1$	S_y^2	$2S_x^2S_z^1$
2IX	$-S_x^2$	$-2S_z^1S_z^2$	$-S_z^2$	$2S_x^2S_z^1$
2IY	$-S_z^2$	$2S_y^2S_z^1$	S_y^2	$2S_z^1S_z^2$
2XI	$-S_x^2$	$2S_x^1S_y^2\sin(\theta)+2S_y^1S_y^2\cos(\theta)$	S_y^2	$2S_x^1S_x^2\sin(\theta)+2S_x^2S_y^1\cos(\theta)$
2XX	$-S_x^2$	$-2S_x^1S_z^2\sin(\theta)-2S_y^1S_z^2\cos(\theta)$	$-S_z^2$	$2S_x^1S_x^2\sin(\theta)+2S_x^2S_y^1\cos(\theta)$
2XY	$-S_z^2$	$2S_x^1S_y^2\sin(\theta)+2S_y^1S_y^2\cos(\theta)$	S_y^2	$2S_x^1S_z^2\sin(\theta)+2S_y^1S_z^2\cos(\theta)$
2YI	$-S_x^2$	$-2S_x^1S_y^2\cos(\theta)+2S_y^1S_y^2\sin(\theta)$	S_y^2	$-2S_x^1S_x^2\cos(\theta)+2S_x^2S_y^1\sin(\theta)$
2YX	$-S_x^2$	$2S_x^1S_z^2\cos(\theta)-2S_y^1S_z^2\sin(\theta)$	$-S_z^2$	$-2S_x^1S_x^2\cos(\theta)+2S_x^2S_y^1\sin(\theta)$
2YY	$-S_z^2$	$-2S_x^1S_y^2\cos(\theta)+2S_y^1S_y^2\sin(\theta)$	S_y^2	$-2S_x^1S_z^2\cos(\theta)+2S_y^1S_z^2\sin(\theta)$

Table B.11: Signal in the experiment with systematic phase error θ.

This time, the reconstruction of the density matrix is just slightly more difficult. We may combine results of two measurements to find two elements of the density matrix using trigonometric identities. For example, the $2S_y^1S_x^2$ can be recovered from real sine in 1IX and 1IY, by multiplying the first signal by $\sin(\theta)$, the second by $\cos(\theta)$ and adding them together. The contribution from $2S_y^1S_y^2$ then cancels. This is how most of the entangling gate experimental data described in 7.6.2 was analyzed.

B.3 Least squares fitting of the parameters in the tomography procedure

The fitting function also provides a covariance matrix of the parameters, which contains information on how close data follow the requested model function. As

each expected value in the table 7.1 appears in 4 or 6 measurements, a standard error-weighted average is used to recover the best fit value for the specific expected value of a product operator, collecting the values according to the table 7.1. If $\langle\hat{A}\rangle$ is an expectation value of one operator, $\langle\hat{O}\rangle_1, \ldots, \langle\hat{A}\rangle_n$ are its estimates from n appropriate measurements, and $\sigma_1^2, \ldots, \sigma_n^2$ associated variances, we write:

$$\langle\hat{A}\rangle = \frac{\sum_{k=1}^{n} \frac{\langle\hat{A}\rangle_k}{\sigma_k^2}}{\sum_{k=1}^{n} \frac{1}{\sigma_k^2}} \tag{B.8}$$

The variance of this weighted average is then calculated according to [165]:

$$\sigma^2_{\langle\hat{A}\rangle} = \frac{n}{(n-1)\left(\sum_{k=1}^{n} \frac{1}{\sigma_k^2}\right)} \sum_{k=1}^{n} \frac{\left(\langle\hat{A}\rangle - \langle\hat{A}\rangle_k\right)^2}{\sigma_k^4} \tag{B.9}$$

The variance $\sigma^2_{\langle\hat{A}\rangle}$ allows to enforce the ideas explained in Table 7.2. By minimizing the sum of variances of all 15 components of the density matrix in respect to the global parameters, the origin position t_0, the two phases ϕ_1 and ϕ_2 and the amplitude ratio α, it is possible to sidestep the lack of their direct calibration. This is effectively another least squares fitting, but performed on a higher level. If these parameters are far away from their optimal values, different measurements of the same component of the density matrix will give vastly different results, which will be reflected in the total variance.

Bibliography

[1] Richard P. Feynman. "Simulating physics with computers". In: *International Journal of Theoretical Physics* 21.6 (June 1982), pp. 467–488. URL: https://doi.org/10.1007/BF02650179.

[2] Lov K. Grover. "Quantum Mechanics Helps in Searching for a Needle in a Haystack". In: *Phys. Rev. Lett.* 79 (2 July 1997), pp. 325–328. URL: https://link.aps.org/doi/10.1103/PhysRevLett.79.325.

[3] P. Shor. "Polynomial-Time Algorithms for Prime Factorization and Discrete Logarithms on a Quantum Computer". In: *SIAM Journal on Computing* 26.5 (1997), pp. 1484–1509. URL: https://doi.org/10.1137/S0097539795293172.

[4] John Preskill. *Quantum computing 40 years later*. 2021. arXiv: 2106.10522 [quant-ph].

[5] Andreas J. Heinrich et al. "Quantum-coherent nanoscience". In: *Nature Nanotechnology* 16.12 (Dec. 2021), pp. 1318–1329. URL: https://doi.org/10.1038/s41565-021-00994-1.

[6] M. H. Devoret and R. J. Schoelkopf. "Superconducting Circuits for Quantum Information: An Outlook". In: *Science* 339.6124 (2013), pp. 1169–1174. URL: http://science.sciencemag.org/content/339/6124/1169.

[7] P. Krantz et al. "A quantum engineer's guide to superconducting qubits". In: *Applied Physics Reviews* 6.2 (June 2019), p. 021318. URL: http://dx.doi.org/10.1063/1.5089550.

[8] Jerry M. Chow et al. "Simple All-Microwave Entangling Gate for Fixed-Frequency Superconducting Qubits". In: *Phys. Rev. Lett.* 107 (8 Aug. 2011), p. 080502. URL: https://link.aps.org/doi/10.1103/PhysRevLett.107.080502.

[9] H. Häffner, C.F. Roos, and R. Blatt. "Quantum computing with trapped ions". In: *Physics Reports* 469.4 (2008), pp. 155–203. URL: http://www.sciencedirect.com/science/article/pii/S0370157308003463.

[10] Anasua Chatterjee et al. "Semiconductor qubits in practice". In: *Nature Reviews Physics* 3.3 (Mar. 2021), pp. 157–177. URL: https://doi.org/10.1038/s42254-021-00283-9.

[11] Jarryd J. Pla et al. "A single-atom electron spin qubit in silicon". In: *Nature* 489.7417 (Sept. 2012), pp. 541–545. URL: https://doi.org/10.1038/nature11449.

[12] R. Härtle et al. "Decoherence and lead-induced interdot coupling in nonequilibrium electron transport through interacting quantum dots: A hierarchical quantum master equation approach". In: *Phys. Rev. B* 88 (23 Dec. 2013), p. 235426. URL: https://link.aps.org/doi/10.1103/PhysRevB.88.235426.

[13] John Preskill. "Quantum Computing in the NISQ era and beyond". In: *Quantum* 2 (Aug. 2018), p. 79. URL: https://doi.org/10.22331/q-2018-08-06-79.

[14] Yulin Wu et al. "Strong Quantum Computational Advantage Using a Superconducting Quantum Processor". In: *Phys. Rev. Lett.* 127 (18 Oct. 2021), p. 180501. URL: https://link.aps.org/doi/10.1103/PhysRevLett.127.180501.

[15] Frank Arute et al. "Quantum supremacy using a programmable superconducting processor". In: *Nature* 574.7779 (Oct. 2019), pp. 505–510. URL: https://doi.org/10.1038/s41586-019-1666-5.

[16] Michael N. Leuenberger and Daniel Loss. "Quantum computing in Molecular Magnets". In: *Nature* 410 (Apr. 2001), 789 EP -. URL: http://dx.doi.org/10.1038/35071024.

[17] J Tejada et al. "Magnetic qubits as hardware for quantum computers". In: *Nanotechnology* 12.2 (2001), p. 181. URL: http://stacks.iop.org/0957-4484/12/i=2/a=323.

[18] A. Schweiger and G. Jeschke. *Principles of Pulse Electron Paramagnetic Resonance*. Oxford University Press, 2001. URL: https://books.google.co.uk/books?id=tkvQQElkW1wC.

[19] Eufemio Moreno-Pineda and Wolfgang Wernsdorfer. "Measuring molecular magnets for quantum technologies". In: *Nature Reviews Physics* 3.9 (Sept. 2021), pp. 645–659. URL: https://doi.org/10.1038/s42254-021-00340-3.

[20] David P. DiVincenzo. "The Physical Implementation of Quantum Computation". In: *Fortschritte der Physik* 48.9-11 (2000), pp. 771–783.

[21] S. Carretta et al. "A perspective on scaling up quantum computation with molecular spins". In: *Applied Physics Letters* 118.24 (2021), p. 240501. eprint: https://doi.org/10.1063/5.0053378. URL: https://doi.org/10.1063/5.0053378.

[22] Arne Laucht et al. "Electrically controlling single-spin qubits in a continuous microwave field". In: *Science Advances* 1.3 (2015), e1500022. eprint: https://www.science.org/doi/pdf/10.1126/sciadv.1500022. URL: https://www.science.org/doi/abs/10.1126/sciadv.1500022.

[23] Guilherme Tosi et al. "Silicon quantum processor with robust long-distance qubit couplings". In: *Nature Communications* 8.1 (Sept. 2017), p. 450. URL: https://doi.org/10.1038/s41467-017-00378-x.

[24] Stefan Thiele et al. "Electrically driven nuclear spin resonance in single-molecule magnets". In: *Science* 344.6188 (2014), pp. 1135–1138. URL: http://science.sciencemag.org/content/344/6188/1135.

[25] Michael A. Nielsen and Isaac L. Chuang. *Quantum Computation and Quantum Information: 10th Anniversary Edition*. 10th. New York, NY, USA: Cambridge University Press, 2011.

[26] Jun Zhang et al. "Geometric theory of nonlocal two-qubit operations". In: *Phys. Rev. A* 67 (4 Apr. 2003), p. 042313. URL: https://link.aps.org/doi/10.1103/PhysRevA.67.042313.

[27] Daniel Gottesman and Isaac L. Chuang. "Demonstrating the viability of universal quantum computation using teleportation and single-qubit operations". In: *Nature* 402.6760 (Nov. 1999), pp. 390–393. URL: https://doi.org/10.1038/46503.

[28] Richard Jozsa and Noah Linden. "On the role of entanglement in quantum-computational speed-up". In: *Proceedings of the Royal Society of London. Series A: Mathematical, Physical and Engineering Sciences* 459.2036 (2003), pp. 2011–2032. eprint: https://royalsocietypublishing.org/doi/pdf/10.1098/rspa.2002.1097. URL: https://royalsocietypublishing.org/doi/abs/10.1098/rspa.2002.1097.

[29] Arzhang Ardavan et al. "Engineering coherent interactions in molecular nanomagnet dimers". In: *Npj Quantum Information* 1 (Dec. 2015). Article, 15012 EP -. URL: http://dx.doi.org/10.1038/npjqi.2015.12.

[30] Jae-Seung Lee. "The quantum state tomography on an NMR system". In: *Physics Letters A* 305.6 (2002), pp. 349–353. URL: https://www.sciencedirect.com/science/article/pii/S0375960102014792.

[31] G L Long, H Y Yan, and Yang Sun. "Analysis of density matrix reconstruction in NMR quantum computing". In: *Journal of Optics B: Quantum and Semiclassical Optics* 3.6 (2001), p. 376. URL: http://stacks.iop.org/1464-4266/3/i=6/a=305.

[32] M. Mehring, J. Mende, and W. Scherer. "Entanglement between an Electron and a Nuclear Spin $\frac{1}{2}$". In: *Phys. Rev. Lett.* 90 (15 Apr. 2003), p. 153001. URL: https://link.aps.org/doi/10.1103/PhysRevLett.90.153001.

[33] Stephanie Simmons et al. "Entanglement in a solid-state spin ensemble". In: *Nature* 470.7332 (Jan. 2011), nature09696. URL: http:https://doi.org/10.1038/nature09696.

[34] I. L. Chuang et al. "Bulk quantum computation with nuclear magnetic resonance: theory and experiment". In: *Proceedings of the Royal Society of London A: Mathematical, Physical and Engineering Sciences* 454.1969 (1998), pp. 447–467. URL: http://rspa.royalsocietypublishing.org/content/454/1969/447.

[35] Jonathan A. Jones. "Quantum computing with NMR". In: *Progress in Nuclear Magnetic Resonance Spectroscopy* 59.2 (2011), pp. 91–120. URL: http://www.sciencedirect.com/science/article/pii/S0079656510001111.

[36] Benjamin Kintzel et al. "Molecular electronic spin qubits from a spin-frustrated trinuclear copper complex". In: *Chem. Commun.* 54 (92 2018), pp. 12934–12937. URL: http://dx.doi.org/10.1039/C8CC06741D.

[37] Junjie Liu et al. "Electric Field Control of Spins in Molecular Magnets". In: *Phys. Rev. Lett.* 122 (3 Jan. 2019), p. 037202. URL: https://link.aps.org/doi/10.1103/PhysRevLett.122.037202.

[38] Charles P. Poole. *Electron Spin Resonance: A Comprehensive Treatise on Experimental Techniques*. 2nd. Dover Publications Inc., 2003.

[39] B. Bleaney A. Abragam. *Electron Paramagnetic Resonance of Transition Ions*. Reprint. The International Series of Monographs on Physics. Oxford University Press, 2012.

[40] Gareth R. Eaton et al. *Quantitative EPR*. SpringerWienNewYork, 2010.

[41] Anatole Abragam, Maurice Henry Lecorney Pryce, and Franz Eugen Simon. "Theory of the nuclear hyperfine structure of paramagnetic resonance spectra in crystals". In: *Proceedings of the Royal Society of London. Series A. Mathematical and Physical Sciences* 205.1080 (1951), pp. 135–153. eprint: https://royalsocietypublishing.org/doi/pdf/10.1098/rspa.1951.0022. URL: https://royalsocietypublishing.org/doi/abs/10.1098/rspa.1951.0022.

[42] Claude Bloch. "Sur la theorie des perturbations des etats lies". In: *Nuclear Physics* 6 (1958), pp. 329–347. URL: https://www.sciencedirect.com/science/article/pii/0029558258901160.

[43] C Rudowicz and C Y Chung. "The generalization of the extended Stevens operators to higher ranks and spins, and a systematic review of the tables of the tensor operators and their matrix elements". In: *Journal of Physics: Condensed Matter* 16.32 (Aug. 2004), pp. 5825–5847. URL: https://doi.org/10.1088/0953-8984/16/32/018.

[44] I.D. Ryabov. "On the Generation of Operator Equivalents and the Calculation of Their Matrix Elements". In: *Journal of Magnetic Resonance* 140.1 (1999), pp. 141–145. URL: https://www.sciencedirect.com/science/article/pii/S1090780799917834.

[45] G. Jeschke and H.W. Spiess. "Distance Measurements in Solid-State NMR and EPR Spectroscopy". In: *Novel NMR and EPR techniques*. Berlin, Heidelberg: Springer Berlin Heidelberg, 2006, pp. 21–63. URL: https://doi.org/10.1007/3-540-32627-8_2.

[46] Gunnar Jeschke. "DEER Distance Measurements on Proteins". In: *Annual Review of Physical Chemistry* 63.1 (2012). PMID: 22404592, pp. 419–446. URL: https://doi.org/10.1146/annurev-physchem-032511-143716.

[47] A. Bencini and D. Gatteschi. *EPR of Exchange Coupled Systems*. Dover Books on Chemistry. Dover Publications, 2012. URL: https://books.google.co.uk/books?id=jdjCAgAAQBAJ.

[48] Giulio Racah. "Theory of Complex Spectra. II". In: *Phys. Rev.* 62 (9-10 Nov. 1942), pp. 438–462. URL: https://link.aps.org/doi/10.1103/PhysRev.62.438.

[49] B. Stich, S. Greulich-Weber, and J.-M. Spaeth. "Electrical detection of electron paramagnetic resonance: New possibilities for the study of point defects". In: *Journal of Applied Physics* 77.4 (1995), pp. 1546–1553. eprint: https://doi.org/10.1063/1.358906. URL: https://doi.org/10.1063/1.358906.

[50] Alexander V. Balatsky, Mitsuaki Nishijima, and Yishay Manassen. "Electron spin resonance-scanning tunneling microscopy". In: *Advances in Physics* 61.2 (2012), pp. 117–152. eprint: https://doi.org/10.1080/00018732.2012.668775. URL: https://doi.org/10.1080/00018732.2012.668775.

[51] Kai Yang et al. "Coherent spin manipulation of individual atoms on a surface". In: *Science* 366.6464 (2019), pp. 509–512. eprint: https://www.science.org/doi/pdf/10.1126/science.aay6779. URL: https://www.science.org/doi/abs/10.1126/science.aay6779.

[52] Ralph T. Weber and Aaron H. Heiss. *ELEXSYS E 580 Pulse EPR Spectrometer User's Manual*. 1st ed. An optional note. Bruker Biospin Corporation. Billerica, MA USA, July 2001.

[53] A.S. Gilmour. *Klystrons, Traveling Wave Tubes, Magnetrons, Crossed-Field Amplifiers, and Gyrotrons*. Artech, 2011.

[54] Alice Bowen. "Magnetic Resonance Studies of Proteins and Model Systems". PhD thesis. University College Oxford, 2012.

[55] David P. Goldenberg. "The Product Operator Formalism: A Physical and Graphical Interpretation". In: *Concepts in magnetic resonance. Part A, Bridging education and research* 36A.2 (Mar. 2010). PMC3088292[pmcid], pp. 49–83. URL: https://doi.org/10.1002/cmr.a.20156.

[56] Christopher E. Spiese. "A Simplified Approach to Product Operator Formalism". In: *Journal of Chemical Education* 81.1 (Jan. 2004), p. 134. URL: https://doi.org/10.1021/ed081p134.

[57] U Fano. "Description of States in Quantum Mechanics by Density Matrix and Operator Techniques". In: *Rev. Mod. Phys.* 29 (1957), pp. 74–93. URL: https://doi.org/10.1103/revmodphys.29.74.

[58] K Blum. *Density Matrix Theory and Applications*. Berlin: Springer, 2012.

[59] U Fano. *Lectures on the Many-body Problems—Liouville Representation of Quantum Mechanics with Application to Relaxation Processes*. New York: Academic, 1964.

[60] Jerryman A Gyamfi. "Fundamentals of quantum mechanics in Liouville space". In: *European Journal of Physics* 41.6 (Oct. 2020), p. 063002. URL: https://doi.org/10.1088/1361-6404/ab9fdd.

[61] Gen Kimura. "The Bloch vector for N-level systems". In: *Physics Letters A* 314.5 (2003), pp. 339–349. URL: https://www.sciencedirect.com/science/article/pii/S0375960103009411.

[62] L. Jakóbczyk and M. Siennicki. "Geometry of Bloch vectors in two-qubit system". In: *Physics Letters A* 286.6 (2001), pp. 383–390. URL: https://www.sciencedirect.com/science/article/pii/S0375960101004558.

[63] J. E. Campbell. "On a Law of Combination of Operators (Second Paper)*". In: *Proceedings of the London Mathematical Society* s1-29.1 (1897), pp. 14–32. eprint: https://londmathsoc.onlinelibrary.wiley.com/doi/pdf/10.1112/plms/s1-29.1.14. URL: https://londmathsoc.onlinelibrary.wiley.com/doi/abs/10.1112/plms/s1-29.1.14.

[64] Robert D. Nielsen and Bruce H. Robinson. "The spherical tensor formalism applied to relaxation in magnetic resonance". In: *Concepts in Magnetic Resonance Part A* 28A.4 (2006), pp. 270–290. eprint: https://onlinelibrary.wiley.com/doi/pdf/10.1002/cmr.a.20055. URL: https://onlinelibrary.wiley.com/doi/abs/10.1002/cmr.a.20055.

[65] H.J. Hogben et al. "Spinach – A software library for simulation of spin dynamics in large spin systems". In: *Journal of Magnetic Resonance* 208.2 (2011), pp. 179–194. URL: http://www.sciencedirect.com/science/article/pii/S1090780710003575.

[66] U. Haeberlen and J. S. Waugh. "Coherent Averaging Effects in Magnetic Resonance". In: *Phys. Rev.* 175 (2 Nov. 1968), pp. 453–467. URL: https://link.aps.org/doi/10.1103/PhysRev.175.453.

[67] F. Bloch and A. Siegert. "Magnetic Resonance for Nonrotating Fields". In: *Phys. Rev.* 57 (6 Mar. 1940), pp. 522–527. URL: https://link.aps.org/doi/10.1103/PhysRev.57.522.

[68] David L. Goodwin et al. "Feedback control optimisation of ESR experiments". In: *Journal of Magnetic Resonance* 297 (2018), pp. 9–16. URL: https://www.sciencedirect.com/science/article/pii/S1090780718302349.

[69] E. L. Hahn. "Spin Echoes". In: *Phys. Rev.* 80 (4 Nov. 1950), pp. 580–594. URL: https://link.aps.org/doi/10.1103/PhysRev.80.580.

[70] W. B. Mims. "Electron Echo Methods in Spin Resonance Spectrometry". In: *Review of Scientific Instruments* 36.10 (1965), pp. 1472–1479. eprint: https://doi.org/10.1063/1.1719359. URL: https://doi.org/10.1063/1.1719359.

[71] S. Stoll and B. Kasumaj. "Phase Cycling in Electron Spin Echo Envelope Modulation". In: *Applied Magnetic Resonance* 35.1 (Nov. 2008), pp. 15–32. URL: https://doi.org/10.1007/s00723-008-0140-6.

[72] A. G. Redfield. "On the Theory of Relaxation Processes". In: *IBM Journal of Research and Development* 1.1 (1957), pp. 19–31.

[73] Sandra S. Eaton and Gareth R. Eaton. "Relaxation times of Organic Radicals and Transition Metal Ions". In: *Distance Measurements in Biological Systems by EPR*. Ed. by Sandra S. Eaton, Gareth R. Eaton, and Lawrence J. Berliner. Kluwer Academic Publishers, 2001. Chap. 2, pp. 29–130.

[74] S.A. Dikanov and Y. Tsvetkov. *Electron Spin Echo Envelope Modulation (ESEEM) Spectroscopy*. Eseem Spectroscopy. Taylor & Francis, 1992. URL: https://books.google.co.uk/books?id=Vch6Pzbjt5wC.

[75] C. J. Wedge et al. "Chemical Engineering of Molecular Qubits". In: *Phys. Rev. Lett.* 108 (10 Mar. 2012), p. 107204. URL: https://link.aps.org/doi/10.1103/PhysRevLett.108.107204.

[76] Stephen Wimperis. "Composite pulses with rectangular excitation and inversion profiles". In: *Journal of Magnetic Resonance (1969)* 83.3 (1989), pp. 509–524. URL: http://www.sciencedirect.com/science/article/pii/0022236489903466.

[77] Stephen Wimperis. "Broadband and narrowband composite excitation sequences". In: *Journal of Magnetic Resonance (1969)* 86.1 (1990), pp. 46–59. URL: http://www.sciencedirect.com/science/article/pii/002223649090210Z.

[78] S. Wimperis. "Iterative schemes for phase-distortionless composite 180? pulses". In: *Journal of Magnetic Resonance* 93.1 (June 1991), pp. 199–206. URL: http://eprints.gla.ac.uk/52528/.

[79] S. Wimperis. "Broadband, Narrowband, and Passband Composite Pulses for Use in Advanced NMR Experiments". In: *Journal of Magnetic Resonance, Series A* 109.2 (1994), pp. 221–231. URL: http://www.sciencedirect.com/science/article/pii/S1064185884711594.

[80] Arnold L. Bloom. "Nuclear Induction in Inhomogeneous Fields". In: *Phys. Rev.* 98 (4 May 1955), pp. 1105–1111. URL: https://link.aps.org/doi/10.1103/PhysRev.98.1105.

[81] W. B. Mims. "Spin Echoes from Broad Resonance Lines with High Turning Angles". In: *Phys. Rev.* 141 (2 Jan. 1966), pp. 499–502. URL: https://link.aps.org/doi/10.1103/PhysRev.141.499.

[82] Riaz Hussain et al. "Coherent Manipulation of a Molecular Ln-Based Nuclear Qudit Coupled to an Electron Qubit". In: *Journal of the American Chemical Society* 140.31 (Aug. 2018), pp. 9814–9818. URL: https://doi.org/10.1021/jacs.8b05934.

[83] Antonio Fernandez et al. "Making hybrid [n]-rotaxanes as supramolecular arrays of molecular electron spin qubits". In: *Nature Communications* 7.1 (Jan. 2016), p. 10240. URL: https://doi.org/10.1038/ncomms10240.

[84] M. D. Jenkins et al. "A scalable architecture for quantum computation with molecular nanomagnets". In: *Dalton Trans.* 45 (42 2016), pp. 16682–16693. URL: http://dx.doi.org/10.1039/C6DT02664H.

[85] Paul W. K. Rothemund. "Folding DNA to create nanoscale shapes and patterns". In: *Nature* 440.7082 (Mar. 2006), pp. 297–302. URL: https://doi.org/10.1038/nature04586.

[86] Daniel Gottesman. *Stabilizer Codes and Quantum Error Correction*. 1997. arXiv: quant-ph/9705052 [quant-ph].

[87] Panjin Kim and Daewan Han. *Measurement-based Uncomputation Applied to Controlled Modular Multiplication*. 2021. arXiv: 2102.01453 [quant-ph].

[88] C. Godfrin et al. "Operating Quantum States in Single Magnetic Molecules: Implementation of Grover's Quantum Algorithm". In: *Phys. Rev. Lett.* 119 (18 Nov. 2017), p. 187702. URL: https://link.aps.org/doi/10.1103/PhysRevLett.119.187702.

[89] Arzhang Ardavan et al. "Will Spin-Relaxation Times in Molecular Magnets Permit Quantum Information Processing?" In: *Phys. Rev. Lett.* 98 (5 Jan. 2007), p. 057201. URL: https://link.aps.org/doi/10.1103/PhysRevLett.98.057201.

[90] Muhandis Shiddiq et al. "Enhancing coherence in molecular spin qubits via atomic clock transitions". In: *Nature* 531.7594 (Mar. 2016), pp. 348–351. URL: https://doi.org/10.1038/nature16984.

[91] Chung-Jui Yu et al. "Long Coherence Times in Nuclear Spin-Free Vanadyl Qubits". In: *Journal of the American Chemical Society* 138.44 (Nov. 2016), pp. 14678–14685. URL: https://doi.org/10.1021/jacs.6b08467.

[92] Simon C Benjamin et al. "Towards a fullerene-based quantum computer". In: *Journal of Physics: Condensed Matter* 18.21 (2006), S867. URL: http://stacks.iop.org/0953-8984/18/i=21/a=S12.

[93] Joseph M. Zadrozny et al. "A Porous Array of Clock Qubits". In: *Journal of the American Chemical Society* 139.20 (May 2017), pp. 7089–7094. URL: https://doi.org/10.1021/jacs.7b03123.

[94] Joseph M. Zadrozny et al. "Millisecond Coherence Time in a Tunable Molecular Electronic Spin Qubit". In: *ACS Central Science* 1.9 (2015). PMID: 27163013, pp. 488–492. URL: https://doi.org/10.1021/acscentsci.5b00338.

[95] A. Chiesa et al. "Molecular Nanomagnets as Qubits with Embedded Quantum-Error Correction". In: *The Journal of Physical Chemistry Letters* 11.20 (Oct. 2020), pp. 8610–8615. URL: https://doi.org/10.1021/acs.jpclett.0c02213.

[96] A. Chiesa et al. "Embedded quantum-error correction and controlled-phase gate for molecular spin qubits". In: *AIP Advances* 11.2 (2021), p. 025134. eprint: https://doi.org/10.1063/9.0000166. URL: https://doi.org/10.1063/9.0000166.

[97] Danielle Kaminski. "Electron Spin Resonance of Molecular Magnets for Quantum Information Processing". PhD thesis. Magdalen College Oxford, 2015.

[98] Stergios Piligkos et al. "EPR Spectroscopy of a Family of CrIII7MII (M = Cd, Zn, Mn, Ni) "Wheels": Studies of Isostructural Compounds with Different Spin Ground States". In: *Chemistry – A European Journal* 15.13 (2009), pp. 3152–3167.

[99] Florian Meier and Daniel Loss. "Thermodynamics and spin-tunneling dynamics in ferric wheels with excess spin". In: *Phys. Rev. B* 64 (22 Nov. 2001), p. 224411. URL: https://link.aps.org/doi/10.1103/PhysRevB.64.224411.

[100] Fabrizio Moro et al. "Coherent electron spin manipulation in a dilute oriented ensemble of molecular nanomagnets: pulsed EPR on doped single crystals". In: *Chem. Commun.* 50 (1 2014), pp. 91–93. URL: http://dx.doi.org/10.1039/C3CC46326E.

[101] Finn K. Larsen et al. "Synthesis and Characterization of Heterometallic Cr7M Wheels". In: *Angewandte Chemie International Edition* 42.1 (2003), pp. 101–105.

[102] Nico W. Hendrickx et al. "A four-qubit germanium quantum processor". In: *Nature* 591.7851 (Mar. 2021), pp. 580–585. URL: https://doi.org/10.1038/s41586-021-03332-6.

[103] D. M. Zajac et al. "Resonantly driven CNOT gate for electron spins". In: *Science* 359.6374 (2018), pp. 439–442. eprint: https://www.science.org/doi/pdf/10.1126/science.aao5965. URL: https://www.science.org/doi/abs/10.1126/science.aao5965.

[104] Murad A. AlDamen et al. "Mononuclear Lanthanide Single Molecule Magnets Based on the Polyoxometalates [Ln(W5O18)2]9- and [Ln(β2-SiW11O39)2]13- (LnIII = Tb, Dy, Ho, Er, Tm, and Yb)". In: *Inorganic Chemistry* 48.8 (Apr. 2009), pp. 3467–3479. URL: https://doi.org/10.1021/ic801630z.

[105] Sanhita Ghosh et al. "Multi-frequency EPR studies of a mononuclear holmium single-molecule magnet based on the polyoxometalate [HoIII(W5O18)2]9-". In: *Dalton Trans.* 41 (44 2012), pp. 13697–13704. URL: http://dx.doi.org/10.1039/C2DT31674A.

[106] B. E. Kane. "A silicon-based nuclear spin quantum computer". In: *Nature* 393.6681 (May 1998), pp. 133–137. URL: https://doi.org/10.1038/30156.

[107] Mircea Trif et al. "Spin-Electric Coupling in Molecular Magnets". In: *Phys. Rev. Lett.* 101 (21 Nov. 2008), p. 217201. URL: https://link.aps.org/doi/10.1103/PhysRevLett.101.217201.

[108] Serwan Asaad et al. "Coherent electrical control of a single high-spin nucleus in silicon". In: *Nature* 579.7798 (Mar. 2020), pp. 205–209. URL: https://doi.org/10.1038/s41586-020-2057-7.

[109] Andrew Palii et al. "Electric field control of the optical properties in magnetic mixed-valence molecules". In: *Chem. Sci.* 5 (9 2014), pp. 3598–3602. URL: http://dx.doi.org/10.1039/C4SC01056F.

[110] Salvador Cardona-Serra et al. "Electrically Switchable Magnetic Molecules: Inducing a Magnetic Coupling by Means of an External Electric Field in a Mixed-Valence Polyoxovanadate Cluster". In: *Chemistry – A European Journal* 21.2 (2015), pp. 763–769. eprint: https://chemistry-europe.onlinelibrary.wiley.com/doi/pdf/10.1002/chem.201404055. URL: https://chemistry-europe.onlinelibrary.wiley.com/doi/abs/10.1002/chem.201404055.

[111] A. Gaita-Ariño et al. "Molecular spins for quantum computation". In: *Nature Chemistry* 11.4 (Apr. 2019), pp. 301–309. URL: https://doi.org/10.1038/s41557-019-0232-y.

[112] Matteo Atzori and Roberta Sessoli. "The Second Quantum Revolution: Role and Challenges of Molecular Chemistry". In: *Journal of the American Chemical Society* 141.29 (July 2019), pp. 11339–11352. URL: https://doi.org/10.1021/jacs.9b00984.

[113] W. Eerenstein, N. D. Mathur, and J. F. Scott. "Multiferroic and magnetoelectric materials". In: *Nature* 442.7104 (Aug. 2006), pp. 759–765. URL: https://doi.org/10.1038/nature05023.

[114] Fumihiro Matsukura, Yoshinori Tokura, and Hideo Ohno. "Control of magnetism by electric fields". In: *Nature Nanotechnology* 10.3 (Mar. 2015), pp. 209–220. URL: https://doi.org/10.1038/nnano.2015.22.

[115] Filippo Troiani. "Manipulation of spin cluster qubits by electric field induced modulation of exchange coupling, g-factor, and axial anisotropy". In: *Phys. Rev. B* 100 (15 Oct. 2019), p. 155424. URL: https://link.aps.org/doi/10.1103/PhysRevB.100.155424.

[116] Richard E. George, James P. Edwards, and Arzhang Ardavan. "Coherent Spin Control by Electrical Manipulation of the Magnetic Anisotropy". In: *Phys. Rev. Lett.* 110 (2 Jan. 2013), p. 027601. URL: https://link.aps.org/doi/10.1103/PhysRevLett.110.027601.

[117] F. R. Bradbury et al. "Stark Tuning of Donor Electron Spins in Silicon". In: *Phys. Rev. Lett.* 97 (17 Oct. 2006), p. 176404. URL: https://link.aps.org/doi/10.1103/PhysRevLett.97.176404.

[118] Junjie Liu et al. "Quantum coherent spin–electric control in a molecular nanomagnet at clock transitions". In: *Nature Physics* (Oct. 2021). URL: https://doi.org/10.1038/s41567-021-01355-4.

[119] W.B. Mims. *The Linear Electric Field Effect In Paramagnetic Resonance*. Oxford University Press, 1976. URL: https://books.google.co.uk/books?id=dTKaAAAAIAAJ.

[120] W. B. Mims. "Measurement of the linear electric field effect in EPR using the spin echo method". In: *Review of Scientific Instruments* 45.12 (1974), pp. 1583–1591. eprint: https://doi.org/10.1063/1.1686567. URL: https://doi.org/10.1063/1.1686567.

[121] Mircea Trif et al. "Spin electric effects in molecular antiferromagnets". In: *Phys. Rev. B* 82 (4 July 2010), p. 045429. URL: https://link.aps.org/doi/10.1103/PhysRevB.82.045429.

[122] Athanassios K. Boudalis, Jérôme Robert, and Philippe Turek. "First Demonstration of Magnetoelectric Coupling in a Polynuclear Molecular Nanomagnet: Single-Crystal EPR Studies of $[Fe_3O(O_2CPh)_6(py)_3]$ ClO_4py under Static Electric Fields". In: *Chemistry – A European Journal* 24.56 (2018), pp. 14896–14900. eprint: https://chemistry-europe.onlinelibrary.wiley.com/doi/pdf/10.1002/chem.201803038. URL: https://chemistry-europe.onlinelibrary.wiley.com/doi/abs/10.1002/chem.201803038.

[123] Jérôme Robert et al. "Polyanisotropic Magnetoelectric Coupling in an Electrically Controlled Molecular Spin Qubit". In: *Journal of the American Chemical Society* 141.50 (2019). PMID: 31762270, pp. 19765–19775. eprint: https://doi.org/10.1021/jacs.9b09101. URL: https://doi.org/10.1021/jacs.9b09101.

[124] Maria Fittipaldi et al. "Electric field modulation of magnetic exchange in molecular helices". In: *Nature Materials* 18.4 (Apr. 2019), pp. 329–334. URL: https://doi.org/10.1038/s41563-019-0288-5.

[125] Andrea Morello et al. "Donor Spins in Silicon for Quantum Technologies". In: *Advanced Quantum Technologies* 3.11 (2020), p. 2000005. eprint: https://onlinelibrary.wiley.com/doi/pdf/10.1002/qute.202000005. URL: https://onlinelibrary.wiley.com/doi/abs/10.1002/qute.202000005.

[126] Youngkyu Sung et al. "Realization of High-Fidelity CZ and ZZ-Free iSWAP Gates with a Tunable Coupler". In: *Phys. Rev. X* 11 (2 June 2021), p. 021058. URL: https://link.aps.org/doi/10.1103/PhysRevX.11.021058.

[127] Stephen von Kugelgen et al. "Spectral Addressability in a Modular Two Qubit System". In: *Journal of the American Chemical Society* 143.21 (June 2021), pp. 8069–8077. URL: https://doi.org/10.1021/jacs.1c02417.

[128] Richard Jozsa. "Fidelity for Mixed Quantum States". In: *Journal of Modern Optics* 41.12 (1994), pp. 2315–2323. eprint: https://doi.org/10.1080/09500349414552171. URL: https://doi.org/10.1080/09500349414552171.

[129] Michael A Nielsen. "A simple formula for the average gate fidelity of a quantum dynamical operation". In: *Physics Letters A* 303.4 (2002), pp. 249–252. URL: https://www.sciencedirect.com/science/article/pii/S0375960102012720.

[130] Ryszard Horodecki et al. "Quantum entanglement". In: *Rev. Mod. Phys.* 81 (2 June 2009), pp. 865–942. URL: https://link.aps.org/doi/10.1103/RevModPhys.81.865.

[131] Asher Peres. "Separability Criterion for Density Matrices". In: *Phys. Rev. Lett.* 77 (8 Aug. 1996), pp. 1413–1415. URL: https://link.aps.org/doi/10.1103/PhysRevLett.77.1413.

[132] Earl T. Campbell. "Distributed quantum-information processing with minimal local resources". In: *Phys. Rev. A* 76 (4 Oct. 2007), p. 040302. URL: https://link.aps.org/doi/10.1103/PhysRevA.76.040302.

[133] Martin B. Plenio and Shashank Virmani. "An Introduction to Entanglement Measures". In: *Quantum Info. Comput.* 7.1 (Jan. 2007), pp. 1–51. URL: http://dl.acm.org/citation.cfm?id=2011706.2011707.

[134] Yeong-Cherng Liang et al. "Quantum fidelity measures for mixed states". In: *Reports on Progress in Physics* 82.7 (June 2019), p. 076001. URL: https://doi.org/10.1088/1361-6633/ab1ca4.

[135] M. B. Plenio. "Logarithmic Negativity: A Full Entanglement Monotone That is not Convex". In: *Phys. Rev. Lett.* 95 (9 Aug. 2005), p. 090503. URL: https://link.aps.org/doi/10.1103/PhysRevLett.95.090503.

[136] M. S. Anwar et al. "Preparing High Purity Initial States for Nuclear Magnetic Resonance Quantum Computing". In: *Phys. Rev. Lett.* 93 (4 July 2004), p. 040501. URL: https://link.aps.org/doi/10.1103/PhysRevLett.93.040501.

[137] David G. Cory, Mark D. Price, and Timothy F. Havel. "Nuclear magnetic resonance spectroscopy: An experimentally accessible paradigm for quantum computing". In: *In Proceedings of the Fourth Workshop on Physics and Computation. New England Complex Systems Institute*. 1996.

[138] J.A. Jones. "NMR quantum computation". In: *Progress in Nuclear Magnetic Resonance Spectroscopy* 38.4 (2001), pp. 325–360. URL: https://www.sciencedirect.com/science/article/pii/S0079656500000339.

[139] Warren S. Warren. "The Usefulness of NMR Quantum Computing". In: *Science* 277.5332 (1997), pp. 1688–1690. URL: http://science.sciencemag.org/content/277/5332/1688.

[140] Ranabir Das, T. S. Mahesh, and Anil Kumar. "Efficient quantum-state tomography for quantum-information processing using a two-dimensional Fourier-transform technique". In: *Phys. Rev. A* 67 (6 June 2003), p. 062304. URL: https://link.aps.org/doi/10.1103/PhysRevA.67.062304.

[141] Soumya Singha Roy and T.S. Mahesh. "Density matrix tomography of singlet states". In: *Journal of Magnetic Resonance* 206.1 (2010), pp. 127–133. URL: https://www.sciencedirect.com/science/article/pii/S1090780710002028.

[142] Costantino S. Yannoni et al. "Nuclear magnetic resonance quantum computing using liquid crystal solvents". In: *Applied Physics Letters* 75.22 (1999), pp. 3563–3565. eprint: https://doi.org/10.1063/1.125389. URL: https://doi.org/10.1063/1.125389.

[143] Werner Scherer and Michael Mehring. "Entangled electron and nuclear spin states in N15@C60: Density matrix tomography". In: *The Journal of Chemical Physics* 128.5 (2008), p. 052305. eprint: https://doi.org/10.1063/1.2819310. URL: https://doi.org/10.1063/1.2819310.

[144] Navin Khaneja, Roger Brockett, and Steffen J. Glaser. "Time optimal control in spin systems". In: *Phys. Rev. A* 63 (3 Feb. 2001), p. 032308. URL: https://link.aps.org/doi/10.1103/PhysRevA.63.032308.

[145] Gunnar Jeschke and Yevhen Polyhach. "Distance measurements on spin-labelled biomacromolecules by pulsed electron paramagnetic resonance". In: *Phys. Chem. Chem. Phys.* 9 (16 2007), pp. 1895–1910. URL: http://dx.doi.org/10.1039/B614920K.

[146] Sunil Saxena and Jack H. Freed. "Theory of double quantum two-dimensional electron spin resonance with application to distance measurements". In: *The Journal of Chemical Physics* 107.5 (1997), pp. 1317–1340. eprint: https://doi.org/10.1063/1.474490. URL: https://doi.org/10.1063/1.474490.

[147] G. Jeschke et al. "Dipolar spectroscopy and spin alignment in electron paramagnetic resonance". In: *Chemical Physics Letters* 331.2 (2000), pp. 243–252. URL: https://www.sciencedirect.com/science/article/pii/S0009261400011714.

[148] A.D. Milov, A.B. Ponomarev, and Yu.D. Tsvetkov. "Electron-electron double resonance in electron spin echo: Model biradical systems and the sensitized photolysis of decalin". In: *Chemical Physics Letters* 110.1 (1984), pp. 67–72. URL: https://www.sciencedirect.com/science/article/pii/0009261484801487.

[149] A. D. Milov and Yu. D. Tsvetkov. "Double electron-electron resonance in electron spin echo: Conformations of spin-labeled poly-4-vinilpyridine in glassy solutions". In: *Applied Magnetic Resonance* 12.4 (May 1997), pp. 495–504. URL: https://doi.org/10.1007/BF03164129.

[150] Andrin Doll et al. "Gd(III)–Gd(III) distance measurements with chirp pump pulses". In: *Journal of Magnetic Resonance* 259 (2015), pp. 153–162. URL: https://www.sciencedirect.com/science/article/pii/S1090780715001779.

[151] Suzanne Brandon, Albert H. Beth, and Eric J. Hustedt. "The global analysis of DEER data". In: *Journal of Magnetic Resonance* 218 (2012), pp. 93–104. URL: https://www.sciencedirect.com/science/article/pii/S1090780712001061.

[152] A. Marko, V. Denysenkov, and T. F. Prisner. "Out-of-phase PELDOR". In: *Molecular Physics* 111 (Oct. 2013), pp. 2834–2844.

[153] J. Stark. "Beobachtungen über den Effekt des elektrischen Feldes auf Spektrallinien. I. Quereffekt". In: *Annalen der Physik* 348.7 (Jan. 1914), pp. 965–982.

[154] E. Burzurı´ et al. “Direct Observation of Magnetic Anisotropy in an Individual Fe_4 Single-Molecule Magnet”. In: *Phys. Rev. Lett.* 109 (14 Oct. 2012), p. 147203. URL: https://link.aps.org/doi/10.1103/PhysRevLett.109.147203.

[155] K. Fujisawa. “General Treatment of Klystron Resonant Cavities”. In: *IRE Transactions on Microwave Theory and Techniques* 6.4 (1958), pp. 344–358.

[156] Jian-She Wang and Nathan Ida. “Eigenvalue analysis in electromagnetic cavities using divergence free finite elements”. In: *IEEE Transactions on Magnetics* 27.5 (1991), pp. 3978–3981.

[157] Petr. P. Borbat and Jack. H. Freed. “Double-Quantum ESR and Distance Measurements”. In: *Distance Measurements in Biological Systems by EPR*. Ed. by Lawrence J. Berliner, Gareth R. Eaton, and Sandra S. Eaton. Boston, MA: Springer US, 2000, pp. 383–459. URL: https://doi.org/10.1007/0-306-47109-4_9.

[158] Jonathan A. Jones. *Composite pulses in NMR quantum computation*. J. Ind. Inst. Sci. 89, 303 (2009). 2009. eprint: arXiv:0906.4719.

[159] John J. L. Morton et al. “Measuring errors in single-qubit rotations by pulsed electron paramagnetic resonance”. In: *Phys. Rev. A* 71 (1 Jan. 2005), p. 012332. URL: https://link.aps.org/doi/10.1103/PhysRevA.71.012332.

[160] John J. L. Morton et al. “High Fidelity Single Qubit Operations Using Pulsed Electron Paramagnetic Resonance”. In: *Phys. Rev. Lett.* 95 (20 Nov. 2005), p. 200501. URL: https://link.aps.org/doi/10.1103/PhysRevLett.95.200501.

[161] Jonathan A. Jones. “Suppressing weak Ising couplings: tailored gates for quantum computation”. In: *Physics Letters A* 316.1 (2003), pp. 24–28. URL: http://www.sciencedirect.com/science/article/pii/S0375960103011307.

[162] Jonathan A. Jones. “Robust Ising gates for practical quantum computation”. In: *Phys. Rev. A* 67 (1 Jan. 2003), p. 012317. URL: https://link.aps.org/doi/10.1103/PhysRevA.67.012317.

[163] Jakub J. Mrozek. *Spinach Tomography Simulations*. https://github.com/msciwoj1/spinachent_jakub. 2021.

[164] Steven Worswick et al. “Deep neural network processing of DEER data”. In: *Science Advances* 4 (Aug. 2018), eaat5218.

[165] Donald F. Gatz and Luther Smith. “The standard error of a weighted mean concentration—I. Bootstrapping vs other methods”. In: *Atmospheric Environment* 29.11 (1995), pp. 1185–1193. URL: https://www.sciencedirect.com/science/article/pii/135223109400210C.